ISTANBUL TECHNICAL UNIVERSITY ★ EURASIA INSTITUTE OF EARTH SCIENCES

A NUMERICAL INVESTIGATION OF MESO-SCALE FLOW AND AIR POLLUTANT TRANSPORT PATTERNS OVER THE REGION OF ISTANBUL

Ph.D. Thesis by
Yasemin EZBER

Department : Climate and Marine Sciences

Programme : Earth System Science

Thesis Supervisor: Mehmet KARACA

DECEMBER 2009

ISTANBUL TECHNICAL UNIVERSITY ★ EURASIA INSTITUTE OF EARTH SCIENCES

A NUMERICAL INVESTIGATION OF MESO-SCALE FLOW AND AIR POLLUTANT TRANSPORT PATTERNS OVER THE REGION OF ISTANBUL

Ph.D. Thesis by
Yasemin EZBER
(601032004)

Date of submission : **14 September 2009**
Date of defence examination: **4 December 2009**

Supervisor (Chairman) : **Prof. Dr. Mehmet KARACA (ITU)**
Co-Supervisor : **Assoc. Prof. Dr. Ömer L. ŞEN (ITU)**
Members of Examining Committee : **Prof. Dr. H. Nüzhet DALFES (ITU)**
Assoc. Prof. Dr. Yurdanur S. ÜNAL (ITU)
Assoc. Prof. Dr. Ş. Sibel MENTEŞ (ITU)
Assoc. Prof. Dr. İsmail YÜCEL (METU)
Assis. Prof. Dr. Alper ÜNAL (ITU)

DECEMBER 2009

İSTANBUL TEKNİK ÜNİVERSİTESİ ★ AVRASYA YER BİLİMLERİ ENSTİTÜSÜ

İSTANBUL BÖLGESİ ÜZERİNDEKİ MEZO-ÖLÇEK AKIŞIN ve KİRLETİCİ TAŞINIM PATERNİNİN SAYISAL OLARAK İNCELENMESİ

DOKTORA TEZİ

Yasemin EZBER
(601032004)

Tezin Enstitüye Verildiği Tarih : 14 Eylül 2009
Tezin Savunulduğu Tarih : 4 Aralık 2009

Tez Danışmanı : Prof. Dr. Mehmet KARACA (İTÜ)
Eş Danışman : Doç. Dr. Ömer L. ŞEN (İTÜ)
Diğer Jüri Üyeleri : Prof. Dr. H. Nüzhet DALFES (İTÜ)
Doç. Dr. Yurdanur S. ÜNAL (İTÜ)
Doç. Dr. Ş. Sibel MENTEŞ (İTÜ)
Doç. Dr. İsmail YÜCEL (ODTÜ)
Yrd. Doç. Dr. Alper ÜNAL (İTÜ)

ARALIK 2009

To my family

My mother, my father, my sisters, and my brother

FOREWORD

Understanding of the circulation dynamics is essential to obtain the knowledge of the underlying mechanism of the weather systems, which play important role on the day-to-day life of human being. Thermally driven mesoscale circulations such as sea-land breeze and urban heat island circulations are important since they contribute to the microscale properties over regions. Diurnal cycle of the circulations may influence the quality of the air either positively or negatively. Urbanization is the most significant negative effect since it brings more polluted air over a region. The sea-land breeze circulation may result in more air pollution by interacting with urban heat island circulation or controversially it may keep the pollution away from the region. This study is conducted to understand the mesoscale circulations interaction in Istanbul and their effects on the air pollution.

This thesis owes its existence to the help, support, and inspiration of many people. In the first place, I would like to thank to my advisor, Prof. Dr. Mehmet Karaca for his supervision, advice, and guidance from the first to the final level. I am indebted to my co-advisor Assoc. Prof. Dr. Ömer L. Şen for his guidance of this research and for being always available for scientific discussions. I also would like to thank one of my committee members, Prof. Dr. Mete Tayanç for his helpful and insightful advices during my presentations. I also would like to thank members of my Advisory Committee, Prof. Dr. Nüzhet Dalfes, Assoc. Prof. Dr. Yurdanur S. Ünal and members of my Doctoral Examination Committee, Assoc. Prof. Dr. Sibel Menteş, Assoc. Prof. Dr. İsmail Yücel and Assist. Prof. Dr. Alper Ünal for their time and guidance.

I owe my deepest gratitude to Assoc. Prof. Dr. Zafer Boybeyi from George Mason University, who provided me the opportunity to work in his lab, Laboratory for Atmospheric Hazardous Modelling. He has made available his support in a many ways. This thesis would not have been possible without his support. His valuable advice in scientific discussions, his constructive comments and crucial contributions to my research deserve my greatest acknowledgments. I also thank for him for his financial support during my stay in US. I am also heartily thankful to his wife, Ayşe Boybeyi, for her hospitality when I first went to US and for her friendship during my stay in US.

I would like to thank to the Scientific and Technological Research Council of Turkey for providing scholarship and initial financial support to my research. I would also thank to Turkish Meteorological Service for providing me observation data.

My gratitude extends to Dr. Ananthakrishna Sarma and Dr. Nash'at Ahmad for their time and patience for answering my questions. I would also like to thank to Dr. Guido Cervone, who helps me with data managing and makes me simile with his jokes.

I would also like to thank to my roommates and lab mates who make my life easy in US. Huma Tasleem for sharing happiness and sadness, cheerful conversations about

life, religion and culture and for helping me when I was adopting the life in US. Sujata Nyhan for the conversations about religion and life and for her help to improve my knowledge about language and culture. The wonderful people at the Laboratory for Atmospheric Hazardous Modelling who have always been helpful, made the environment warmth and enjoyable so that I never felt alone: Jacek Radzikowski, Priyanka Roy, Laura Clemente and John Lindeman. My special thanks go to Dr. József Bakosi, whenever I had a problem with our clusters he solved immediately. It would not have been possible to complete my simulations without his help.

I am also thankful to my friends for their continuous supports throughout the years. One of my best friends, Ümmühan Saadet Sancar, who always encourages and makes me feel strong during our long conversations. Special thanks go to my lovely friend, Aşse Gül Güngör, for her support, guidance, and for our mostly enjoyable but sometimes dangerous road trips. Thanks for encouraging me anytime and also thanks for your time for reading and correcting my manuscript. I would like to extend my thanks to my friend Demet Biltekin and Beyza Ustaoğlu.

The last but not least, my deepest gratitude goes to my parents, my mom Zehra Ezber and my dad Bayram Ezber , who never ceased encourage and believe in me from the beginning until the accomplishment of my thesis. I would like to thank to my sisters, Seçil Ezber, H. Sevil Ezber, Yeşim Ezber Yıldızöz, my brother Ufuk Ezber and my brother-in-law Hakan Yildizoz for their love and supports. And I would also thank to my little niece, Ecem Yıldızöz, for providing me more energy with her being to finish my thesis.

December 2009

Yasemin Ezber

Climate and Marine Sciences

TABLE OF CONTENTS

Page

ABBREVIATIONS

ADM : Atmospheric Dispersion Model
AT&D : Atmospheric Transport and Dispersion
AWOS : Automatic Weather Observation Station
AVHRR : Advanced Very High Resolution Radiometer
AVN : National Center for Environmental Prediction Aviation
BATS : Biosphere-Atmosphere Transfer Scheme
BS : The Black Sea
CBL : Convective Boundary Layer
CCN : Cloud Condensation Nuclei
CFD : Computational Fluid Dynamics
FNMOC : Fleet Numerical Meteorology and Oceanography Center
GED : Global Ecosystem Database
GMT : Greenwich Mean Time
GVI : Global Vegetation Index
HIC : Heat Island Circulation
IN : Ice Nuclei
LAI : Leaf Area Index
LCL : Lifting Condensation Level
LES : Large Eddy Simulations
LST : Local Standard Time
LW : Longwave radiation
mAE : Mean Absolute Error
mE : Mean Error
METROMEX : METROpolitan Meteorological Experiment
MM5 : The Fifth Generation Mesoscale Model
MODIS : Medium Resolution Imaging Spectroradiometer
MRF : Medium Range Forecast
MS : The Marmara Sea
NCAR : National Center for Atmospheric Research
NCEP : National Center for Environmental Prediction
NDVI : Normalized Difference Vegetation Index
NOGAPS : Navy Operational Global Atmospheric Prediction System
OI : Optimum Interpolation
OMEGA : Operational Multi-scale Environment model with Grid Adaptivity
PBL : Planetary Boundary Layer
PSU : Penn State University
RAMS : Regional Atmospheric Model System
RMSE : Root Mean Square Error
RRTM : Rapid Radiative Transfer Model
SAIC : Science Applications International Corporation
SB : Sea Breeze
SBC : Sea Breeze Circulation

SST **:** Sea Surface Temperature
T&D **:** Transport and Diffusion
TKE **:** Turbulence kinetic energy
UBL **:** Urban Boundary Layer
UHI **:** Urban Heat Island
USGS **:** U.S. Geological Survey
WRF **:** Weather Research and Forecasting

LIST OF TABLES

Page

LIST OF FIGURES

Page

LIST OF SYMBOLS

A	Advection
A_S	Soil albedo depending on soil wetness
A_g	Soil Albedo
A_o	Basic soil albedo
A_p	Cross-sectional area of the spherical particle
A(z)	Root extraction
a	Aerosol or gases
b	Parameter indicator for moistening
C	Cloud production per unit time and concentration
C_1	Coefficient of soil textures
C_2	Coefficient of soil hydraulic conductivities
C_D	Drag coefficient
C_I	Specific heat of ice
C_T	Thermal capacity
C_g	Capacity of soil
C_p	Specific heat at constant pressure
C_s	Specific heat of soil
C_{veg}	Capacity of vegetation
C_w	Specific heat of water
c_{i+1}	Total path length for carbon dioxide
D	Particle diameter
D_η	Diffusivity
D_v	Diffusivity of water vapor in air
d_1	Top soil thickness
d_2	Deep soil thickness
d_e	Stack exit diameter
d_s	Soil depth
E	Evapotranspiration or energy density
E_g	Evaporation from the soil surface
E_r	Direct evaporation
E_{tr}	Transpiration from vegetation canopy
E_v	Evaporation from the vegetation
E_{RCD}	Collection efficiency of cloud droplets
E_{SCI}	Collection efficiency of snow
e	Turbulent kinetic energy and Coriolis force
e_{sat}	Saturation water-vapor partial pressure
e_{si}	Saturation vapor pressure over ice
e_{sw}	Saturation vapor pressure over water
F	Buoyancy flux or sub-grid scale turbulence contribution
f_g	Cloud mass fraction reaching the ground reaching the ground reflected back into the cloud

f_m	Cloud mass fraction reaching the ground reaching the mixed layer reflected back into the cloud
f_{root}	Fraction of root
G_o	Heat storage rate in the soil-vegetation medium
g	Gravity acceleration
H	Solar hour angle
$H_{anthrop}$	Anthropogenic heat flux
H_o	Sensible heat flux
H_s	Stack height
H_{ts}	Uppermost stretchable levels
h_w	Maximum storage of water
I_s	Thermal inertia
K	Eddy diffusivity
K_η	Hydraulic conductivity
$K_{\eta s}$	Saturated hydraulic conductivity
k	von-Karman's constant
k_T	Thermal conductivity of air
L	The Monin-Obukov length
L_c	Latent heat of condensation
L_f	Latent heat of fusion
L_{hf}	Latent turbulent surface heat flux
L_j	Latent heat
L_s	Latent heat of sublimation
L_v	Latent heat of vaporization
L_cE_o	Latent heat flux
L	Turbulent length scale
l_∞	Primary length scale
M_1	Condense and precipitate part of moisture
M_2	Remainder of moisture
M_c	Total amount of water vapor
M_n	Non-precipitating microphysics
M_p	Particle momentum or precipitating microphysics
M_s	Heat consumed for melting snow
M_t	Total rate of moisture accession
M	Map scale factor
N	Vertical layer indicator or total number of vertical levels
N_E	Effective cloud cover
N_L	Low cloud cover
N_{OR}	Inverse exponential distribution of rain
N_{OS}	Inverse exponential distribution of snow
N_T	Total cloud cover
N_c	Cloud condensation nuclei
$N_{(dR)}$	Number concentration for rain
$N_{(dS)}$	Number concentration for snow
N_s	Number of stretchable levels
N_{sc}	Schmidt number
n	A positive exponent
n_{IN}	Number concentration of ice nuclei
P	Precipitation rate or pressure (mb)
P_{IDEP}	Ice deposition rate

P_j	Pressure at j^{th} vertical layer (in mb)
P_g	Ground surface flux of liquid water
P_{ref}	Reference pressure
P_{RAC}	Production rate of raindrop via collection of cloud droplets
P_{RACV}	The rate of rain from cloud droplets via autoconversion
P_{RCND}	Rate of condensation on raindrop
P_{SACI}	Production rate of snow via collection of ice
P_{SDEP}	Rate of deposition onto snow
P_{SRCV}	Rate of cloud ice conversion to snow
pr_{cl}	Rate of precipitation in the column
Q	Mass of puff
Q_C	Cloud droplets mixing ratio
Q_I	Ice mixing ratio
Q_{IMAX}	Maximum cloud ice ratio
Q_R	Mixing ratio of rain
Q_S	Mixing ratio of snow
Q_V	Mixing ratio of water vapor
Q_n	Non-precipitating water substances
Q_p	Precipitating water substances
Q_{si}	Saturation mixing ratio over ice
Q_v	Water vapor
Q_{vs}	Saturation mixing ratio over water
q	Moisture or mixing ratio
q_1	Specific humidity at the first model layer
q_a	The air mixing ratio over the sea
q_c	Cloud column mixing ratio
q_e	Environment mixing ratio
q_s	Saturation mixing ratio or surface air humidity
q_{sat}	Saturation mixing ratio
q_*	Sub-grid scale moisture flux
$R\uparrow$	Upward radiative flux
$R\downarrow$	Downward radiative flux
RH	Relative humidity
RH_c	Critical relative humidity
$\overline{RH}$	Mean environmental relative humidity
R_L	Longwave radiation
R_S	Net shortwave solar radiation
R_o	Net radiation at the surface
R_d	Gas constant of day air
R_e	Reynolds number
R_r	Runoff
$R_{u'}$	Auto-correlation coefficient for u velocity component
$R_{v'}$	Auto-correlation coefficient for v velocity component
$R_{w'}$	Auto-correlation coefficient for w velocity component
r_c	Mean cloud droplet radius
r_{earth}	Curvature effect
r	Optical path length or precipitation
r_{i+1}	Total path length for water vapor
$\hat{r}$	The radial unit vector
S	Atmospheric stability or moisture surplus

S_j	Rate of phase conservation
S_o	Solar constant
S_t	Tracer source/sink
S_H, S_M	Non-dimensional eddy diffusivity
S_R	Contribution of radiation flux
SR	Radiative source/sink term
T	Ambient temperature
T_G	Temperature at the ground level
T_M	0^oC
T_c	Cloud column temperature
T_{ds}	Mean soil temperature
T_e	Stack gas exit temperature, environment temperature
T_s	Skin temperature
T_{sea}	Surface temperature of the water body
T_{top}	Temperature at the model top
$T_L^{u'}, T_L^{v'}, T_L^{w'}$	Lagrangian integral time scale of the sub-grid scale turbulence
t	Travel time or local time in hours
t_g	Ground temperature
u	Horizontal velocity in x direction
u_1	Wind speed at 30 m
u_2	Wind speed at 10 m
u_*	Friction velocity
$\bar{u}$	Resolvable scale wind component in x direction
u'	Sub-grid scale turbulent velocity fluctuation in x direction
u''	Random uncorrelated turbulent velocity component in x direction
V	Horizontal wind speed
V_1	Wind speed at the first model layer
V_o	Wind speed at the surface layer
V_s	Critical wind speed for stable conditions
V_n	Critical wind speed for unstable or neutral conditions
V_t	Vertical velocity
v_e	Stack gas exit speed
v	Horizontal velocity in y direction
$\bar{v}$	Resolvable scale wind component in y direction
v'	Sub-grid scale turbulent velocity fluctuation in y direction
v''	Random uncorrelated turbulent velocity component in y direction
veg	Vegetation fraction
W	Vertical velocity
W_1	Soil moisture at the beginning of the month
W_2	Soil moisture at the beginning of the month
W_R	Fall velocity of rain
W_S	Fall velocity of snow
W_a	Terminal velocity of hydrometeors
W_d	Amount of liquid water
W_{dmax}	Maximum amount of liquid water
W_p	Terminal velocity of precipitating water substances
W_r	Interception water store
W_{rmax}	Maximum of the reservoir water content
W_s	Soil moisture flux

w	Particle velocity perpendicular to the ground
w_{fl}	Soil moisture field capacity (soil porosity)
w_{g1}, w_{g2}	Moisture content of the top and deep soil
w_{sat}	Soil moisture saturation value
w_{wilt}	Soil moisture at wilting point
w_o	Vertical velocity at the surface
w_p	Plume rise
$\overline{w}$	Resolvable scale wind component in z direction
w'	Sub-grid scale turbulent velocity fluctuation in z direction
w''	Random uncorrelated turbulent velocity component in z direction
x,y,z	Particle position
x_c,y_c,z_c	Position of the puff center point
x_i,y_i,z_i	Position of receptor
Z	Solar zenith angle
Z_m	Mixed layer height
Z_{max}	Maximum plume rise
z	Height
z_1	The height of the first model layer
z_{cb}	Bottom of the cloud
z_{ct}	Top of the cloud
z_o	Surface roughness height
z_t	Model top
z'	Local vertical direction
α	Drag coefficient multiplier or constant coefficient
α_i	Local geometric factor
α_{max}	Maximum geometric factor
β_g	Halstedt parameter
δ	Solar declination or canopy fraction
δ_c	Indicator of land/water
δ_s	Density of snow
δ_w	Density of water
ε	Total emissivity or energy dissipation
ε_g	Ground surface emissivity
ε_r	Emissivity for water vapor
ε_{CO_2}	Emissivity for carbon dioxide
ϕ	Longitude
ϕ_c	Central longitude
η	Volumetric soil moisture content
η_1	Upper layer volumetric water content
η_2	Lower layer volumetric water content
η_{fs}	Field capacity
η_s	Soil moisture
χ	Dosage or gaseous and atmospheric materials
χ_1	Gas concentration at the first model layer
χ_s	Gas concentration at the surface
Λ_R	Slope of inverse-exponential distribution of rain
Λ_S	Slope of inverse-exponential distribution of snow

λ	Latitude
λ_s	Thermal soil conductivity
∇r	Radial gradient
υ	Molecular viscosity
υ_m	Molecular viscosity
μ	Dynamic viscosity
μ_D	Dynamic viscosity
ρ	Density of air
ρ_o	Air density at the surface layer
ρ_a	Ambient air density
ρ_p	Particle density
ρ_s	Density of soil
ρ_w	Density of liquid water
$\rho_i\, c_i$	Dry volumetric soil heat capacity
$\rho_s\, c_s$	Soil heat capacity
$\rho_w\, c_w$	Liquid water heat capacity
Ω	Angular velocity of the earth
Ψ	Latitude or moisture potential
Ψ_M, Ψ_H	Integral functions
Ψ_m, Ψ_h	Dimensionless stability functions of height
Ψ_s	Saturated moisture potential
σ	Stefan-Boltzmann's constant or dispersion coefficient of the cloud droplet distribution and sigma coordinate system
$\dot{\sigma}$	Total derivation of sigma coordinate system
σ_h	Horizontal standard deviation
σ_x	Variance in x direction
σ_y	Variance in y direction
σ_z	Variance in z direction
σ^2_{ru},	Radiance for sub-grid scale turbulent velocity component in x direction
σ^2_{rv},	Radiance for sub-grid scale turbulent velocity component in y direction
σ^2_{rw},	Radiance for sub-grid scale turbulent velocity component in z direction
τ_1	Period of one day
θ	Potential temperature
θ_1	Potential temperature at the first model layer
$\bar{\theta}$	Average air temperature near the surface
θ_e	Equivalent potential temperature
θ_s	Potential temperature at surface
θ_{sfc}	Potential temperature at surface
θ_*	Sub-grid scale temperature flux
Δcj	Path length for carbon dioxide
ΔQ_1	Amount of water vapor condensed
ΔQ_2	Amount of extra vapor
ΔQ_{CCND}	Amount of water vapor to be condensed
ΔQ_{FRZN}	Amount of freezing raindrops
ΔQ_{IMLT}	Amount of melting ice

ΔQ_{SMLT}	Amount of melting snow
ΔQ_{I1}	Maximum ice mixing ratio
ΔQ_{I2}	Maximum ice mixing ratio driven by supersaturation
ΔQ_{ICWV1}	Condensation adjustment
ΔQ_V	Amount of condensed water vapor
Δrj	Path length for water vapor
Δt	Time interval
Δz_o	The height of the first layer of triangle

A NUMERICAL INVESTIGATION OF MESO-SCALE FLOW AND AIR POLLUTANT TRANSPORT PATTERNS OVER THE REGION OF ISTANBUL

SUMMARY

Atmospheric motion is affected by wide range of scales from a few millimeters to thousands of kilometers. It is important to understand the behaviour of the atmospheric flows on these scales. Although all these scales play a role on the transport and dispersion of the pollutant, mesoscale atmospheric processes are significant over the traveling time and distance for short and long-range transport and dispersion of pollutants. Thermally and terrain induced circulations contribute to the transport and dispersion pattern of the pollutants via terrain characteristics and the surface inhomogeneities. Besides of these, growing urbanization modify the mesoscale circulation characteristics. The response of the local-scale circulation to the other scales or its interaction with them influences the characteristics of pollutant transport by means of the modified mesoscale circulation. Therefore, understanding mechanism of the development and evolution of local-scale flow features and their interaction with large-scale flow features is one of the desires.

The research is concentrated on the mesoscale circulations (i.e. sea-land breeze, urban heat island). It is focused on a statistical and numerical investigation of the urbanization in Istanbul in the first part of the study. Mann-Kendall Trend test is applied to the minimum temperature dataset for urban, suburban and rural station in Istanbul to determine the existence and significance of trends, and starting year for the abrupt change in the trends. Limited area, non-hydrostatic, terrain-following sigma coordinate mesoscale model MM5 is also used for the modeling analyses. Mann-Kendall test indicates the statistically significant positive trends in the minimum temperature time series between urban and rural stations. Seasonal trend analyses depicts that the most pronounce urbanization effect occurs in summer. The changes in the trends are observed in 1970s and 1980s consistent with the increase in the population growth rate. The model results show the expansion of the urban heat island depending on the expansion of the city boundaries in Istanbul from 1951 to 2004. A two-cell structure of the urban heat island: one on the European side and the other one on the Asian side is observed at the surface from the July simulations with current and past landscape. The maximum surface level temperature difference between past and current simulations is about 1^{o}C. The modeling experiment shows that the city reduces the prevailing northeasterly wind speed and water vapor mixing ratio. The heating effect of the urbanization penetrates about 600-800 m height in the atmosphere over the city, and the two surface heat island cells combines aloft.

The idealized numerical simulations are performed on the second part of the study to investigate the details of the mesoscale circulations such as sea-land breezes and urban heat island effect on the local flow of Istanbul. A fully non-hydrostatic, three-

dimensional numerical model (OMEGA) with unstructured grid and uniform initial flow at horizontal and vertical directions is performed for the simulations since its grid technique better captures the land-water boundaries. Relative effects of geographic features on the local circulation are exemplified by means of the idealized simulations. Furthermore, effect of the presence of a strait and urbanized area on the local circulation is analyzed. Topography-induced effect is observed over the hilly topography of Istanbul. Moreover, different background flow conditions are also examined for Istanbul. Uniform geostrophic wind with different wind direction also shows changes on the circulation characteristics. Results show that the channeling is occurred because of the Bosphorus and enhanced by the topography. Significant contribution to the local flow comes from urbanization by arranging the sea-land breeze existence or penetration over the domain. Real case simulations are also performed using OMEGA based on atmospheric conditions which are required for existence of a sea breeze and urban heat island over the Bosphorus. Furthermore, the analyses are conducted for two different dates. One of these dates is specified in summer and the other one is in winter. The flow conditions on these dates are compared and evaluated in the light of hypothetic simulations. The results show that OMEGA performs reasonably well. The fully developed sea breeze exits at 1000 UTC (1200 LST) in winter case while it is observed at 0700 UTC (1000 LST) in summer case. Re-current circulations are also observed on both simulations. However, it occurs higher in the atmosphere in summer case than the winter case. The convergence occurs at 1300 UTC (1500 LST) in winter case and 1000 UTC (1300 LST) in summer case. The land breeze occurs at 1700 UTC (1900 UTC) in winter whereas it is at 1900 UTC (2200 LST) for summer simulation.

Another concern on this study is to investigate the behaviour of transport and dispersion of pollutants over the Marmara Region using numerical model (OMEGA) with its embedded Atmospheric Dispersion Model (ADM). The Marmara Region is located at strategically important waterway with its two narrow straits, the Bosphorus and the Dardanelles. The particular attention is focused on mapping risky area for the Straits, resulting from release of pollutants after a tanker accident. Lagrangian dispersion model is used to disperse materials from the specified release points. Probability of exceedance of dosages is calculated at the surface for these release points. Results depict the most common direction of the particle dispersion is south-southwesterly, and the most risky areas are located close to the release points. Also, the sensitivity simulations depict that the probability of exceedance values are sensitive to the source strength and threshold values of dosage and concentration.

İSTANBUL BÖLGESİ ÜZERİNDEKİ MEZO-ÖLÇEK AKIŞIN VE KİRLETİCİ TAŞINIM PATERNİNİN SAYISAL OLARAK İNCELENMESİ

ÖZET

Atmosferik hareket, birkaç milimetre'den birkaç kilometere'ye kadar geniş bir ölçek aralığından etkilenir. Bu nedenle, atmosferik akışın bu ölçeklerdeki davranışını anlamak oldukça önemlidir. Bütün bu ölçeklerin kirletici taşınım ve yayılımında önemli rolü olmasına rağmen, mezo-ölçek atmosferik işlemler, kirleticilerin kısa ve uzun mesafeli taşınım ve yayılımı için taşınma zamanı ve mesafesi üzerindeki rolü bakımından önemlidir. Termal ve topoğrafya etkisi ile oluşan sirkülasyonlar, topoğrafya karakteristikleri ve homojen olmayan yüzeyler yardımı ile kirleticilerin taşınım ve yayılımına katkıda bulunur. Bunların yanısıra, artan şehirleşme de mezo ölçek dolaşım karakteristiklerini değiştirmektedir. Lokal ölçekteki dolaşımların diğer ölçeklerdeki hareketlere tepkisi ya da onlarla olan etkileşimi, mezo-ölçek dolaşımların kirletici taşınım karakteristiklerini etkiler. Bu nedenle, küçük ölçek akışların oluşum ve gelişimi ve küçük ölçek hareketlerin büyük ölçek haraketlerle ekileşimini anlamak gerekmektedir.

Bu çalışmada, kara-deniz meltemi, şehir ısı adası gibi mezo-ölçek dolaşımlar incelenmiştir. Çalışmanın ilk kısmında, İstanbul'da şehirleşmenin istatistiksel ve sayısal olarak incelenmesi üzerinde durulmuştur. Mann-Kendall trend testi, İstanbul'daki trendin olumasını ve önemini ve ani trend değişikliğinin başlamasını belirlemek için, şehir, banliyö ve kırsal alanlardaki gözlem istasyonlarının minimum sıcaklık verilerine uygulanmıştır. Bununla birlikte, sınırlı alan, hidrostatik olmayan ve topoğrafyayı takip eden koordinatları kullanan, bir mezo-ölçek atmosfer model olan MM5'da modelleme analizlerinde kullanılmıştır. Mann-Kendall istatistik testi şehir ve kırsal alanlar arasındaki minimum sıcaklıklarda istatistiksel olarak anlamlı pozitif bir trendin olduğu gözlenmiştir. Mevsimsel analizler ise, şehirleşmenin yaz aylarında hakim olduğunu göstermiştir. Artan nüfus ile birlikte trenddeki ani değişikliklerin 1970 ve 1980'li yıllarda meydana geldiği tespit edilmiştir. Model çalışmaları ise, İstanbul'un genişleyen şehir sınırları ile birlikte şehir ısı adasının da 1951'den 2004'e genişlediğini göstermiştir. Temmuz ayı için gerçekleştirilen, geçmiş ve şuanki durumu temsil eden şehir görünümü benzeşim farklarından, şehrin Avrupa ve Asya yakasında, iki-hücreli şehir ısı adası yapısının varlığı tespit edilmiştir. İki benzeşim için, yüzey sıcaklığındaki maksimum fark yaklaşık 1^{o}C'dir. Model çalışması, şehrin hakim kuzeydoğulu rüzgar hızının ve subuharı karışma oranının azaldığını göstermiştir. Şehirleşmenin neden olduğu ısınma etkisi, şehir üzerinde 600-800 m yüksekliğe kadar etkisini sürdürmekte ve yukarı seviyelerde meydana gelen iki ısı adası hücresi birleşmektedir.

Çalışmanın ikinci kısmında, idealize edilmiş sayısal benzeşimler, kara-deniz meltemi ve şehir ısı adası gibi mezo-ölçek dolaşımların İstanbul'un yerel akışına etkisinin detaylı olarak incelenmesi için gerçekleştirilmiştir. Kara-su sınırlarını daha iyi cozen bir grid tekniğine sahip olmasından dolayı, düzensiz (unstructured) grid yapısı olan

üç boyutlu hidrostatik olmayan sayısal bir model olan OMEGA, yataydaki homojen başlangıç rüzgarı, yerden modelin en üst atmosferik sınırına kadar kullanılarak ideal sayısal benzeşimler yapmak için çalıştırılmıştır. Yapılan ideal sayısal benzeşimler yardımı ile, göreceli olarak bölgenin coğrafi özelliklerinin; İstanbul Boğazı'nın ve şehirleşmenin lokal dolaşımlara etkisi incelenmiştir. Yapılan önceki araştırmalarda, topoğrafyanın yüksek olmadığı bölgelerde, topoğrafyanın lokal sirkülasyona etkisi olmadığı ifade edilmesine rağmen, İstanbul ve çevresinde varolan topoğrafyanın dolaşımı etkilediği görülmektedir. Sayısal modelin farklı başlangıç rüzgarları ile de benzeşim çalışmaları yapılmış ve dolaşım karakteristikleri farklılıklar göstermiştir. Araştırma sonuçları, İstanbul Boğazı'nın bir kanal akışının oluşumuna neden olduğunu ve topoğrafyanında bu akışı güçlendirdiğini göstermektedir. Şehirleşme, kara-deniz melteminin oluşmasını ve kara içlerine ilerlemesini düzenleyerek, lokal akışa katkıda bulunur. İdeal sayısal benzeşimlere ilave olarak, kara-deniz meltemi ve şehir ısı adası oluşumu için gerekli şartları sağlayan gerçek zamanlı benzeşimler de gerçekleştirilmiştir. Her bir ideal benzeşimin lokal sirkülasyona katkısı detaylı olarak incelenmiştir. Ayrıca, analizler yaz ve kış aylarındaki durumu belirlemek amacı ile, belirlenen iki gün için gerçek zamanlı simülasyonlar gerçekleştirilmiştir. Gerçekleştirilmiş olan hipotetik benzeşimlerin sonuçları ışığında bu iki simülasyon karşılaştırılmış ve değerlendirilmiştir. Sonuçlar, OMEGA'nın oldukça iyi bir şekilde belirlenen tarihler için benzeşimler gerçekleştirdiğini göstermiştir. Kış benzeşimi için deniz melteminin 1000 UTC (1200 LST) meydana gelirken, yaz simülasyonu için 0700 UTC'de (1000 LST) meydana geldiğini göstermiştir. Her iki simülasyonda da yukarı seviyelerde tersine dolaşımlar meydana gelmiş ancak, yaz ayında meydana gelen dolaşımın atmosferin daha yukarı seviyelerinde olduğu gözlenmiştir. Konverjans ise kış ayı için 1300 UTC (1500 LST) ve yaz ayı için 1000 UTC'de (1300 LST) meydana gelmektedir. Kara meltemi ise, kış benzeşimi için 1700 UTC (1900 UTC) ve yaz ayı için 1900 UTC'de (2200 LST) başladığı tespit edilmiştir.

Bu araştırmada yürütülen diğer bir çalışmada, sayısal model OMEGA ve atmosferik yayılma modelini kullanılarak Marmara Bölgesi'ndeki kirleticilerin taşınım ve yayılımı incelenmiştir. İstanbul ve Çanakkale Boğazları ile önemli bir su yolu olan Marmara Bölgesi, stratejik olarak önem arz etmektedir. Çalışmanın bu bölümünde, meydana gelebilecek bir tanker kazası sonucunda kirletici salınımının risk haritasının hazırlanmasına çalışılmıştır. Belirlenen noktalardan atmosfere salınan kirleticilerin dağılımı, Lagrangian yayılma modeli kullanılarak belirlenmiştir. Çalışmada, kirletici salınım noktaları için, kirletici dozunun oluşma olasılığı hesaplanmıştır. Sonuçlar yaygın partikül yayılma yönünün güney-güneydoğulu olduğunu ve oluşma olasılığının kirletici salınım noktalarına yakın bölgelerde yüksek olduğunu göstermiştir. Ayrıca yapılan duyarlılk testleri ile oluşma olasılığının, kaynaktan çıkan kirletici miktarına ve konsantrasyon ve dozaj için belirlenen eşikdeğerine hassas olduğu tespit edilmiştir.

1. INTRODUCTION

A major problem in the atmospheric science is to describe the atmospheric motion fully. Atmospheric motion ranges in size from a few millimeters (e.g., turbulence) to thousands of kilometers (e.g., planetary waves). Energy spectrum divides the atmospheric motion in three different scales; large scale, mesoscale, and micro scale. This scale differentiation of horizontal dimensions makes our understanding in atmospheric circulations difficult. Not in all size of atmospheric motions can be explained by the same theoretical approaches since some terms weaken or enhance their effects from scale to scale. For instance, large scale motions are strongly affected by the Coriolis force however dominant governing effect of the motion is not the Coriolis force in other scales such as mesoscale or microscale. Aside from the horizontal spatial scale, atmospheric circulations indicate variability in time from a few days (e.g. depressions) to a few seconds (e.g. turbulence). It appears from the kinetic energy spectrum that the mesoscale is the scale on which energy is transferred from large scale to the microscale or vice versa (Lin, 2007).

Mesoscale flow features are quite complex and variable in all scales. Mesoscale flow may be either hydrostatic or non-hydrostatic. Hydrostatic motion contains motions with the scale larger than the non-hydrostatic motion which is embedded in the hydrostatic motion. However, non-hydrostatic motion ranging from several meters to several tens of kilometers with time scale from minutes to many hours may include significant features (Boybeyi and Bacon, 1996). It is difficult to discriminate dynamics of motions due to nonlinear interactions of time and space scale. Therefore, scale interaction is significant in terms of understanding the characteristics of the flow. For example, scale interaction refers to the interaction between the zonal flow and limited set of waves in the planetary-scale motion while it means the interaction between a continuous spectrum of eddies in all sizes in turbulence theory. And in mesoscale meteorology, scale interaction is expressed as the interaction among the discrete scales as the meso-γ, the meso-β, and the meso-α (Boybeyi and Raman, 2000). Horizontal scale of meso-γ is defined 2 km-20 km, the

meso-β 20 km-200 km, and the meso-α 200 km- 2000 km by Stull (1988). Scale interaction depends on the degree of relative strength of the fluid motion, for instance; for a slowly changing mean flow with embedded very weak disturbance, the interaction occurs from the mean flow to the weak disturbance (Lin, 2007).

Effect of terrain heterogeneities and surface inhomogeneties on mesoscale circulation evolution and the synoptic forcing of the mesoscale circulation are the examples for scale interactive processes at the mesoscale. Lee cyclogenesis, sea-land breeze, urban heat island circulation, mountain-valley winds, cumulus scale convection, tropical cyclones, squall lines, tornadoes, mesoscale rain bands, Kelvin-Helmholtz instability waves, inertial gravity waves, fronts and jet breaks can be ranked in the mesoscale circulations. The large number of mesoscale processes is responsible for natural disaster, flash flooding, and wind damaging (Lin, 2007). In addition to these hazardous events, mesoscale weather system is important for short and long range transport and diffusion of air pollutants.

Mesoscale diffusion takes place between local scale and synoptic scale dispersion. Since local scale features affects the mesoscale circulations by means of the terrain heterogeneities and surface inhomogeneties, mesoscale processes become more complex. Thus, determining the mesoscale dispersion can not be easily accomplished. Therefore, it is crucial to identify the development and evolution of the local scale flow. Besides, it is necessary to have information of interaction between local scale and mesoscale circulation as well as interaction with synoptic scale motion. Although atmospheric processes are divided into scales, it is not possible to isolate each scale since in reality all those scales interact with each other.

Thermally-induced and topographically-induced circulations such as sea-land breeze, urban heat island, and mountain-valley circulations are well-known mesoscale circulations that affect the local circulations. Strength of day and night heating difference depends on the surface heterogeneities. Different characteristics of the surface result in a flow with a different manner. For example; land and water contrast by means of their diurnal differential surface heating is the reason for a sea-land breeze existence. Local scale pressure difference occurs as a result of the heat capacity difference between land and water. The sea breeze begins at the coast and moves farther inland and reaches its maximum penetration distance in daytime. However, the land breeze is more gentle and shallower than the sea breeze.

Analytical and numerical studies have been conducted to understand the dynamical theory of the sea-land breeze. Early theoretical and observational treatments of the sea breeze were studied by Haurwitz (1947), Schmidt (1947), Neuamnn (1977), Fisher (1960) and Frizzola and Fisher (1963). Linear theory was proposed by Walsh (1974) and Rotunno (1983). The 2-D nonlinear numerical modeling studies have been conducted by Fisher (1961) and Estoque (1962). 2-D hydrostatic numerical model was used to simulate vertical structure of the sea breeze with its return flow at the North Sea by Tijm et al., 1999. McPherson (1970) was the first who did calculations of the sea breeze using a 3-D simulations. Pielke (1974) introduced 3-D primitive equation model including detailed boundary layer parameterization. Thompson et al., 2007 worked on the sea breeze front in an urban area using a coupled ocean/atmosphere mesoscale model. In addition to these studies, lake breeze prediction was conducted by Lyons (1972) for the Chicago Lake and a statistical sea breeze prediction was studied using sea breeze index by Frysinger et al. (2003). The role of the sea breeze convergence zone on the mesoscale convective system was emphized by Nicholls et al. (1991).

The Earth's surface modification by human may play a significant role in local scale climate changes (Brown and Arnold, 1998). As similar to the sea-land breeze dynamics, one of the other important thermally driven mesoscale circulation is the urban heat island circulation. Urbanization causes significant changes in the surface parameters, which have potential to alter the local climate in cities by making changes in the surface-atmosphere interaction processes (Oke et al., 1992). Physical processes in the urban surface layer affect the atmosphere above the surface. Thus understanding and modeling of these physical processes are critical for the progress in urban meteorology.

The generalization of the meteorological features over cities is difficult because of the complex three dimensional geometry of the urban infrastructure (Kanda, 2007). Theoretical and observational urban studies have been concentrated on the effects of the urban area on the wind, temperature, moisture, evapotranspiration and precipitation (Huff and Changnon, 1972; Khemani and Murty, 1973; Loose and Borntein, 1977; Changnon, 1978; Shreffler, 1979a and 1979b; Taha, 1997; Lowry, 1998 and Thorsson and Eliasson, 2003). In addition to those studies, mesoscale models have been utilized to gain more insight about urbanization and its possible

effect on the local scale climate (Vukovich et al., 1979; Richiardone and Brusasca, 1989; Atkinson, 2003; Rozoff et al., 2003; Best, 2006). Mesoscale circulation and its interaction with differential terrain heating circulations are also important in terms of the microscale circulations. Depending on the interaction of those scales, circulation characteristics of the local flow alters. These changes become important due to their effects on the cumulus convection, boundary layer characteristics and precipitation regime. The quality of the air is also affected by the thermally-induced circulations. Urban Heat Island (UHI) circulation brings the polluted air over the city due to human activities. On the other hand, the effect of the sea breeze circulation may bring welcome relief however it is noted that this is not observed in all areas. For some regions, the sea breeze may bring high pollution to the cities depending on the vertical structure of the sea breeze. Long time scale of urban heat island and sea breeze phenomena make them significant thermal effects on pollution wind (Anderson, 1971). Description of the mesoscale flow features is, therefore, important in order to understand the transport and dispersion patterns of pollutants. In other words, there is a particular need for knowledge of mesoscale wind fields to be used in calculation of the dispersion of atmospheric pollutants (Anderson, 1971). The spatial distribution and the availability of pollutants have been studied for the urban regions under the sea-land breeze conditions (Kallos et al., 1993; Melas et al., 1995; Moorthy et al., 2003; Rotach, 1999; Sarrat et al., 2006, Thompson et al., 2007).

In summary, mesoscale atmospheric flows possess various time and space scales arising from mechanisms such as diurnal cycle, the atmospheric inertial mode (e.g., gravity waves), thermal and mechanical forcing (e.g., urban heat island, land-sea breeze, mountain-valley circulations), terrain inhomogeneities, precipitation systems (e.g., squall lines, mesoscale convective systems), downscale energy transfer due to nonlinear flow interactions, density stratification, the presence of flow shear in the atmosphere, large-scale baroclinicity and synoptic scale circulations. This wide range of flow scales and their associated vertical ascents and descents can have a significant impact on the transport and dispersion patterns of hazardous material releases (Boybeyi and Bacon 1996). For example, vertical motions of these atmospheric flows can lift hazardous materials from the planetary boundary layer to higher altitudes mainly by either convective processes or non-convective processes (i.e., synoptic scale vertical motions).

In this study, Istanbul region was chosen to investigate the local flow effects owing to the four reasons;

- Istanbul is the most densely populated city in Turkey with more than 10 million inhabitants,
- The urbanization increases proportional to the fast increase of the population,
- The city is located in between two large water bodies (Marmara Sea on the south and Black Sea on the north) and thus, two hilly peninsulas are connected to each other by means of the Bosphorus,
- The observation data network is denser in Istanbul than the other cities in Turkey even it is not enough to study the fine scale structures effectively. For example, Goztepe is the only available upper air station in Istanbul.

The lack of a dense data network makes monitoring local meteorology difficult over city of Istanbul. Deficiency of the data also limits the verification of the numerical studies. Limited statistical and numerical investigations have been conducted for Istanbul. For example, UHI was previously studied by Karaca et al., (1995a, 1995b) using longterm temperature data from observation stations around the city. Therefore, there is a strong need to detailed investigations to understand mesoscale phenomena such as land-sea, urban-rural contrast and mountain-valley circulations, local effects (e.g., topography) and their interaction.

One of the objectives of this study is to investigate the local and mesoscale features (such as urban heat island, sea/land breezes, etc.) of the region. Statistical method is used to understand the long term treatments of the urban heat island. Although the recent models have advantages and disadvantages, they indicate their ability to reproduce the urban heat island and some of its consequences such as urban heat island circulation, storm initiation, and interaction with sea breeze (Masson, 2006). Complexity of the region due to the water bodies, topography and urbanization makes it important to study the mesoscale circulations in Istanbul. Thus, investigation of mesoscale circulations in a densely urbanized coastal city, Istanbul, is the main goal of the study to understand the spatial and temporal behaviour of the local flow.

Second objective of this study is to determine the T&D patterns of hazardous material releases in Marmara region, Turkey, especially over Istanbul and Canakkale

when any tanker accident happened during their passage through the straits after gain insight about the local flow behavior. This task can be accomplished by producing probability contours for risk assessment of these cities to give an idea to decision-makers which part of the city mostly in danger when they encounter such hazardous releases. These issues will be explored by using a non-parametric statistical method (Mann-Kendall test) and mesoscale numerical models MM5 and OMEGA. MM5 is three dimensional, non-hydrostatic with structured horizontal grid and terrain following sigma coordinate model, was developed by National Center for Atmospheric Research (NCAR) and Penn State University (PSU). However, OMEGA is based on an unstructured grid technology, Operational Multi-scale Environment model with Grid Adaptivity (OMEGA), developed by Center for Atmospheric Physics, Science Applications International Corporation (SAIC). And observational datasets, surface and upper air, are obtained via automatic weather stations and observation stations operated by Turkish State Meteorological Service.

Brief background information for synoptic weather patterns over Turkey and thermally and topographically induced mesoscale circulations (sea-land breezes, urban heat island and mountain-valley wind circulations) will be explained in Chapter 2. The atmospheric mesoscale models used in this study, MM5 and OMEGA, will be described in Chapter 3. The statistical and numerical analysis of urbanization in Istanbul using Mann-Kendall trend test and performing mesoscale model MM5 will be given in Chapter 4. Description of idealized and real case numerical simulations conducted for understanding the local flow in Istanbul will be presented in Chapter 5. Model and observation comparison and the risk assessment study are explained in Chapter 6. Discussion and conclusion will be given in Chapter 7 with future study plan.

2. BACKGROUND

Synoptic scale (2000 km-10 000 km) atmospheric circulation determines the weather condition over a region. However, genetic characteristics of the weather is definitely affected by the underlying surface and therefore, the original form of the air mass such as, moisture contents, stability characteristics, is changed depending on the characteristics which path the air mass tracks. Therefore, orientation of the topographic structures causes mesoscale circulations such as, sea-land breezes near the coastal regions, mountain-valley circulation within and around the topography or urban heat island around the city centers. In the following sections, important physical and dynamical features of mesoscale circulations will be discussed.

2.1 Synoptic Weather Patterns over Turkey

Large and local scale flows control the local weather features. Micro-climate or local weather is affected by the specific features of the area such as, mountain ranges, and proximity to a water body while large scale flow identifies the general characteristics of the weather. It is important to know macro, regional and local climate conditions to explain the spatial and temporal distribution of the air masses which affect Turkey (Erinç, 1996). Turkey is located on the path of different air-masses, which play a significant role in shaping its climate types. Dynamically and thermally developed continental and maritime air masses affect the region. Thermal air masses occur due to the cooling or heating from the large continental regions. Continental polar (cP), maritime polar (mP), continental tropical (cT) and maritime tropical (mT) are the major air masses that influence Turkey (shown in Figue 2.1). Large temperature difference between winter and summer results from the effects of polar air masses in winter and tropical air masses in summer in Turkey (Turkes, 1996). Since these air masses travel trough long distances, they lose their characteristics they gain at their origins. Siberia High and part of Monsoon Low (Persian Trough) are the thermally related with these air-masses that affect the study area. Beside of those, dynamically existed Azor High and Iceland Low are important air masses influencing Turkey.

The region is impacted by polar air masses with continental origin (Iceland Low and cold Siberia High) in the winter and by subtropical air-masses (Azor High and part of Monsoon Low) in the summer. Underlying surface modifies the properties of these air masses, for instance when Siberia High crosses the Black Sea approaching the northern coasts of Turkey, cold, and dry air changes its moist contents, cold air due to the gained moisture from the sea. In addition to these synoptic systems, the Cyprus low in winter and the Red Sea trough in summer reach the Turkish coastline (Alpert et al., 2004)

The diversity of the geographic structure, extension of the mountains and effects of the seas in the vicinity of the land determine the climate types of the region. There are four basic climate types which control climate over different regions in Turkey. The continental type is observed over the Anatolia, the Black Sea type is predominant in the northern part, the Mediterranean type is observed both south and west part of Turkey, and the Marmara (transition from Mediterranean to the Black Sea) type is over Marmara region.

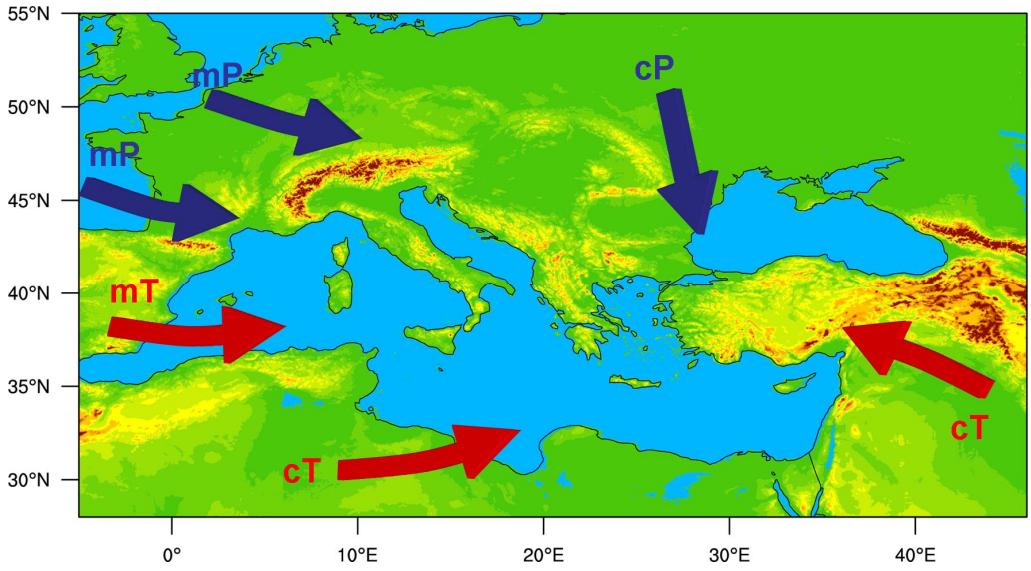

Figure 2. 1 : Air masses paths over Turkey (adapted from Sensoy et al.,2008).

The annual precipitation amount over Turkey is approximately 630 mm and high precipitation is observed in the Mediterranean and Black Sea regions (approximately 1000 mm) whereas inland regions has low precipitation amount (approximately 300 mm). Istanbul presents different behaviour in precipitation depending on its geographic orientation, which is confined by the Marmara Sea and Black Sea. It has approximately 30 km territory between these seas and with the highest hill is

approximately 350 m in Istanbul province. Annual precipitation is approximately 850 mm and precipitation distribution shows increase from coastal areas to inland areas. High precipitation rates occur in the winter due to the frequency of the passing synoptic depressions and cyclone tracks whereas in the summer convective precipitation is the mechanism for the rainfall. Temperature distribution over Turkey is mostly relevant to insolation and elevation that Mediterranean shore of the country is warmer than the Black Sea. The temperature distribution of the province of Istanbul is mostly affected Black Sea climate type as it lies on the Black Sea coast. Prevailing winds in Istanbul are from NE-NNE and SSW wind directions. 21% of time period from 1974 to 2005 wind is from NNE, 11% is from NE, 8% SSW and 5% is from SW. It is observed that general wind direction is from NE and NNE in the summer whereas it is from NNE, NE, SW, and SSW in the winter. High wind speed can flow along the Bosphorus. Maximum wind speed can be reach up to 30 m/s (Turkish State Meteorological Service, 2008).

2.2 Sea-Land Breeze Circulation

Sea and land breezes are well known thermally driven mesoscale circulations (*c.f.* Figure 2.2). Different thermal properties of land and water surfaces are the main reason for the development of the sea-land breeze circulation. As sea has greater heat capacity than land, land heats and cools faster than sea creating strong horizontal temperature and pressure gradients during a diurnal cycle. After sunrise, air over the land heats up faster than air over the surrounding water and the heated air is transported to higher levels, which causes to a strong pressure gradient aloft and a low-pressure area occurs over the land. On the other hand, offshore winds occur higher levels in the atmosphere, which goes down to the sea surface causing a high-pressure. The air tries to balance heating difference by bringing cool air toward the land surfaces. The returning flow at the near surface, blowing onshore, is known as sea breeze in the literature. Gravity current or density current results from density difference between the fluids under the influence of gravity. Many thermally-induced mesoscale atmospheric motions may be considered as gravity current (Sha et al., 1991). Gravity current may results in the form of front depending on the strength of the converging winds called sea-breeze front. Sea breeze front, a kind of special position of a sea breeze, exists between two densely different air masses, cold dense

sea air and warmer land air. Sea breeze front is affected by the flow characteristics. For instance, opposing flow intensification has effects on the sea breeze front formation and its penetration ratio (Simpson, 1994). A sudden increase in wind speed and changes in wind direction, a fall in temperature and a rise in humidity are indicators of the sea breeze front. The traveling distance of the sea breeze depends on the intensity of the total heat input to the air and the latitude (Pearson, 1973). In the later hours, all these occurrences reverse since the land surfaces rapidly cools and air sinks over the land while increasing over the sea surfaces that causes pressure gradient aloft and low-pressure over the sea surfaces. Horizontal temperature gradients are removed by local winds and pressure surfaces become horizontal as they are in the early morning. In this case, offshore winds occur with developing land breeze at the near surface. Offshore penetration of the land breeze depends on the magnitude of cooling over land. The land breeze is a shallower and weaker phenomenon than the sea breeze since existence of stably stratified planetary boundary layer causes less intensive vertical mixing over land at night that is the reason why (Pielke, 1984).

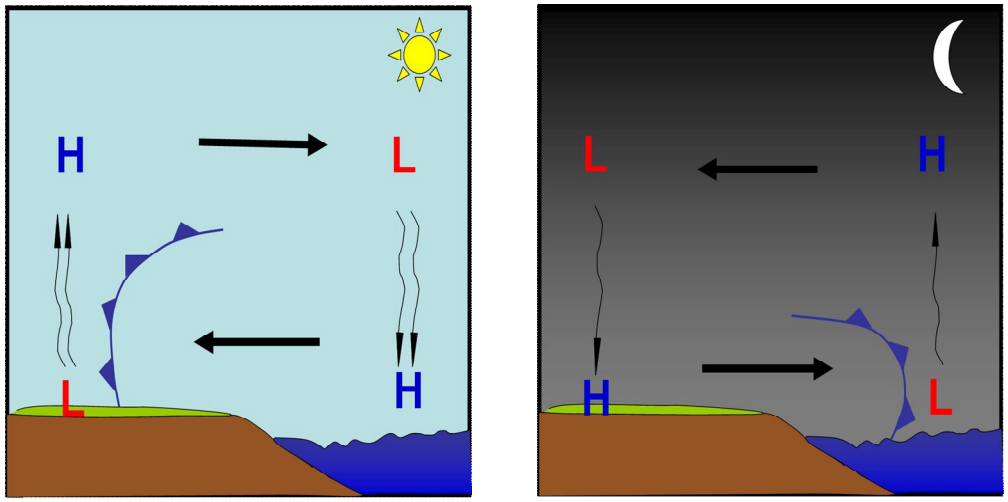

Figure 2. 2 : Schematic illustration of the development of sea-land breeze circulation; sea breeze (left), and land breeze (right), (adopted from http://www.srh.weather.gov)

Observational and numerical studies have been conducted to investigate the behaviour of the atmospheric parameters under the passage of the sea breeze front and inland and offshore penetration of the sea breeze. Over the past several decades, many observational and numerical studies have improved our understanding of the physical-dynamical mechanisms of the sea and land breeze circulations and the

intensifying or weakening effects on these flows. Atmospheric factors (e.g. geostrophic winds and thermal stability), surface characteristics (e.g. topography), geographic location and sea surface temperature affect the development of sea-breeze and land-breeze circulations. Strength of the sea-land breeze depends on geostrophic wind directions to the coast (onshore, offshore or parallel to the coastline), and thermal stability (stable, less stable and unstable atmospheric conditions) alters the intensity of the vertical and horizontal extension of the circulation. Also, vegetation coverage and land formation may affect the sea-land breeze circulation (Atkinson, 1981). Numerical model was used to describe the dynamical theory of the sea breeze by Fisher (1961) who showed that not only the large scale flow affect the stages of existing, development, and decay of the sea breezes but also the over-riding gradient flow distorts the temperature field. After Fisher (1961), 2-D, linear numerical models, which took into account of rotation, friction and advection, are used to develop the theory of the sea and land breezes (Walsh, 1974 and Rottuno, 1983). Most of the sea breeze studies have investigated prevailing synoptic flows impacts on the sea-land breeze circulation (e.g. Estoque, 1962; Pielke, 1974; Yoshikado,1981; Arritt, 1993; Srinivas et al., 2006). Beside of these studies, thermal stabilities, coastal irregularities, sea surface temperature changes and the Coriolis acceleration have been studied. More detailed information will be given in the following sections.

2.2.1 Large scale flow impact on development of the sea breeze

Intensity and inland penetration of the sea breeze depend upon the prevailing geostrophic wind direction. Yoshikado (1981) used observational data to illustrate the wind direction effect on the sea breeze. Satisfoctorily strong offshore geostrophic wind can generate a fully developed sea breeze. However, onshore geostrophic wind suppresses the sea breeze perturbation (Estoque, 1962; Bechtold et al., 1991; Arritt, 1993; Simpson, 1994). First studies were conducted by Estoque (1962), and Walsh (1974).

Estoque (1962) modeled the development of a sea breeze circulation under variety of prevailing synoptic wind and thermal stratification conditions. Opposing large scale flow advects the warm air over the land towards the sea, which produces a strong horizontal temperature gradient in a thick atmospheric layer and a strong pressure gradient in the surface layer (Estoque, 1962; Zhong and Takle, 1993). However,

under the onshore large flow condition, the increase in the temperature of the atmosphere is hindered by the advection that weakens the pressure gradient and the sea-breeze circulation. The inland penetration of the sea breeze was also affected by prevailing winds (Estoque, 1962). Walsh (1974) found maximum vertical velocity of 7 cm s^{-1} in the updraft and -3 cm s^{-1} in the downdraft when a large-scale wind is offshore. Bechtold et al, (1991) revealed that the maximum circulation intensity (i.e., vertical velocity was used as an indicator) occurs with offshore wind, while the winds parallel to the coast do not generally alter the circulation intensity. In contrast to finding of Estoque (1962) and Arritt (1993), who showed that the strong stable atmosphere brings about weak sea breeze circulation, Bechtold et al. (1991) showed that a less stable atmosphere can lead to weak sea breeze circulation.

The intensity of the prevailing synoptic flow makes the developing sea breeze more complicated. The strength of the synoptic wind weakens or strengthens the offshore and onshore extension of the sea breeze circulation. For example, a synoptic wind from colder to warmer surface (i.e. flow from comparatively cold water to the land) weakens the local flow by decreasing the horizontal temperature gradient and consequently weakens the intensity of the sea breeze circulation. On the other hand, same strength of the synoptic flow from warmer to colder surface (i.e. flow from warm water to the land) intensifies the horizontal temperature gradient and generates stronger local winds (Pielke, 1984). Offshore inland propagation speed of sea breeze was found to be a function of wind speed by Finkele (1998). The offshore winds effects on the sea breeze evolution and inland penetration was investigated by classifying the background winds into three classes (light, moderate and stronger winds). Results showed that light and variable wind speed results in the stronger inland propagation. Offshore extent of a sea breeze is also affected by the presence of ambient wind, coastal irregularities and latitude (Arritt, 1989).

2.2.2 Factors of diurnal rotation of sea breeze and effects of geographic location and topography on the sea breeze

The causes and the affect of wind rotation in the sea and land breezes have been investigated in detail in the literature. Historical information about rotation of the sea-land breeze was given by Neumann (1984). Pioneering studies in which Coriolis parameters were taken into account to explain the rotation of the sea breeze were made by Haurwitz (1947) and Schmidt (1947). Fisher (1960, 1961) used both

observations and a numerical model to describe the dynamical theory of the sea breeze, which showed that the large scale winds affect the stages of existence, development, and decay of the sea breezes and rotation of the sea breeze with time is influenced by the Coriolis parameter, despite of obscuring by the large scale flow pattern. Neumann (1977) discussed three terms in rotation of the sea breezes; the Coriolis parameter, mesoscale pressure gradient, and large-scale pressure gradient. Furthermore he showed that the interaction of the pressure gradient and friction has a modifying effect on the sea breeze rotation. However, the Coriolis force may not be the most significant factor that controls the direction of the sea breeze (Simpson, 1996). The main factors are determined as the Coriolis effect, mesoscale pressure gradient and frictional force (Garratt and Physick, 1985; Atkinson, 1981; Zhong and Takle, 1993). Zhong and Takle, (1993) implied that rotation of the sea-land breeze winds results from the imbalance between the Coriolis, mesoscale and large scale pressure gradients, horizontal and vertical advection. Diurnal distribution, the magnitude, and the rotation of all forces are found to be a function of large scale wind direction in existence of the sea and land breezes. Mesoscale pressure gradient and friction balance the rate of the sea-land breeze rotation during the daytime, but the Coriolis force has also effect on the land breeze during the night and from sunset to midnight (Zhong and Takle, 1993).

Geographic location is another factor, which affects development and life span of the sea-land breeze by reason of solar insolation and the Coriolis effect. As known the thermal heating rate between land and water drives evolution of the sea-land breeze circulation. Therefore, the sea breeze circulation should be stronger in summer days since solar insolation is much higher in summer than in winter (i.e., longer day length in the summer provides longer duration of the sea breeze life). For example, Zhu and Atkinson (2004) found that the sea breeze is stronger and wider in summer than in winter. On the other hand, they concluded that land breeze lasts longer in winter than in the summer. Furberg et al., (2002) also showed the sea breeze most frequently occurs in the summer months on the island of Sardinia, Italy. Horizontal inland extent of the sea breeze fronts vary in latitude (e.g., it is 25-50 km in mid-latitudes, while it is about 300 km in tropics, Atkinson, 1981). Frequency of the sea breeze occurrence increases with decreasing latitude (Neumann, 1951). Yan and Anthes (1987) depicted the evolution of the sea and land breeze circulations related to

latitude that distinct circulations develop at the different latitudes. Due to the absence of the Coriolis force, the sea breeze develops stronger at the equator, while the land breeze occurs stronger in high latitudes.

Topography and coastal irregularity can influence the sea-land breeze circulation by means of the form of mountain-valley topography and shape of the shoreline. Modification of the coastal irregularities was examined using three-dimensional model by McPherson (1970). It was shown that the presence of a bay produced an inland distortion of the sea breeze convergence zone. It was also shown that the Coriolis acceleration and the component of the pressure gradient force act in a different manner both in the west and east side of the concave shoreline. Subsidence behind the sea-breeze front depends on the coastline shape. A concave geometry increases the subsidence and suppresses clouds, whereas a convex geometry decreases the subsidence (Arritt, 1989). Development of thunderstorms is affected by shape of the shoreline. Curvature of the coastline is a significant factor in terms of the diurnal frequency of thunderstorms occurrence and coastline structure determines the convergence or divergence of the sea-land breezes (Neumann, 1951). Thunderstorms are categorized as nocturnal and daytime thunderstorms. Land breeze opposed to the onshore wind and onshore wind directions merge and increased the convergence over the area that cause the nocturnal-thunderstorms. It was implied that nocturnal-thunderstorms may be more frequent than the daytime-thunderstorms in concave coastline under ashore large-scale flow especially in the cold months. If inland penetration of the sea breeze attended by downward motion of air, daytime-thunderstorm occurs in convex shoreline (Neumann, 1951). Gilliam et al., (2004) showed that the coastline shape and synoptic flow relative to the coastline have a dominant influence on the sea breeze evolution. In contrast to the flat topography assumption for sake of simplicity, in reality coastal regions are surrounded by hills or steep mountains which may have effects on development and movement of sea-land breeze. Mahrer and Pielke (1977) found that combination of the mountain circulation and the sea-breeze in case of zero prevailing wind conditions enhanced the circulation both in day and night than their separate effects. In the case of opposing flow, topography is of the greatest importance and existing convergence in the consequences of differential heating (e.g., sea breeze or slope flows) is enhanced by the surrounding orography (Abbs, 1986). Hills can accentuate the sea breeze effect

and mountain and valley can completely change the sea breeze direction (Atkinson, 1981). Diurnal influence of topography on the intensity of the sea breeze was shown by Kondo (1990). Presence of orography intensifies the sea breeze in the morning whereas topography stops the advance of the sea breeze in the late afternoon. Topographic influence on the sea breeze studied by Lemonsu et al., (2006) who investigated the sea breeze in two parts: shallow sea breeze driven by the local coastal temperature gradient and deep sea breeze forced by the regional temperature gradient between land and sea. In this study, the shallow sea breeze blows perpendicular to the coastline and deep sea breeze perpendicular to the regional temperature gradient flows combined with synoptic flow at higher levels. The results showed that topography strengthens the shallow sea breeze while weakens the deep sea breeze.

The sea breeze effect on the air pollution problem in and around the coastal cities is another important topic, which is relevant to the land-sea breeze reversal. The inland transportation of a polluted air mass by means of sea breeze was shown by Ueda et al. (1988). Investigation of the role of sea breeze in the dispersion in the coastal terrain of Australia by Physick and Abbs (1991) showed that polluted air replaced with marine air by means of sea breeze and in the afternoon pollutants did not mix to the ground. When inversion exists over large cities, the strong stability, acting as a lid in the inversion layer, causes to intensify the pollution problem. Re-circulation of the wind traverses the polluted air and provides to maintain the high concentration and returns it back to the started locality in 24 hours causing dangerous chemical changes on pollutants (Simpson, 1994). It is expected that the sea breeze brings a fairly good weather condition in coastal regions however this can turn to be the worst conditions in terms of pollution transportation with sea breeze flow. Sea breeze impacts on the air pollution have been studied for problematic cities suffering from pollution, such as Los Angles, Athens, and Tokyo (Lu and Turco, 1995; Clappier et al., 2000; Svensson, 1998; Kondo and Gambo, 1979). Kondo and Gambo (1979) stated that when the sources of pollutants are near the coast, no high concentration occurs in the mixing layer. The source of the pollutants are left out the mixing layer due to the inland penetration of the sea breeze. Lu and Turco (1995) found that pollution layer can be generated by the sea breeze circulation by undercutting the mixed layer and rising pollutants into the stable layer.

2.3 Urban Heat Island and Heat Island Circulation

Different surface characteristics over cities and their surrounding suburban areas cause different thermal and mechanic properties similar to the mechanism which results in a sea-land breeze circulation. Many studies in the last three decades have well documented the effect of urbanization on the climate. As shown in Figure 2. 3, the air over the urban canopy is warmer than the surrounding suburban or rural, known as urban heat island (UHI) (Oke, 1987).

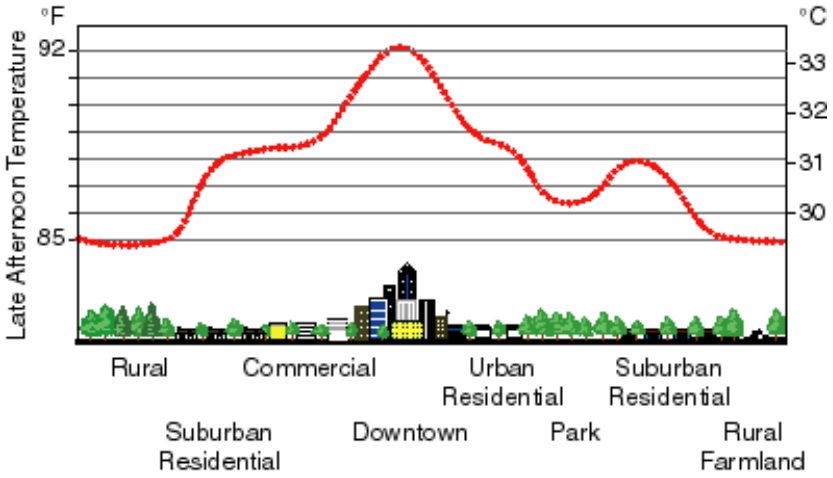

Figure 2. 3 : Temperature difference between urban area and its vicinity (heat island group, LBNL, http://EETD.LBL.gov/HeatIsland).

Air, flowing from rural to urban surface encounters different boundary layer conditions. This causes the development of an *internal boundary layer* between the urban and rural boundary layers (*c.f.* Figure 2.4). Urban atmosphere is characterized in two layers; the *urban boundary layer* (UBL) is a layer in which local to mesoscale phenomena exist due to the effect of the urban surface and the *urban canopy layer* is a layer under the rooftop, which is governed by microscale processes between the buildings, street etc. (Oke, 1987).

Over the past several decades, many statistical and modeling UHI studies have been conducted for the mid to large size cities. For example, Bornstein and Johnson (1977) in New York, Vukovich and Dunn (1978) in St. Louis, Shreffler (1979a, 1979b) in St. Louis, Yoshikado (1989, 1992) in Tokyo, Bornstein and Lin (2000) in Atlanta, Lemonsu and Masson (2002) in Paris, and Gedzelman et al., (2003) in New York have conducted studies to understand the fundamental structure of the UHI circulations. UHI characteristics show variation in time and space depending on

meteorological conditions, morphology of the urban areas, and different urban characteristics (Oke, 1987). Urbanization alters the surface and boundary layer properties of a region, such as its radiative, thermal, moisture, and aerodynamic characteristics. Additionally, energy and water balance is disrupted. The increase in the build-up area changes the impermeability of the surface, which influences the flux (sensible and latent heat fluxes) and soil moisture patterns between the urban and rural areas.

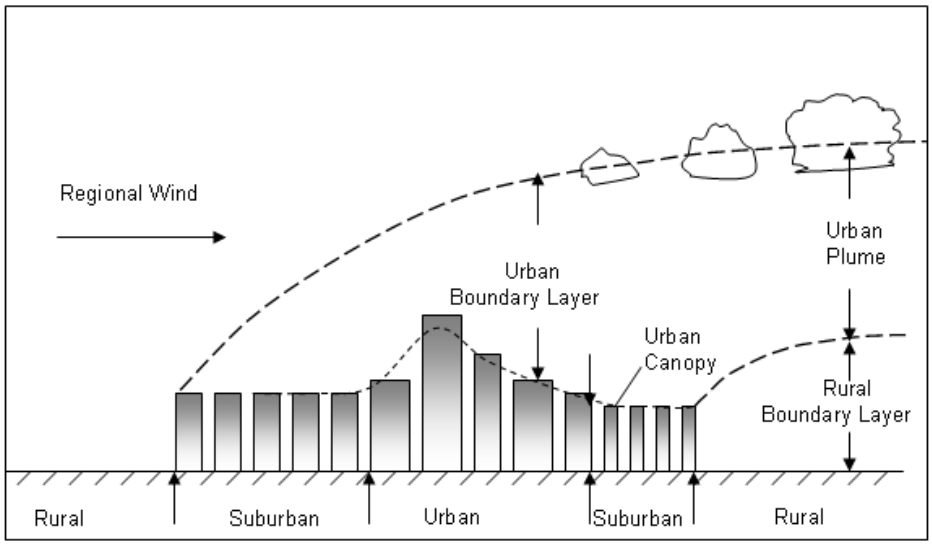

Figure 2. 4 : Schematic representation of the urban atmosphere (modified from Oke, 1997).

The calm, cloudless night conditions under the high pressure system are the most favorable condition for the development of UHI. Arnfield (2003) showed that UHIs display distinct characteristics and different energy exchange assemblages. General characteristic of the decreasing UHI is an increase in the wind speed and cloud cover. Effect of cloud cover and wind speed was studied by investigators (Morris et al., 2001; Unger et al., 2001; Lemonsu, 2002). Presence of clouds declines nocturnal radiative cooling from urban areas. Emitted long-wave radiation from a surface is prevented by clouds and absorbed radiation re-emitted to the surface, which reduces the temperature difference between the urban and rural regions. Negative effect of the increasing cloudiness and wind speed on the development of UHI was shown by Unger (2001) in Szeged, Hungary. UBL is governed by the presence of the city which is warmer, rougher due to the buildings than the surrounding countryside. Increased drag and turbulence by means of increasing roughness length gives rise to

a decrease in the wind speed. Changing the wind speed by the friction reduces the Coriolis force which alters the balance and deflects the wind direction. Presence of a large city may show its thermal effect throughout the entire planetary boundary layer (PBL). During the daytime, both thermal and mechanical production of turbulent kinetic energy (TKE) enhances the UBL height. However, at night stable PBL hampers TKE, thus the PBL height is low (Oke, 1987). Nevertheless, presence of the warm urban surface is able to erode the stable rural air while advecting over the city. Stability of the urban boundary layer does not show strong variations comparing to rural atmosphere. Bornstein (1968) observed that inversion layer over urban areas is less intense and frequent than the rural or suburban areas and an elevated inversion layer exist over the city. UBL breaks up the strong temperature gradient and disrupts the existence of the extreme instable and stable atmosphere. UBL is well-mixed both during the day and night in contrast to the rural atmosphere (Oke, 1987). Variability of wind speed in the UBL influences TKE which can be induced by mechanical and thermal production in UBL (Martilli, 2002). Strong wind dilutes the nocturnal radiative cooling due to the strong vertical mixing (Fast et al. 2005). Effects of the UHI on the wind flow are implied by Bornstein and Johnson (1977) in two ways, the fist one is, the excess of urban temperature induced a sea breeze type circulation cell towards the warm city near the surface and the second one is, increasing of the downward momentum because of the reduced nocturnal stability of the urban increases the flow speed.

Urban heat island intensity ($\Delta T_{u\text{-}r}$) is strongly controlled by the temperature differences between the urban and rural areas. Differences in the heat storages between these distinct surfaces induce thermodynamically driven urban scale flows (Brown, 2000). The urban surfaces made of different materials, which have different thermal characteristics (such as absorption, emissivity, thermal conductivity, etc.) and hence cause different absorption rate of solar radiation. After sunset, urban areas emit the absorbed heat at almost at the same rate of absorption. Heating and cooling rates of the urban and rural areas make differences during the day that a rural area cools faster than an urban area after sunset and heats up faster after sunrise. Descending cooling in the urban area gives rise to a high minimum temperature values in the city. After sunrise, warm-up amount of the urban area is slower, which reaches a maximum $\Delta T_{u\text{-}r}$ 3 to 5 hour later. Intensity of the UHI decreases rest of the

night and rapidly diminishes after sunrise (Oke, 1987). In vertical, intensity of the UHI is a maximum near the surface and becomes zero at a certain level (Bornstein, 1968). Diurnal variation of the air temperature, cooling and heating rate and UHI intensity between the urban and rural areas was given by Oke (1987) as an example of the canopy layer heat island (seen in Figure 2.5).

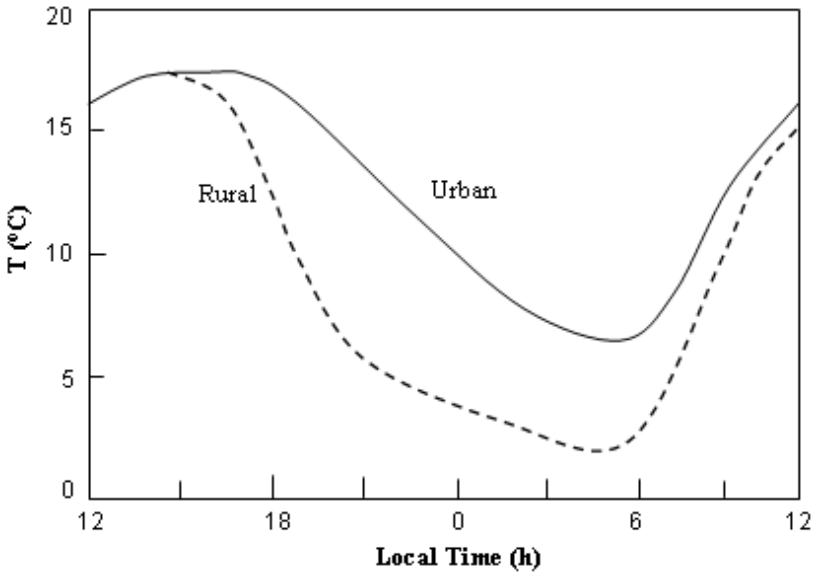

Figure 2. 5 : Temporal variation of urban and rural areas (adapted from Oke, 1987; Stull, 1988).

Morris et al. (2001) investigated the influences of wind speed and cloud cover on the UHI intensity in the city of Melbourne, Australia. They evaluated seasonal and annual observation dataset to understand the effect of these two factors individually and also their joint effects on the UHI. They showed that increase in wind speed and cloudiness reduced the UHI and summer season was found the best indicator of UHI. In terms of interactive effect of these two parameters, wind speed is influential to UHI intensity. When the mean wind speed is ≥ 5 ms^{-1}, variation in the cloud covers from 0 to 8 octas had very little influence on the UHI. Nevertheless, calm wind with cloudiness from 0 to 8 octas produced the greatest UHI intensity. Lemonsu (2002) implied that UHI circulation can exist in the afternoon under weak and disorganized synoptic wind conditions.

Vukovich and Dunn (1978) concluded that roughness length had a small effect on the heat island circulation conducting sensitivity study with a 3-D numerical model. A series of modeling studies was performed by Atkinson (2003) so as to conceive the contribution of parameters such as albedo, anthropogenic heat, emissivity, sky-view

factor, surface resistance of evaporation, thermal inertia and roughness length on the UHI intensity. He showed that roughness length and surface resistance of evaporation are the most important factors during the daytime whereas anthropogenic heat was the most important factor influencing the intensity of UHI during the nighttime. In addition, he also showed that the absence of urban roughness length increases the intensity of UHI. In order to get precise information from mesoscale numerical models and urban air quality models, geometric characteristic of the cities should be represented within the models. The study which was conducted by Fast et al. (2005) for Phoenix, Arizona showed that in contrast to the previous studies, UHI intensity decrease when wind speed is greater than 7 m s^{-1}. They concluded that UHI intensity is independent of wind speed when it is less than 7 ms^{-1}. Coceal and Belcher (2005) used canopy parameters (e.g. canopy density, canopy height) obtained morphological data of the urban area. Results showed that increase in canopy density with tall canopy cause to decrease in mean wind speed. Nonetheless, near the ground this behaviour may be reversed and wind speed may increase.

UHI intensity was associated to city size which tends to increase the UHI intensity. Oke, (1987) used population as an indicator of the city size and suggested that urban heat island effect on its surroundings is inversely proportional to the large scale wind speed and directly related to the logarithm of the population. Using a 2-D mesoscale model Savijarvi and Liya (2001) also depicted that the size of city influences the local winds over the flat terrain so that horizontal extend of the urban area (i.e., the size of city) trigger stronger urban heat island circulations. In contrast to Oke (1987) and Savijarvi and Liya (2001), Atkinson (2003) inferred from his 3-D mesoscale modeling study that the size of the urban areas effects on UHI intensity is minimal.

2.3.1 UHI effect on the precipitation and air pollution

Local meteorological balance is disturbed by the change in surface properties. Perturbations from urban heat island induce changes in evapotranspration, snow coverage and duration period of snow. Ascending impermeability because of the removal of vegetation can cause an increase in runoff (Oke, 1987). Also, cloud microphysics and precipitation pattern may be changed. Precipitation may increase due to the urbanization also associates with increase in frequency of severe weather phenomena (Huff and Changnon, 1973). Atkinson (1971) implied that cloud grows

rapidly and heavy rain occurs, crossing the city. High values of potential and wet-bulb potential temperature are explained as a reason for the cloud growth. Huff and Changnon (1972) briefly explained the four possible causes of the urban-induced potential modifications on precipitation;

1) Atmospheric destabilization from the well-developed UHI,
2) Modification of dynamics and microphysics in passing clouds by means of addition of cloud condensation nuclei and ice nuclei from industrial regions,
3) Increase of low-level mechanical turbulence,
4) Modification of the low-level atmospheric moisture by addition from industrial plumes and modification of the natural evapotranspiration within the city.

METROpolitan Meteorological Experiment (METROMEX) was a comprehensive field project in St. Louis to provide information on cloud and precipitation formation, urban heat budget, chemistry of aerosol and rainwater, and 3-D patterns of precipitation elements (Changnon et al., 1971). Data from the METROMEX are used by many scientists in order to understand characteristics of precipitation, thunderstorm, and hailstorm conditions in and over the urban regions. Huff and Changnon (1972), and Rozoff et al. (2003) found increase in precipitation downwind of St. Louis. Huff and Vogel (1978) depicted that urban region has the most important effect on rainfall frequency and amount during the peak rainfall period. Changnon (1978) illustrated increases in thunderstorm characteristics ranging of 11%-116% and in heavy rain by 35%-97%, located 40 km downwind of the St. Louis. The study indicated that urban impact intensifies the storm rather than initiating convective activity. Changnon and Huff (1986) also concluded that nocturnal rainfall results from urban influences. They showed that the nocturnal urban-induced rain cells are larger and longer lasting than rural rain cells. Although urban effects occurred in all seasons and with all synoptic weather types in St. Louis, increasing downwind rainfall of the city was found to be most pronounced in wet summers and squall-lines and cold fronts. Traveling air mass types towards urban regions play a key role on initiation of precipitation. Dry summer seasons showed the suppression of the urban-induced rain in St. Louis (Huff and Changnon, 1972; Changnon, 1978). Moisture availability over the urban areas is a curial impact on evolution of convection and precipitation. Low evaporation is the greatest factor in the urban area. The upward motion was found located downwind of the maximum

convergence at the surface downwind of the city (Seaman et al, 1989). The updraft cell induced by the urban region downwind of the city can initiate and cause surface precipitation in favorable thermodynamic conditions and strength of the updraft cell enhanced due to the increase in UHI or decrease in wind speed (Baik et al., 2001). On the other hand, reduction of convergence and upward motion was found in the expanded size of the urban region. Rozoff et al. (2003) showed the UHI circulation was the pronounced effect on initiating thunderstorm. They also showed that the initiated deep, moist convection and convective clouds formation downwind of the St. Louis urban area result in an increase in precipitation. Dixon and Mote (2003) found that low level moisture context was the most pronounced factor when compared to the UHI intensity for urban-induced precipitation by. In addition, they concluded that convection occurs in very unstable atmospheric conditions regardless urban effect. Nonetheless, the anomalous heat of the UHI under slightly unstable atmosphere may play a role for initiation of convection. Enhanced wet season rainfall and sever weather events over Mexico City due to the urbanization were shown by Jauregui and Romales (1996). Increasing urban-induced rainfall over and downwind of Huston, Texas was revealed by Shepherd and Burian (2003) and Burian and Shepherd (2005). The later study by Burian and Shepherd (2005) showed that the 25% of increase in the warm season rainfall amount was due to the urbanization. Modification of the precipitation pattern by means of UHI strength and roughness length was shown by Thielen et al. (2000) over metropolitan Paris, which indicated increase in rainfall downwind of the urban area with stronger UHI intensity and higher roughness length.

UHI effects on the cloud cover and the convective storm was studied by Thielen and Gadian, (1997) using 3-D numerical model in Manchester (England). It was concluded that convection is enhanced and continued by the UHI inclusion and enhanced convection and rainfall exits downwind of the urban area. Bornstein and Lin (2000) found urban-induced initiation of convection and precipitation in Atlanta. However, it cannot be generalized that enhancement of urban-induced precipitation occurs downwind of the city. Enhancement of convergence and precipitation is influenced by city characteristics (e.g. size, morphology etc.), distance of industrial regions, and synoptic weather condition over the cities. Huff and Changnon (1973) revealed that each city has distinct precipitation patterns in the vicinity of urban

regions. Bornstein and Lin (2000) showed the different regional flow could affect the location of heavy precipitation. As a local force, urbanization causes an increase in rainfall amounts as implied in the previous paragraph. However, beside the positive feedback of the urbanization on the rainfall, increasing industrialization and population result in increasing pollutant sources (e.g. traffic, fossil fuel usage etc.) which may suppress precipitation over the cities. Aerosols change radiative forces and microphysical processes. Rosenfeld (2000) studied suppression of the rain by urban pollution using satellite data. The author revealed that pollution suppresses precipitation in two mechanisms; one prevents coalescence of the cloud droplets into the raindrops and another mechanism hinders the ice-particles formation and cold-precipitation processes of the clouds. Anthropogenic aerosols enhance scattering and absorption of solar radiation. Large number of CCN (Cloud Condensation Nuclei) nucleates small cloud droplets which causes insufficient coalescence into raindrops and suppress rain over polluted regions (Ramanathan et al., 2001). Givati and Rosenfeld (2004) investigated precipitation changes in California and Israel, which showed a decrease in precipitation amount of 15%-25% downwind of coastal urban area of California and in the land of Israel by means of increasing emissions. Van Den Heever and Cotton (2007) indicated that although urban-enhanced aerosols have complex and nonlinear relationships between microphysics and dynamics of the downwind convective storms, development of convergence and storm are driven by the urban land use characteristics. Unless storm develops downwind of the urban region, presence of urban-enhanced aerosols CCN and giant CCN do not exert a significant effect on precipitation and convection. Their findings also showed that urban aerosol effects on downwind convection and precipitation is greater in the low background concentration of aerosols.

Growing urbanization increases pollutant sources (e.g. increasing mobile sources) and hence emissions. Increasing concentration of pollutants in urban areas may affect atmospheric chemistry and climate on regional and global scale (Crutzen, 2004). Dynamics and chemistry over the urban areas are studied by Vukovich et al. (1979), Yoshikado and Tsuchida (1996), Martilli et al., (2003), and Sarrat et al. (2006). Primary and secondary pollutants such as nitrogen oxide (NOx) and ozone (O_3) are affected by urban-induced boundary layer structure. Vukovich et al. (1979) and Yoshikado and Tsuchida (1996) found the highest concentration of O_3 in a

convergence zone associated with urban heat island respectively for St. Louis and Tokyo, respectively. Sarrat et al. (2006) conducted a study over Paris, which showed that the enhanced turbulence within the UBL modifies the spatial distribution and the availability of pollutants and both diurnal and nocturnal UHI have a significant effect on primary and secondary regional pollutants.

2.4 Mountain-Valley Wind System

Irregularities in the topography give rise to more complex flows. Two types of flows can be seen in mountainous region: modified large-scale flow or channeled flow by underlying complex topography called terrain-forced flow and thermally-driven circulation which is caused by diurnal thermal changes between the topographic structures. Different thermal characteristics between hills and valleys cause for the development of local flows similar to the sea-land breeze and the urban heat island circulations as discussed in earlier sections. Underlying terrain can change the flow structure. For instance, air flow, approaching to the mountain barrier blows over or around the barrier, is forced to flow through gaps between the mountains or is blocked by the barriers. Local wind systems, forced by the complex topography characterize thermally and dynamically induced processes (Kossmann and Sturman, 2003). While diurnal differential heating on the mountain or valley causes thermally induced mechanisms such as mountain-valley winds under calm synoptic conditions, dynamically induced mechanisms exist due to the synoptic wind modifications on the irregular terrain such as gravity waves or channeling (Kossmann and Sturman, 2003).

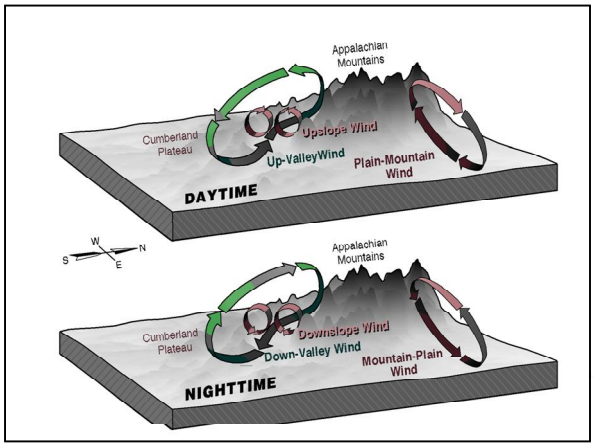

Figure 2. 6 : Schematic of Mountain-Valley Wind System for both daytime and nighttime (Whiteman, 2000).

Thermally driven mountain-valley wind system includes four wind structures in the course of the day; the slope winds, along-valley winds, cross-valley winds, and mountain-plain winds (Whiteman, 2000);

1. Diurnal heating or cooling difference in the air between top of the hills and over adjacent valleys (at the same altitude) brings along-slope mountain winds. During the daytime, the air on the summit of mountains becomes warmer than the air at the same altitude over adjacent valleys under calm weather. The warmer air rises up over the summit and creates low pressure. The air is drawn up from the valley to mountain, called as up-slope (anabatic) winds (shown in Figure 2.6a). Reverse mechanism cause to develop down-slope (katabatic) winds. Because of the rapid long-wave radiation cooling effect in a clear night, the air near the mountain summit becomes colder than the air at the same altitude over adjacent valleys. Dense and cold air creates high pressure on the top of the mountain and slides down to the valley floor, known as katabatic or down-slope winds (Figure 2. 6b).
2. The along valley wind is driven by horizontal temperature difference along the valley axis or between the air within a valley and the air over the adjacent plain (Whiteman, 2000). Orientation and geometric structure of the valley constitute the valley wind system (Oke, 1987).
3. The cross-valley wind flows when the horizontal temperature difference occurs between the air over the one side of the valley and the air over the opposing sidewalls. Flow is perpendicular to the valley axis, which blows toward the more heated sidewall.
4. The mountain-plain wind results from horizontal temperature difference between the air over a mountain and the air over the surrounding plain. Topography does not have any impact on the upper level return flow of the mountain-plain circulation (Whiteman, 2000).

Geographic and atmospheric features, such as geographic orientation of a valley, valley slope and width, mountain slope, stability of the atmosphere and synoptic flows, influence mountain-valley flow direction. The reason why the valley heats (cools) more than the plain during the course of the day (night) was the issue that scientists tried to elucidate. Geometric structures of the valley were used to infer the mechanism of the heating (cooling) differences between the valley and the plain. The geometric factor, called topographic amplification factor in the previous studies, the

ratio of the volume of air in a valley cross section to the volume of air in a plain with the same width, which was used by McKee and O'Neal (1989) to investigate how the valley geometry control the along-valley pressure gradient depending on the developing along-valley temperature gradient at night. Diurnal wind system, in the variety of distinct valley shapes, has been studied in different regions (e.g. Alpine region, Himalayan valley, etc.).

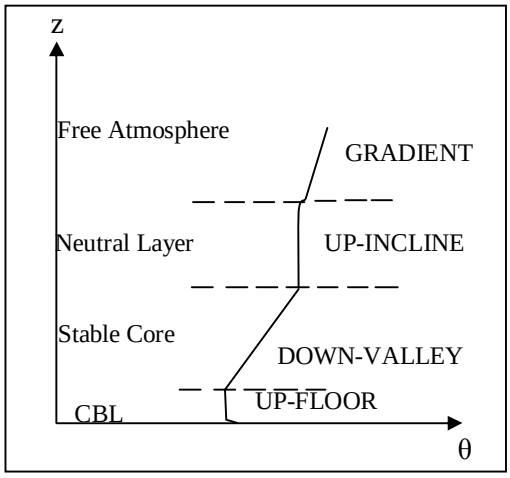

Figure 2. 7 : Vertical potential temperature evolution and wind structure during the valley breakup inversion (Whiteman, 1982).

The erosion of the nocturnal inversion over the valley studied by means of observation and modeling by Whiteman (1982) and Whiteman and McKee (1982). The valley atmosphere layered in four sections, convective boundary layer (CBL), stabile core (inversion layer), neutral layer, and free atmosphere (Figure 2.7). The local valley wind system is thermodynamically-induced rather than momentum transport from aloft the valley under weak upper level wind conditions. In the free atmosphere, wind is forced by pressure gradient without orographic effect (Whiteman, 1982). Whiteman (1982) revealed the vertical potential temperature evolution and wind behaviour by means of observations in the western Colorado valleys and he asserted the breakup inversion mechanism as shown in Figure 2.8.

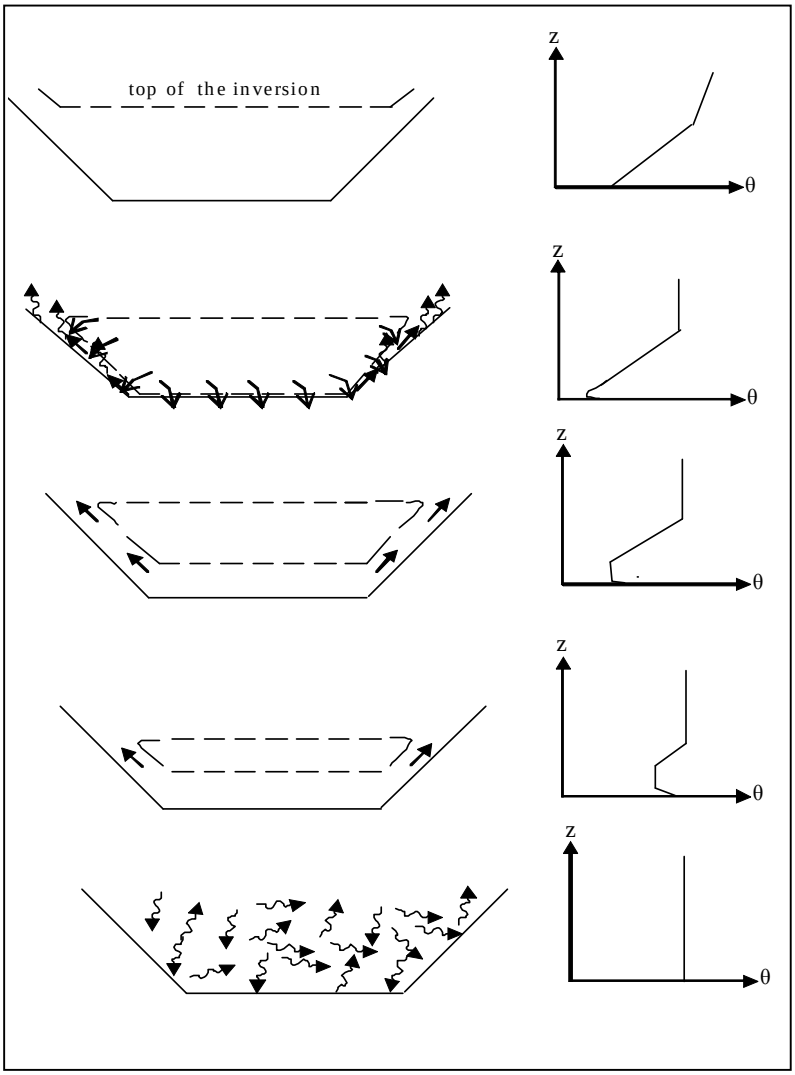

Figure 2. 8 : Evolution of the inversion breakup mechanism (Whiteman, 1982).

After sunrise, convective boundary layer develops over valley floor and sidewalls, resulted from sensible heat flux from valley surface. Isolated stable core over the valley provides the mass and heat entrainment into the convective boundary layer, which results in sink of the inversion. Warming convective layer causes up-slope flow within the boundary layer and sidewalls. Continuity of the up-slope flows is provided from subsidence of the inversion. Until the inversion is broken, the convective boundary layer growth and a well-mixed neutral atmosphere become effective in the valley (Whiteman, 1982). Moisture properties of the surface and cloud cover influence the inversion over the valley. When the cloudiness increases, the inversion strength decreases, however snow cover increases the inversion strength (Whiteman, 1982). Model simulations by Whiteman, and McKee (1982)

predicted the vertical potential temperature evolution and time of the inversion destruction quite well. Development of the cooling valley atmosphere was studied by McNider and Pielke (1984). Beside the circulation structure within in valleys, enclosed basins and their distinct sizes and climate features influences on the evolution of the local flow have been ascertained by many scientists by means of observation and numerical methods (Whiteman et al. 1996, Fast et al. 1996, Whiteman et al. 2004a, Whiteman et al. 2004b, Whiteman et al. 2004c). In Colorado's Sinbad Basin, it was evaluated from investigation of the individual atmospheric heat budget terms, turbulent sensible heat flux divergence, radiative flux divergence that the well-drained valley atmosphere cooling is weak in time due to the subsidence warming aloft the valley, however cooling in a confined terrain such as, basins, sinkholes etc. is stronger because of the weak drainage wind system (Whiteman et al., 1996). Fast et al. (1996) showed in the same basin that the cooling in the center of the basin is due to the local radiative flux divergence and cold air advection from sidewalls while the cooling above the basin sidewalls is because of the turbulent sensible heat flux divergence. Depending on the underlying topography, direction of the ambient winds makes a contribution on the amount of cooling and the acceleration of the ambient wind affects the vertical and horizontal advection in the basin. Comparison between the ambient wind direction and the vegetation coverage revealed the only marginal impact of the vegetation on the basin heat budget (Fast et al. 1996). Inversion breakup structure of the enclosed basin was investigated by Whiteman et al. (2004a) showed the similarity with the well-drained valley structure (*c.f.* Figure 2.7). Furthermore, this study demonstrated that along-valley system has no effect on the inversion breakup. Inversion destruction period took 2.6-3 h for closed basin after sunset whereas breakup period in the deeper valley was 3.5-5 h reported by Whiteman (1982).

Forced wind, flowing along the valley axis by means of enclosing topography is known as a channeling effect over the valley. Danard (1977) described simple one-level model studying orographic channeling in Juan de Fuca and Georgia Straits, British Colombia. In this investigation, it was inferred that up-slope (down-slope) flow motion causes cooling (heating), which increases (decreases) the surface pressure in a stable atmosphere. When the wind flows with an angle in the valley, horizontal pressure gradient force is directed across the valley. This mechanism

causes the wind to blow parallel to the valley. It was emphasized that the more stability the more channeling is within the valley. Gross and Wippermann (1987) made a comprehensive explanation for channeling in a rotating coordinate system; if a perpendicular airflow crosses a valley it deflects and channeled within the valley. The flow has to stream to the larger cross section along the valley. Hence, the deceleration of the flow results in a deflection which is to the left in the Northern Hemisphere. The equilibrium between horizontal pressure gradient and the Coriolis force is interrupted due to the retardation and then the flow is deflected in the direction of the large-scale pressure gradient. The air restricted by sidewalls of the valley forced to flow with effects of the component of the large-scale horizontal pressure gradient, parallel to the along valley, is described as a channeling by Gross and Wippermann, 1987. They simulated channeling and countercurrent with non-hydrostatic mesoscale numerical model. According to their findings, flat and broad valleys even with low sidewalls result in a channeling when the geostrophic wind flows at a certain angle respect to the orientation of the valley. Opposite flow along the valley was called countercurrent for special geostrophic winds by the authors. They also computed windborne particle trajectories and surface concentration by taking account the channeling and countercurrent. They concluded that flow field is much more irregular than their expectation for regular topography under the effects of channeling and countercurrent in the special geostrophic winds. They also pointed out that irregular flow field causes an irregularity in the surface concentration field. After Gross and Wippermann (1987) who studied channeling only in the Rhine Valley, Germany, Whiteman and Doran (1993) put an effort to make a more comprehensive study. Thermal forcing occurred when along-valley pressure gradient developed and there was no relation between the within valley winds and geostrophic winds. Pressure gradient is produced from temperature difference along-valley axis. In a weak geostrophic wind conditions, thermally driven local flows produce up-valley and down-valley winds within the Tennessee Valley.

Whiteman and Doran (1993) came up with four different mechanisms (shown in Figure 2. 9), using wind relations between above (geostrophic wind) and within the valley. These four concepts are briefly specified below. First mechanism occurs depending on diurnal thermal difference: the valley wind is generated by along-valley pressure gradient which is produced hydrostatically from temperature

difference along-valley axis. Second concept is downward transport of horizontal momentum from above the valley that causes the same wind direction within the valley as geostrophic wind. The authors implied that the most preferable condition to form this type channeling is under unstable or neutrally stratified condition in a wide flat valley with low mountain borders. In the third process, forced channeling, ambient wind which is in geostrophic balance above the valley will be channeled by the valley sidewalls. The flow blows through the valley axis. Authors emphasized that the flow would either blow up or down from the valley axis, depending on the geostrophic wind direction of the flow to the valley axis. The fourth possible process exists when the flow is driven by the geostrophic pressure gradient component along the length of the valley, which is called pressure driven channeling which is also known as gap wind. The early description of gap wind was given by Reed (1931). Pressure-driven channeling or gap wind occurs at sea level straits on the lee side of high mountains. Large scale pressure gradient along the straits (or channels) causes to develop strong winds along the straits, which is more strength at the low pressure end of the valley. Interaction of regional or mesoscale pressure gradient and topography was studied in different regions such as in Shelikof Strait, Alaska by Lackmann and Overland (1989), in Howe Sound, British Columbia by Jackson and Steyn (1994), in Juan de Fuca in between British Columbia and Washington by Colle and Mass (2000), in Lut valley by Liu et al. (2000), and in Mexico City basin by Doran and Zhong (2000).

Depending on the changes in the geostrophic wind direction, flows within the valley shift from up to down valley or from down to up valley. If the geostrophic wind direction is along the valley, the along-valley component of the pressure gradient force will be zero. Four conceptual models, explained in the previous paragraphs and shown in Figure 2.9, are obtained using geostrophic wind and valley surface wind relationship. Kuwagata and Kimura (1997) investigated the daytime Planetary Boundary Layer (PBL) evolution in the Ina Valley, Japan using two-dimensional numerical model and observational data. The PBL structure, heat and water vapor transport mechanism were revealed that heat was transported from mountainous region to the valley region because of the thermally induced cross-valley winds. The reverse situation is valid for the water vapor transportation.

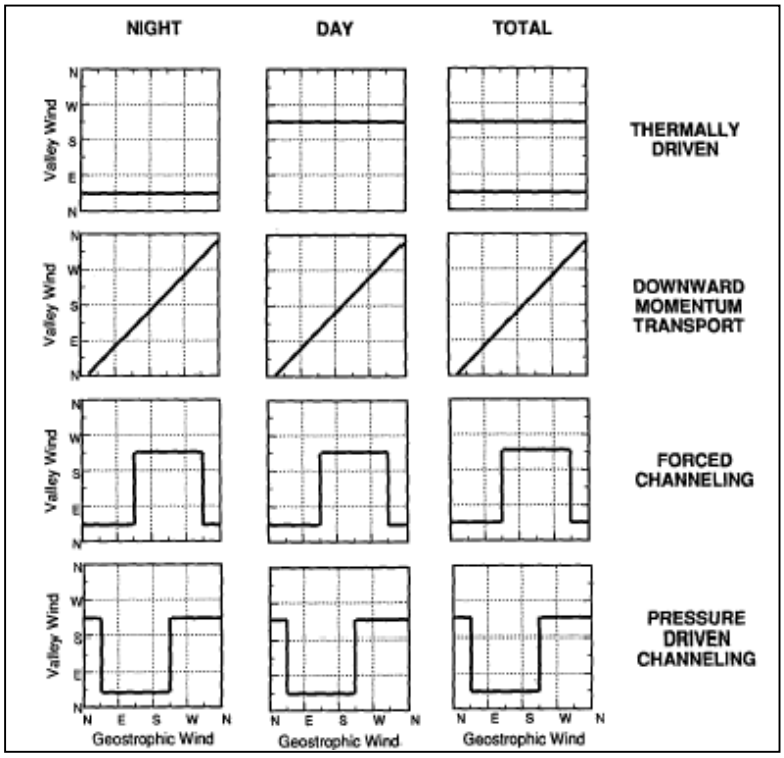

Figure 2. 9 : Above-within valley winds relationships for four possible mechanisms (Whiteman & Doran, 1993).

Weber and Kaufmann (1998) investigated the dominant channeling process in Basel, Switzerland based on the conceptual models suggested by Whiteman and Doran (1993). It was demonstrated that different channeling mechanisms influence the valley from broad to narrow. Even two of the mechanisms which are introduced by Whiteman and Doran (1993) can superimpose in their study area depending on the valley shape. The authors studied the effects of different synoptic wind speeds -low, moderate and high-and they concluded that strong synoptic wind can suppress the valley wind. Kaufmann and Weber (1998) also clustered the wind direction data for the same region and they indicated that wind directions are more relevant to the orographic features and the altitude of the stations than the horizontal distance between the stations. Eckman (1998) utilized the Whiteman and Doran's channeling categorization in order to study the channeling of the wind using observation and numerical model in Tennessee Valley where previous study was conducted by Whiteman and Doran (1993). The mountain range under stably stratified flow has blockage effects that cause a development of high pressure on the windward side of the mountain, and low pressure on the leeward side of the mountain (Smith, 1982, and Eckman, 1998). Eckman (1998) pointed out that pressure-driven channeling and

blockage of the mountain range have close relation. It was also demonstrated that seasonal vegetation and soil water are not dominant factors in the channeled flow (Eckman, 1998). Bergström and Juuso (2006) performed model simulation for idealized valley using mesoscale numerical model which shows that more stable conditions cause increase in within valley wind and roughness has not major effect within the valley.

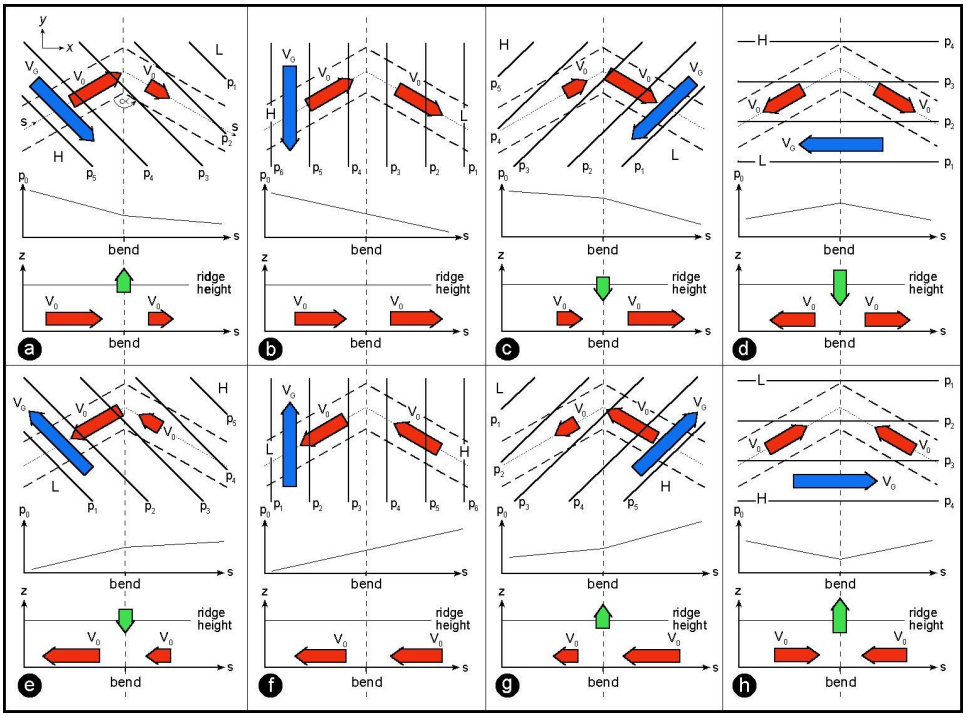

Figure 2. 10 : Pressure-driven channeling in a bent valley with $\alpha=120^{o}$ and different geostrophic wind directions (a) north, (b) northeast, (c) east, (d) southeast, (e) south, (f) southwest, (g) west, and (h) northwest (Kossmann and Sturman, 2003).

Kossmann and Sturman (2003) presented pressure-driven channeling for both in strait and bend valleys. They pointed that when the geostrophic wind is directed parallel to the bisecting line of the bend valley (which is indicated with S in Figure 2.10), along valley pressure-gradient and wind are constant (Figure 2.10a and 2.10e). If the geostrophic wind blows from a direction, between bisection and bisection, the along valley pressure gradient has the same sign on both sides of the valley whereas its magnitudes are different (shown in Figure 2.10b, 2.10d, 2.10f, and 2.10h). The detailed explanation was not given for this occurrence. However, it should be related to the magnitude of the pressure gradient force, which is not the same along the bisected valley angle in a certain distance. Remaining two cases (Figure 2.10c and

Figure 2.10g) show the easterly and westerly geostrophic wind directions. The along valley pressure gradient has a different direction but same magnitude on both sides of the valley. The vertical air motion features are perpendicular and parallel to the bisection angle in the bent valley. The decrease in the bisection angle causes an increase in the amount of the convergence or divergence.

It is clear that the occurrence of a thermally-induced valley wind is not a simple mechanism since it is affected by many other factors such as facing-slope, the slope of valley floor, shading by topography, atmospheric stability, bend valley, the Coriolis effect, etc. Zängl et al., 2001). Gravity waves and large-scale pressure gradient can also contribute to the structure of diurnal winds. In Kali Gandaki valley, Nepal, while large-scale pressure gradient enhances the up-valley wind, it attenuates the down-valley winds (Egger et al., 2000 and Zängl et al., 2001).

In addition to the theoretical studies mentioned above, observational and numerical applications were conducted by the scientists to better understand the mechanism within and around the valley. East and west facing-slopes of mountains have different radiation properties. A semi-empirical method developed by Matzinger et al. (2003) shows that insolation increases in the west facing slopes in the mid-afternoon whereas east facing-slopes is exposed by the sun in the late morning.

Rampanelli et al. (2004) tried to make an explanation on physical mechanism of the evolution of the up-valley wind simulating the flow numerically over the idealized three-dimensional topography. They concluded that stability of the atmosphere above the valley is important and up-valley wind can be observed in a valley with vertical sidewalls. Their findings showed that subsidence heating within the valley constitutes different vertical structure of the convective boundary layer between outside and within valley. Weigel and Rotach (2004) investigated the flow and turbulence characteristics in the steep and narrow Riviera valley based on aircraft measurements, sonic data and radio sounding datasets. It was claimed that thermally driven up-valley wind pronounced in all the studied days which have fairly weather conditions. The study by Weigel and Rotach (2004) revealed the existing clockwise circulation on the east slope of the Riviera Valley from their observation. They discussed this feature in terms of facing-slope perspective which was claimed by Matziger et al. (2003) and also synoptic flow perspective. However, Weigel and Rotach (2004) came up with a secondary circulation concept which was explained

that it results from imbalance between pressure gradient and centrifugal force due to the strong curvature of the flow in the valley entrance. It was found that profile of potential temperature is not good indicator for boundary layer thickness in a curved valley and TKE threshold criteria was employed to define the boundary layer height by Weigel and Rotach (2004). In addition to this observational study, Chow et al. (2006), and Weigel et al. (2006) used Large Eddy Simulations (LES) to do some research on flow structure, heat budget, sensitivity experiments, and data verification studies in the Riviera valley for the observed days. Chow et al. (2006) found that the better predictions of the wind transition and heat flux can be obtained when soil and surface initialization is done. They also commented that the use of topographic shading in the model makes an improvement to capture the diurnal radiation distribution well. Nevertheless, the model did not accurately solve the terrain slopes. Findings of Weigel et al. (2006) supported the mechanism of heating valley of Rampanelli et al. (2004). They also emphasized the curvature effects on the existed flow which was defined as a curvature–induced secondary circulation within the Riviera Valley by Weigel and Rotach (2004).

2.5 Scale Interaction

Populated cities located near water bodies expose to both sea-land breeze circulation (SBC) and heat island circulation (HIC) effects in their vicinity. In addition to these two important circulations, terrain-induced effect (mountain-valley circulation) is another important feature on coastal regions. Complex terrain combined with steep orography along the coastal region can modify the mesoscale circulation pattern (Nitis et al., 2005). Both thermally and dynamically induced local flows conduct the meteorology of the cities in point of circulation dynamics and air quality perspectives. In order to characterize local-scale flow impacts over the coastal areas, contribution of each mesoscale circulations on the local flow and their interaction (sea-land breeze, heat island circulation and mountain wind system) should be defined. Several different studies have been conducted to investigate the interactions of the sea breeze and heat island circulation for different coastal areas, such as Yoshikado and Kondo (1989), Yoshikado (1992), and Kusaka et al. (2000) performed studies for Tokyo, Gedzelman et al. (2003) and Childs and Raman (2005) for New York. Yoshikado and Kondo (1989) suggested that the sea breeze front

structure was strengthened by urban influence or by differences in thermal characteristics between the urban and rural areas. (i.e., abrupt change in wind speed and direction, specific humidity and enhanced mixing length due to the penetration of the sea breeze front were observed). Until the sea breeze reaches the urban area, temperature is intensified during the night or maintained after sunrise and suburban areas hinder the penetration of the sea breeze (Yoshikado, 1992). Urban region accelerates development of the sea breeze, whereas inland penetration of the sea breeze front is slower over the flat topography (Martilli, 2003). Delay of inland penetration of the sea breeze and enhanced upward motion associated with sea breeze front are affected by presence of UHI (Yoshikado, 1994; Kusaka et al., 2000). Ohashi and Kida (2002) conducted numerical studies using a 3-D mesoscale model to show HIC and SBC effects and their contribution to the pollution transportation, on an inland urban area and a coastal urban area, in Japanese cities Kyoto and Osaka, respectively. HIC, over the coastal area intensified the SBC in the morning. Presence of the inland urban area strengthened the SBC and HIC interaction and hence SBC and HIC maintained longer in time. They demonstrated that suburban area in between these two urban areas was suffered from high concentration of pollution in both lower and upper levels by the circulation of SBC-HIC interaction and inland HIC. They also showed that coastal pollutant transportation to the inland urban area depends on the distance between two urban areas. In point of pollution perspective, during the nighttime pollutants disperse into a deeper layer rather than transport to the sea since the presence of the city produces weaker land breeze. In the morning, pollutants over the sea are brought back to the city by the sea breeze and presence of the city accelerates the recirculation processes (Martilli, 2003). Also, Gedzelman et al., (2003) implied that sea breezes diminish the UHI effect in the spring and summer seasons. Using meteorological observation network datasets, it was suggested that sea breeze switches the center of the UHI early in the morning for New York City. Intensity of the UHI and sea-breeze interaction depends on the size of the urban area, distance from the sea and the intensity of the UHI (Yoshikado, 1994). He implied that when the size of urban area exceeds 10 km, interaction of UHI and sea breeze is significant and affects local climate.

When the coast takes place near a high ground, effect of mountain-valley wind system must be taken into consideration beside the other effects (i.e., sea-land

breeze, heat island circulation), which superimposes the total circulation (Simpson, 1994). Topography exposes the other local flows (e.g., sea-land breeze is forced to channel along the valley axis by the underlying terrain and speed of the channelled wind inclines, Whiteman, 2000). Thermal and dynamic effects of mountains on the sea-land breezes was investigated by Ookouchi et al. (1978) who showed mountain can prevent the inland penetration of the sea breeze as a barrier and can intensify the sea breeze associated with mountain-valley wind system (i.e., up-slope or down-slope wind). Distance from the sea, height of mountains and their orientation influence the sea breeze characteristics and hence air pollution transport. Topography (including complex valley-plain-plateau structure) and sea breeze interaction was conducted by Kondo (1990) using both 2-D and 3-D numerical models, which showed that if the distance is short between coastline and inland topography, the sea breeze is intensified in the morning, on the contrary the sea breeze is hindered in the afternoon. Additionally, it was depicted that narrowest valley causes strongest along-valley winds. Interaction between the local flows also plays an important role for transportation of heat, moisture and pollutant. Sea breeze and terrain induced flows control air pollution pattern and cause elevated pollution layer (Lu and Turco, 1994 and 1995). Existence of the different air pollution layers was explained in four processes in a mountainous coastal region; mixed layer growth and sea breeze propagation, mixed layer stabilization, interaction of the sea breeze with upslope flow and generation of upslope flow by mountain surface heating (Lu and Turco, 1994). Moisture and pollution behaviour of such a complex flow that includes urban and coastal circulation characteristics was studied by Ohashi and Kida (2004) for Kyoto and Osaka urban areas in Japan including mountain effect in their previous study (Ohashi and Kida, 2002). They revealed that SBC interaction of HIC and valley circulation (induced by mountains) caused to dry the suburban area between the coastal and inland urban regions. Amount of the dry atmosphere depends on the distance between two urban regions. It was concluded that pollutants were transported by both coastal and inland UHI and valley circulations and deformed by SBC. Modification of the local climate over Marseille (France) by means of interaction of UHI, sea breeze and topography was investigated by Lemaonsu et al., (2006). In contrast to the many other cities, urban effect on the local flow is inhibited over Marseille and topography and sea breeze interaction drives the local flow dynamics.

3. DESCRIPTION of MESOSCALE MODELS

This chapter gives a brief description of the mesoscale meteorological models, MM5 and OMEGA, used in this study. General information and grid structures of the models will be explained in this chapter. Fundamental equations details of the models will be given in Appendix.

3.1 Overview of the MM5 Model

The Fifth-Generation NCAR/Penn State Mesoscale Model is developed from a mesoscale model used by Anthes at Penn State in the early 1970s. Since that time many changes were designed to broaden its applications. For instance, a multiple-nest capability, non-hydrostatic dynamics, a four-dimensional data assimilation capability, increased number of physics options and portability to a wider range of computer platforms.

The MM5 model is a limited area, non-hydrostatic with terrain following sigma coordinate to simulate or predict mesoscale atmospheric circulations. The model contains several physical options for radiation, cumulus, planetary boundary layer, surface and explicit moisture parameterizations.

3.2 Horizontal and Vertical Grid Structure of MM5

The model analyzes the data on pressure surfaces, however, before give the data to the model, data has to be interpolate to the model's vertical coordinate. The vertical coordinate is terrain following which means that the lower grid levels follow the terrain while the upper surface is flat. Since the pressure decrease in height, intermediate levels progressively flatten.

Dimensionless σ values are calculated as:

$$\sigma = (p_0 - p_t)/(p_{S0} - p_t) \qquad \textbf{(3.1)}$$

where p_0 is the reference state pressure, p_t is a specified constant top pressure and p_{S0} is the reference state surface pressure. The model vertical resolution is defined by a list of values between zero and on based on the formulae (Figure 3.1). Resolution in the boundary layer is much finer than the above, and the level numbers vary from ten to forty.

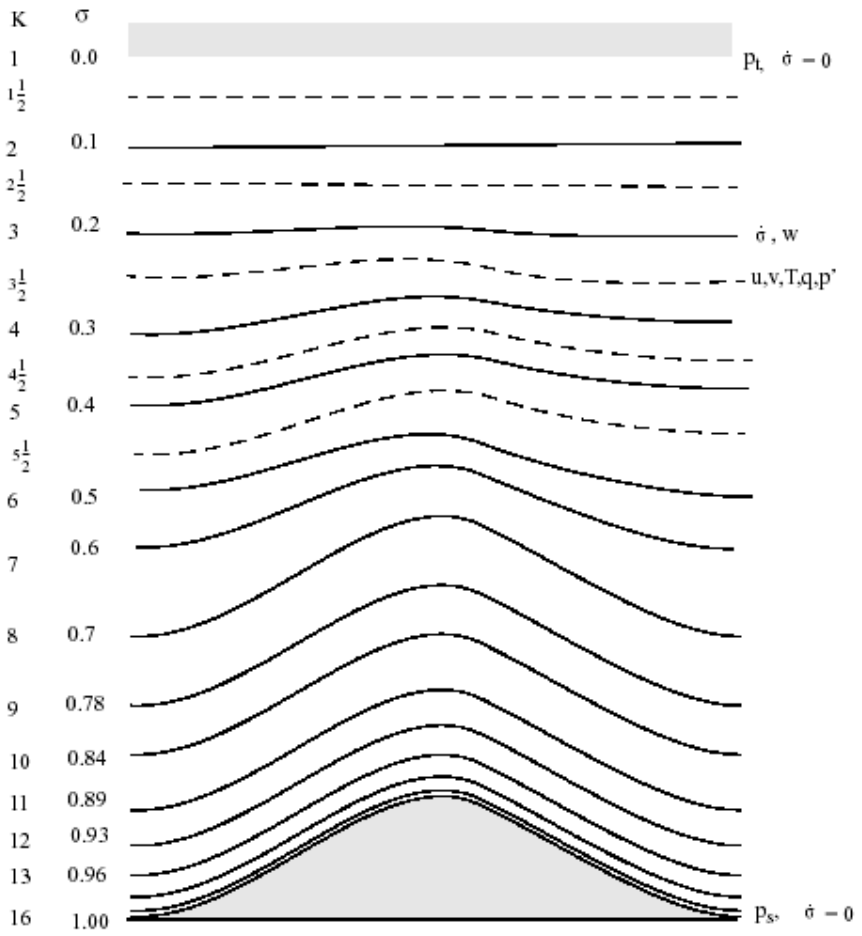

Figure 3.1 : Schematic representation of the vertical structure of the model. The example is for 15 vertical layers. Dashed lines denote half-sigma levels, solid lines denote full-sigma levels.

The horizontal grid used in the model is Arakawa-Lamb B-staggering. As it is shown in Figure 3. 2, the scalar variables (T, q etc.) are defined at the center of the grid while wind components are at the corners. The center point of the grid is referred as cross points, and the corners are dot points. Therefore, horizontal velocity is defined at the dot points in the model. All variables are defined in the middle of each model vertical layer, which is referred to as half levels and represented by the dashed lines

in Figure 3.1. Vertical velocity is carried at the full levels (solid lines). The number of model layers is therefore always one less than the number of full σ levels. Equations are solved using finite difference method with the I, J, and K index directions in the modeling system.

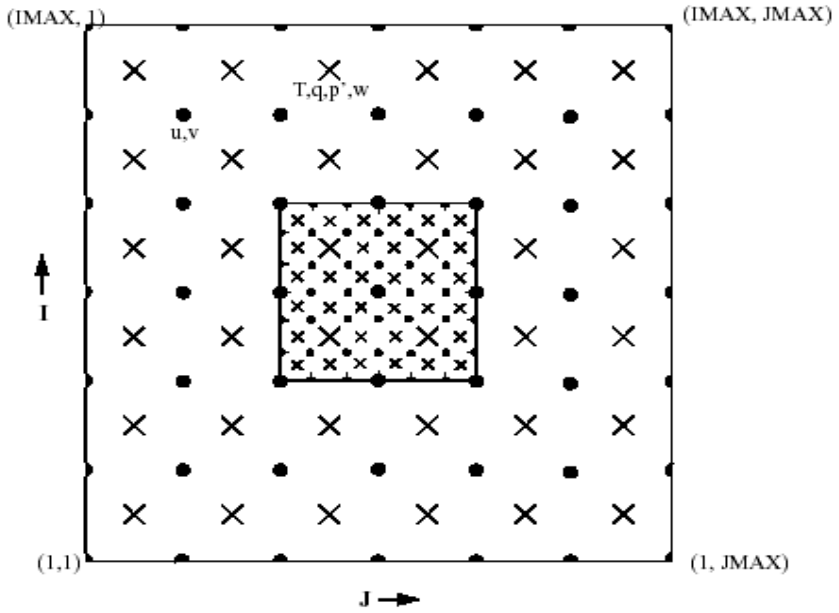

Figure 3. 2 : Schematic representation showing the horizontal Arakawa B-grid staggering of the dot (l) and cross (x) grid points. The smaller inner box is a representative mesh staggering for a 3:1coarse-grid distance to fine-grid distance ratio.

MM5 is also capabile to multiple nesting with up to nine domains running at the same time. It is possible to use two nesting models; one-way and two-way interaction with 3:1 nesting ratio. “Two-way interaction” means that input of the nest comes from the coarse mesh via its boundaries, while the coarser mesh get feedback form the inner nest. One-way nesting differs from two-way nesting with no feedback and coarser temporal resolution at the boundaries.

3.3 Surface Characteristics of MM5

Terrain elevation and vegetation (land-use) datasets are interpoled to the regular latitude-longitude onto the determined mesoscale domain. If the land surface model (LSM) is used in the MM5 model, soil types, vegetation fraction, and annual deep soil temperature is generated. Terrain elevation, landuse/vegetation, land/water mask, soil types, vegetation fraction and deep soil temperature are availabile at six

resolutions: 1 degree, 30, 10, 5 and 2 minutes, and 30 seconds. Vegetation and land-use data are avaliable in three sets; 13-category, global coveraging with 1 degree 30 and 10 minute resoultion, 17-category, North American coverage with 1 degree, 30,10,5 and 2 minutes and 30sec resolution and 25-category,global coverage with 1 degree, 30, 10, 5, 2 minutes and 30sec from USGS. Elevation data is avaliable at six resolution from USGS. Land/water mask data is tow types with 17-category and 25-catagory with six resolutions. There are three types soil, vegetation fraction, and annual deep soil temperature datasets; 17-category, 12 monthly and 1 degree are available for LSM option in MM5. Fundamental equation sets of MM5 can be found in Appendix A1.

3.4 Overview of the OMEGA Model

The Operational Multiscale Environment Model with Grid Adaptivity (OMEGA) has been performed in this study for numerical model simulations. OMEGA is a fully non-hydrostatic, three-dimensional prognostic atmospheric model with an adaptive grid which is unstructured triangular prism referenced to a rotating Cartesian coordinate system in horizontal and terrain following is in vertical grid structure. The model uses a finite-volume flux-based numerical advection algorithm derived from Smolarkiewicz (1984). OMEGA has a detailed physical model for the planetary boundary layer (PBL) with a 2.5 level κ-ε turbulence closure scheme (Mellor and Yamada, 1974). A modified Kuo (Kuo, 1965; Anthes, 1977) and Kain-Fritsch (Kain and Fritsch, 1990) schemes are used for cumulus parameterization, and an extensive bulk-water microphysics package derived from Lin et al. (1983) in OMEGA. OMEGA models the shortwave absorption by water vapor and longwave emissivities of water vapor and carbon dioxide using the computationally efficient technique of Sasamori (1972). OMEGA uses an Optimum Interpolation (OI) analysis scheme (Daley, 1991) to create initial and boundary conditions. In addition, OMEGA contains both embedded Eulerian and Lagrangian dispersion models.

3.5 The OMEGA Grid Structure

A unique feature of the OMEGA model is its unstructured grid, which provides flexibility to facilitate the gridding of arbitrary surfaces and volumes in three dimensions (*e.g.*, to sharp local terrain features). In particular, unstructured grid cells

in the horizontal dimension can increase local resolution to better capture the terrain inhomogeneties and associated important physical features of atmospheric flow and cloud dynamics (Bacon et al., 2000). This grid feature provides smooth transition from high resolution where needed to low resolution rest of the domain.

In the unstructured grid architecture, definition of the elemental objects is necessary to describe the volumetric mesh. The lowest-order object in the mesh is the *vertex* which is specified by its position (x, y, z). The other elements *edge* provides the connectivity of the mesh and the indices of the starting and terminating vertices define the edge. The *face* represents the interface area between adjacent volumetric cells and can be described from the list of edges that bound it, or by the sequence of vertices that forms its corners. The *cell* or *control volume* is in turn specified by the lists of faces that contain it. While scalar quantities are defined in the cell centroid the vector quantities are defined at the center of the vertically stacked faces in the volumetric mesh shown on Figure 3.3 (Bacon, 2003).

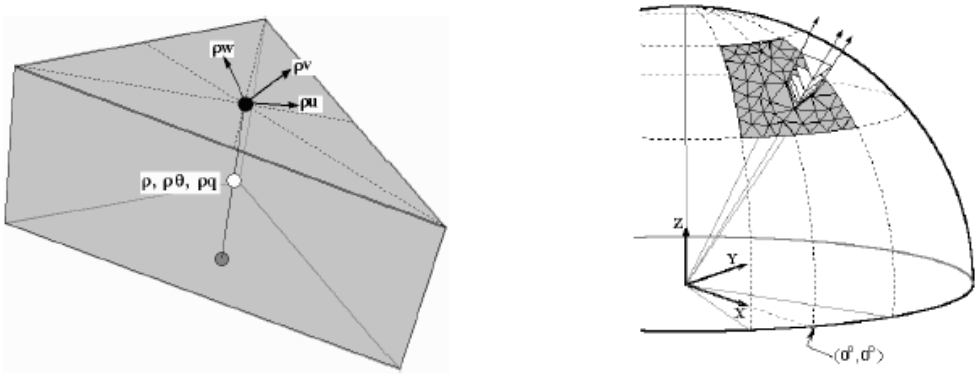

Figure 3. 3 : OMEGA grid element (Bacon, 2003).

The arbitrary number of edges meets at a vertex and there is no longer a simple algebraic structure that can be deduce the relationship of indices for the various elemental objects as in the case of traditional structured atmospheric models. While generating a mesh either surface features or other fixed terrain features or the initial weather can be used. Calculation of the flux across the face requires the calculation of the normal to each face for the unstructured triangular grid structure. Natural separation occurs between the coordinate system for the fundamental equation set and the grid structure. The coordinate system can be as simple as possible while the grid structure is complex in this coordinate system. Rotating Cartesian coordinate system is used in OMEGA and the grid structure is terrain following. Rotating

Cartesian system in which the origin is the center of the earth, the z axis passes through the North Pole, the x axis passes through the intersection of the equator and the prime meridian, and y axis is orthogonal to both. The form of equations of motion is as simple as possible however only two terms are somewhat non-conventional: gravity and the Coriolis acceleration. Gravity in the rotating Cartesian coordinate system is directed in the radial ($-\hat{r}$), which has components in three coordinate directions. By definition, the Coriolis force is $-2\rho\Omega\times v$ and has components in all directions.

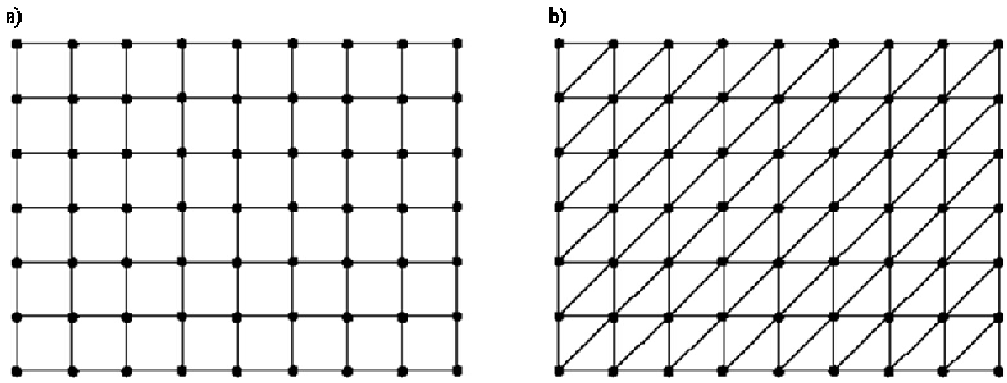

Figure 3. 4 : Initial rectangular grid, a) before triangularization and b) after triangularization (Bacon, 2003).

3.5.1 Initial grid

Desired horizontal resolution is specified in kilometers while longitude and latitude are input for the domain boundaries. For construction of the initial rectangular mesh, meters per degree of longitude are determined at the center of the domain. Meters per degree of latitude are globally constant. Since longitude and latitude is used to express the coordinates of each vertex, the grid is rectangular in latitude/longitude space. The initial rectangular grid is equal to the minimum resolution requested for the primary domain (Figure 3.4). Selecting a subset of edges randomly and forcing reconnection produces randomization to prevent the too "regular" final grid. The reconnection process is described below.

3.5.2 Refinement of the grid

First step for the refinement process is the calculation of the area of each triangle, which is then compared to the areas of equilateral triangles having edge lengths equal to the minimum and maximum resolutions specified in the input file. A triangle is

“flagged” for refinement if trisection will not result in new cells having areas less than or equal to the area of an equilateral triangle with the minimum allowable edge length, and the cell satisfies one or more of the following (Bacon, 2003):

- The area of the triangle exceeds the area of an equilateral triangle with edges equal to the maximum edge length specified for the domain in which the centroid is located.
- The average elevation of the three vertices, since elevation is a vertex-based quantity. The elevation gradient between the triangle and its neighbors set to 1.5 percent of the variation in elevation throughout the domain.
- The land/water index is set to zero or one depending on the location of cell centroid. If the land/water indices of any of the cell's neighbors (the three cells that share edges with the target cell) differ from that of the target cell, the target cell is on a land-water boundary.
- The area of the cell is greater than four times the area of its smallest neighbor.

If the triangle is in the interior of the grid, adding a vertex at the cell centroid enables to refinement of a triangle or if the triangle is on the boundary refinement is accomplished by bisecting the boundary edge (*c.f.*, Figure 3.5). Then the cell is flagged for recombination and the vertex opposite from the longest edge will be deleted from the grid if it satisfies any or all of the following (Bacon, 2003):

- The minimum edge length, specified by the user as a horizontal resolution for domain is of an equilateral triangle edge. The area of the cell where the centroid is located is less than the area of an equilateral triangle.
- The cell is water surrounded by water, and combining three cells of the same size into one will not result in a cell whose area exceeds the allowable maximum value.
- The cell has aspect ratio less than 0.33. The aspect ratio is defined as the height of the triangle divided by the length of the longest edge.

Certain criteria forces refinement or recombination of the cells to occur without considering any other properties of triangle. If triangles are too large or too small, they forced to trisect or recombine to prevent adverse effects on the time-step, and triangles with poor aspect ratios are forced to recombine to avoid instabilities in the solution. Corner triangles are bisected to avoid triangles having two boundary edges.

Figure 3.5 shows the grid in Figure 3.4 after two triangles, one in the interior and one on the boundary, have been refined. Adding and deleting vertices results in an unequally created edge lengths. The grid is relaxed in order to prevent possible instabilities due to the irregularities in the grid. Relocating each vertex to a point equidistant from its connecting neighbors is included in relaxation procesdure. This stage is shown in Figure 3.5. After relaxation, triangle shape is optimized through the process of reconnection. During reconnection, one edge is the shared from a quadrilateral, which is formed by the two neighboring triangles. If new-composed triangles are nearly equilateral, the original shared edge is deleted from the grid, and the new edge added. Figure 3.6 shows the grid in Figure 3.5 after reconnection.

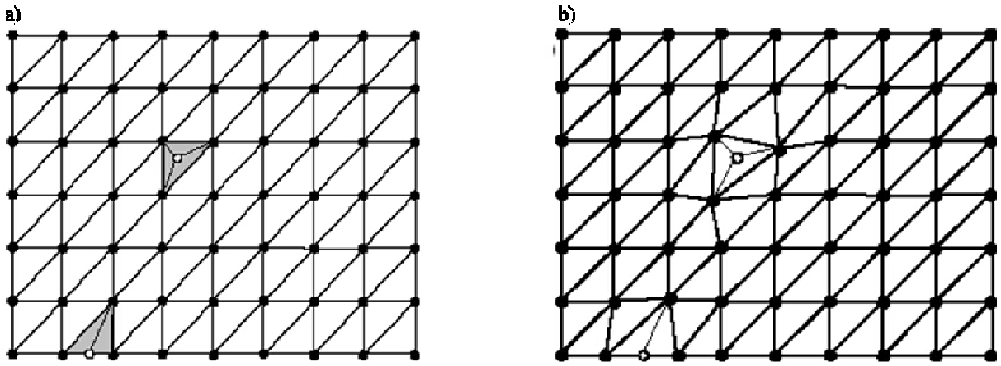

Figure 3. 5 : Grid refinement, a) initial rectangular grid with two vertices added and b) after triangles are refined, the vertices are relaxed (open circles), (Bacon, 2003).

After all of the flagged cells have been altered an iteration is complete. Also, interpolation to the underlying databases, terrain and land/water is iterated during the grid refinement. Bilinear interpolation is used to calculate both elevation and the land/water index. The land/water index has a value between zero and one, which is then rounded to zero or one. Refinement and interpolation processes are repeated until the grid converges. Convergence occurs when two consecutive iterations result in changes to fewer than 5 and 1 percent of the cells, respectively. The ratio between the minimum and maximum resolution defines the number of iteration to obtain the final grid. A final step prior to the creation of the vertical levels consists of bisecting any corner triangles that have two boundary edges. This process has been found to improve the solution at the corners of the domain (*c.f.*, Figure 3.6).

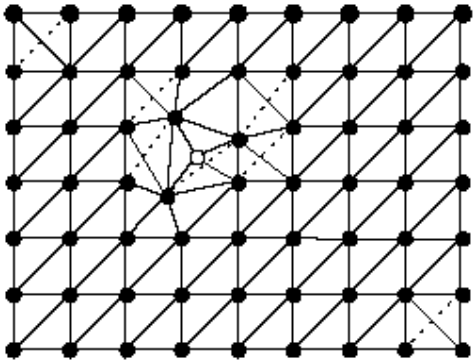

Figure 3. 6 : Grid after reconnection.The deleted edges (dashed line) the new edges (thin lines) (Bacon, 2003).

3.5.3 Vertical levels

In order to provide high resolution near the surface, the OMEGA grid is constructed in two parts: low levels are considered "stretchable" while the upper part represents the "spherical surfaces". The user determines both the total number of levels, N, and the number of stretchable levels, N_s.

There are different ways creating the vertical layers: one is, the height of the first layer of triangles, Δz_o, is specified by the user. The heights of the prisms will increase in the radial direction in the stretchable layers above the surface of the earth along with the maximum geometric factor, α_{max}.

The layers are constructed by taking each surface vertex and constructing an array of vertices along the radial through that vertex. The resulting vertices are connected to form the OMEGA grid volumes. The top of the uppermost stretchable level (H_{ts}) above the lowest point in the domain is utilized to compute the height of each of the vertices (*c.f.,* Figure 3.7 right). This height is then used as a spherical top for the stretchable levels uses the height and a local geometric factor α_i for each radial is used to compute the heights of each of the other vertices in the stretchable levels. α_i will always be less than α_{max} because H_{ts} was computed using the lowest point in the terrain. The resulting grid is terrain following at the surface, but has a constant mean sea level altitude at the top of the uppermost stretchable layer. An alternative setup method is the top of the total domain is specified by the user, and the OMEGA grid generator calculates the geometric stretching factor. The grid generator input file is edited by the user to provide the height of each vertical level above the surface to

specify the vertical grid structure. These heights are used by the grid generator to construct the radial through the lowest point on the surface grid, and then adjust the other radials to produce a spherical top to the stretchable layers. Calculation of the vertical levels completes the construction of the OMEGA model grid. The number of vertices, edges, and faces, and the arrays that contain the vertex locations, their connectivity, the edge connectivity, and the face connectivity is obtained after grid completion, which is used in model preprocessor (Bacon, 2003).

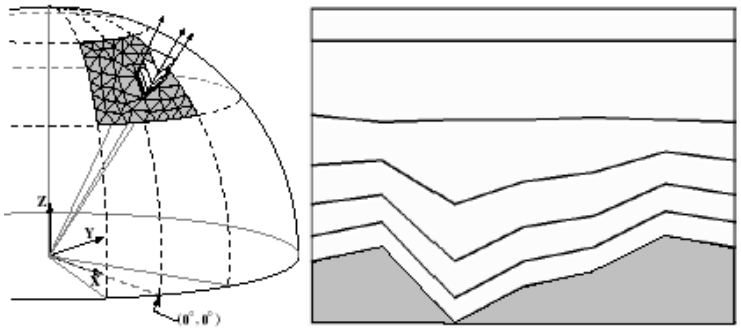

Figure 3. 7 : The vertical levels of the OMEGA grid are constructed by extending radials through each surface vertex. A set of stretchable layers exists near the surface with constant thickness layers above (Bacon, 2003).

3.6 Surface Characteristics Databases

Some of the datasets are used (e.g., terrain elevation, land/water fraction) during the adaptation process, however some of the surface data such as, soil type, climatological vegetation index, land use/land cover, climatological sea surface temperature, climatological subsurface temperature and climatological soil moisture are assigned to each grid after grid is generated. Soil type and climatological vegetation index are determined from global datasets, which have been widely used for numerical modeling. For vegetation index and land cover two different datasets are provided. One of those datasets is high resolution at North America, and the other covers the whole globe with less resolution. Global Vegetation Index (GVI) has a resolution about 13 km, and the USGS has published a 1 km Normalized Difference Vegetation Index (NDVI) over the U.S. Two climatological NDVI datasets were created for OMEGA: a 4 km dataset covering the U.S., and a 55 km dataset covering the globe. Global soil type database created from Global Ecosystem Database is 110 km resolution in the OMEGA. The twelve soil types are used in the model. Vegetation is significant in terms of atmospheric circulation since it modifies the

thermal moisture budgets of the earth surface. Two land use datasets were created: one is a 4 km land-use dataset covering U.S. that was formed from a 1 km Biosphere-Atmosphere Transfer Scheme (BATS) dataset and Advanced Very High Resolution Radiometer (AVHRR) data, and the other is a 55 km global dataset which was formed from the Olson (1992). In addition, OMEGA can use the 1km USGS landuse database based on 1-km AHVRR data. The dataset uses the Global Ecosystem Classification Scheme, which has 94 different landuse categories including urban areas and inland water and sea water separately. Terrain elevation is provided by 1 km USGS terrain elevation data in the OMEGA.

OMEGA uses a global sea surface temperature climatological dataset produced by the USGS (Schweitzer, 1993). The data has been processed into a bi-weekly global, 0.2 degree (about 20 km) dataset. This data does not extend beyond about 70 degrees latitude in either hemisphere. Some areas are not covered resulting in large lakes without data; for example the Caspian Sea in central Asia is completely missed. The original dataset was weekly; every other week was processed for OMEGA (Bacon, 2003). Monthly global subsurface temperature climatology was built from monthly average surface air temperatures from the Global Ecosystems Database (Legates and Willmott, 1992). This 30 minutes resolution data was built by using monthly average surface air temperature as an estimate of subsurface temperature. Although soil moisture is an important variable in numerical weather prediction but is difficult to determine. Soil moisture data is generated from the temperature and precipitation data (Legates and Willmott, 1992) using Budyko's simple soil moisture budget equation as described by Sellers (1965) in OMEGA. The monthly budget equation is given by:

$$W_2 = W_1 + r - E - S \qquad \textbf{(3.2)}$$

where W_2 is the soil moisture value at the end of a month, W_1 is the soil moisture at the beginning of the month, r is the precipitation, E is the evapotranspiration, and S is the moisture surplus term. Evaporation is a function of the monthly mean temperature. Although this simple approach does not provide perfect solution, it gives reasonable results for a range of climatic types. Volumetric soil water content, which balanced the annual water cycle, is obtained by using an iterative application of the Budyko equations (Bacon, 2003). Detail information about OMEGA will be given in Appendix A2.

4. A STATISTICAL and NUMERICAL ANALYSIS of URBANIZATION EFFECTS in ISTANBUL

Anthropogenic changes in the earth landscape such as cultivation, deforestation and desertification are the most important factors that affect the atmosphere (Ramankutty and Foley, 1999; Wang and Jenkins, 2002; Sen at al., 2004a,b). In addition to these significant anthropogenic changes, urbanization has become another important factor reshaping the land surface.

Approximately 47% of the world's population is living in cities and it is expected to increase in this percentage due to the immigration from countryside to the cities. According to Population Referans Bureau (2005), 41% of the population lives in cities in less developed countries while this percentage is 76% in the more developed countries in 2005. Therefore, changes in the climate due to the urbanization are important, and many studies have been conducted to understand the urban climatology. Arnfield (2003) and Voogt and Oke (2003) present reviews of progress in urban climatology. Yagüe et al. (1991) reveal that heat of anthropogenic origin and air pollution, replacement of the natural surfaces by buildings and impermeable pavements give rise to impact on urban atmosphere. Changes over the surface properties influence the surface water, energy and radiation balance. Warming over an urban area results from a decrease in evapotranspiration and loss of latent heat from the impermeable ground (Kalande and Oke, 1980). Besides, impermeable surfaces have greater specific heat capacity that delays the loss of energy from the ground (Yagüe, 1991).

City geometry also contributes to the heating of the urban areas or prevents the cooling of the urban areas. Warmer urban atmosphere than the its outskirting is known as "urban heat island (UHI)". Since radiative cooling difference is maximized between urban and rural areas, UHI is clearly observed on clear and calm nights (Voogt and Oke, 2003). Different methods have been applied to understand the characteristics of UHI. Longterm temperature data from urban and rural areas were commonly used method investigating UHI (e.g. Colacino and Rovelli, 1983; Yagüe

et al., 1991; Karaca et al., 1995a,b; Philandras et al., 1999; Montavez et al., 2000; Tereshchenko and Filonov, 2001; Zhou et al., 2004). Data network in or around a city is another method to study the UHI characteristics (e.g. Landsberg, 1981; Oke, 1982; Park, 1986; Montavez et al., 2000; Kim and Baik, 2005). Remote sense measurements and surface-atmosphere models are also used in UHI studies (e.g. Gallo et al., 1993; Kinouchi and Yoshitani, 2001; Streutker, 2003; Kusaka and Kimura, 2004; Dandou et al., 2005; Jin et al., 2005; Lamptey et al., 2005).

4.1 Description of the Study Area and Climate

Istanbul, the largest city of the Turkey with a population of over 10 million, is located at 41.01°N, 28.58°E. The Bosphorus, a 30 km strait which connects the Black Sea and the Marmara Sea, is a boundary between Europe and Asia.

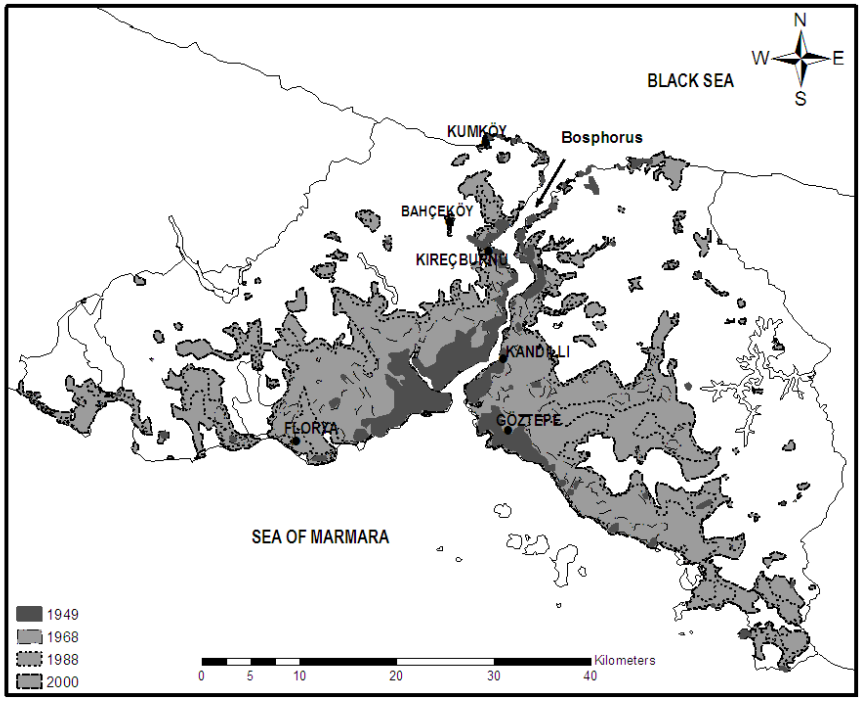

Figure 4. 1 : Expansion of urban areas of Istanbul from 1949 to 2000 (adapted from Celikoyan, 2004). Six meteorological stations are also shown in the map. western and eastern peninsulas are called the European and Asian side, respectively.

The urbanized region of the city is located on both sides of the southern part of the strait (shown in Figure 4.1). The city has historically expanded in east-west direction along the Marmara shore however northerly expansion has also occurred in recent years. The north part of the city towards the Black Sea is covered by forest. The

settelment areas along the Bosphorus at the cliffs looking over the strait are somewhat greener than the rest of the city. The most densely populated part of the city lies in the south, along the Sea of Marmara. Figure 4.1 depicts the expansion of the urbanization with respect to the years 1949, 1968, 1988 and 2000. This city information is taken from Çelikoyan (2004) who defined the city boundaries in these years based on airborne and spaceborn measurements. The author combined the three different aerial photographs 1940, 1942 and 1949 to defined the 1949 images by assuming the city expanded little in 1940s.

The population changes in Istanbul between 1935 and 2000 is shown Figure 4.2. The city's population increases fast in last 20 years from 1980 to 2000. The population grow rate of Istanbul was 29.64% for urban part and 81 % for the rural part of the city for the 1990-2000 period. The ratio of urban population to total population in Turkey increased from 59% to 65% from 1990 to 2000.

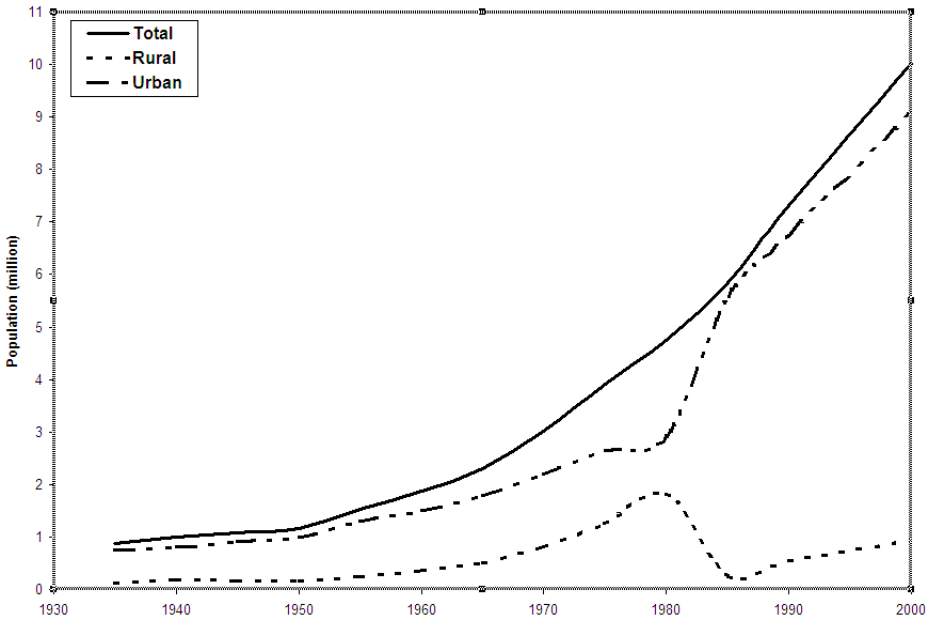

Figure 4. 2 : Population growth in Istanbul from 1935 to 2000.

The climate of the city shows difference between southern and northern part of Istanbul. The southern part of the city, where urban areas lie, show the general characteristics of the Mediterranean climate while on the north, the Mediterranean type climate is modified by the cooler Black Sea and northerly cold air masses of maritime and continental origins, locally called The Black Sea Climate. This type of climate have cooler temperatures in both winter and summer and have experiences

with more rain compared to the Mediterranean coast of Turkey. Hence, northern part of Istanbul have cooler temperature than the south. In addition, precipitation regime is different over the Istanbul. That is, while the south recieves about 650 mm annual precipitation, it is 850 mm on the northern coast and 1050mm on the inland part. Based on the stations averages, average annual total precipitation is around 800 mm and average temperature is 28^{o}C in summer and 8^{o}C in winter in Istanbul. The city is subject to moisture laden mid-latitude cyclones during winter months (Karaca et al., 2000); thus most of the precipitation falls in winter. The prevailing wind is northeasterly however southwesterly winds also blow during the year.

4.2 Statistical and Numerical Analysis of Urbanization in Istanbul

The statistical method used in this study is the non-parametric Mann-Kendall test. Mann-Kendall test is used to determine the existence of the trends in the station data. This method provides to find the approximate starting point and abrupt changes in climate (Goossens and Berger, 1986; Karaca et al., 1995a; Tayanc et al., 1997).
In Mann-Kendall test, climate data is enumerated in the time series. For each y_i, the number n_i of elements y_j preceding it *(i > j)* is calculated in such a way that $y_i > y_j$. The t test statistics is obtained by

$$t = \sum_i n_i \qquad \textbf{(4.1)}$$

and under null hypothesis, t is distributed nearly normal with an expected value and variance;

$$E(t) = \frac{n(n-1)}{4} \text{ and,} \qquad \textbf{(4.2)}$$

$$\text{var}(t) = \frac{n(n-1)(2n+5)}{72} \qquad \textbf{(4.3)}$$

The null hypothesis is rejected for high values of $|u(t)|$ when a trend exists.

$$u(t) = \frac{[t - E(t)]}{\sqrt{\text{var}(t)}} \qquad \textbf{(4.4)}$$

If $u_t > 0$ the trend is positive and if $u_t < 0$ the trend is negative and the significance level is 95%. The same principle can be applied to the backward time series data. For

each y_i term, the number n_i' of y_j is calculated. u_i' is given for the backward time series are given as;

$$u_i' = -u(t_{i'}) \quad \textbf{(4.5)}$$

The intersection between u_i and u_i' curves show the starting point of the changing trend of the data. This approach is known as 'Sequential Mann-Kendall Test' (Goossens and Berger, 1986).

Data for statistical analysis is obtained from the State Meteorological Service of Turkey. Monthly minimum temperature time series for the stations (shown in Figure 4.1) located in Istanbul is used for the Mann-Kendall test. The term monthly minimum temperature refers to the average daily minimums in month. Annual minimum temperature time series which refers to average of monthly minimum temperatures in year and seasonal minimum temperature time series refers to average monthly minimum temperature in season are calculated from this dataset. The period of the data is different in the stations. For example, Kandilli has the longest (1912-2004) records while the records are the shortest (1951-2004) in Kumkoy. 1951-2004 period is used since the minimum temperature difference between stations is the method that is used in the statistical test.

The stations are classified in three groups depending on population density of the area; urban, suburban and rural (Tayanc et al., 1997). The urban station Goztepe station is surrounded by building while another urban station Florya is directly open to the Marmara Sea. Kandilli and Kirecburnu are defined as suburban stations, which are located on the hills overlooking the Bosphorus. Bahcekoy and Kumkoy stations are assumed as rural stations. Bahcekoy is an inland rural station that is surrounded by mostly forest areas however Kumkoy is located on the Black Sea coast. Elevation difference between the stations is not more than 100m.

4.3 Results of the Statistical Analysis

Minimum temperature is used to study the urbanization effect on climate since it clearly shows the different behaviour between urban area and its outskirts (Landsberg, 1981). Thermal property of a city is different from its surroundings,

therefore urban area has higher thermal inertia which delays the cooling of the cities at nights when compared to the rural areas (Yagüe et al., 1991).

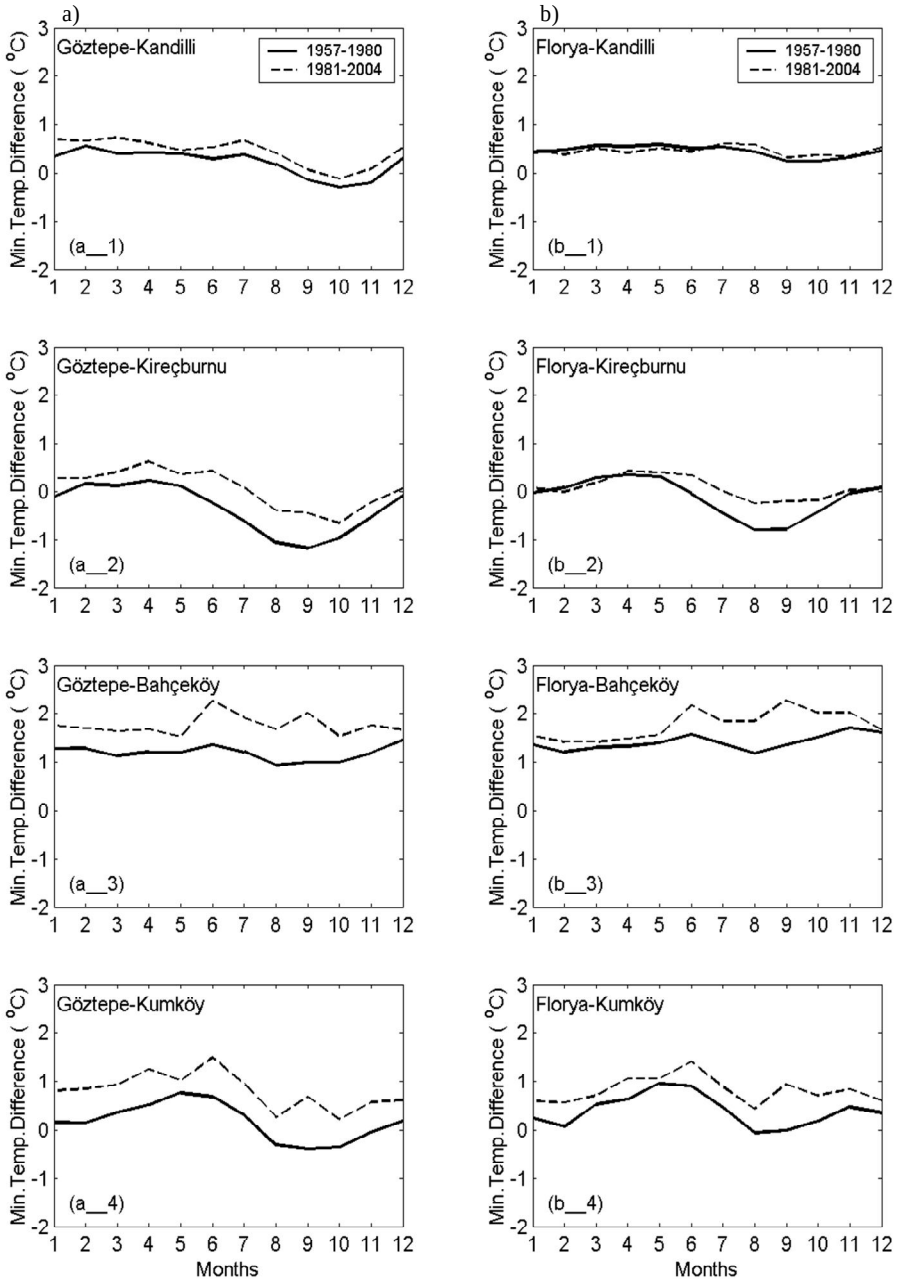

Figure 4. 3 : Difference of average monthly minimum temperatures between urban and suburban/rural stations for 1957-1980 (solid line) and 1981-2000 (dashed line) periods.

Average monthly minimum temperature difference between the urban stations (Goztepe (a) and Florya (b)) and the other four stations (Kandilli (a_1 and b_1), Kirecburnu (a_2 and b_2), Bahcekoy (a_3 and b_3) and Kumkoy (a_4 and b_4) are shown in Figure 4.3. The average monthly minimum temperature indicates the two

24-year period before and after 1980 that is the indicator of the fast growth of the population in Istanbul. Figure 4.3 shows the increase in minimum temperature difference between an urban and suburban/rural stations for period 1981-2004 than the period 1957-1980. The annual average difference increases from 0.17 ^{o}C for period 1957-1980 to 0.81 ^{o}C for the period 1981-2004 (shown in Figure 4.3 (a_4)). Similar to the Goztepe-Kumkoy (Figure 4.3 (a_4)), Florya-Kumkoy (Figure 4.3 (b_4) illustrates the increase in annual average minimum temperature from 0.39 ^{o}C to 0.82 ^{o}C. Also, from suburban to rural stations, the minimum temperature shows increase in disparity after and before 1980. For instance, it increases from 0.23 ^{o}C for Goztepe-Kandilli (Figure 4.3 (a_1)) to 0.41 ^{o}C for Goztepe-Kirecburnu (Figure 4.3(a_2)) to 0.57 ^{o}C for Goztepe-Bahcekoy (Figure 4.3 (a_3)) to 0.64 ^{o}C for Goztepe-Kumkoy (Figure 4.3 (a_4)). In addition, although the disparity occurs in all months, it is usually larger and most emphasized during the summer and fall months.

Table 4. 1 : Mann-Kendall statistics from the analysis of time series of seasonal and annual minimum temperature data between 1951 and 2004. (Statistically significant values are marked bold).

Stations	Spring	Summer	Fall	Winter	Annual
Göztepe	**4.13**	**4.89**	1.70	0.84	**4.19**
Florya	**2.93**	**4.26**	1.04	-0.49	**3.13**
Kandilli	**2.84**	**4.07**	0.41	-0.31	**2.31**
Kireçburnu	**2.65**	**2.84**	-0.49	-0.34	1.35
Bahçeköy	**3.01**	**2.56**	-0.80	-0.80	1.20
Kumköy	1.29	1.23	-1.56	-0.98	-0.75

The Mann-Kendall trend test is not adequate method to detect the sole urbanization effect on climate. The obtained trends may be affected by the other climate change signal. Thus, in order to avoid incorrect interpretation of the Mann-Kendall test, it is applied to the time series of temperature difference between urban/suburban stations and rural stations (Karaca et al., 1995a,b). The proportion of the climate change signals is reduced from the time series by this way and hence, it is expected that the rest of the signal gives the effect of urbanization.

The positive trends in all stations except Kumkoy are obtained from Mann-Kendall test which is applied to the annual minimum temperature (shown in Table 4.1). Urban stations, Goztepe and Florya, indicate the high Mann-Kendall values 4.19 and 3.13, respectively, with 95% (1.96) confidence level. Suburban station Kandilli has

also the positive trend with value 2.31. However, although another suburban station Kirecburnu has positive trend, it is not statistically significant. In terms of rural stations, while Bahcekoy shows the positive but insignificant trend, Kumkoy has negative insignificant trend (Table 4.1). In addition to the annual trends behaviour, it is possible to obtain information about seasonal trends in the stations from Table 4.1. It is inferred that spring (March, April and May) and summer (June, July and August) is the most pronounced seasons in terms of urbanization effects on climate. Positive significant trends from Mann-Kendall statistics are found for all stations except Kumkoy which has positive insignificant trend for summer and spring seasons. In contrast to the spring and summer seasons, there is no significant trend for fall (September, October and November) and winter (December, January and February) in any station. Sequential Mann-Kendall method, which indicates the starting point of the changing trend, is applied to the time series of annual minimum temperature difference between the four urban/suburban stations and Bahcekoy station. Bahcekoy is an inland station and it is located in a village in the middle of a forest area.

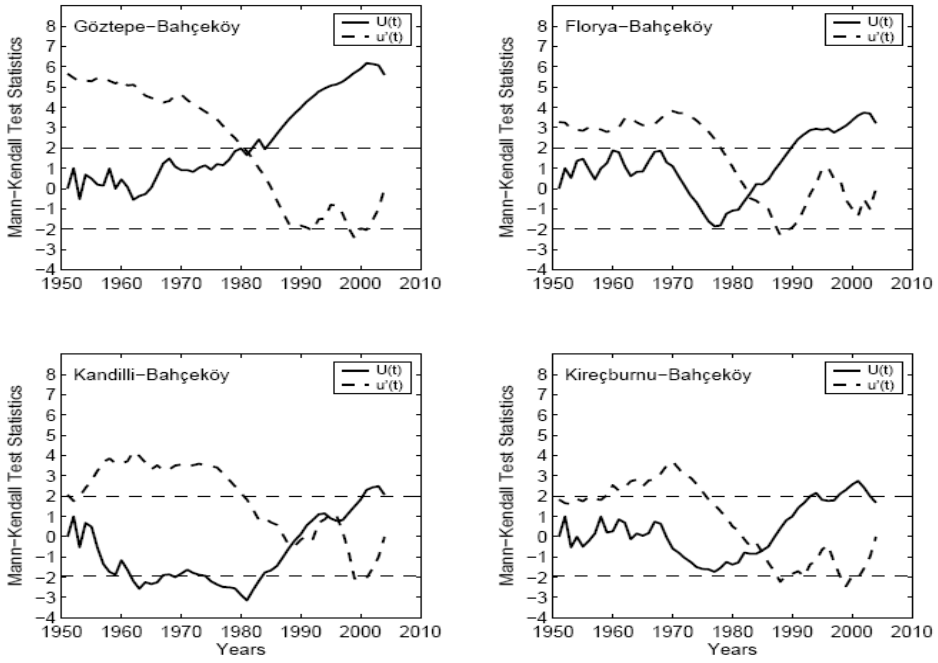

Figure 4. 4 : Results of sequential Mann-Kendall test applied to annual minimum temperature differences between urban/suburban stations (Göztepe, Florya, Kandilli, Kirecburnu) and a rural station (Bahçeköy). The value ±1.96 (the 95% confidence level) is represented with horizontal lines.

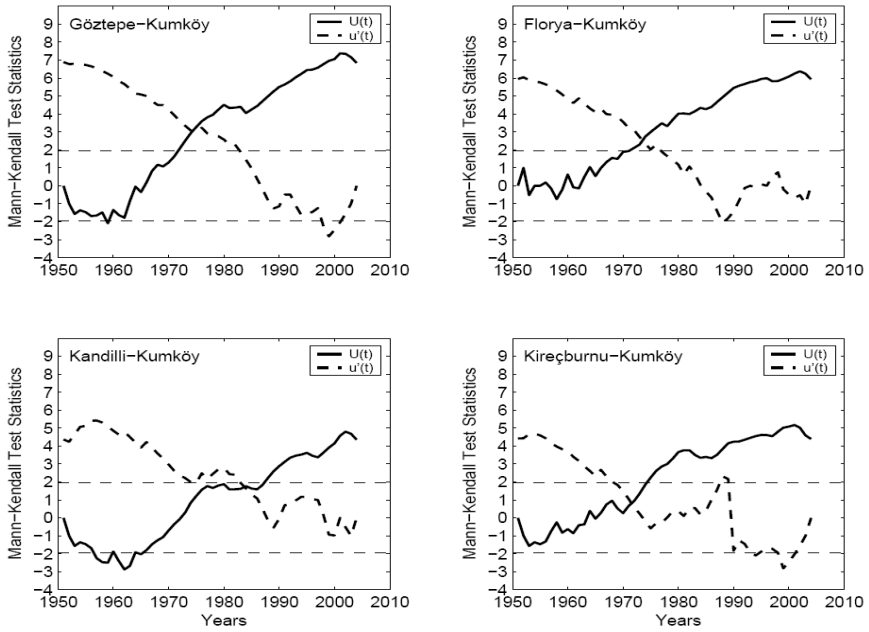

Figure 4. 5 : Results of sequential Mann-Kendall test applied to annual minimum temperature differences between urban/suburban stations (Göztepe, Florya, Kandilli,Kireçburnu) and a rural station (Kumköy). The value ±1.96 (the 95% confidence level) is represented with horizontal lines.

Figure 4.4 indicates that time series of annual minimum temperature difference between Goztepe, Florya, Kandilli and Bahcekoy (Figure 4.4a, b and c) have significant positive trends. For Kirecburnu station (Figure 4.4d) significant positive trend is observed for a few years around 2000 however the significance level is under 95% confidence level in 2004. The changes in the trend start in early 1980s for Goztepe and Florya stations while it is in late 1980s for Kandilli and Kirecburnu stations. The same analysis was conducted by using Kumkoy, rural station, as a reference station instead of Bahcekoy (shown in Figure 4.5). The analysis depicted that all four time series of differences obtained from subtracting urban and suburban annual minimum temperatures from Kumkoy annual minimum temperature positive trends with 95% confidence level. The analysis also showed that changing point of the trends began in the early 1970s for Goztepe and Florya (shown in Figure 4.5a,b) and early 1980s for Kandilli and Kirecburnu (shown in Figure 4.5c,d). Table 4.2 summarizes the Mann-Kendall statistics for these analyses. Table 4.2 also provides the seasonal statistics that are calculated by subtracting urban and suburban station data from rural station data. In all seasons, summer has the highest values for all pairs except for Kirecburnu-Bahcekoy and Kirecburnu-Kumkoy. Both stations have the highest values in winter instead of summer, however the Kirecburnu-Bahcekoy

does not have significant value. It can be deduced from all these statistics that fall has higher values than spring, however, analysis based on individual station data illustrates higher Mann-Kendall values in spring than fall. Linear regression is also applied to the minimum temperature difference between the urban/suburban and rural stations so as to understand the UHI intensity change for 1951-2004 period. UHI intensity is characterized as the temperature difference between the city peak and the rural background temperature of the night, cloudless skies and light wind conditions.

Table 4. 2 : Annual and seasonal Mann-Kendall statistics from the analysis of time series of minimum temperature differences between urban and rural stations for the period between 1951 and 2004 (Statistically significant numbers are marked bold and highest seasonal values are underlined).

Station pairs	Spring	Summer	Fall	Winter	Annual
Göztepe-Bahçeköy	**4.26**	**6.31**	**5.00**	**3.42**	**5.60**
Göztepe-Kumköy	**5.51**	**6.96**	**5.78**	**4.89**	**6.84**
Florya-Bahçeköy	0.18	**4.33**	**3.48**	0.35	**3.22**
Florya-Kumköy	**3.48**	**5.25**	**4.62**	**3.05**	**5.93**
Kandilli-Bahçeköy	0.64	**3.27**	**2.59**	0.29	**2.07**
Kandilli-Kumköy	**2.98**	**4.08**	**3.76**	**2.62**	**4.35**
Kireçburnu-Bahçeköy	0.09	0.55	0.89	1.30	1.68
Kireçburnu-Kumköy	**3.39**	1.87	**3.10**	**4.46**	**4.39**

The linear fit assumption is applied as a measure of the change of average UHI intensity over time since there is not enough information about the definition. The linear fit approach eliminates the year-to-year variability. UHI changes between 1951 and 2004 are given in the Table 4.3 for the station pairs. These values are calculated from linear fit and imply the linear regression values between 1951 and 2004. The minimum temperature differences between urban/suburban and rural stations are larger when Kumkoy is used as the reference rural station. As it is expected maximum differences are observed in the urban-rural pairs. For example, annual UHI intensity increases 1.43^{o}C for Goztepe-Kumkoy pair and 0.94^{o}C for Florya-Kumkoy pair over the 54-year period. This analysis shows that UHI intensity changes are the largest in the summer and lowest in the winter. If the UHI intensity values are compared to the other cities in the literature, changes is smaller in Istanbul. The reason for this behaviour could be due to the fact that the Istanbul is located in between large water bodies, which is connected by the narrow strait (the Bosphorus).

Table 4. 3 : Annual and seasonal warming values (in ^{o}C) from 1951 to 2004 based on linear regression analysis of time series of minimum temperature differences between urban and rural stations for the period between 1951 and 2004.

Station pairs	Spring	Summer	Fall	Winter	Annual
Göztepe-Bahçeköy	0.75	1.40	1.24	0.66	1.00
Göztepe-Kumköy	0.25	1.75	1.68	1.19	1.43
Florya-Bahçeköy	0.10	0.87	1.21	0.10	0.52
Florya-Kumköy	0.67	1.17	1.65	0.63	0.94
Kandilli-Bahçeköy	0.10	0.65	0.55	0.02	0.31
Kandilli-Kumköy	0.61	1.00	0.98	0.54	0.73
Kireçburnu-Bahçeköy	0.04	0.16	0.19	0.22	0.18
Kireçburnu-Kumköy	0.54	0.50	0.63	0.75	0.60

Kim and Baik (2004) mentioned that coastal cities have smaller UHI intensity values than the inland cities. It is inferred from the statistical analysis that urbanization is the reason behind the increase in minimum temperature in Istanbul. It is difficult to understand the whole structure of the urban heat island in Istanbul since there are not enough observation stations uniformly distributed across the city. Also it is important to understand the urbanization effects the upper atmospheric levels, which is not possible to have on from the surface data. Because of these discrepancies, mesoscale atmospheric model experiment, which is given in the following section, is conducted.

4.4 Numerical Modeling Experiment

Mesoscale atmospheric model, MM5, is utilized in this part of the research. Model is set up as three nests with horizontal resolution with 27, 9 and 3km, respectively, and 23 vertical layers. Model main domain covers an area including western part of Turkey, Balkans and eastern part of Italy (shown in Figure 4.6). The innermost domain spans 111 km east-west direction and 111 km north-south direction that covers the city of Istanbul and surrounding land and water masses. In this study, 3 km horizontal resolution is used due to the lack of computational facility. Although this resolution provides information about urbanization effect in both lower and upper atmospheric levels in Istanbul, unfortunately, the resolution is not high enough to solve the Bosphorus and some other feature of the city.

Model uses USGS (United State Geological Survey) 25 category land-use and terrain data with 30-s resolution in the simulations. Initial and boundary conditions are prepared by using 2.5 x 2.5 degrees NCEP/NCAR reanalysis data with 17 vertical

levels. Although model has several physics options, rapid radiative transfer model (RRTM) atmospheric radiation scheme, Grell (for the two outermost domains) and Kain-Fritsch (for the innermost domain) cumulus parameterization schemes, MRF (NCEP Medium Range Forecast) planetary boundary layer scheme, 5-layer soil scheme and mixed-phase microphysical scheme is used for the simulations.

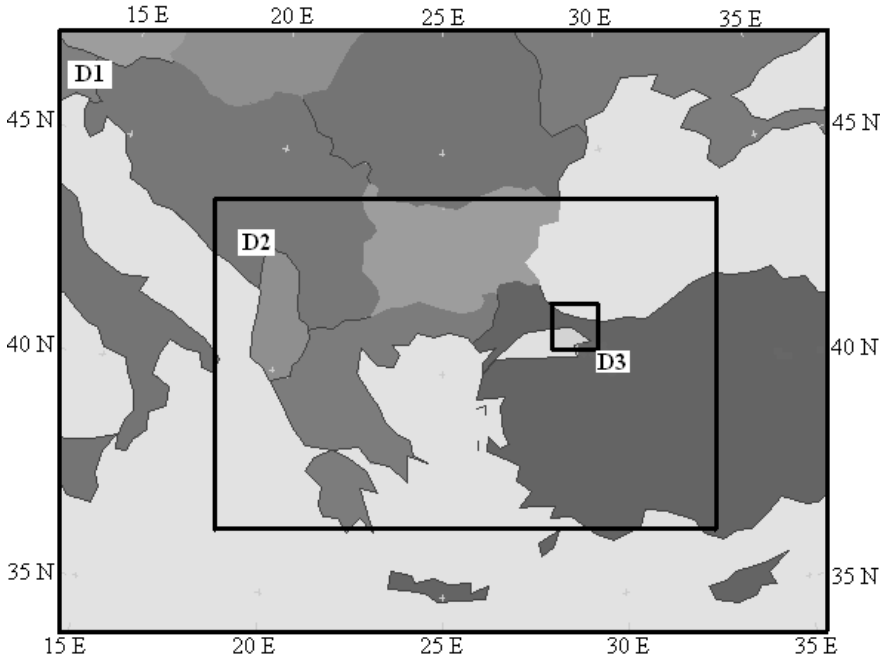

Figure 4. 6 : MM5 nested model domains. The outermost domain (D1), the middle domain (D2) and the innermost domain (D3) have 27, 9 and 3 km spatial resolutions respectively.

Depending on the statistical analysis results, it is found that summer season has largest effect of urbanization on the local climate. Therefore, summer month July 2004 is determined for the model experiment. Two different landscapes are prepared by MM5 model using data by Celikoyan (2004). The growth of the urbanization in Istanbul is investigated by designing landscape as “past” and “recent” in order to take UHI into consideration. The city urban boundaries provided by Celikoyan (2004) are only for the certain years. Therefore, closest years to 1951 and 2004, which are used in statistical part of the study, are utilized in the model’s surface map. For the past simulation map is modified to the 1949’s landscape, and for the recent simulation 2000 is used. Since land cove/vegetation map used in the model is very old, it does not reflect the current the city urban boundaries. Therefore substantial modification is applied to the model especially for 2000. The model grids most of which are

'dryland crop' type (a small number of them are crop/grass mosaic, grassland, shrubland, and deciduous broadleaf) are assigned 'urban' type. Information of the surface parameters for the land-use types, which are changed in the model is given in the Table 4.4. If the land-use type is change from dryland crop to urban, the albedo changes from 17% to 18%, moisture availability from 30% to a much smaller value (10%), emissivity from 92% to a smaller value (88%), roughness length from 15cm to a much bigger value (50cm), and thermal inertia from 0.04 cal cm^{-2} $k^{-1}s^{-1/2}$ to a smaller value (0.03 cal cm^{-2} $k^{-1}s^{-1/2}$).

Table 4. 4 : Land-use type features in MM5.

Land Use Type	Dryland Crop. Past.	Crop/Grass Mosaic	Grassland	Shurbland	Deciduous Broadleaf	Urban
Albedo(%)	17	18	19	22	16	18
Moisture Availability (%)	30	25	15	10	30	10
Emissivity (% at 9μm)	92	92	92	88	93	88
Roughness Length (cm)	15	14	12	10	50	50
Thermal Inertia (cal $cm^{-2}k^{-1}s^{-1/2}$)	0.04	0.04	0.03	0.03	0.04	0.03

The modeling experiment is designed to simulate the effect of urbanization depending on the changes explained above. There are no changes in structural and geometrical features of the city. The same initial and boundary conditions are applied to the model for 1951 and 2004 cases to understand the response of the urban atmosphere to the urbanization in Istanbul.

4.5 Results of the Numerical Model Experiment

Surface temperature difference is averaged from the simulated 6 a.m. for July for 1951 and 2004 simulations. Two heat island cells are observed over the city as shown in Figure 4.7. One of these cell is located on the European side and the other one is on the Asian side of Istanbul. The expansion of the UHI is only valid after 1951. The complete UHI is expected to cover the urbanized parts of the city before 1951 too. Although the MM5 model cannot solve the Bosphorus, it can be realized that the two-cell structure occurs primarily as a result of pre-1951 urban areas which is located along the Bosphorus. This feature is treated identically in both simulations. The maximum surface temperature difference between 1951 and 2004 is about $1^{o}C$ at 6 a.m. for July. Figure 4.8 indicates the water vapor mixing ratio difference at 6 a.m.

Reduction of moisture availability due to the urbanization results in a decrease in the mixing ratio in the overlying atmosphere. The maximum decrease in mixing ratio is -15 g kg^{-1}. It can be inferred from the Figure 4.8 that the surface mixing ratio is increased over a region to the west of urbanized area in Istanbul. As it is expected urbanization decreases the wind magnitude over the city and surrounding areas. This feature is shown in Figure 4.9 by using 10m wind anomalies between 1951 and 2004.

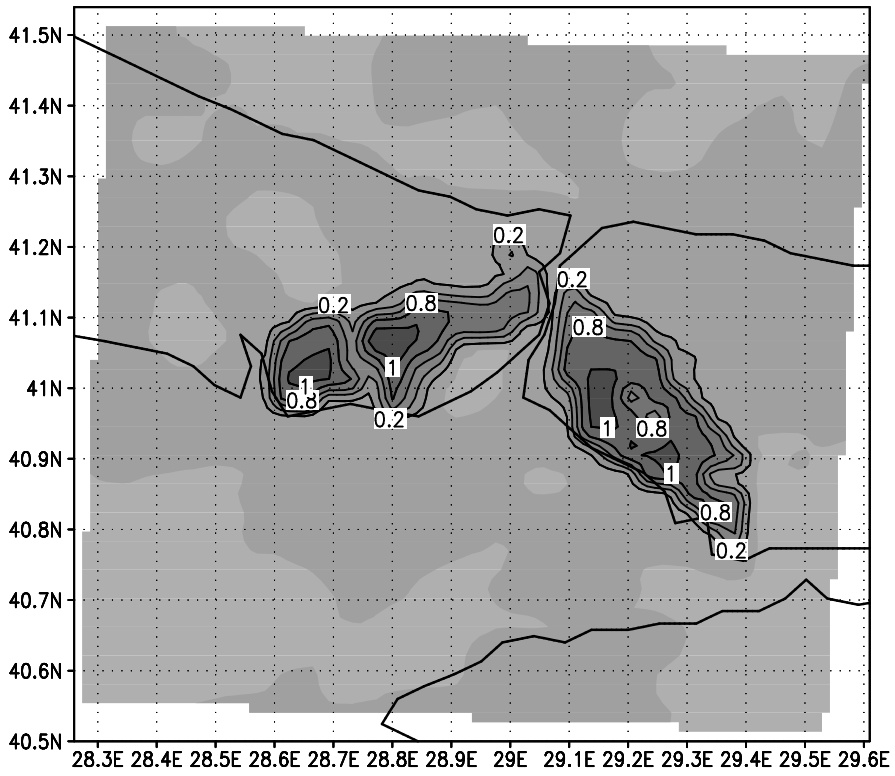

Figure 4. 7 : Surface temperature (reference level) difference (in oC) between 2004 and 1951 July simulations. The difference is calculated from monthly averaged 6am surface temperature outputs of model simulations.

The wind vectors illustrate a southwesterly flow over the city. Changes in wind magnitude and vectors imply that the velocity of the northeasterly winds (prevailing winds in July) is reduced over Istanbul. The increased roughness length can be the primarily responsible reason for the behaviour of the wind. In addition to the investigation of the surface, higher atmospheric layers are also analyzed. Development of the UHI at the higher levels is examined by using temperature difference at different heights. Also, longitudinal cross-sections of air temperature difference on both European and Asian sides to understand how far the urbanization effect the overlying atmosphere.

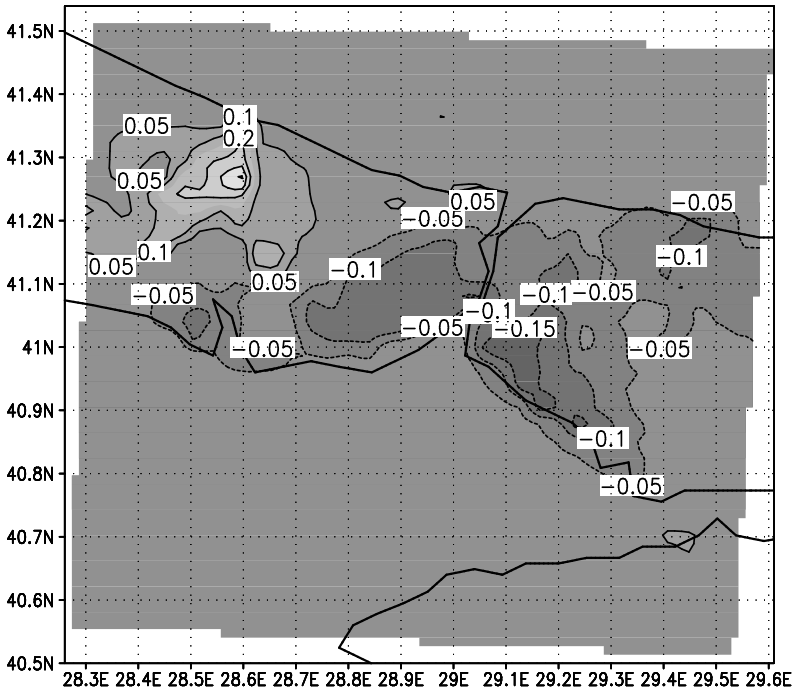

Figure 4. 8 : Mixing ratio difference (in g kg^{-1}) between 2004 and 1951 July simulations. The difference is calculated from monthly averaged 6am surface outputs of model simulations.

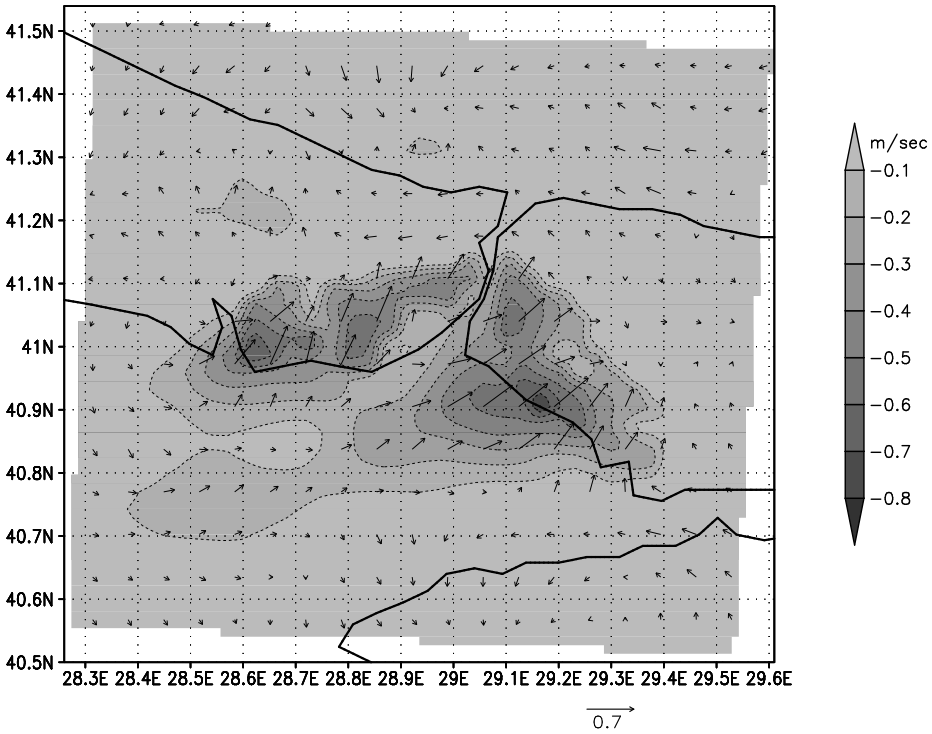

Figure 4. 9 : Difference of wind (vectors and magnitude) between 2004 and 1951 July simulations. The difference is calculated from monthly averaged 6am surface outputs of model simulations.

Temperature differences between 2004 and 1951 at two levels, 36 m and 200m above the ground at 6 a.m. are given in Figure 4.10. Cross sections of the temperature differences along 28.75E and 29.16E, which represent the European and Asian side of the city, are shown in Figure 4.10c and Figure 4.10d. It seems that the two UHI cells observed in the surface air temperature are combined at higher atmospheric levels over the Bosphorus (Figure 4.10a and b), and the combined cell extends southward over the Marmara Sea most likely due to the prevailing northeasterly flow in July however the largest temperature difference occurs over the urban area. The heating effect of urbanization reaches up to 600-800 m height (shown in Figures 4.10c and d). Both European and Asian sides of the city have slightly cooled layers above the ground at different heights. This cooled layer is observed between 600 and 800 m above the ground on the just north of the urbanized area on the European side (Figure 4.10c) while this layer appears between 800 and 1200 m over the urban area on the Asian side (Figure 4.10d).

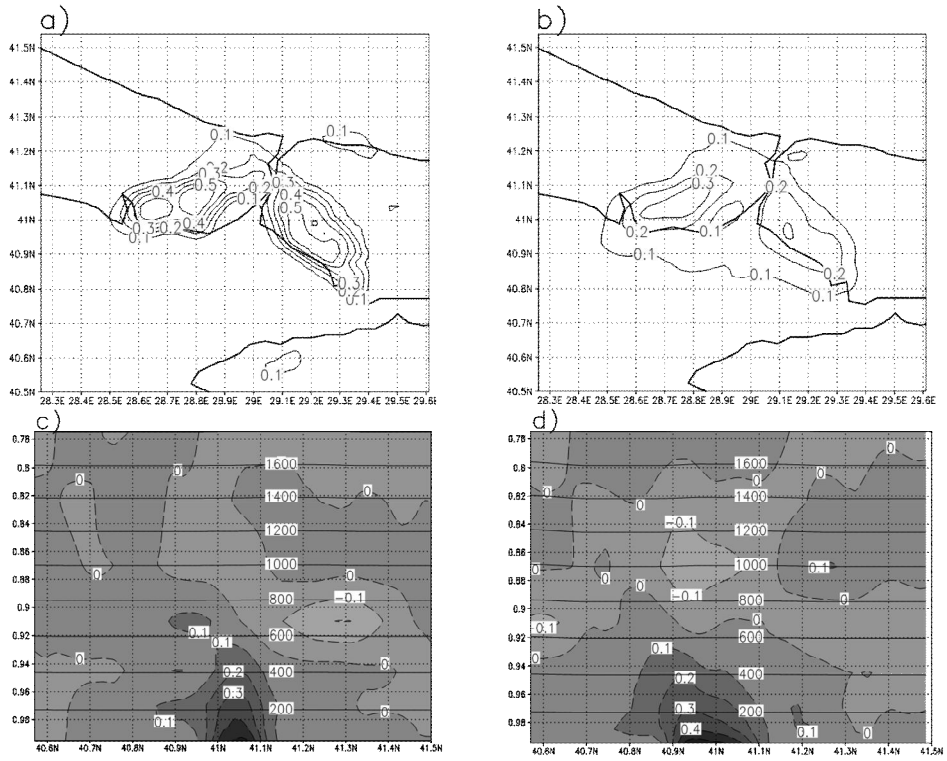

Figure 4. 10 : July (6am average) temperature differences between 2004 and 1951 simulations at two levels, 36m (a) and 200m (b) heights above ground, and cross-sections of the 6am temperature differences along 28.75 E in the European side (c) and 29.16E in the Asian side (d). The parallel lines in the cross-section plots show the heights (in meters) above ground.

5. INVESTIGATION of MESOSCALE-LOCAL FEATURE INTERACTION in ISTANBUL

The knowledge of the sea-land breeze characteristics is important since most coastal cities are preferred as residential areas. Thus, when the crowded cities are in consideration, urbanization must also be taken into account in addition to the thermally driven circulation. The heat capacity difference of urban-rural areas results in another important circulation known as urban heat island. Urbanization alters the characteristics of the circulation around the city either changing the roughness length, heat capacity or albedo. When studying local flows in the coastal areas it should be kept in mind that the sea breeze contributes to the local circulation as a secondary circulation. Moreover, if a coastal city has rough topography, in addition to the combination of urban heat circulation and sea-land circulation as well as mountain-valley circulation will affect the characteristics of the local circulation. The complexity arises due to the combination of those mesoscale circulations. Contribution of these circulations on the local flow is important especially for public health when the urbanized coastal cities are in consideration. Air pollutant can cause serious problem such as pollution from human activities can be transported by means of the sea and land breezes. Re-circulation of pollutants may occur in the urban areas. Besides, pollutants can be transported into the upper air level and change their chemical properties and return back to the surface.

Statistical and modeling effects of urbanization in Istanbul are studied in the first part of the study. However, due to the grid technique the performed model in this part, MM5, is not capable to represent the significant features such as the Bosphorus, coastline shapes of Istanbul and other small water bodies which influence the mesoscale circulations especially sea-land breeze occurrence, penetration and cessation and as a result the local flow in the region. Therefore, the other mesoscale model OMEGA is performed in this part of the study in order to overcome this lackness and capture the small features which are aforementioned. It is assumed that because of the grid technique used in OMEGA, which is a kind of advanced

Computational Fluid Dynamic (CFD) technique, can provide to better capture the unsolved features in MM5. Thus, the OMEGA model is preffered to investigate the relative effects of the features such as the Bosphorus, topograph, urbanization etc. on the local flow in Istanbul.

5.1 Meso-Scale Downscaling

The Marmara region, the interest area of this study, is surrounded by the Black Sea and the Aegean Sea with inland water body, Marmara Sea. Importance of the investigation of the local flow, therefore, is apparent since seas surround the region and settlement locates along the shoreline. However, detailed investigation focuses on the most crowded commerce center in this region, Istanbul. There is another reason to specify Istanbul for the study is that data availability. Although quality of the data is controversial, data network is denser in Istanbul than the other cities in Marmara Region for example Canakkale where the Dardanelles splits the city in two parts and its orientation is similar to Istanbul.

Istanbul is located between $28^{o}01'E$-$29^{o}55'E$ longitudes and $40^{o}28'N$-$41^{o}33'N$ latitudes where two seas that have different physical and chemical properties are combined via a narrow strait. This strait named as Bosphorus splits Asian and European continents. Most of the residential districts are located along the Bosphorus. In Istanbul, the topography rises up to 200 m-350 m where the eastern part is slightly higher than the other parts. The geographic location and physical features of Istanbul allow to study the sea-land breeze and also the urban heat circulation.

Mesoscale models are not able to solve the strait of Bosphorus since the 1 km terrain data resolution is low to represent this narrow strait. The technique, OMEGA uses is sensitive to the land-water boundary. Another important property in terms of the study is that OMEGA allows simulations under the standard atmospheric conditions.

The study is divided into two parts. In the first part, idealized case studies are used to investigate the effect of geographic features (the strait, lake, and island), geostrophic wind direction, and topography on the local flow. In the second part, the real case studies are conducted to understand the behaviour of the flow under realistic atmospheric conditions.

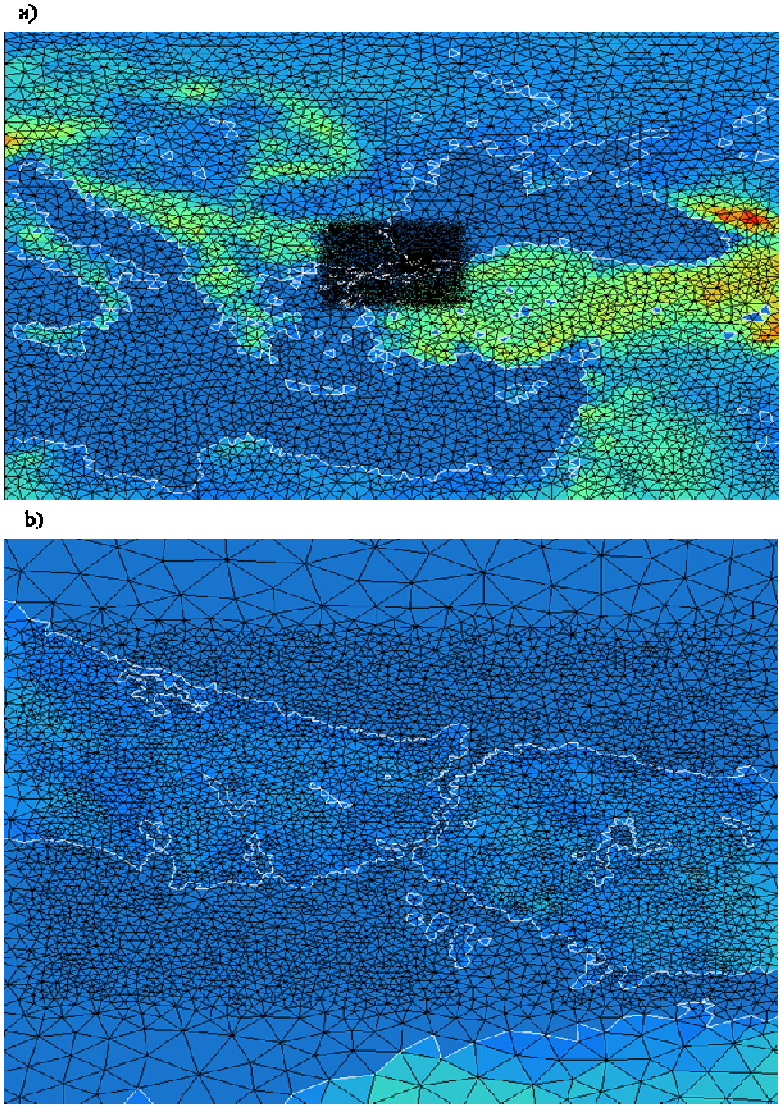

Figure 5. 1 : Mesh structure of the OMEGA simulation for a) coarser domain and b) finer domain.

In the idealized case studies, the specified "standard atmospheric conditions" applied to the OMEGA model to evaluate the impacts of the each feature by changing only one feature in each simulation. For instance, if the effect of geostrophic wind direction is the focus of the investigation than only the wind direction over the region is changed and all the other parameters (i.e., topography, geographic features) kept constant. Triply nested grid domain (shown in Figure 5.1) is used in the OMEGA model. The course domain is located at 52.00 ^{o}N-12.05 ^{o}E and 30.00 ^{o}N-44.00 ^{o}E. Horizontal grid resolution changes 60 km-0.560 km and 35 vertical layers range is 30 m to 20,988 m. 26666 grid cells are generated for the mesh that does not change during the simulations. Since two different types of simulation are performed, initial

and boundary conditions are also different on both simulation types. Temperature and geostrophic wind is specified for standard atmospheric conditions. Temperature is set to 20^{o}C at the surface for all idealized simulations and geostrophic wind is kept constant at vertical. Initial flow changes depending on studied features. Namely, if wind direction difference is investigated, only the direction will be changed. However, NCEP Aviation (AVN) and global gridded analysis dataset is used for real case simulations preparing 3 hourly boundary conditions for the dataset, respectively.

5.2 Sensitivity Simulations

Large scale weather patterns and interactions between mesoscale features affect the atmospheric motion over a region. Therefore, contribution of the physical geographic features and atmospheric dynamics to the region is important to deduce the local flow characteristics. The starting point of the hypothetical cases comes from the complexity of the land-water and geographic properties of Istanbul and its vicinity. Aside to that, sea surface temperature distribution is different over the Black Sea than the Marmara Sea (see Figure 5.2). Figure 5.2 is plotted using 1km MODIS SST satellite data. In order to determine the SST behaviour of the Marmara Sea and the Black Sea, SST data are averaged on randomly taken points that are very close to the Marmara Sea and the Black Sea coasts of Istanbul. Although the general expectation is to see warm water temperature over the Marmara Sea since the Black Sea is semi-closed inland sea, monthly SST data also depict that it is possible to observe the opposite situation for example, in July, August, and September. It is interesting to note that temperature difference between the Seas can increase up to 3^{o}C.

Although atmospheric mesoscale models have some limitations such as, coarse input data in time and space from the models (AVN, MRF etc.) for atmospheric parameters or coarse horizontal resolution for surface paramaters over a domain, effect of geographic features and large scale flow is investigated in this study using fully-nonhydrostatic, unstructured mesoscale model OMEGA to simulate spatial and temporal characteristics of the local flow in Istanbul. This model is chosen because it better represents the land/water boundaries with its unstructured mesh. Features (e.g. topography, a strait etc.) have relative contribution to the local flow over the region. Therefore, different simulations are conducted to answer the inquiry of effects of those features.

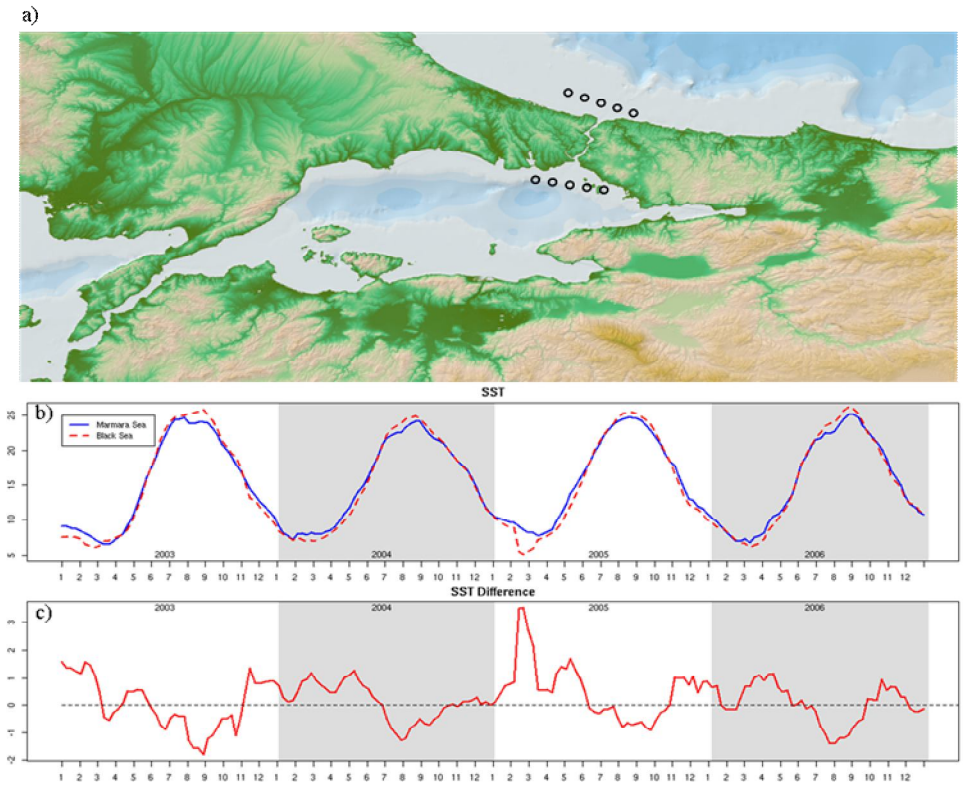

Figure 5. 2 : Satellite Monthly SST distribution over the Black Sea and Marmara Sea for period from 2003 to 2006 a) location of data points b) SST for the Marmara Sea and the Black Sea and c) SST difference between the Marmara Sea and the Black Sea.

As Istanbul is located nearby water bodies, it is not a surprise to encounter the existence of sea and land breezes which are generated by land-water contrast. If the water-land temperature difference is enough to start a sea breeze, it is usual to observe the onset of the sea-land breeze. In addition to the thermally driven effect, the Boshporus, which splits the region into two mainlands, can also contribution to the local circulation by means of channeling the flow over the Bosphorus. Beside of these, surface properties such as roughness length change because of the urbanized areas cause significant contribution on the flow. Analyzing of all those features is conducted by changing one property while keeping rest of them constant.

By using wind rose analysis technique, it is found that wind frequently blows from NE-SW direction in first 100 m for both day (at 1200 GMT) and nighttime (at 0000 GMT) and it is shown in Figure 5.3. If the vertical change of the wind is analyzed similar behaviour is observed at 1500 m, 3000 m and 5000 m. However, general wind direction is blow mostly from the quadrant which contains SW-NE and NW at 5000 m both day and night.

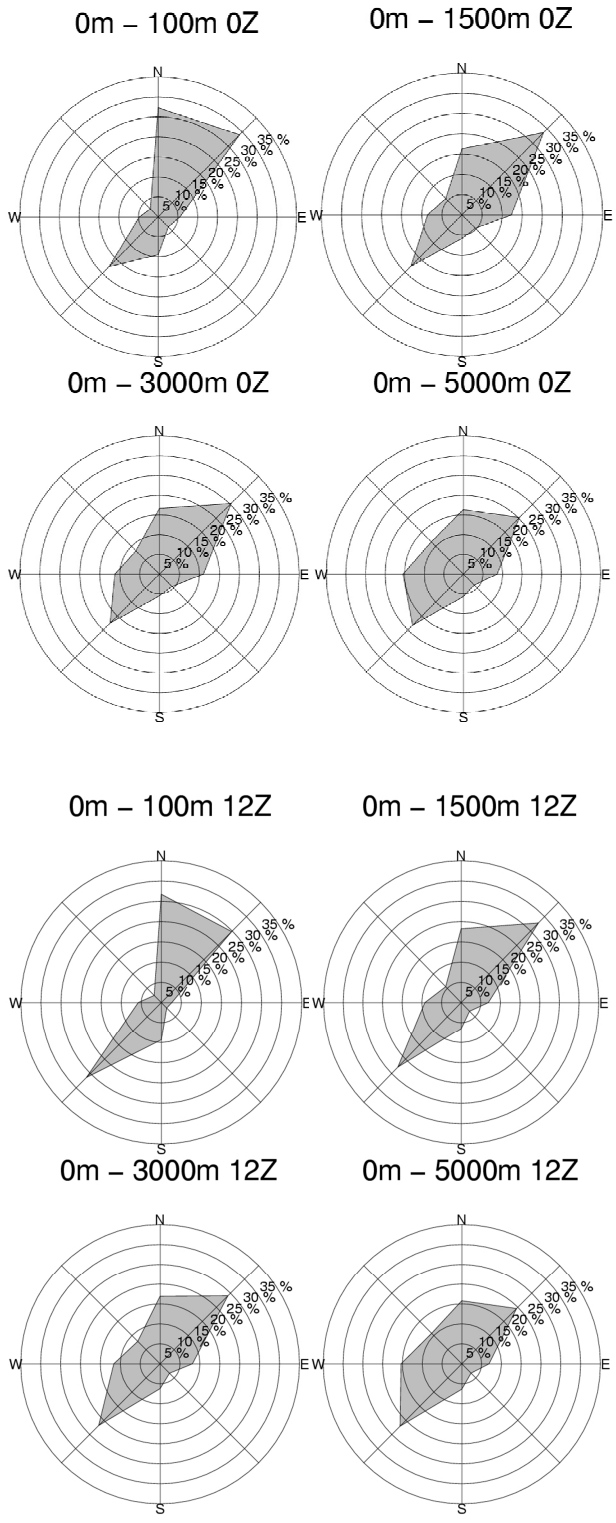

Figure 5. 3 : Istanbul (Goztepe) upper-air station daily wind rose plots between year 2000 and 2005 a) nighttime and b) daytime.

NE-SW is the prevailing wind direction in Istanbul as it is obtained from the wind rose analysis. Therefore, during the simulations, the flow is set initially as

northeasterly (~0.25 m/s) wind direction while determining the effect of geographic physical features. Afterwards, another simulation is conducted for southwesterly wind (~0.25 m/s) to understand the effect of general flow conditions by keeping the other features as similar to the northeasterly cases.

Figure 5. 4 : SST data for the model derived from ground temperature.

During the simulations surface characteristics (such as, soil moisture, soil temperature, etc.) are kept constant for all the idealized cases. Furthermore, a gradual increase (approaximately 1^{o}C) in the sea surface temperature (SST) from the Black Sea to the Marmara Sea is set utilizing the ground temperature. Water surface is 2^{o}C colder than the land in the non-urban areas. If the urban scheme is used while performing OMEGA, urban areas is set 2^{o}C warmer than the non-urban as default (Figure 5.4). This assumption depends on the findings from the previous studies that the urban regions are warmer than the non-urban regions at least 1-2^{o}C and might even be 10^{o}C warmer (Landsberg, 1981; Oke, 1987). The model is initially set to the standard atmospheric conditions that make the study of idealized cases possible. Initially, air temperature is set to 20^{o}C in order to represent the summer surface temperature, pressure is 1013.25 mb and northeasterly calm wind is specified as geostrophic wind. All these assumptions are applied to the entire domain as well as to the all vertical layers.

While conducting the simulations, the geographic physical features are brought from the simplest condition to the actual condition one-by-one. During the simulation,

alterations are applied only to the innermost domain except for the flat topography assumption. Flat topography condition is applied to whole domain from outermost to the innermost domain. A uniform land-use map is utilized on the simulations by manipulating the model land-use (Figure 5.5).

Figure 5.5 : Land-use map for uniform flat simulation.

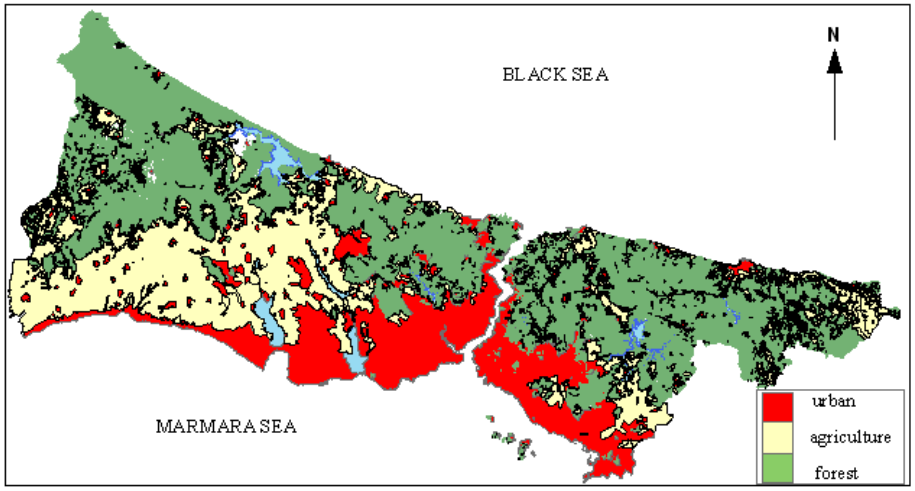

Figure 5. 6 : Land-use types prepared by the Municipality of Istanbul (red is urban region, green area is forest and the rest shows the agricultural area) (adopted from İstanbul Metropoliten Planlama ve Kentsel Tasarım Merkezi).

Modification is fulfilled from the current land-use map prepared by the Municipality of Istanbul. In addition to the urban region, this map also indicates the areas covered by forest and agricultural area. Therefore, entire inner domain is set as a forest on the

simple simulation to eliminate the effect of the roughness length difference in the domain for the sake of simplicity. Map of the land-use types based on the Municipality of Istanbul (shown in Figure 5.6) is used to be able to simulate details of the domain for realistic idealized cases since the land-use/land cover data, which are used in the atmospheric models, do not represent the current land-use characteristics perfectly.

After setting the fundamental characteristics, such as land-water boundary, surface characteristics (soil, moisture, soil temperature etc.), SST, and surface temperature, investigation focuses on dynamic and geographic features which are the components of local scale flow. Since the main objective of this part of the study is to understand the relative effect of each component on the flow, direct effect of the strait (the Bosphorus) is investigated by utilizing flat surface as a first and simplest case.

Not only the topography of Istanbul but also the entire coarser domain is interpolated to the sea level to prevent the disturbance on the initial and boundary conditions in the fine inner domain due to the topography. First idealized case, the simplest condition, is performed setting a uniform flat topography which means that everywhere in the domain is set to land (no strait). After eliminating topography effect, another simulation is conducted to analyze the presence of the strait (the Bosphorus). Therefore, only the strait causes the discrepancy between those two simple cases since the Bosphorus is added to the flat surface. As it is explained in the previous paragraphs, only one feature is changed on each performed run to investigate the relative change of each feature. The way to organize the idealized cases is that the possible simple situation is described as a first step and new features are added into the domain. Hence, topography is added to the domain without doing any changes over the modified land-use to analyze whether wavy hill topography of Istanbul has any contribution to the local flow. Mesoscale models are not able to represent the land-water boundaries in details as in reality because of the horizontal resolution problem and the computational cost. Although OMEGA is able to solve the domain still there is a problem while simulating some features for example the Bosphorus since it is a very narrow strait. Since the resolution is not fine enough to represent the strait over the domain, some cells over the domain are turned into the water for the better representation of the Bosphorus. Although surface is modified as water instead of land, topography created by the model is not changed in the

modified cells but it represents the channel throughout the Bosphorus. Here after, the uniform flat topography is named as flat, flat topography with strait as the flat-strait, real topography with strait as the real topo-strait, real topography with island as the real topo-island, and the real topography with all the geographic features with lakes and actual land-use type for northeasterly wind direction as ne-current and southwesterly wind direction as sw-current. Properties of the simulations are given in Table 5.1.

Table 5. 1 : List of performed simulations.

WIND	Flat	Real Topography	Strait	Island	Urban
NE 0.25	✓				
NE 0.25	✓		✓		
NE 0.25		✓	✓		
NE 0.25		✓	✓	✓	
NE 0.25		✓	✓	✓	✓
SW 0.25		✓	✓	✓	✓

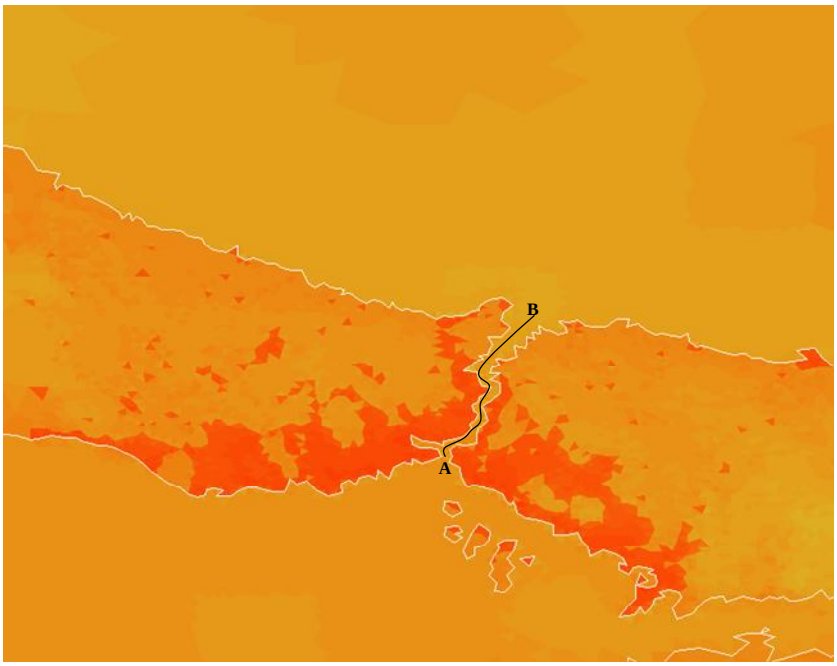

Figure 5.7 : Cross-section location along the Bosphorus.

Cross-section along the strait (seen in Figure 5.7) is utilized to understand the contribution of the strait on the flow behaviour. The main focus of this study is to investigate the thermally driven mesoscale features. It is well known fact that local flow over the domain mainly depends on the different responses of the surfaces to

the diurnal temperature cycle. Temperature distribution between the different surfaces controls the behaviour of the flow. This effect is investigated in detail by comparing the potential temperature distributions for all simulations (see Figure 5.8). The abbreviations BS and MS on the figures represent the Black Sea and the Marmara Sea, respectively.

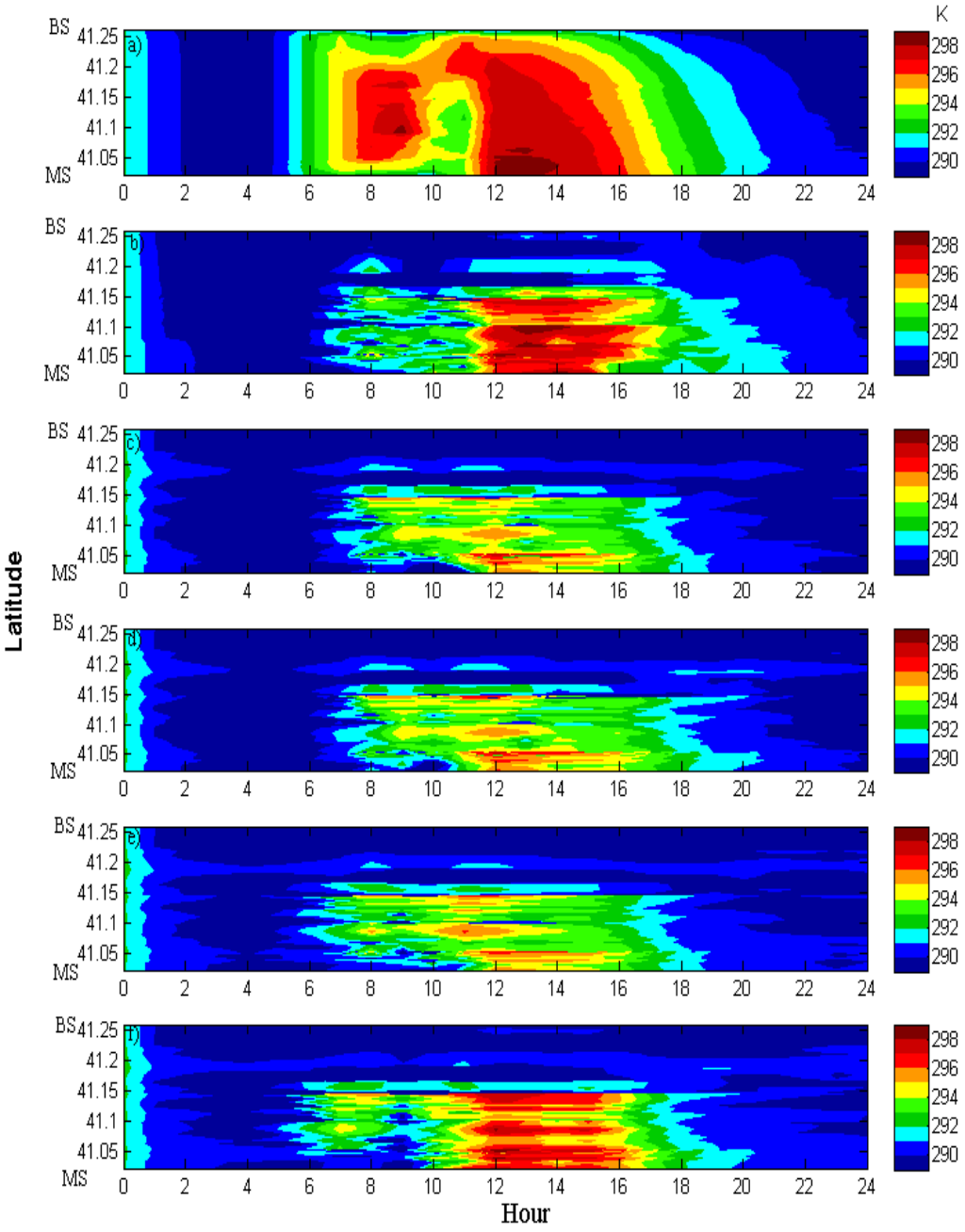

Figure 5.8 : Potential Temperature (K) at 15m along the strait for idealized cases a) flat,b) flat-strait, c) real topo-strait, d) real topo-island e) ne-current and f) sw-current.

It is seen that the flat simulation gives uniform potential temperature distribution over the domain since there is no such a feature that disturbs the given large scale flow. However, Figure 5.8b exhibits the perturbation of the potential temperature due to the presence of the strait. Each new feature contributes to the disturbance of the potential temperature at some degree so the flow behaves in a different manner than the simplest case (the flat simulation). As corresponding with diurnal temperature cycle, the highest temperature values are observed after noon. At this time, the south coast is warmer than the north coast for all the idealized cases.

Flat simulation shows warmer surface than all other simulations where heating starts early (at 0500 UTC) when compared with the other simulations (Figure 5.8). Due to the sea breeze existence and inland penetration on both coasts, maximum heating at morning hours occurs in the middle of the cross-section domain at 0800 UTC except than the flat simulation in which the maximum heating is observed at 0900 UTC. The reason for this manner is because of the presence of the strait, which is added to the study area except the flat case. The presence of the strait makes the domain cooler than the flat case. The sw-current simulation heats the air through the strait on the south earlier than the other simulations (at 0700 UTC) except flat case since the southwesterly wind helps to move the relatively warm Marmara Sea flow towards the Black Sea.

Wind is one of the indicators to better understand the flow structure over a region therefore, V component of the wind, one of the variables from the model outputs, is analyzed to define the flow behaviour depending on the difference in the idealized cases. Analyses of V component of the wind are conducted with cross-section which is previously shown in Figure 5.7. Geostrophic wind is northeasterly during the simulations for five cases (Figure 5.9a-d), which means that wind over the domain initially flows from the Black Sea towards the Marmara Sea. Therefore, the background flow prevents to onset of a land breeze on the north while not on the south, especially seen on both flat and flat-strait simulations.

Analyses show that adding a water body into the environment makes the air cooler than the uniformly flat surface, which affect the balance between land and water (shown in Figure 5.8a and 5.8b). First model simulation hours depict the land breeze only on the south coast of the domain on both flat and flat-strait simulations. The striking point is that if the simulations contain the topography effect, it is possible to

observe the land breeze-like flow on the north coast in contrast to the flat simulations. On the flat runs, northerly background flow suppresses the onset of a land breeze while topography effect makes onset of a land breeze easy by means of the down-slope wind. Characteristics of the sea breezes on both cases are different in a progressing time series. One of the differences in the morning is that the onset time of the sea breeze in the case of flat run is one hour earlier (at 0600 UTC) and more intense than the flat-strait case and also the life time of the sea breeze is short in the flat-strait case. Also, horizontal entrainment from both sides of the strait makes contribution to the local flow by means of a sea breeze which is observed along the strait at the same time in the Black Sea and Marmara Sea.

Two sea breezes exist close to shorelines and they penetrate towards the inland and converge at some point in the domain. This convergence occurs since Istanbul is surrounded by water bodies, Marmara Sea (in the south) and Black Sea (in the north). The convergence zone occurs one hour early on the flat-strait since the strait results in a decrease in the air temperature through northeasterly wind and the sea breeze moves faster due to the increase in land-water temperature gradient over the Bosphorus. Therefore, the convergence zone occurs at 0800 UTC on the flat-strait simulation while it occurs at 0900 UTC on the flat simulation (without the strait).

Theoretical and numerical studies have been conducted to understand the mountain-valley (i.e. topography effect) and sea-land contrast on the local circulation. Federico et al., (2000) mention that the energetics are more efficient over a flat peninsula due to the sea-land interactions. Even though topography is very smooth in Istanbul, it is still the issue whether it contributes to the local flow. It is observed that the sea breeze is onset at 0600 UTC where the presence of the topography attenuates the intensity and inland penetration of the south coast sea breeze (from the Marmara Sea) due to the influence of upslope-downslope flow of the topography. However, the life span of the sea breeze in the real topo-strait simulation is longer than the flat-strait simulation (Figure 5.9b-5.9c). Topography weakens the inland penetration of the southerly sea breeze as well as the intensity of the sea breeze over the strait. Convergence occurs at the same time as the flat-strait case (at 0800 UTC). In terms of onset time of the sea breeze and its life span for the real topo-strait and the real topo-island simulation shows the similar properties. The islands on the Marmara Sea are the only difference between those simulations hence, the cross-section location is

specified for the strait and it is not able to capture the effect of the islands at this point. However, a slight difference, which is observed between those cases, is that the wind speed of the sea breeze is weak on the real topo-island simulation (Figure 5.9d). Modifications on the geographic features are finalized adding the lakes to the domain and applying the actual land-use types to the model in order to simulate the possible realistic condition (Figure 5.9e). The land-use types are totally different from the land-use type used on the previous simulations, for example; southern part of the domain near to the strait is urbanized region and this urbanization continues to the north along the strait. Utilized simple land-use type is shown in Figure 5.6. The north of the domain is mostly covered by forest and small areas are urbanized in the realistic land-use data. As theoretical and observational studies show that urban areas influences the characteristics of the flow by keeping the air warmer than the surrounded rural region and changing the wind characteristics by means of the roughness length. Since the south of the domain is urbanized on the ne-current cases, characteristics of a sea breeze behave in a different manner from the previous cases. First of all, onset time of the sea breeze is earlier (at 0500 UTC) than all the previous simulations. The presence of the urban area provides enough temperature gradient between land and water that causes the early onset of the sea breeze on the south of the domain (from the Marmara Sea). In contrast to the previous simulations, flat-strait, real topo-strait and real topo-island, the sea breeze from the Black Sea part on the ne-current simulation moves fast that can be apparently observed at the existence time of the convergence (i.e. at 0800 UTC) but the intensity of the sea breeze wind is not strong as much as those three simulations. Since prevailing wind over Istanbul is in northeasterly-southwesterly direction, flow characteristics in the case of southwesterly wind is also investigated beside of the northeasterly wind. The sea breeze from the Marmara Sea starts at 0200 UTC due to the southwesterly background flow and influences the south of the domain until 0900 UTC. Onset time of the sea breeze on the north (the Black Sea) is at 0500 UTC on the sw-current case whereas it is at 0600 UTC on the north for the other topography cases (Figure 5.9c-f). Furthermore, the north coast sea breeze on the sw-current simulation is stronger than the ne-current simulation. Also, similar to the other simulations convergence on this simulation is at 0800 UTC (except the flat simulation) and the convergence location is farther inland than the ne-current simulation. The lifetime of the sea breeze in this case is the longest in all simulations.

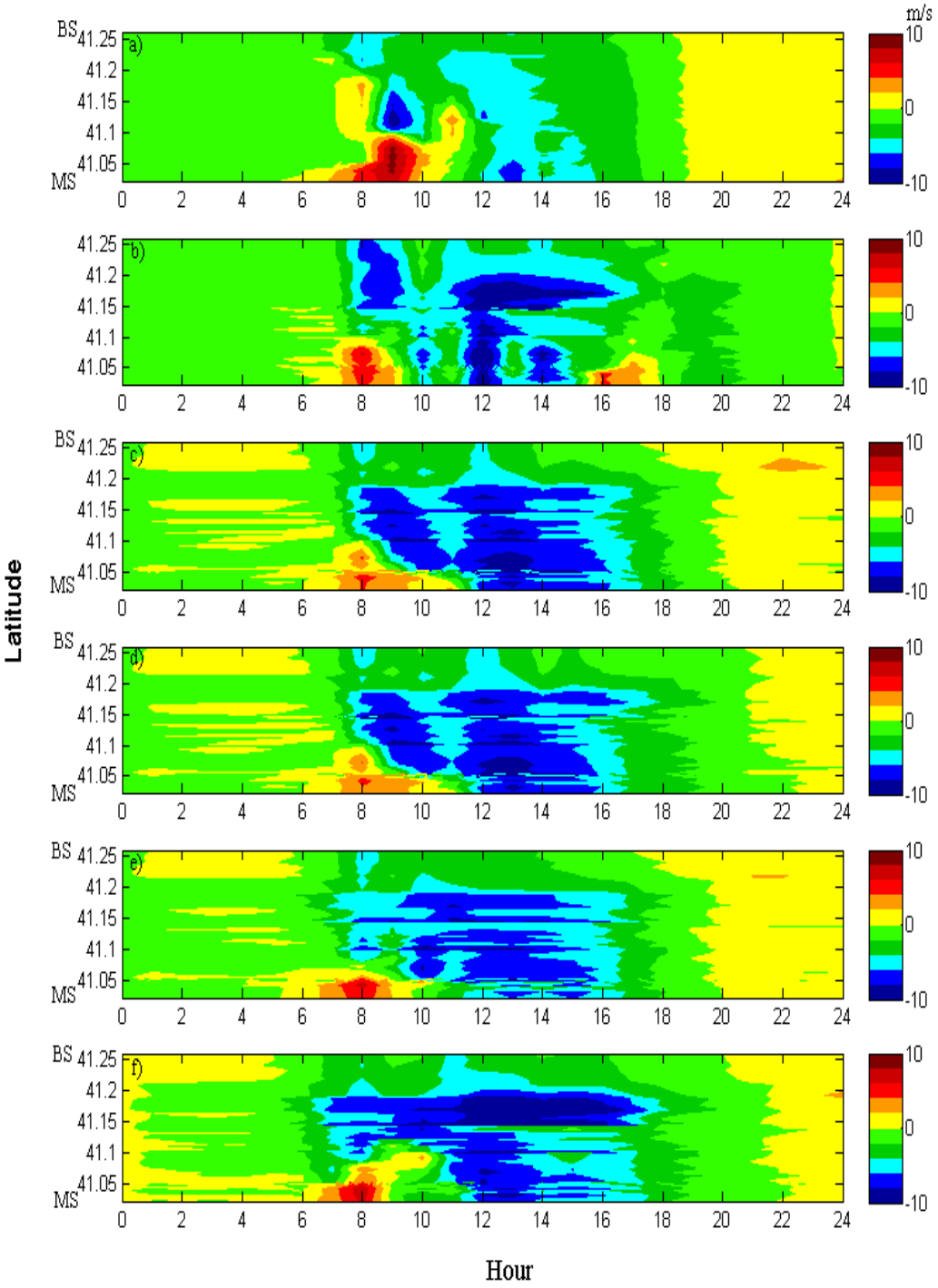

Figure 5.9 : Time series of V component of the horizontal wind (m/s) at 30 m along the strait for idealized cases a) flat, b) flat-strait, c) real topo-strait, d) real topo-island e) ne-current and f) sw-current (V is taken positive towards the north).

The circulation characteristics change in time after convergence occurs due to the meetings of the sea breezes from both sides of Istanbul. While the presence of the strait cools down the domain on the flat-strait case, strong northerly flow

overwhelms the southerly sea breeze at early afternoon. The change in the surface roughness length that is obtained by adding water body into the domain is channeled the flow through the strait (Figure 5.9a and 5.9b). The flow characteristics of each idealized simulation in time is indicated in Figure 5.9. In addition to the flat-strait case, adding topography to the domain instead of the flat topography enhances the northerly flow over the strait (Figure 5.9c and 5.9d), which means that the channeling flow lasts longer by means of the real topography when the Figure 5.9b and 5.9c are compared.

Strong northerly wind persists to flow at late afternoon but the strong wind is observed at 1300 UTC on the real topo-strait simulations. Other two cases which are the ne-current and the sw-current also show the similar behaviour however they are not as strong as real topo-strait and real topo-island cases due to the heating effect of the urban areas. Another striking feature is observed at 1600 UTC. Since the flat simulation has uniform surface, the large scale flow is fairly smooth over the domain whereas the flat-strait case is affected by a sea breeze-like flow from the MS at 1600 UTC (see Figure 5.9b).

This flow is suppressed by the contribution of the real topography and flow turns to the northerly direction as it is observed on the flat case. The flow turns to the southerly direction early at night, however only the flat-strait delays this flow as it is shown in Figure 5.9. Distribution of vertical velocity values is the significant indicator to show the motion of the atmosphere. The positive values for the vertical velocity explain the air transport to the upper atmospheric layers by means of the convergent flow (see Figure 5.10). It is observed from Figure 5.9 and Figure 5.10 that location and occurrence time of the convergence consistent with the positive values of the vertical velocity in all cases.

Abe and Yoshida (1982) states that strong ascending flow exists at the center of a peninsula since the sea breezes from both coast converge (Abe and Yoshida, 1992). Since Istanbul is surrounded by two water bodies, geographic orientation of it allows the existence of a convergence due to the sea breeze penetration from both sides of the domain. As it is explained in the previous paragraphs, southern and northern sea breezes encounter at a point depending on the specified features on the idealized cases which gives rise to changes in the occurrence time, intensity and the place where the convergence exists.

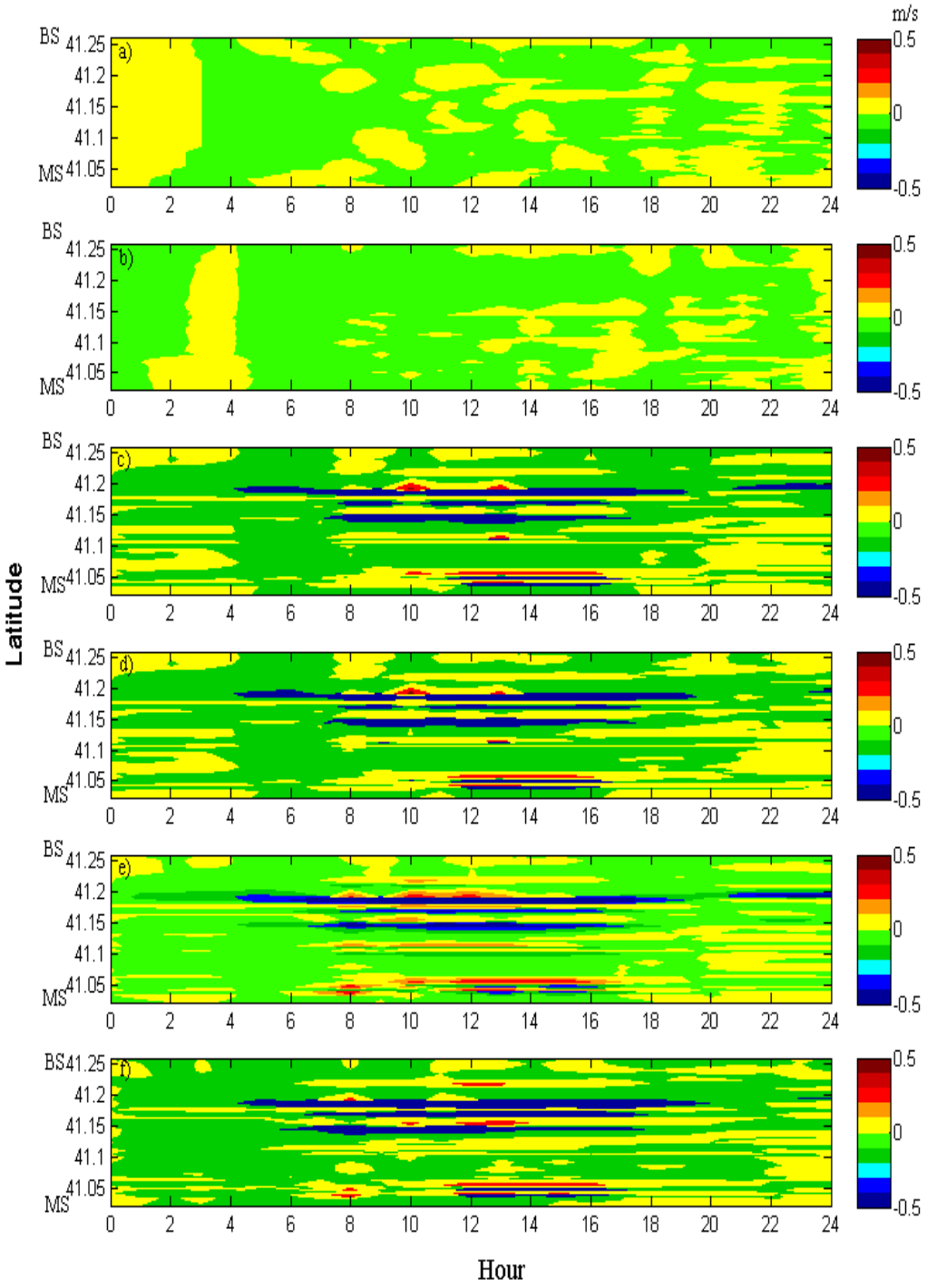

Figure 5.10 : Time series of vertical velocity (m/s) time series at 30 m along the strait for idealized cases a) flat, b) flat-strait, c) real topo-strait, d) real topo-island e) ne-current, and f) sw-current.

Table 5.2 summarizes the information about southerly sea breeze features for all the idealized cases. This information provides to understand the effect of each changed features on the local flow relatively. Maximum inland penetration of the southerly

sea breeze retreats when the conditions are changed to the realistic cases; for example, maximum penetration is 5 km for the ne-current simulation while the flat and real topo-strait and real topo-islands are approximately 8 km. Life span of the southerly sea breeze on the sw-current simulation is longer than the rest of the simulations. When each idealized simulations are compared, realistic land-use type with southwesterly wind direction depicts that urbanization brings about a long lasting sea breeze condition. On the contrary, the life span of the northeasterly wind direction simulation with realistic land-use type is less than the southerly wind because the northerly wind pushes the relatively cooler air towards the south, which distorts the temperature balance on the southern part of the strait and contributes to the onset of a sea breeze. However, the southwesterly background flow makes positive contribution to the flow with urbanization and increases the temperature gradients. Therefore, the duration of the sea breeze on the south is longer.

Table 5. 2 : Characteristics of the southerly sea breeze at the first model layer (~30m) along the strait.

CASE	flat	flat-strait	Real topo-strait	real topo-island	ne-current	Sw-current
max. inland penetration (km)	7.87	7.87	7.87	7.87	5	6.3
intense SB distance (km)	4.56	5.60	2.16	2.16	2.16	2.16
max. SB wind (m/s)	8.94	6.44	4.73	4.31	6.79	7.52
max. SB penetration time (hour)	9	8	8	8	8	8
SB duration (hour)	5	3	5	5	5	8

Since southerly wind moves the relatively warmer air that affects the onset of the sea breeze on the sw-current simulation, onset time of the sea breeze is later and life span of the sea breeze is shorter on the ne-current case than the sw-current case. The maximum speed of V component of the wind occurs at 0800 UTC for all the simulations except flat simulation.

On the flat simulation, the maximum V component occurs at 0900 UTC which is associated with the existence time of the convergence over the domain. Convergence is important in terms of transport and diffusion of pollutant. Therefore, in order to have detail information about the convergence, vertical changes on the vertical velocity and potential temperature are also analyzed. Location (approximately 41.1 ^{o}N) where the convergence occurs shows the rising air at upper atmospheric levels on

sw-current case. However, real topo-strait, real topo-island and ne-current cases show the weak vertical velocity amount at upper atmospheric levels with divergence between the surface and upper atmospheric layers at 0800 UTC (Figure 5.11). Those two topography cases (real topo-strait and realtopo-island) have more intense subsidence than the other cases with height.

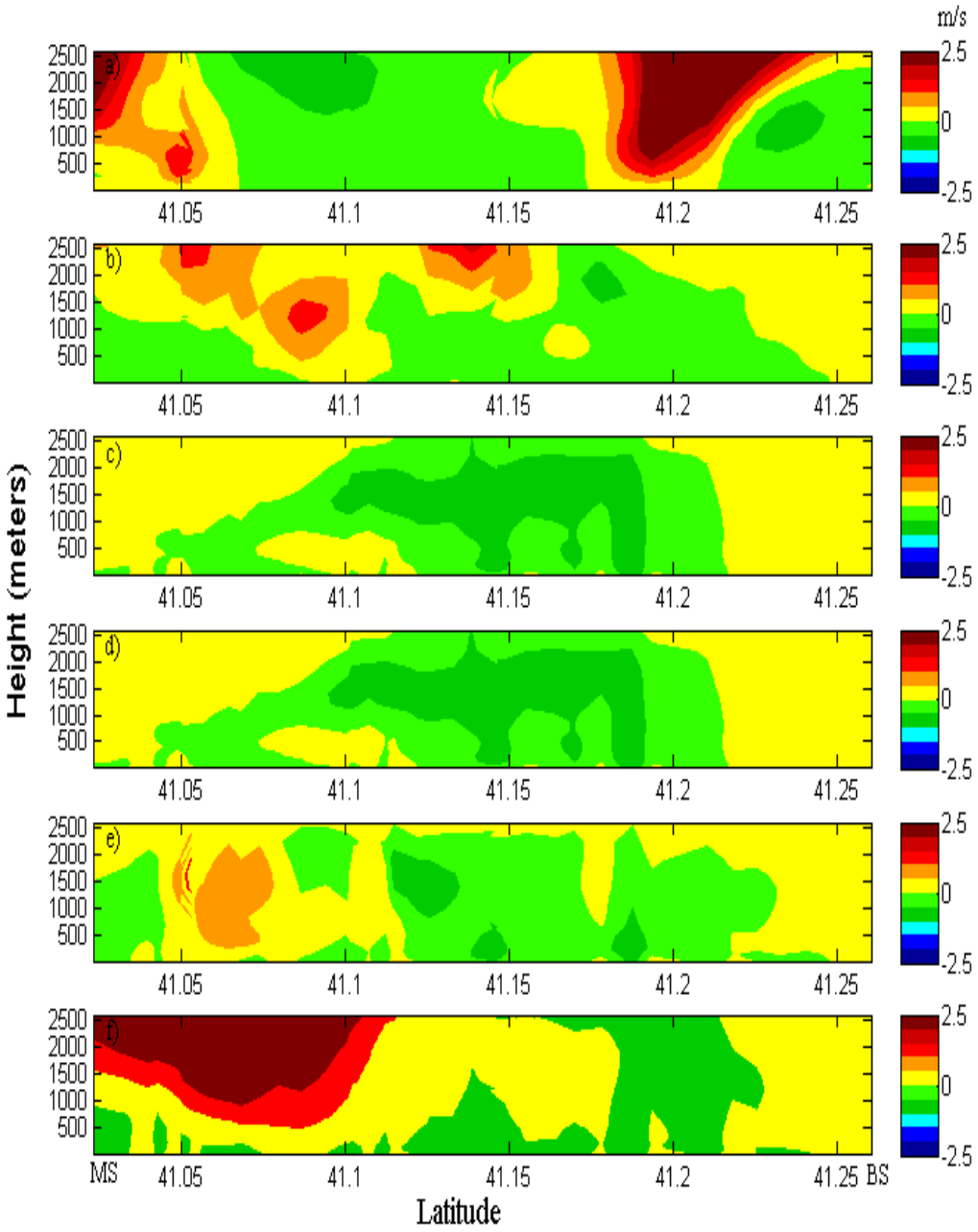

Figure 5.11 : Vertical velocity (m/s) changes in height at 0800 UTC (at 30 m) along the strait for idealized cases a) flat, b) flat-strait, c) real topo-strait, d) real topo-island e) ne-current and f) sw-current.

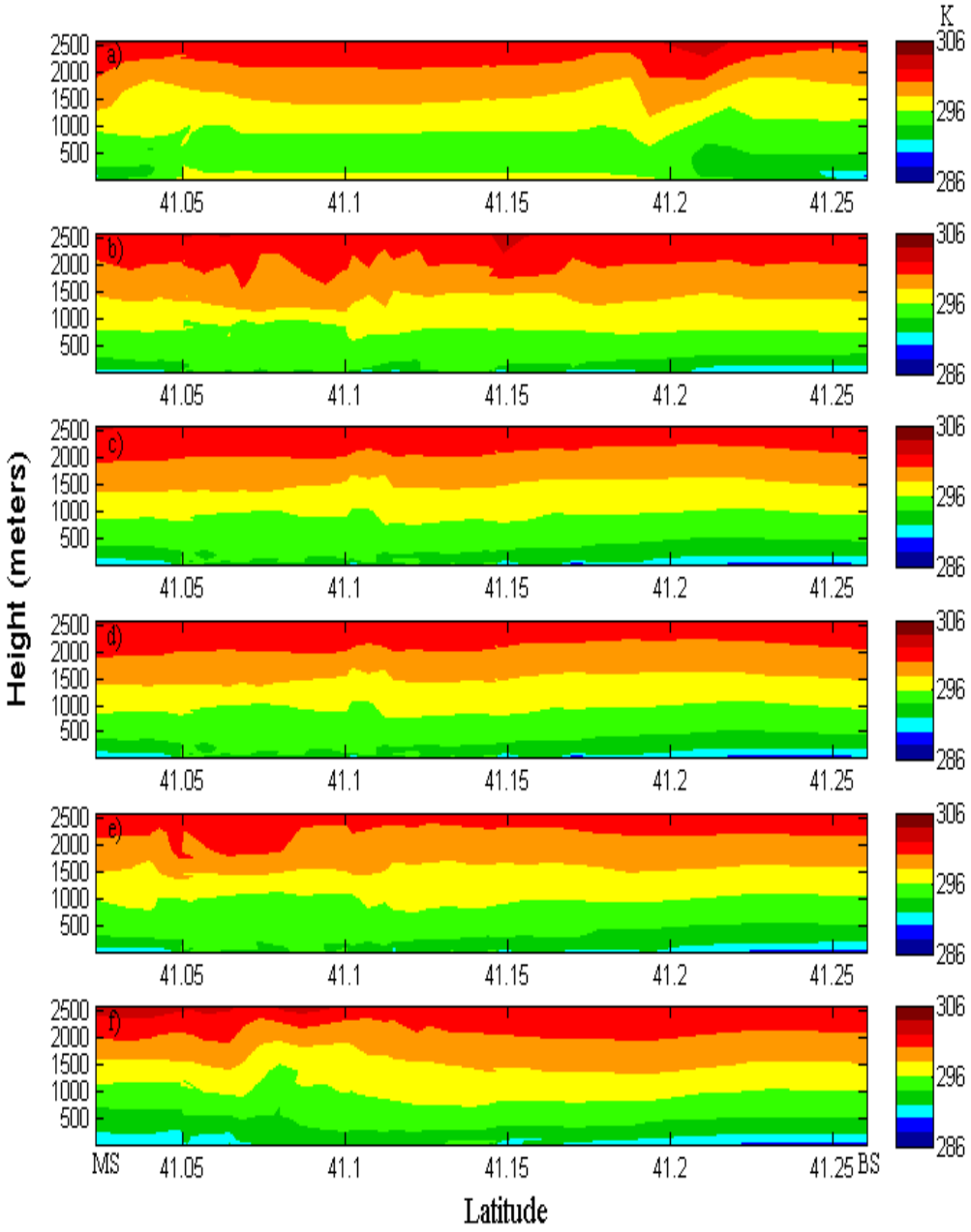

Figure 5. 12 : Potential temperature (K) changes in height at 0800 UTC along the strait for idealized cases a) flat, b) flat-strait, c) real topo-strait, d) real topo-island e) ne-current, and f) sw-current.

Potential temperature indicates the cold water invasion from both north and south parts of the domain (Figure 5.12). Since the domain is assigned as water on the other simulations, potential temperature changes with height indicate that surface is warm on the flat case. Furthermore, advecting colder water air to the warmer land surface causes decrease in potential temperature between 150 m and 950 m (Figure 5.12a) that shows the unstable atmospheric condition.

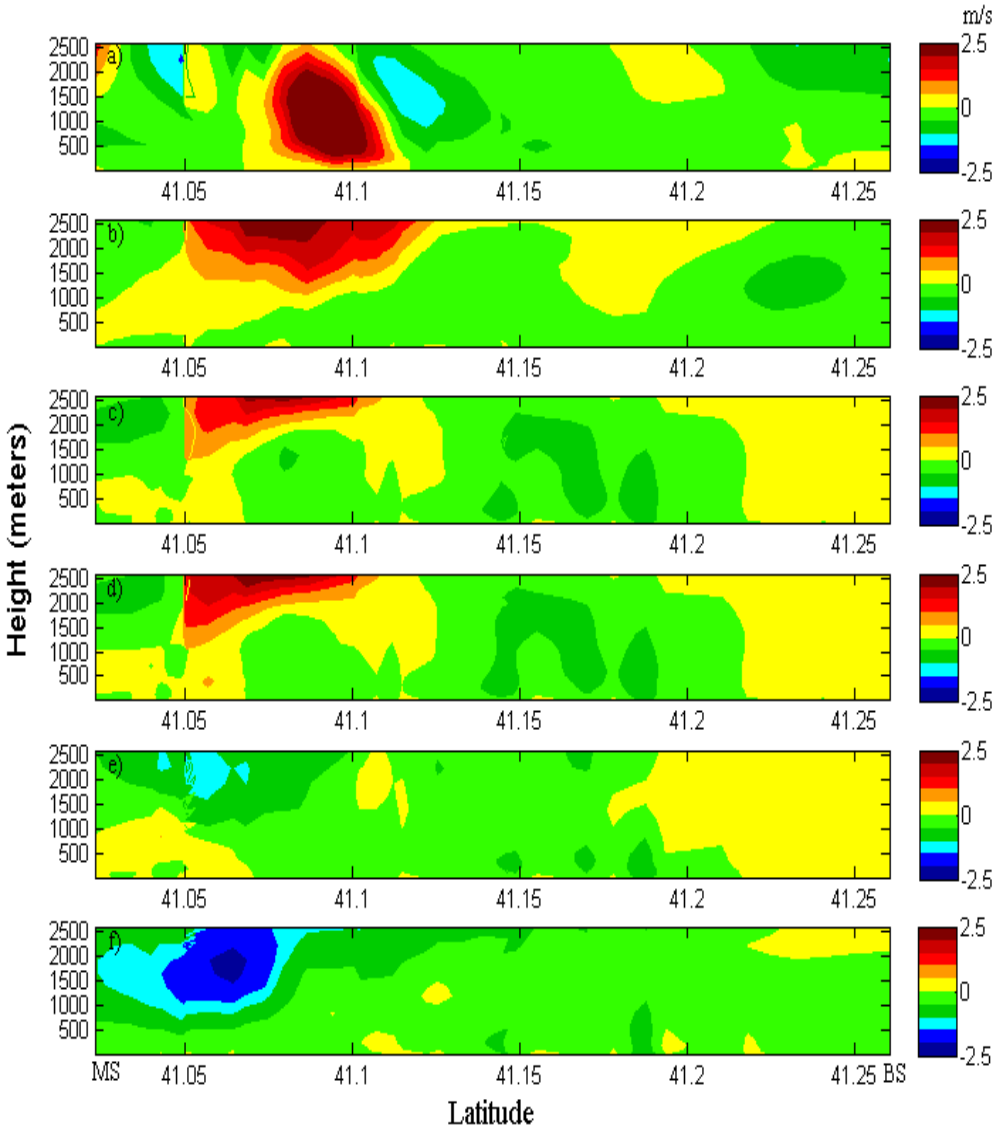

Figure 5.13 : Vertical velocity (m/s) changes in height at 0900 UTC along the strait for idealized cases a) flat, b) flat-strait, c) real topo-strait, d) real topo-island e) ne-current and f) sw-current.

Analyses show that atmosphere becomes more stable when the strait is set over the domain. Convergence exists at 0900 UTC on the flat case in contrast to the rest of the idealized simulations. Therefore, potential temperature and vertical velocity parameters are analyzed at 0900 UTC in a similar way at 0800 UTC. Those two simulation times provide the progress of the convergence and divergence for all cases as seen in Figure 5.13 andFigure 5.14. Convergence loses its strength at 0900 UTC for all cases (the flat-strait, the real topo-strait, the real topo-island, ne-current and sw-current) except for the flat simulation which is experienced by the convergence at that simulation time. Location of the convergence is observed

approximately 41.4°N at the surface and the convection is observed up to approximately 2000 m on the flat case. However, more intense convection, which occurred at 0800 UTC, is observed at the upper layers on the flat-strait, real topo-strait and real topo-island cases at 0900 UTC. In contrast to the flat (the flat and the flat-strait) and real topography (the real topo-strait and real topo-island) cases, downward vertical motion direction which points out the divergence is the most dominant direction of the air motion on the ne-current and sw-current simulations. However, weak patchy convergent areas in the higher levels are seen on these simulations.

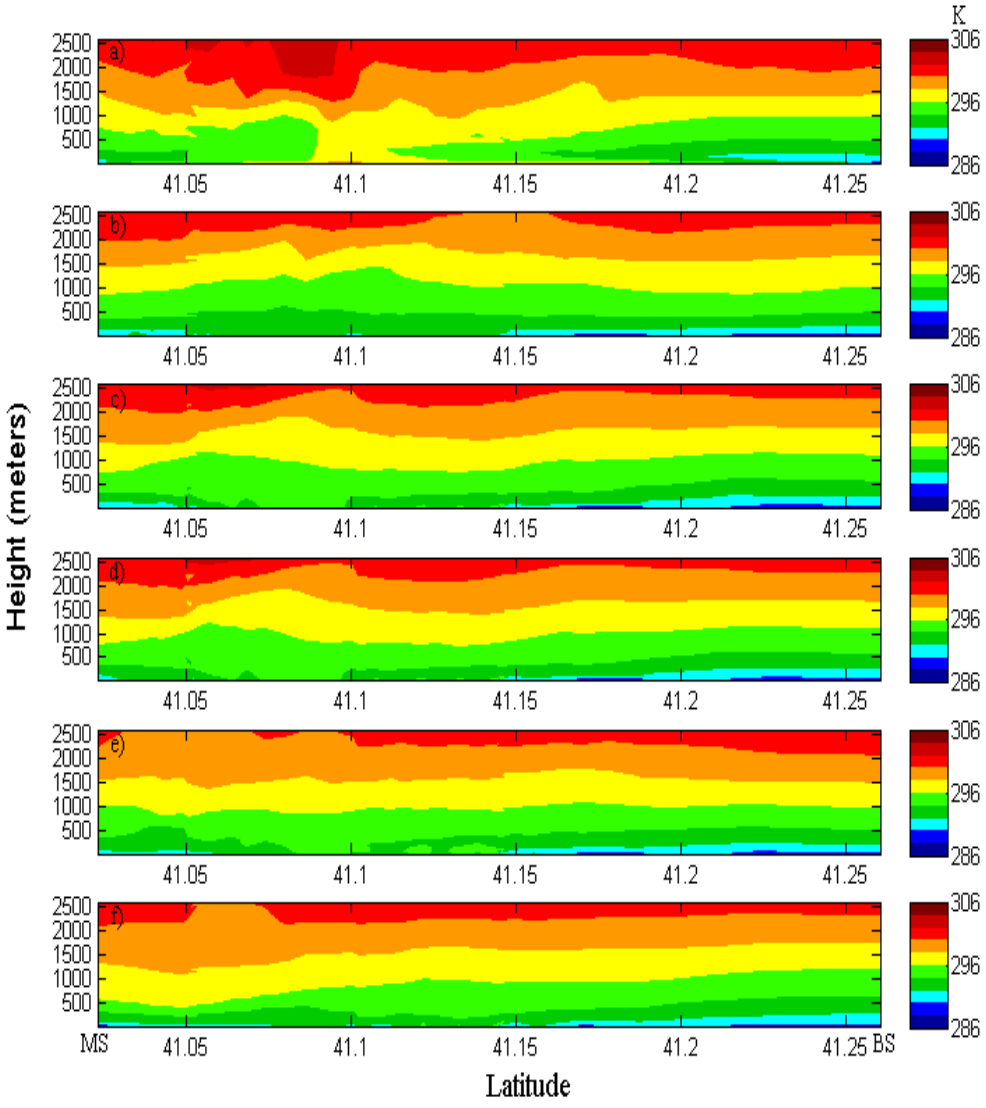

Figure 5.14 : Potential temperature (K) changes in height at 0900 UTC along the strait for idealiz cases a) flat, b) flat-strait, c) real topo-strait, d) real topo-island e) ne-current, and f) sw-current.

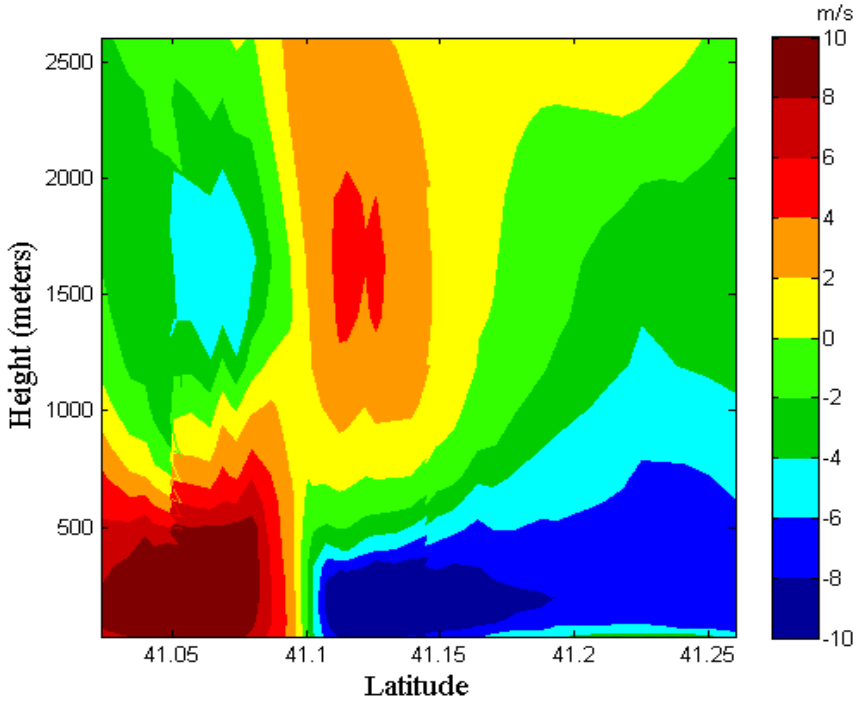

Figure 5.15 : V component of the horizontal wind (m/s) along the strait on the flat simulation at 0900 UTC.

Potential temperature distribution at 0900 UTC depicts increasing surface temperature especially over the MS and the upper layers become colder than at 0800 UTC except the flat simulation. Another different manner on the flat simulation is that a re-current circulation, which means the opposing circulation characteristics, is observed at the upper atmospheric layers at 0900 UTC (Figure 5.15). The re-current circulation starts at above 1000 m and the circulation is not as much as strong the sea breeze is at lower layers. However, re-current circulation is not observed on the other simulations since the sea breeze circulation structure during the convergence continues up to the upper layers by attenuating the intensity on the other simulations.

The cross-section through the strait shows the flow structure over the strait for idealized cases. Although cross-section along the strait provides information to understand the general flow behaviour, this information may not be enough to generalize the flow over the entire domain. Therefore, in addition to the cross-section along the strait, two more cross-sections; one from the west of the strait and the other from the east of the strait are utilized in order to obtain detailed information about the flow over the entire domain. These cross-sections are specified by considering locations which are unaffected by the strait. The cross-section from the western part of Istanbul named as European side is given in Figure 5.16.

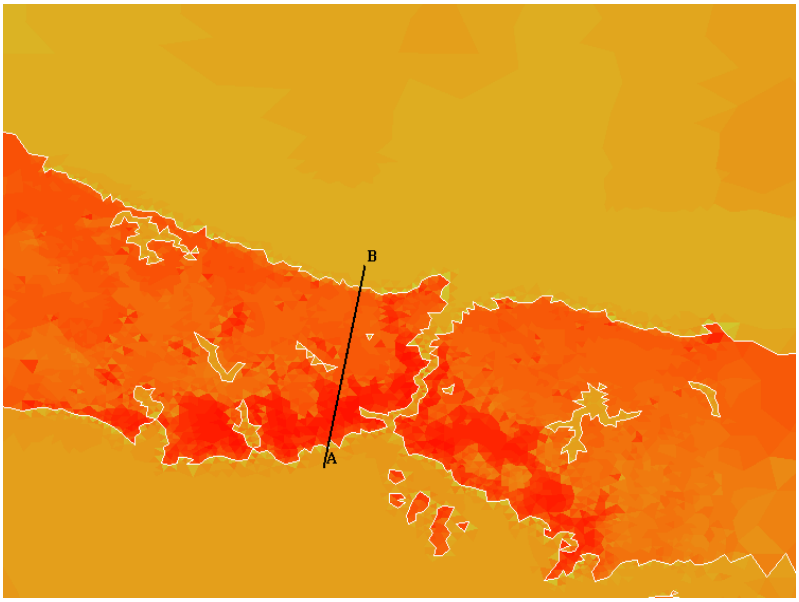

Figure 5.16 : Cross-section locations from the west of the Bosphorus.

Potential temperature distribution indicates the similar behaviour for all four idealized cases. Flat and flat-strait cases have a smooth shape while rest of the simulations has zigzags through the cross-section. These zigzags are the indicator of the topography effect over the domain (Figure 5.17). The main structure follows the diurnal temperature change where warmer temperature is observed at noon for all cases. High temperature values are seen in the middle of the domain at the morning hours. Figure 5.18 gives the distribution of V component of the horizontal wind that shows the southerly (from MS) and northerly (form BS) sea breeze existence for all simulations. The location where the maximum heating is observed over the domain in the early morning (shown in Figure 5.17) is also an indication of the convergence point over the domain.

The sea-land breeze circulation for the western cross-section has quite similar behaviour to the one along strait cross-section. The land breeze circulation is seen only on the southern part of the domain for the flat cases (flat and flat-strait) with the northeasterly background flow (Figure 5.18a and Figure 5.18b). However, adding topography under the same conditions results in a land breeze due to the contribution from the down-slope wind both on the north and south coastlines (shown in Figure 5.18c). It is seen that the islands have no significant effects over this side of the domain since the islands are located on the eastern part of Istanbul. Therefore, it is expected to observe a flow change on that side of the domain.

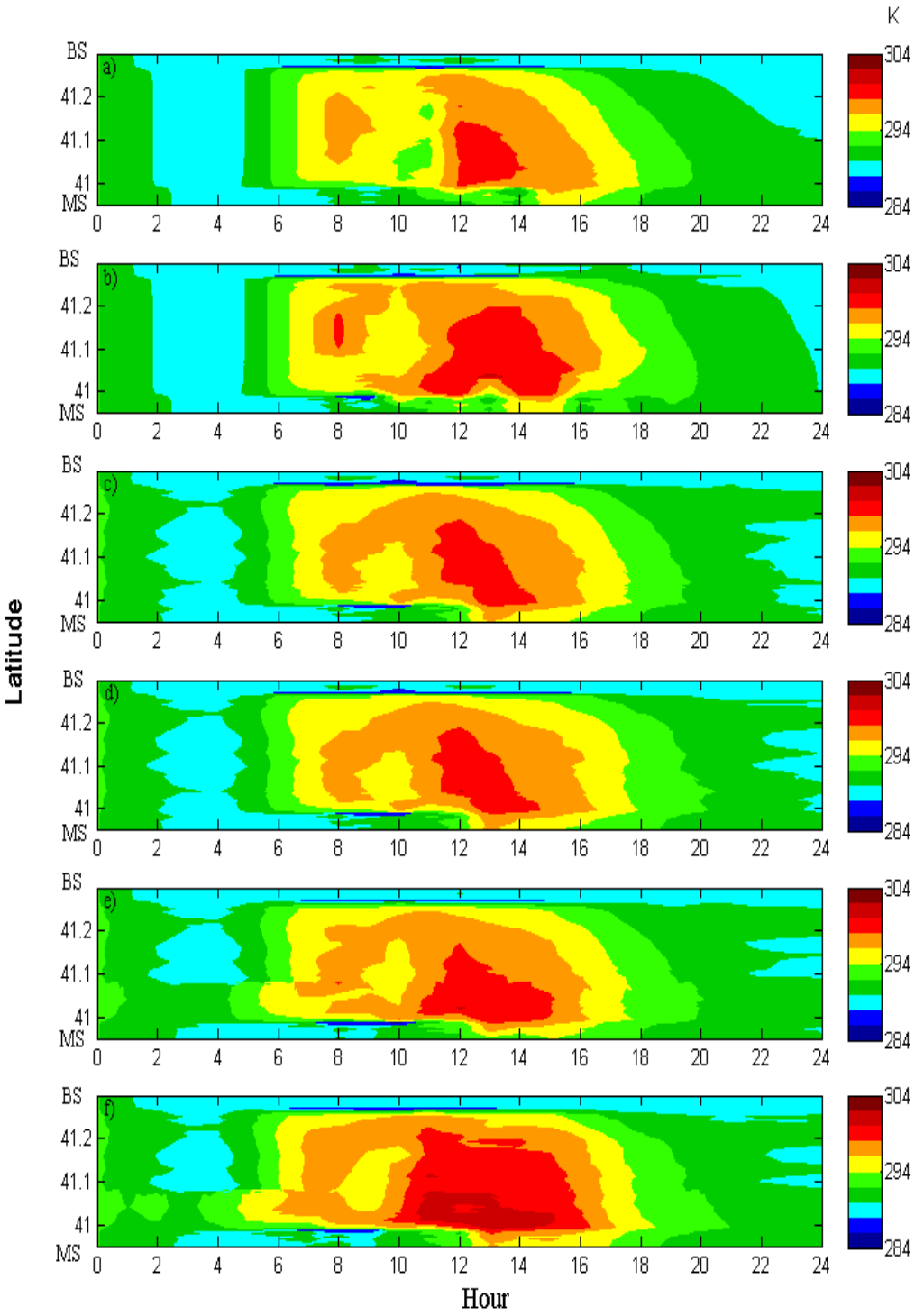

Figure 5.17 : Potential temperature (K) time series (at 15m) for cross-section from west of the Bosphorus a) flat, b) flat-strait, c) real topo-strait, d) real topo-island e) ne-current, and f) sw-current.

Urbanized area prevents onset of a land breeze on the southern shoreline on the ne-current and the sw-current simulations while the north parts of those simulations behave similar to the topography simulations. That is, land breeze can be observed

on the north on ne-current and sw-current cases. The onset time of the southerly sea breeze is similar both on the flat cases and the real topography (real topo-strait and real topo-island) cases at 0600 UTC whereas the urbanization produces the early sea breeze on the ne-current and sw-current cases. Onset of the sea breeze starts at 0700 UTC on the north (BS) for all northerly geostrophic wind directions. On the contrary to the northerly flow, southerly geostrophic wind shows the early onset of a sea breeze at 0600 UTC.

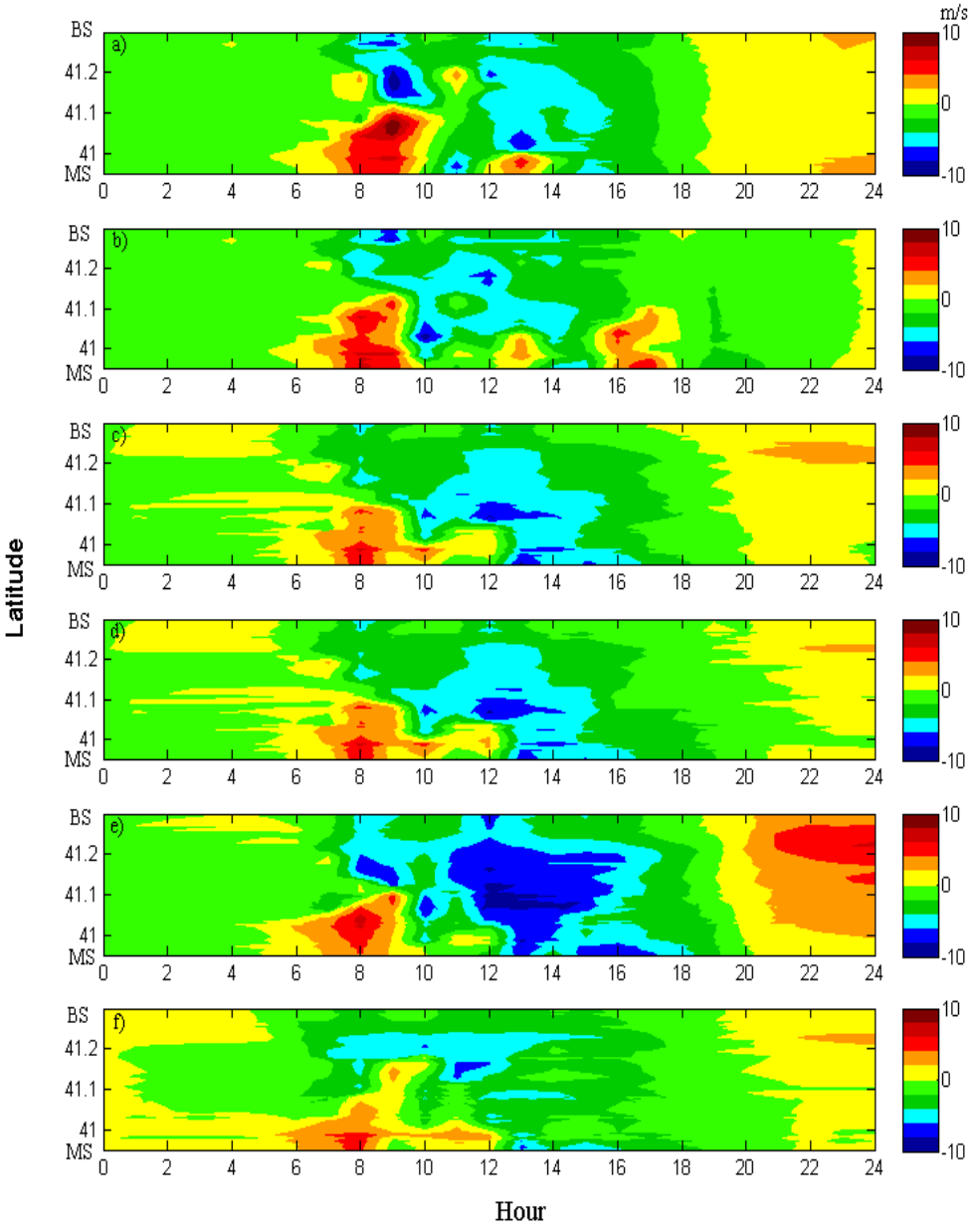

Figure 5.18 : Time series of V component of the horizontal wind (m/s) (at 30 m) for cross-section from west of the Bosphorus a) flat, b) flat-strait, c) real topo-strait, d) real topo-island e) ne-current, and f) sw-current.

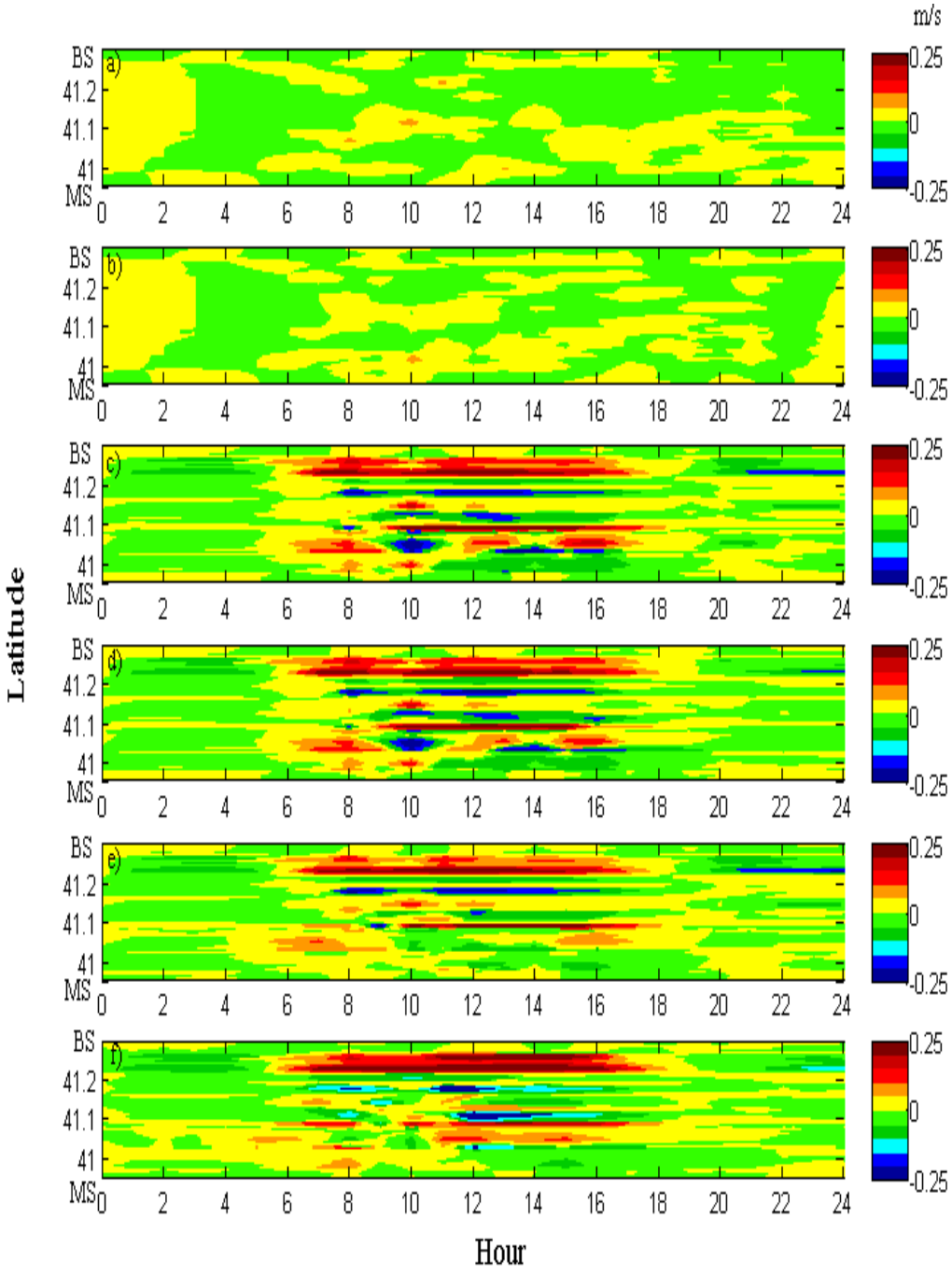

Figure 5.19 : Time series of vertical velocity (m/s) time series (at 30 m) for cross-section from west of the Bosphorus a) flat, b) flat strait, c) real topo-strait, d) real topo-island e) ne-current and f) sw-current.

Flow direction to the coastline controls the penetration of the sea breeze. Comparison of northerly and southerly flow situations enables to deduce the mechanism of the sea breeze progress in Istanbul under different wind direction conditions. Previous studies showed that onshore flow prevents onset of the sea breeze since it creates weak temperature gradient while offshore flow allows existence of a sea breeze

causing strong temperature gradient (Estoque, 1962; Zhong and Takle, 1993). Since Istanbul is a kind of peninsula, wind from north or south acts as an offshore flow for one shoreline while an onshore flow for the other shoreline.

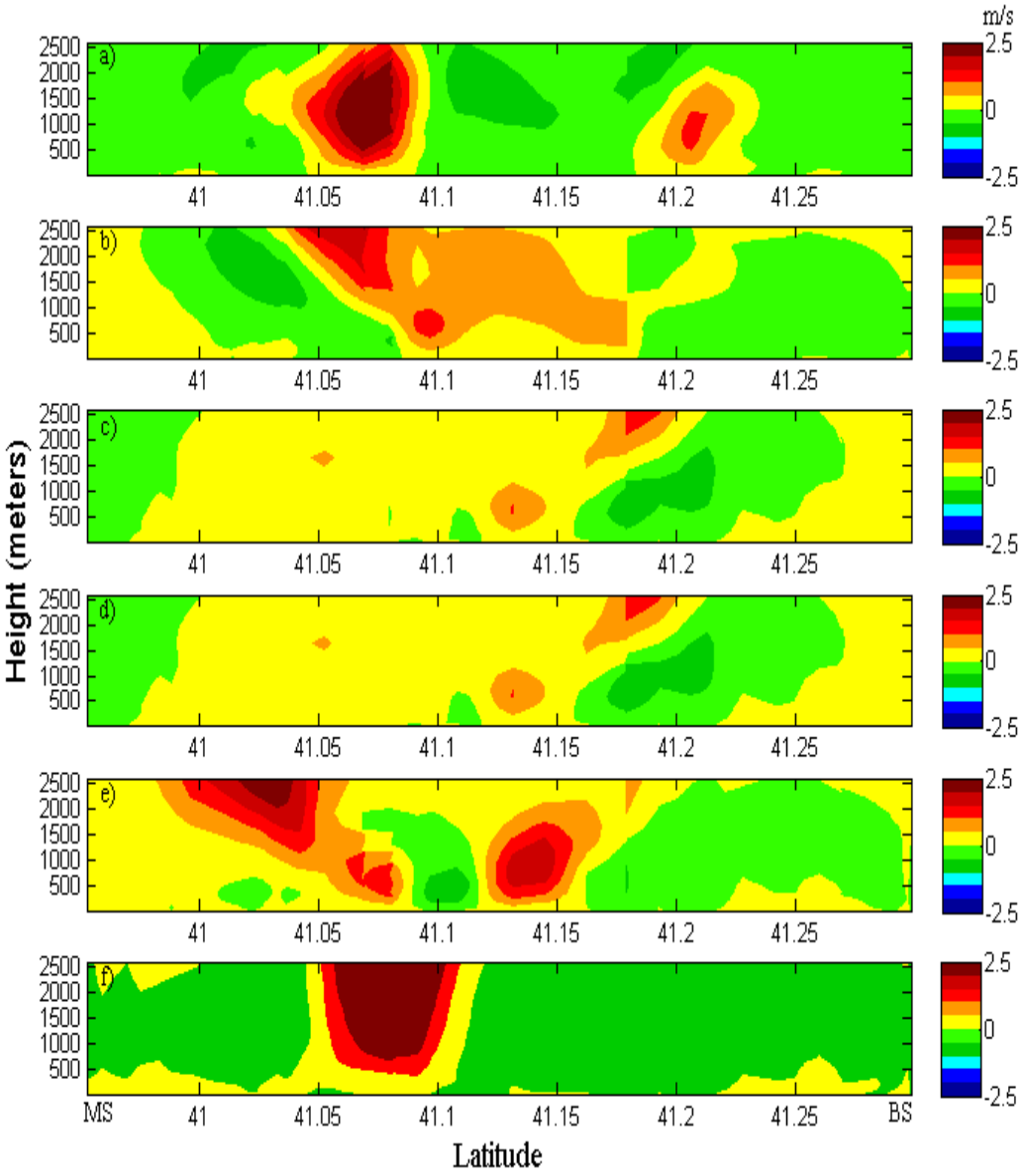

Figure 5.20 : Vertical velocity (m/s) changes in height at 0800 UTC for west of the Bosphorus a) flat, b) flat-strait, c) real topo-strait, d) real topo-island e) ne-current and f) sw-current.

In fact, the northerly flow contributes to the inland penetration of the sea breeze on the southern shoreline because northerly opposing flow (offshore wind for the south of the domain) causing weak temperature gradient and it penetrates farther inland while it keeps the northern sea breeze in a limited extent. On the other hand, in the

case of southerly flow, effect of the sea breeze is observed farther inland on the northern shoreline while inland progress of the southerly sea breeze stays in a short distance since the strong temperature gradient on the south of the domain causes less inland penetration of the sea breeze. Therefore, sea breeze responses to the background wind direction determines the convergence locations over the domain. The vertical velocity distribution for the westerly cross-section given in Figure 5.19 indicates the rising air areas over the domain.

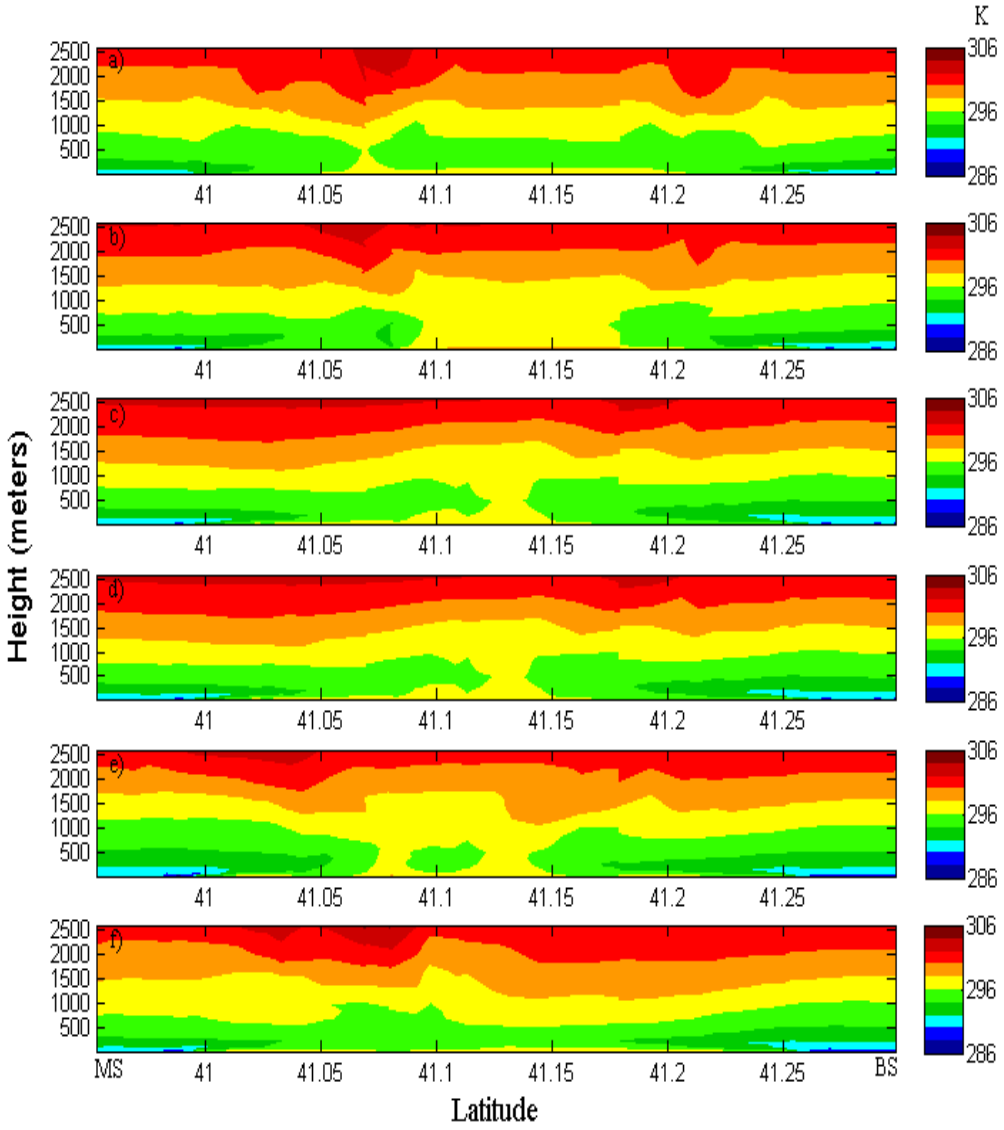

Figure 5.21 : Potential temperature (K) changes in height at 0800 UTC for west of the Bosphorus a) flat, b) flat-strait, c) real topo-strait, d) real topo-island e) ne-current and f) sw-current.

Location where two sea breezes meet shows the convergent flow, which is especially important in the morning hours. Because of these facts, the vertical velocity and

potential temperature structure with height are analyzed at 0800 UTC and 0900 UTC. Figure 5.21 depicts that two cold airs invade from BS and MS to the land at the surface and meet each other at different locations for all simulations. This meeting is experienced by the convergence at the surface and moves towards the upper layers (up to 3000 m) as it is seen in Figure 5.20a-f. The vertical velocity is strong on the sw-current simulation and unstable conditions occur due to the progress of advection of the cooler water over the land at 0800 UTC for all cases.

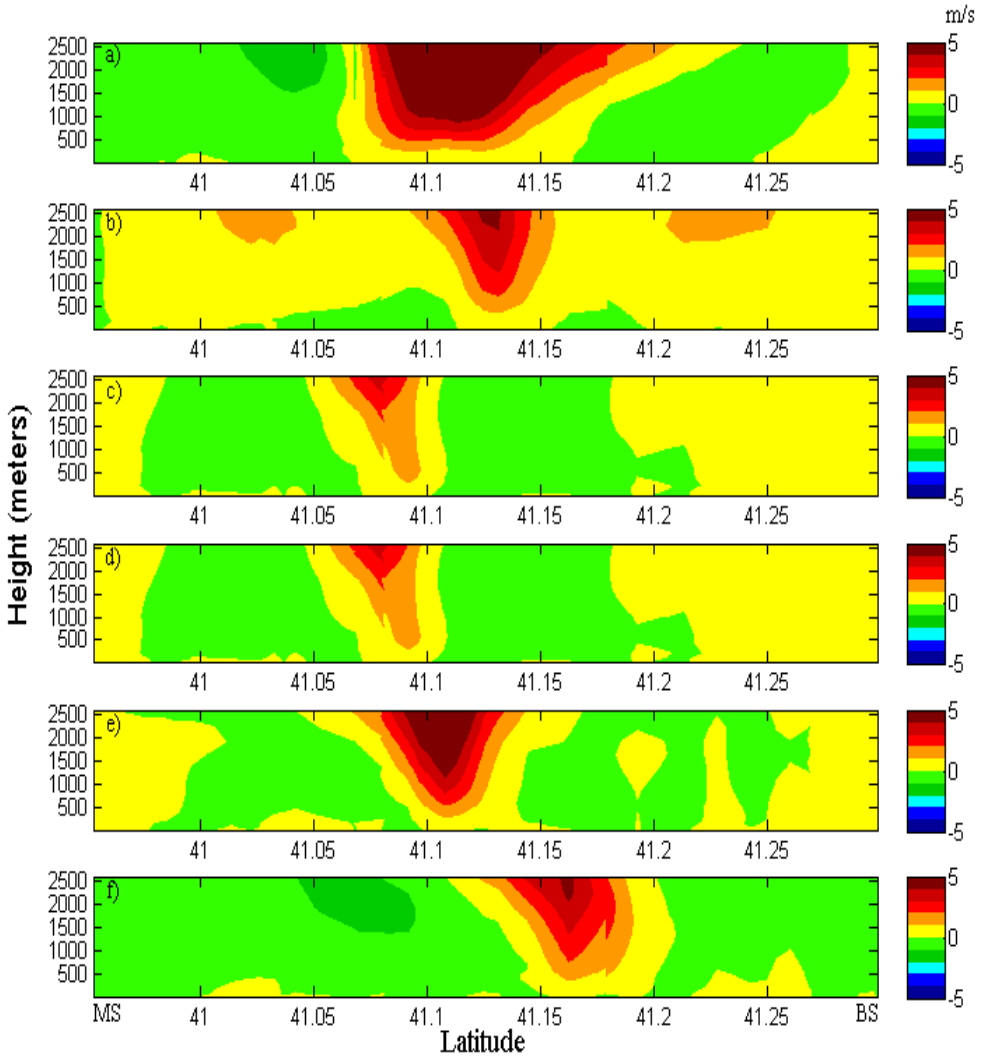

Figure 5.22 : Vertical velocity (m/s) changes in height at 0900 UTC for west of the Bosphorus a) flat, b) flat-strait, c) real topo-strait, d) real topo-island e) ne-current and f) sw-current.

Heating in time associated with diurnal cycle is observed for all the simulations. Convergence zone is observed with its intense magnitude almost in the middle of the cross-section on the flat run at 0900 UTC as seen on Figures 5.18 and 5.19.

Convergence location causes warm region in the domain, which can be observed on potential temperature changes on the flat case as a dome (Figure 5.23).

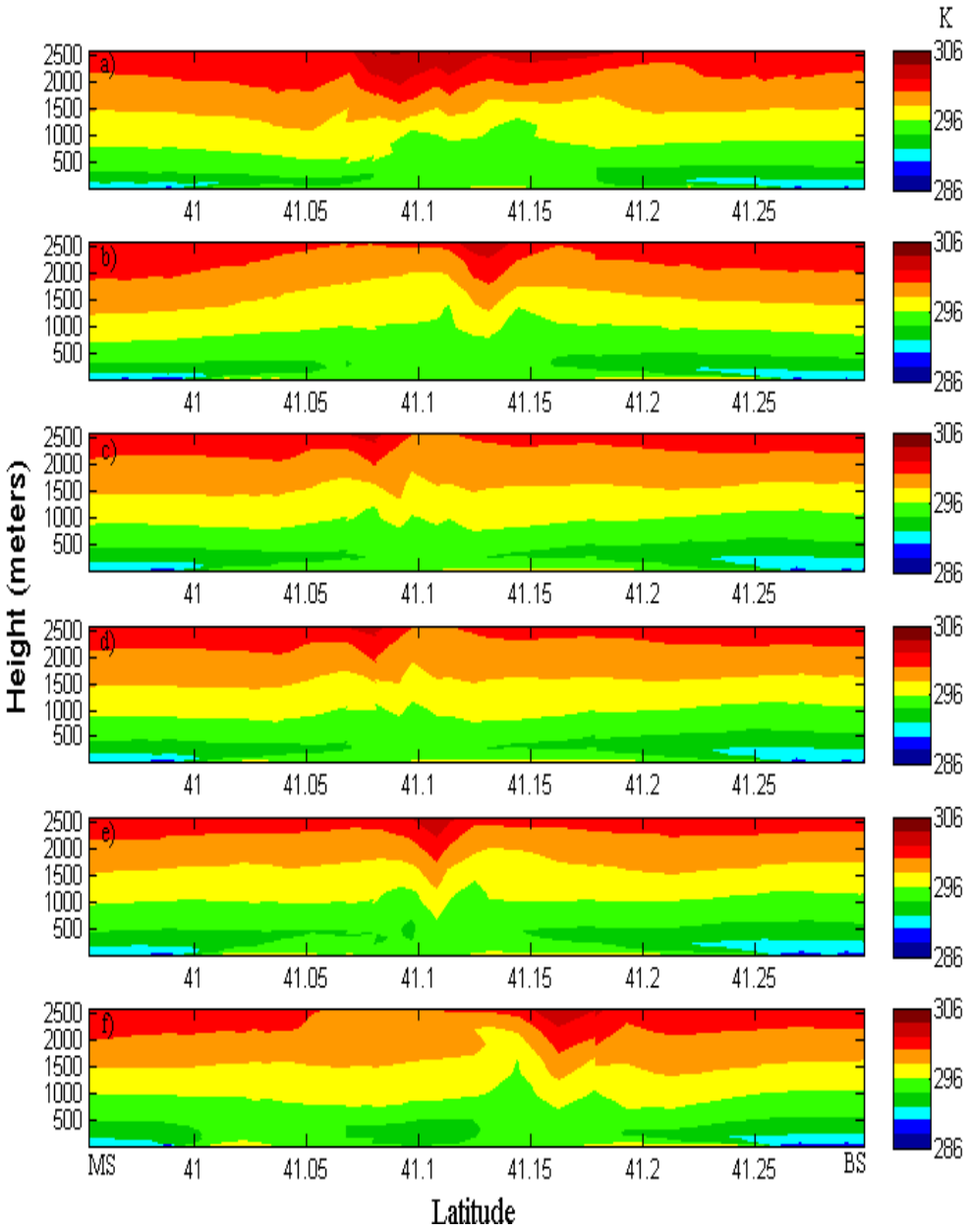

Figure 5.23 : Potential temperature (K) changes in height at 0900 UTC for west of the Bosphorus a) flat, b) flat-strait, c) real topo-strait, d) real topo-island e) ne-current, and f) sw-current.

Real topo-strait and real topo-island simulations show the strong convergence existence (Figure 5.22c and Figure 5.22d). The progress time of the convergence on ne-current and sw-current cases depending on the heating is shown in Figures 5.22e and 5.22f. It is interesting to note that the strength of the convergence attenuates on the sw-current with height while it enhances on the ne-current simulation. Invasion

of cold water air to the land is observed from potential temperature changes with height for both coastlines at 0800 UTC and 0900 UTC for all cases.

Table 5. 3 : Characteristics of the southerly sea breeze at the first model layer (~30m) for the west cross-section.

CASE	Flat	flat-strait	real topo-strait	real topo-island	ne-current	sw-current
max. inland penetration (km)	17.80	19.79	16.01	16.01	16.01	23.26
intense SB distance (km)	12.75	3.94	3.94	3.94	3.94	3.9
max. SB wind (m/s)	10.29	6.93	6.06	6.48	4.77	5.56
max. SB penetration time (hour)	9	8	8	8	9	9
SB duration (hour)	4	4	5	5	8	8

Table 5.3 gives information about southerly sea breeze for the European side cross-section such as maximum inland penetration of southerly sea breeze, existence time of the maximum wind speed, life span of the southerly sea breeze for all idealized cases. Maximum convergence with their strong magnitude occurs at 0900 UTC on flat, ne-current and sw-current cases however it occurs at 0800 UTC for the rest of the simulations. Maximum inland penetration from the south is 23.26 km on sw-current simulation at 0900 UTC while the maximum southerly wind (5.56 m/s) is observed 3.9 km far from the southernmost at 0800 UTC. Although maximum wind speed blows on the flat simulation, maximum life span of the sea breeze, 8 hours, is observed on the current simulations.

While investigating local flow characteristics, flow properties over the Bosphorus is the first focus. After determining the behaviour of the flow over the strait, two cross-sections are investigated also in order to generalize the flow over entire domain. As explained in the previous paragraphs, the first cross-section is taken from the western part of the domain, European side. Second cross-section is from eastern part called Asian side, which is shown in Figure 5.24. In addition to define the general characteristic of the local flow, effect of the islands on the flow is intended to investigate beside of the other effects using the eastern cross-section. The cross-section is started over one of the islands on purpose to capture the flow over the island and also investigate the effect of the presence of the island over the domain.

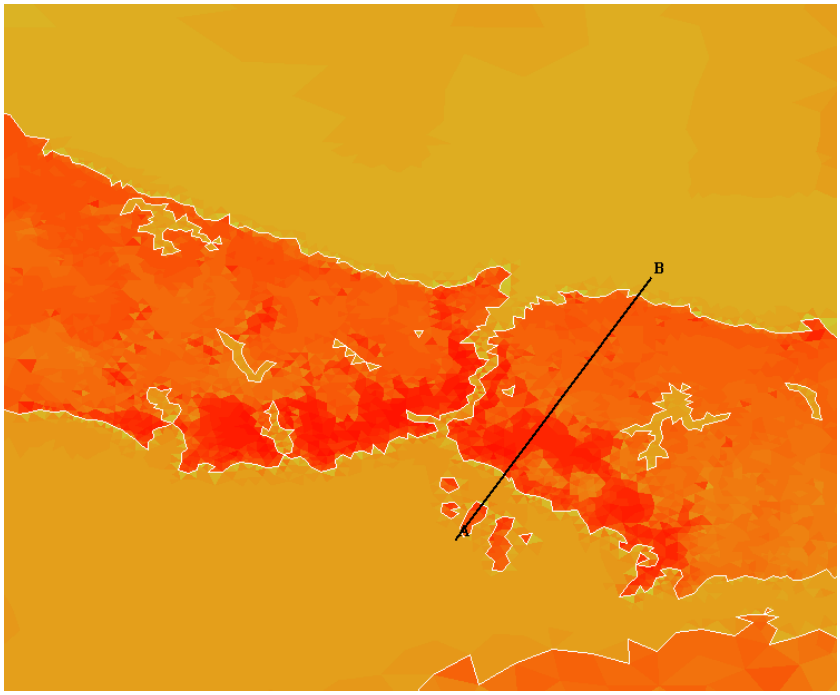

Figure 5.24 : Cross-section locations from the east of the Bosphorus.

The flat-strait case shows the warmer temperature distribution on the MS than the flat case early at noon however the topography ceases the warm temperature structure (see Figure 5.25a, 5.25b and 5.25c). After the islands are added to the domain, temperature structure shows the difference between the real topo-strait and real topo-island (Figure 5.25c-5.25d). The outstanding feature, which is observed in Figure 5.25d, is that two warm surfaces are separated by the water body on the south (MS) when the domain contains the islands. Implementing current conditions to the model causes heating where the urbanized region is located (Figure 5.25e and 5.25f). In addition to that, contribution of the southwesterly wind direction to the heating over the domain is clearly seen at 1200 UTC in Figure 5.25f. Sea-land breeze existence depicts almost the similar structures on the flat cases (see Figure 5.26a-5.26b). The general flow structure shows similar behavior compared to the one obtained in the cross-section along the strait. For instance, the strong southerly flow, observed at 1600 UTC on the flat-strait case is suppressed by the topography (Figures 5.26b and 5.26c) as it is also observed for the cross-sections along the strait and the western part. However, different features are also observed since the cross-section is taken from land. Two southerly flows are seen at 1200 UTC and at 1400 UTC on the real topo-strait flow whereas the islands on the domain suppress these structures.

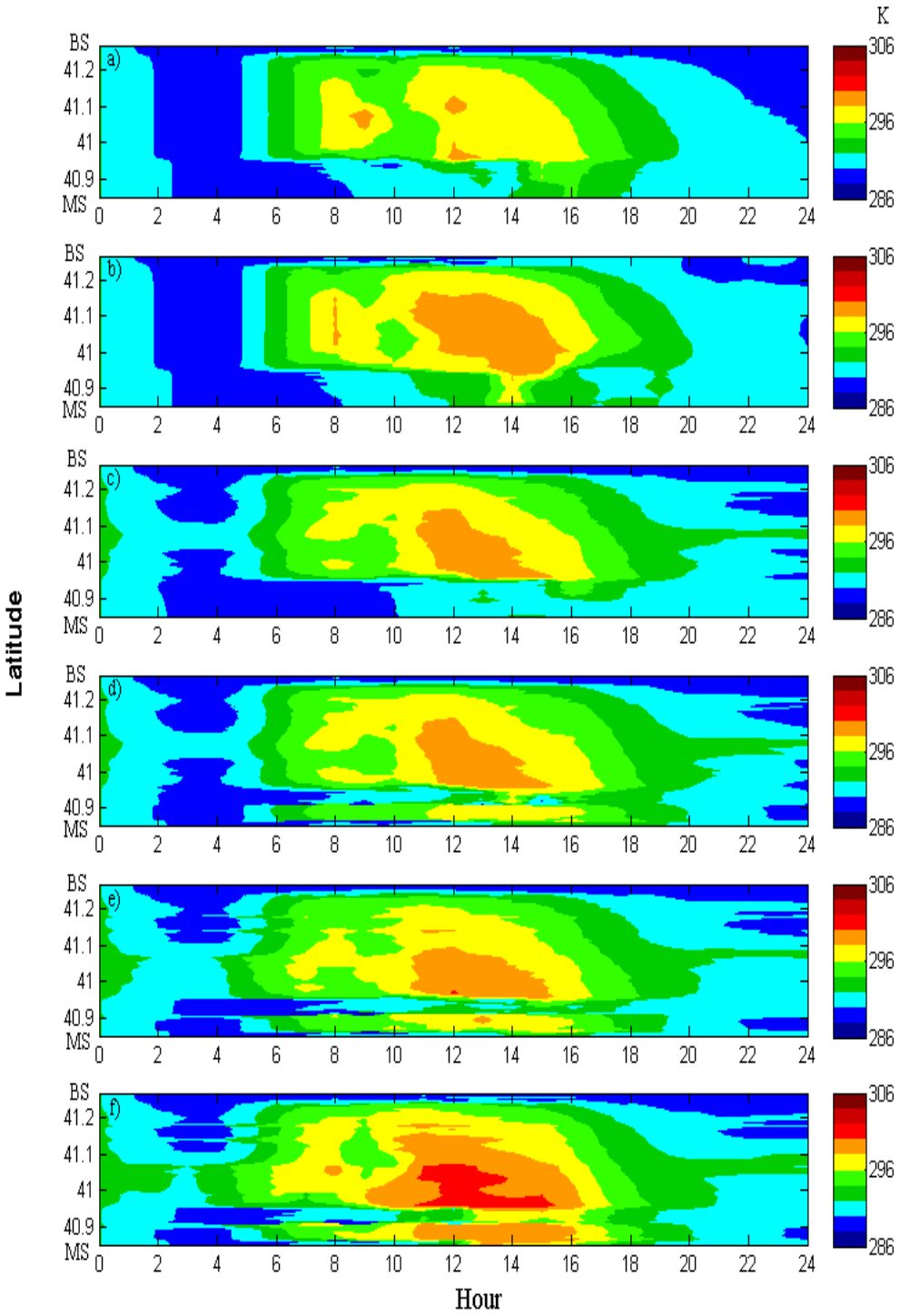

Figure 5. 25 : Potential temperature (K) time series (at 15 m) for cross-section from the east of the Bosphorus a) flat, b) flat strait, c) real topo-strait, d) real topo-island e) ne-current and f) sw-current.

The presence of the islands shows the land breeze at 0400 UTC for both over the island where the cross-section is taken and over the mainland. A sea breeze starts over these two land surfaces at 0600 UTC. The water surface between the island and

the mainland is located 40.9°N splits the southerly wind direction (southerly sea breeze) into two strong parts. Urbanization makes the domain warm on the current simulations (see Figure 5.26e-5.26f) and strong southerly sea breeze is observed under the southwesterly background flow.

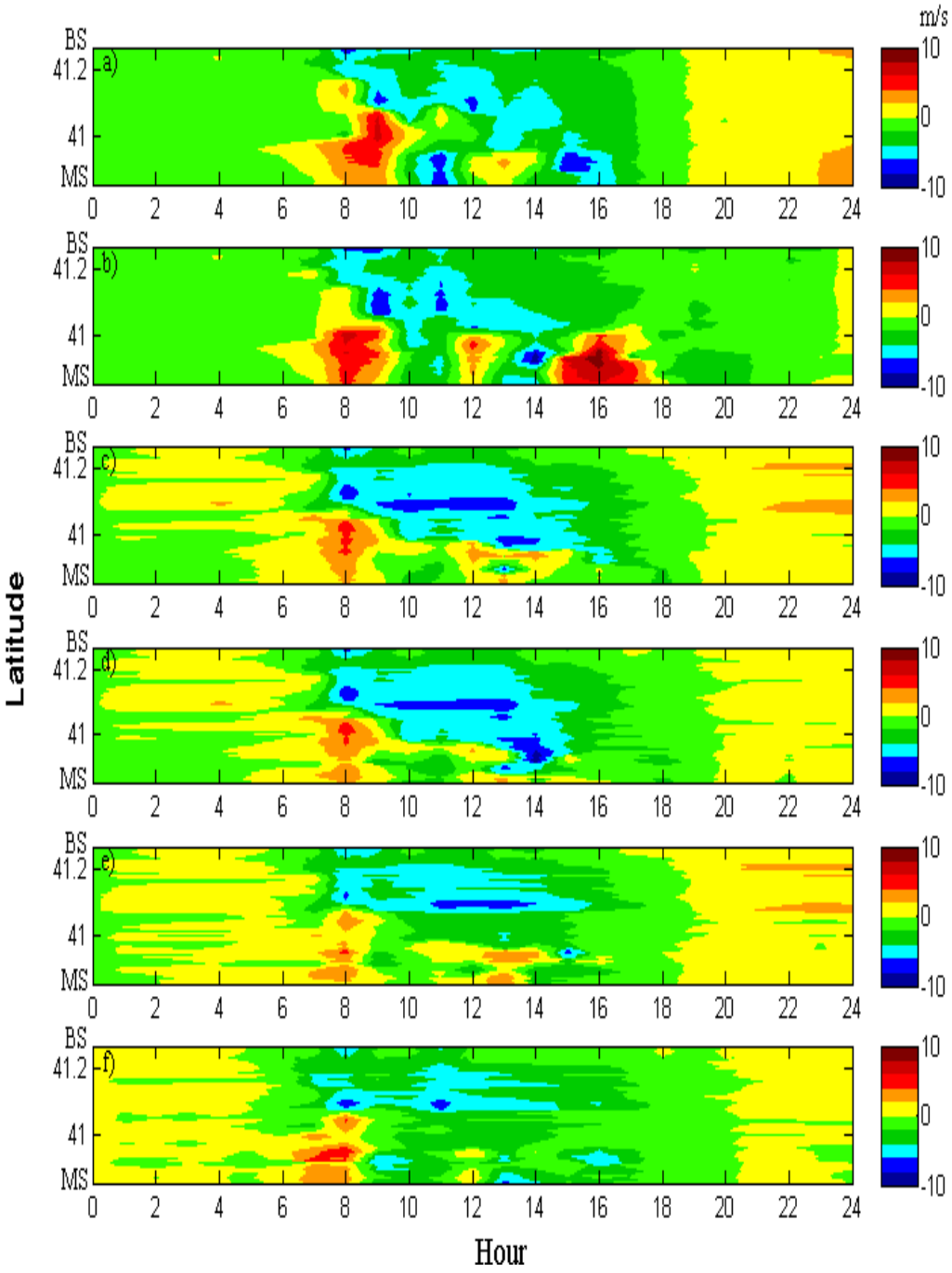

Figure 5. 26 : Time series of V component of the horizontal wind (m/s) (at 30 m) for cross-section from the east of the Bosphorus a) flat, b) flat-strait, c) real topo-strait, d) real topo-island e) ne-current, and f) sw-current.

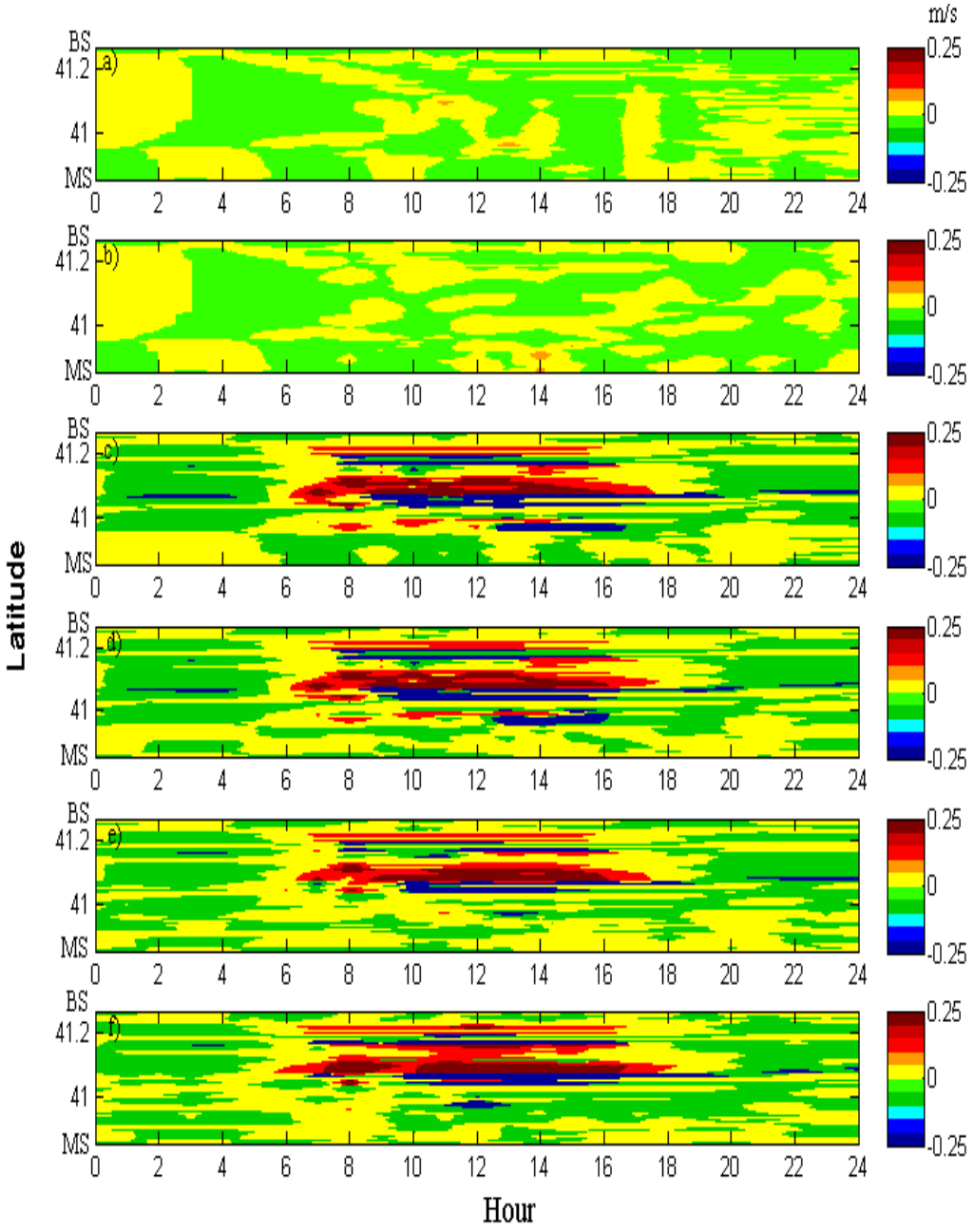

Figure 5.27 : Time series of vertical velocity (m/s) (at 30 m) for cross-section from the east of the Bosphorus a) flat, b) flat-strait, c) real topo-strait, d) real topo-island e) ne-current, and f) sw-current.

Maximum inland penetration of the southerly sea breeze occurs at 0900 UTC on the flat run as it is seen from the other two cross-sections. Rest of the simulations shows the intense penetration at 0800 UTC. Penetration also continues on flat-strait case at 0900 UTC. As the northerly background flow prevents the inland penetration on the north (BS) while it allows the inland penetration on the southern part of the domain (MS), sea breeze is onset close to shoreline on the north. Similar condition is found

for the southerly background wind direction that southern sea breeze cannot progress into the inland while the northerly sea breeze extends to the inland. The maximum inland penetration of the sea breeze is also the location where the convergence occurs.

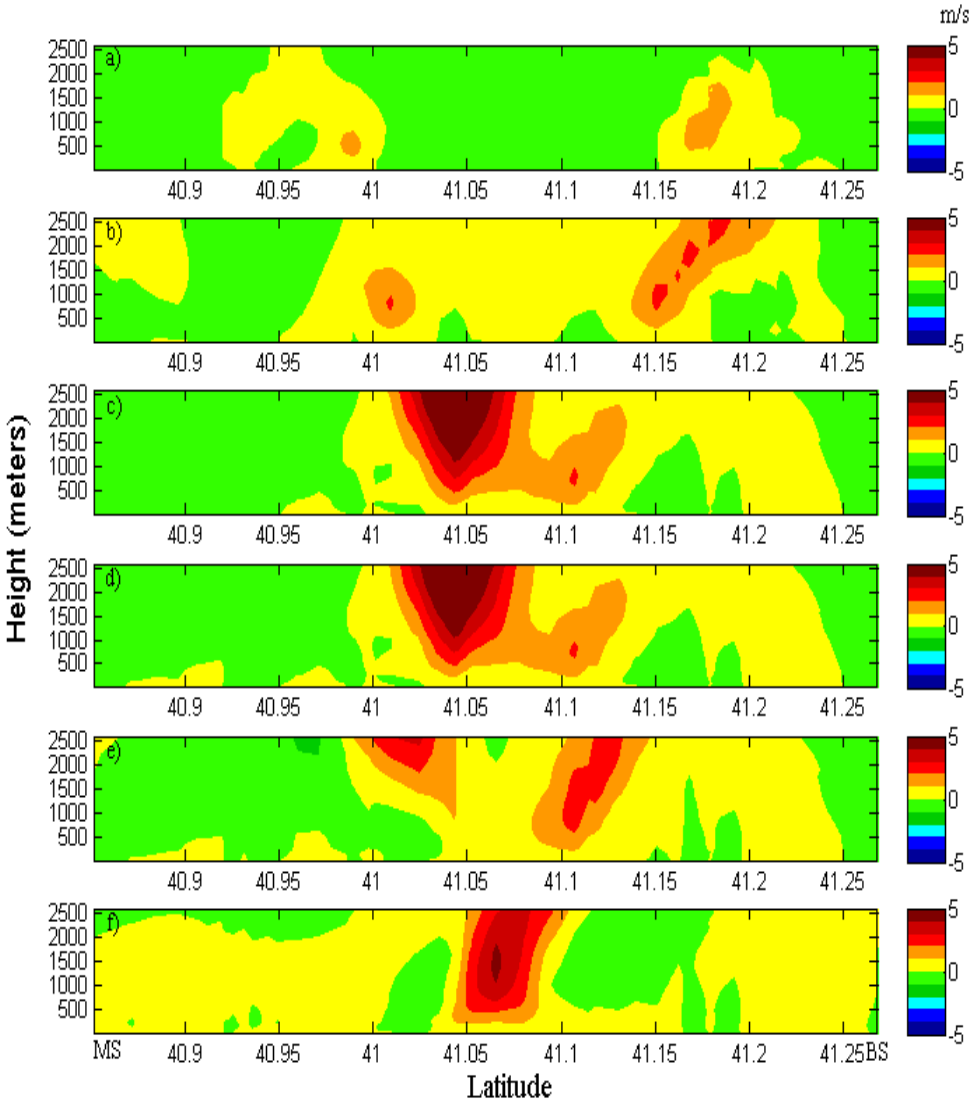

Figure 5.28 : Vertical velocity (m/s) changes in height at 0800 UTC for east of the Bosphorus a) flat, b) flat-strait, c) real topo-strait, d) real topo-island e) ne-current and f) sw-current.

The vertical velocity distribution for the cross-section given in Figure 5.27 indicates the rising air areas over the domain similar to the other cross-sections. Vertical velocity and potential temperature behaviour with height is also analyzed for the existence time of the convergence. Convergence regions at 0800 UTC on the flat run (shown in Figure 5.28a) are not associated with meeting of southern and northern sea

breezes. These convergences directly related to surface parameters response to the sea breezes on both sides of the domain and they are located on where the border of the cold airs invasion is observed from the potential temperature (shown in Figure 5.29a). Similar behaviour is also observed for the flat-strait case. Two convergences, unrelated to the sea breeze meeting occur between the cold temperature boundary with sea breezes over the domain at 0800 UTC (Figures 5.28b and 5.29b). Flat cases (the flat and flat-strait) show the similar behaviour over the domain and the strait strengthens the intensity of the convergence over the uniform surface.

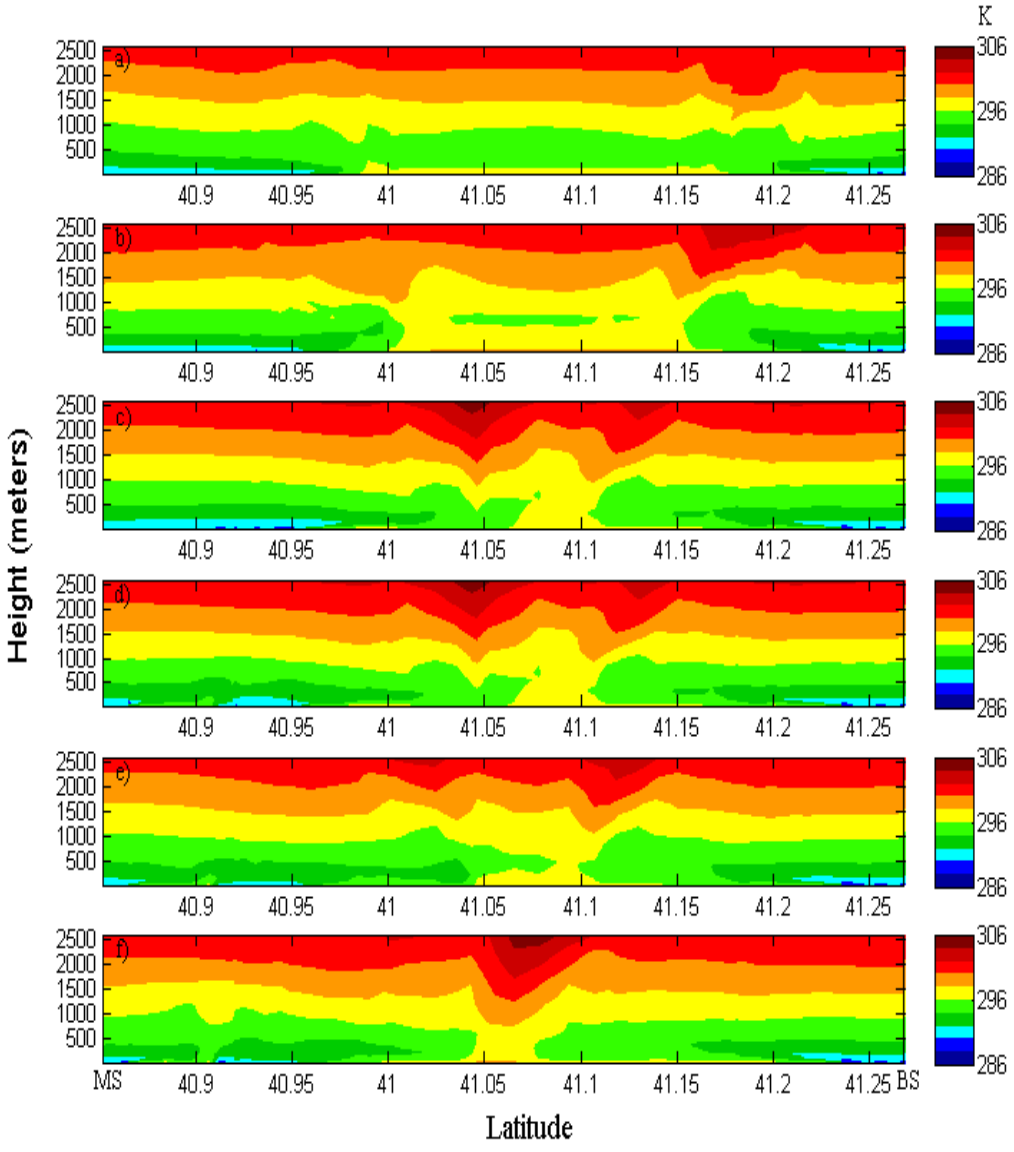

Figure 5.29 : Potential temperature (K) changes in height at 0800 UTC for east of the Bosphorus a) flat, b) flat-strait, c) real topo-strait, d) real topo-island e) ne-current and f) sw-current.

In contrast to the flat cases convergence occurs due to the sea breeze merge over the domain on the real topography runs (Figures 5.28c and 5.28d). Sliding cold airs from BS and MS into the domain and gradient in potential temperature between the adjacent regions where the convergence is observed are shown in Figures 28c and 27d. The vertical velocity is strong on the real topography runs. Furthermore, the intensity of the convergence is low over the island at 40.9°N (Figure 5.28d).

The flow is more complex when the current land-use types and other geographic features are added into the domain. Convergence changes its location depending on the background flow direction. Northerly background flow causes the convergence on the north while the southerly flow makes the convergence stay in the south.

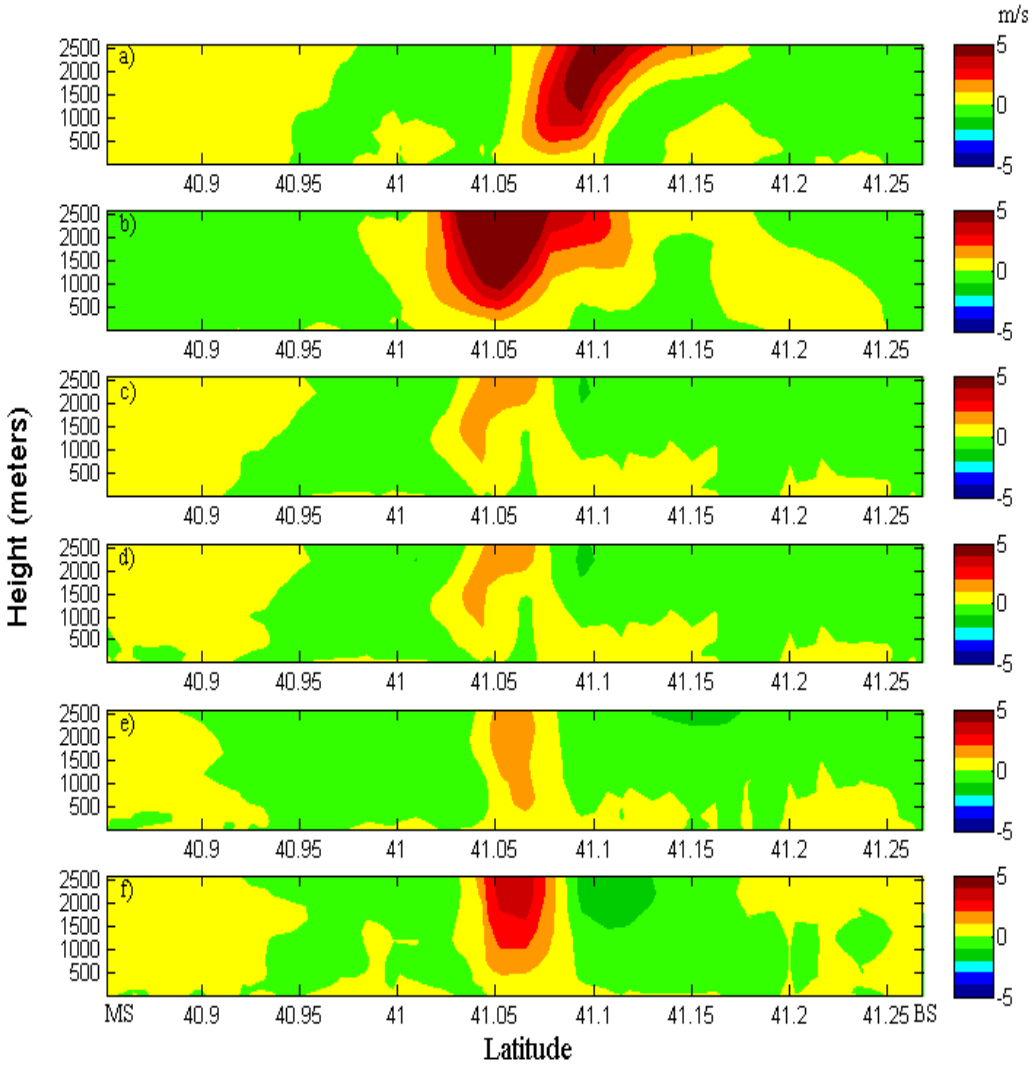

Figure 5. 30 : Vertical velocity (m/s) changes in height at 0900 for east of the Bosphorus a) flat, b) flat-strait, c) real topo-strait, d) real topo-island e) ne-current and f) sw-current.

Vertical extent of the convergence is up to 2000 m on the flat runs while it keeps continue on the rest of the simulations. Corresponding to the potential temperature behaviour convergence moves towards the middle of the domain at 0900 UTC (Figure 5.31). The convergence location is observed at 41.05°N for all the simulations except than the flat simulation whose convergence region is at 41.1°N and extends vertically higher altitude as shown in Figure 5.30. Flat simulations have the strong vertical velocity values in all the simulations. If the current simulations are compared, vertical velocity produced by the sw-current conditions is stronger than the ne-current simulation due to contribution of the onshore flow to the urban-induced convergence.

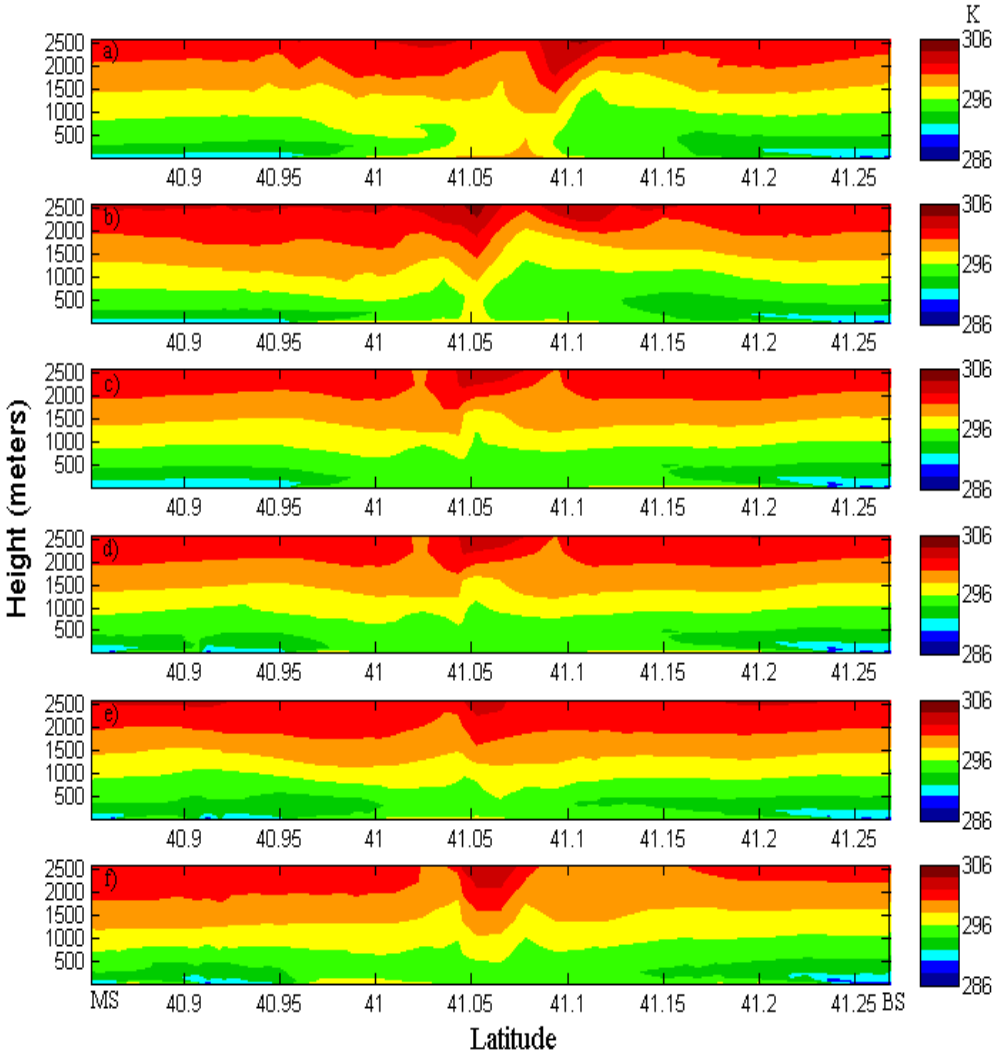

Figure 5. 31 : Potential temperature (K) changes in height at 0900 UTC for east of the Bosphorus a) flat, b) flat-strait, c) real topo-strait, d) real topo-island e) ne-current and f) sw-current.

Table 5.4 is utilized to give general information about southerly sea breeze. It shows that maximum inland penetration occurs on the flat-strait case with 7 m/s wind speed in y-direction. Topography also increases the intense SB penetration distance. Since onshore flow suppresses the inland penetration of the sea breeze, inland penetration of the southerly sea breeze progresses farther inland on the ne-current simulation (23.75 km away from the south) than the sw-current. Maximum duration of the sea breeze is on the ne-current flow simulation, 8 hours, with 4.5 m/s southerly wind speed. However, the sea breeze is observed only 3 hours on the sw-current with 5.9 m/s.

Table 5. 4 : Characteristics of the southerly sea breeze at the first model layer (~30m) for the east cross-section.

CASE	flat	flat-strait	real topo-strait	real topo-island	ne-current	sw-current
max. inland penetration (km)	25.22	31.30	22.34	23.75	23.75	22.3
intense SB distance (km)	15.4	16.23	17.56	17.56	10.85	10.85
max. SB wind (m/s)	6.63	7	5.19	5.12	4.5	5.9
max. SB penetration time (hour)	9	8	8	8	8	8
SB duration (hour)	3	3	4	5	8	3

After all analyses two features are noticeable. First one is the effect of the strait and the second one is the contribution of the urbanization on the flow. Analyses point out that the strong northerly wind blows over the domain after northerly and southerly sea breezes merged. The presence of the strait channeled the flow at noon. However, the channeled flow is sensitive to the topography as well. The strong northerly flow over the domain extends more to the western part of the domain while the channeling is limited on the eastern part. Yet, topography and shape of the strait controls the penetration of the channeled flow. The height of the terrain differs on both sides of the strait where the terrain height is high on the eastern part (shown in Figure 5.32a and 5.32b).

Terrain height difference between both sides of the Bosphorus affects the movement of the flow towards the inland from both sides of the strait. Hence, penetration of the channeling flow is less on the west due to the topography effect while it moves more inland to the east of the strait. Another significant feature over the Bosphorus is that

the flow has a fan shape when it exits from the Bosphorus. This strong outflow feature is continuous in time and progress into the Sea of Marmara (Figure 5.33 and Figure 5.34). Also, urbanization depicts the same strong channeled flow and outflow over the strait. On the other hand, the channeled flow is weakened by the urbanization on both sides of the domain as shown in Figure 5.35.

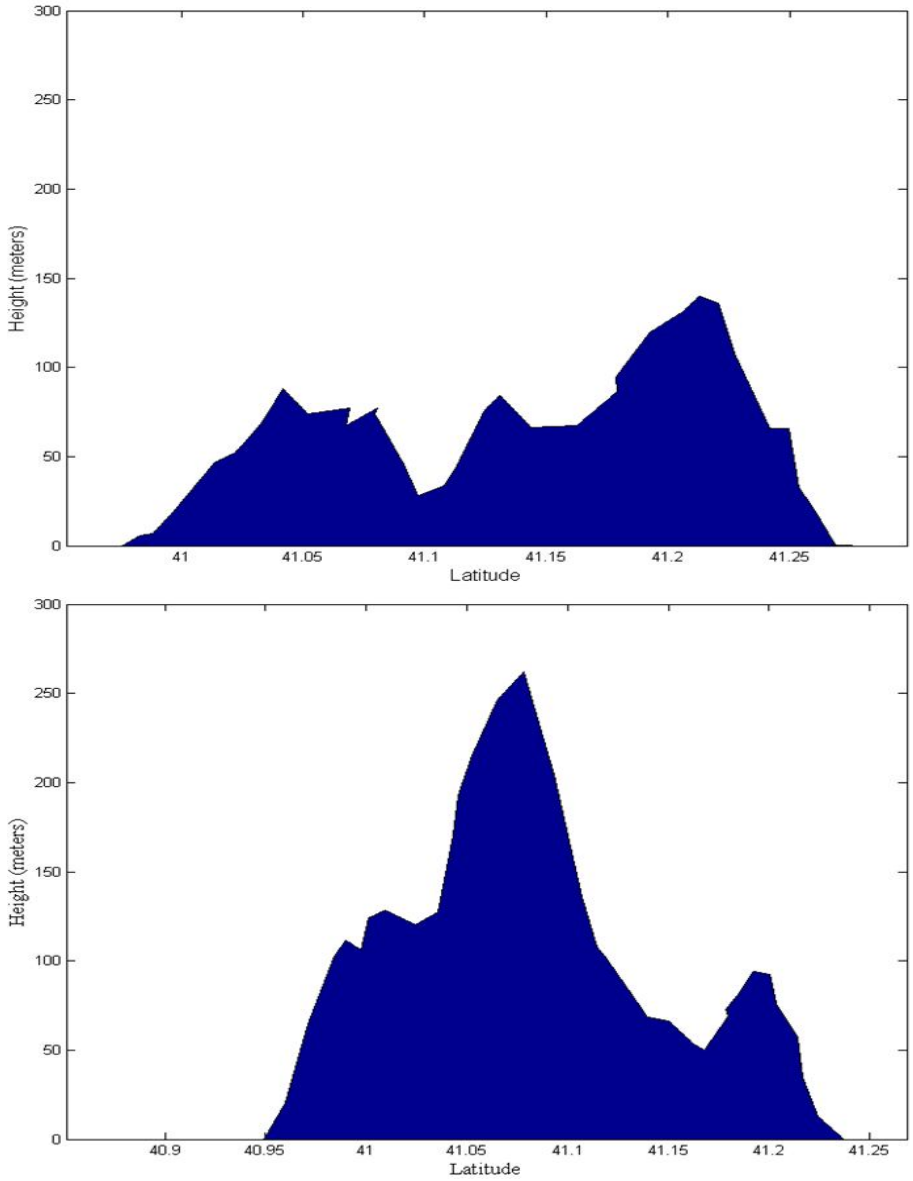

Figure 5.32 : Topography of the cross-sections a) western cross-section and b)eastern cross-section.

Inland penetration of the channeling flow is not strong and broad horizontally on the southerly background wind (Figure 5.36). Yet, the flow along the strait is as strong as the real topo-strait at early noon and it loses its strength after 1600 UTC. Outflow is

not strong enough to move into the Sea of Marmara and it is not continuous in time. In addition to the channeling due to the presence of the strait, the islands distract the flow in a similar way on the flat-strait case. Roughness length changes on the flat-strait case causes the existence of the channeling flow through the strait. Water surface between the mainland and the islands also provides the same condition to produce a channeling flow on the southwest of the domain.

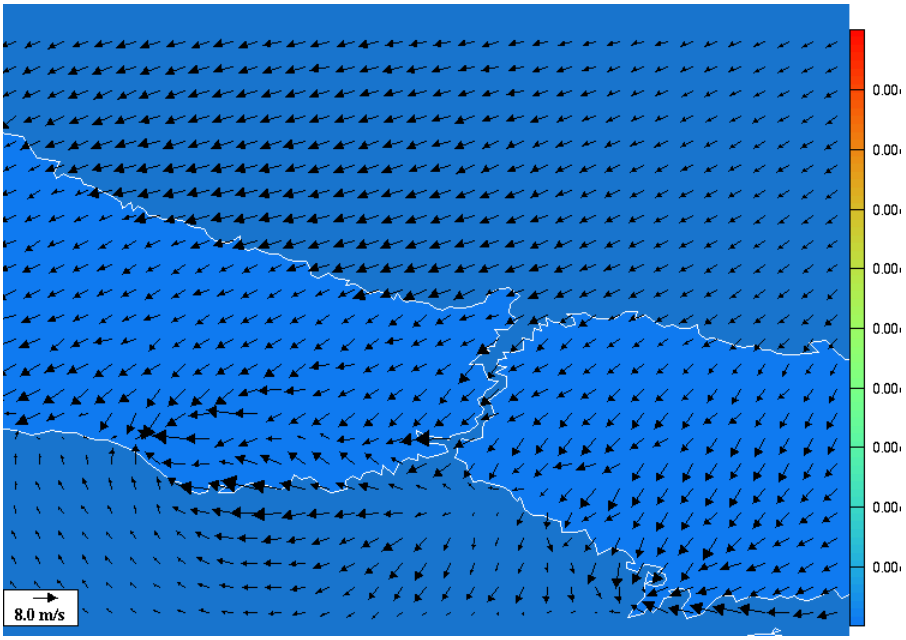

Figure 5.33 : Flow structure on the flat-strait case at 1300 (at 30 m).

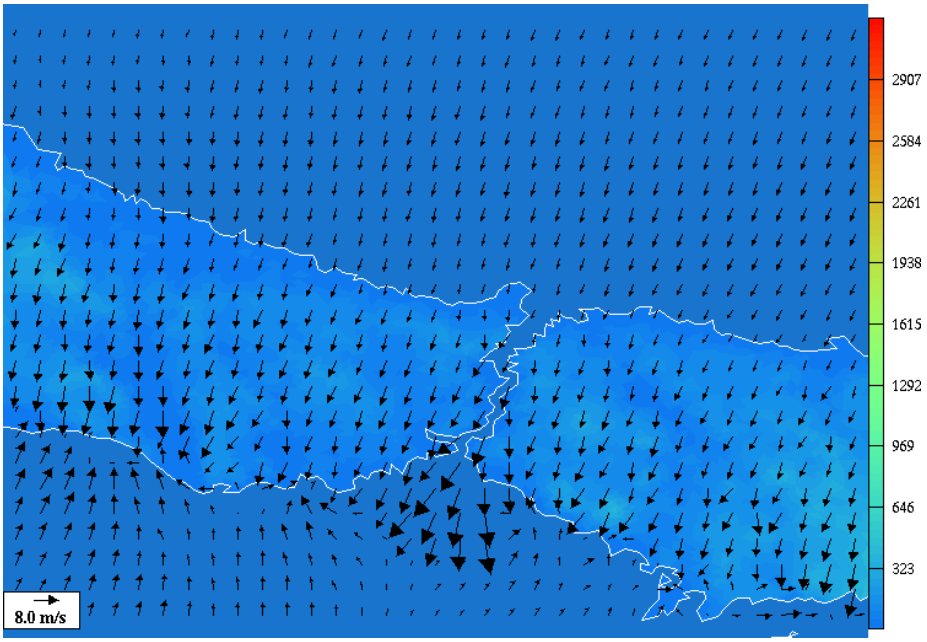

Figure 5.34 : Flow structure on the real topo-strait case at 1300 (at 30 m).

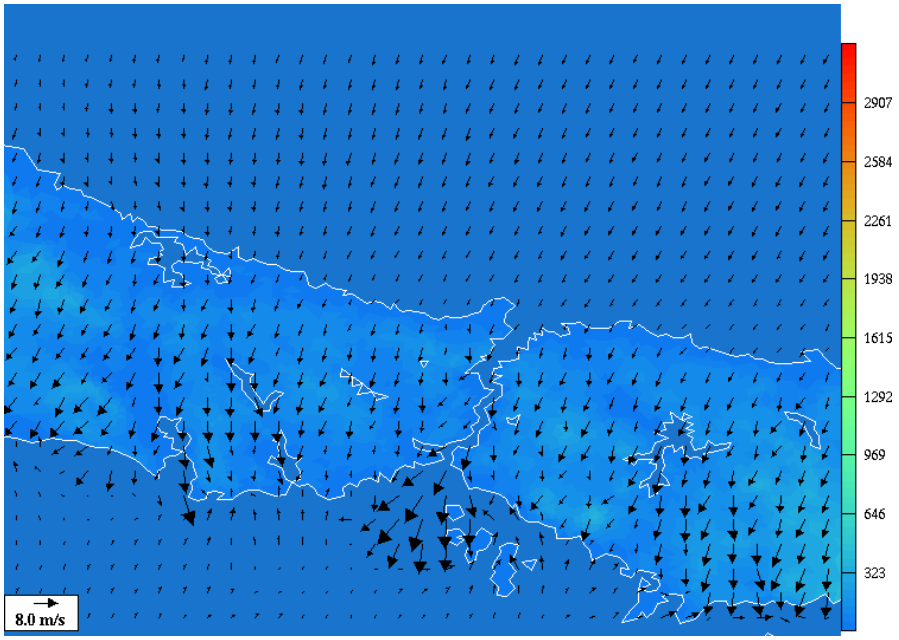

Figure 5.35 : Flow structure on the ne-current case at 1300 (at 30 m).

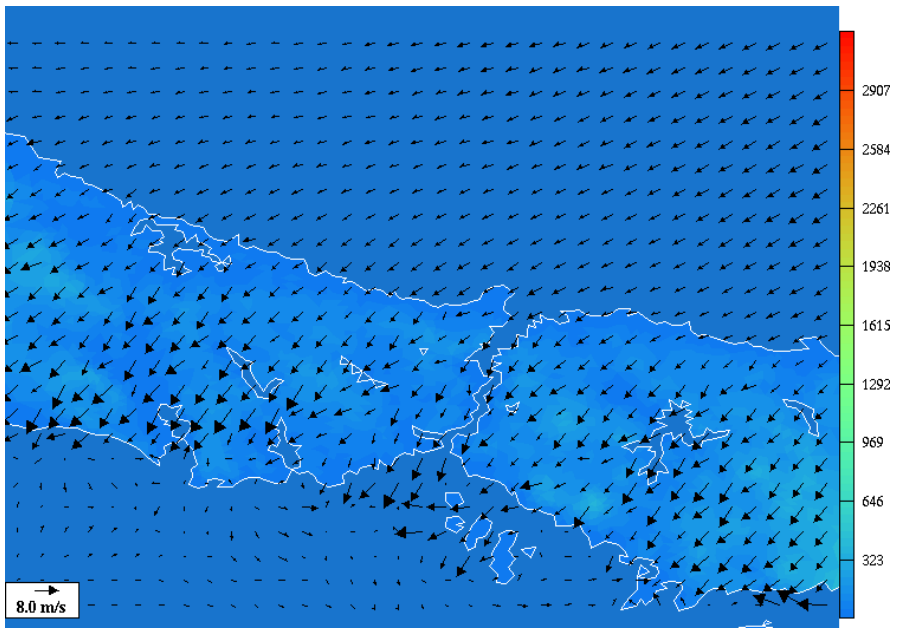

Figure 5.36 : Flow structure on the sw-current case at 1300 (at 30 m).

The second conspicuous contribution comes from the urban effect over the domain. The spatial flow points out that urbanization prevents the fast movement of the sea breeze. Moreover, urban region acts as a buffer zone in between the water surface and the rural region. The sea breeze does not penetrate farther inland because urban heat island is coupled with the sea breeze (Yoshikado et al, 1996). It is important that a convergence zone exists over the urban region since interaction of the sea breeze

and the urban heat island circulation influences air pollution concentration. A convergence zone occurs in the middle of the urban region, which delays the progress of the sea breeze when it is onset (Figure 5.37). Same figure also exhibits the onshore and offshore flow influence on the domain as it was emphasized previously. In order to deduce the details of the urbanization contribution to the flow at vertical, a horizontal cross-section passes through the urban areas is utilized (shown in Figure 5.38).

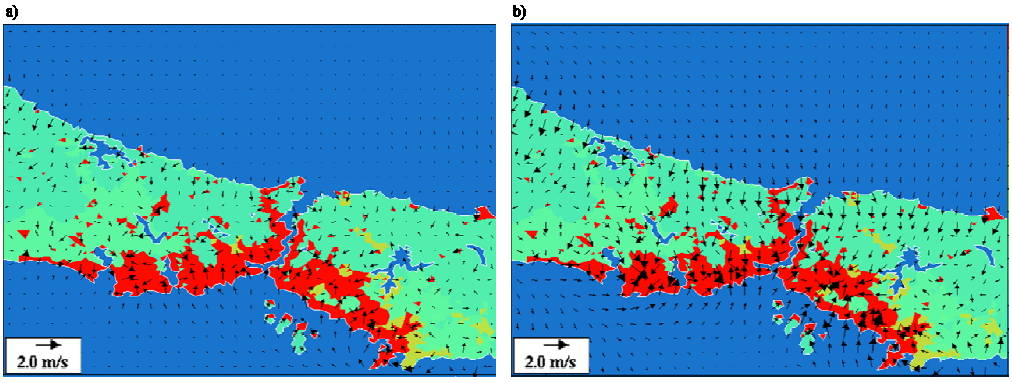

Figure 5.37 : Onset of the sea breeze for current conditions a) ne-current and b) sw-current simulations at 0600 UTC (red color shows the urban area).

Although topography is not rough in Istanbul, it influences the flow properties as given in the previous paragraphs. As it is shown in Figure 5.32a-b and Figure 5.38b, eastern part of the domain is relatively high over the domain. Therefore, attenuation of the flow is observed at that side while the flow extends more inland on the western part of the domain at noon when the flat-strait and real topo-strait simulations are compared.

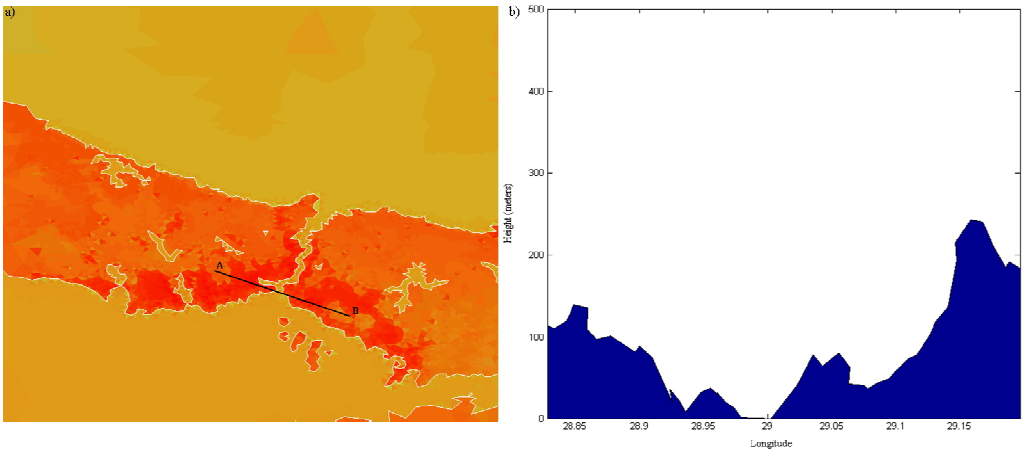

Figure 5.38 : Horizontal cross-section from the south of the domain a) cross-section location and b) topography along the cross-section.

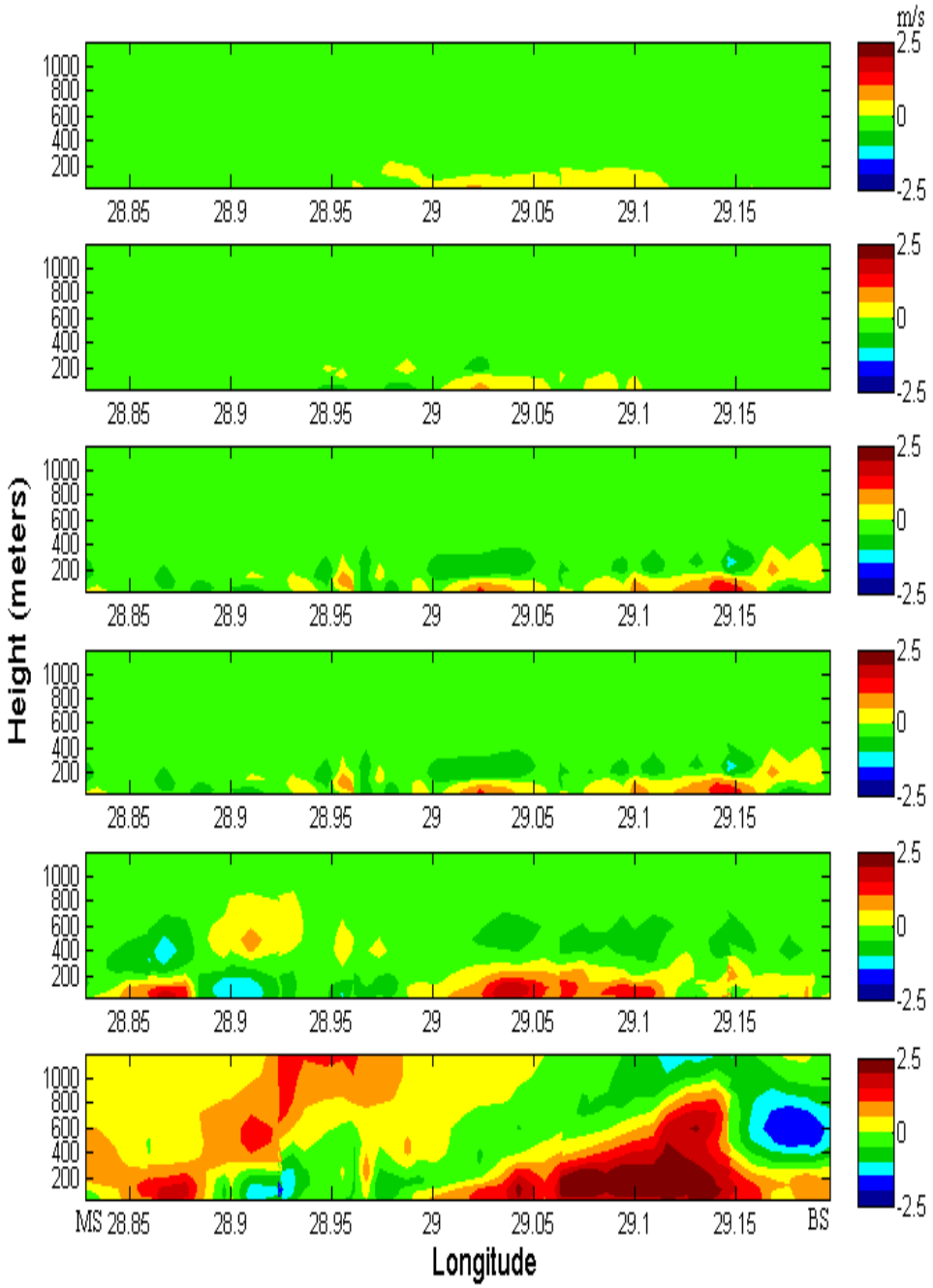

Figure 5.39 : Changes U component of the horizontal wind (m/s) in height at 0600 UTC a) flat, b) flat-strait, c) real topo-strait, d) real topo-island e) ne-current, and f) sw-current.

Horizontal structure of the sea breezes and the urban heat island can be analyzed from the cross-section for all cases. Since the first case has uniform surface, there is no signal about a sea breeze flow at 0600 UTC (Figure 5.39a). After water surface, which is located between the 28.99°N-29.00°N (shown in Figure 5.38b) is added to the domain, onset of a sea breeze flow is observed around the strait as shown in

Figure 5.39b. The onset of sea breeze is specified by positive U component of the wind on the eastern part while by negative values on the west. The sea breeze is also observed over the real topography cases with increased inland penetration due to the topography effect (Figures 5.39c-d). case.

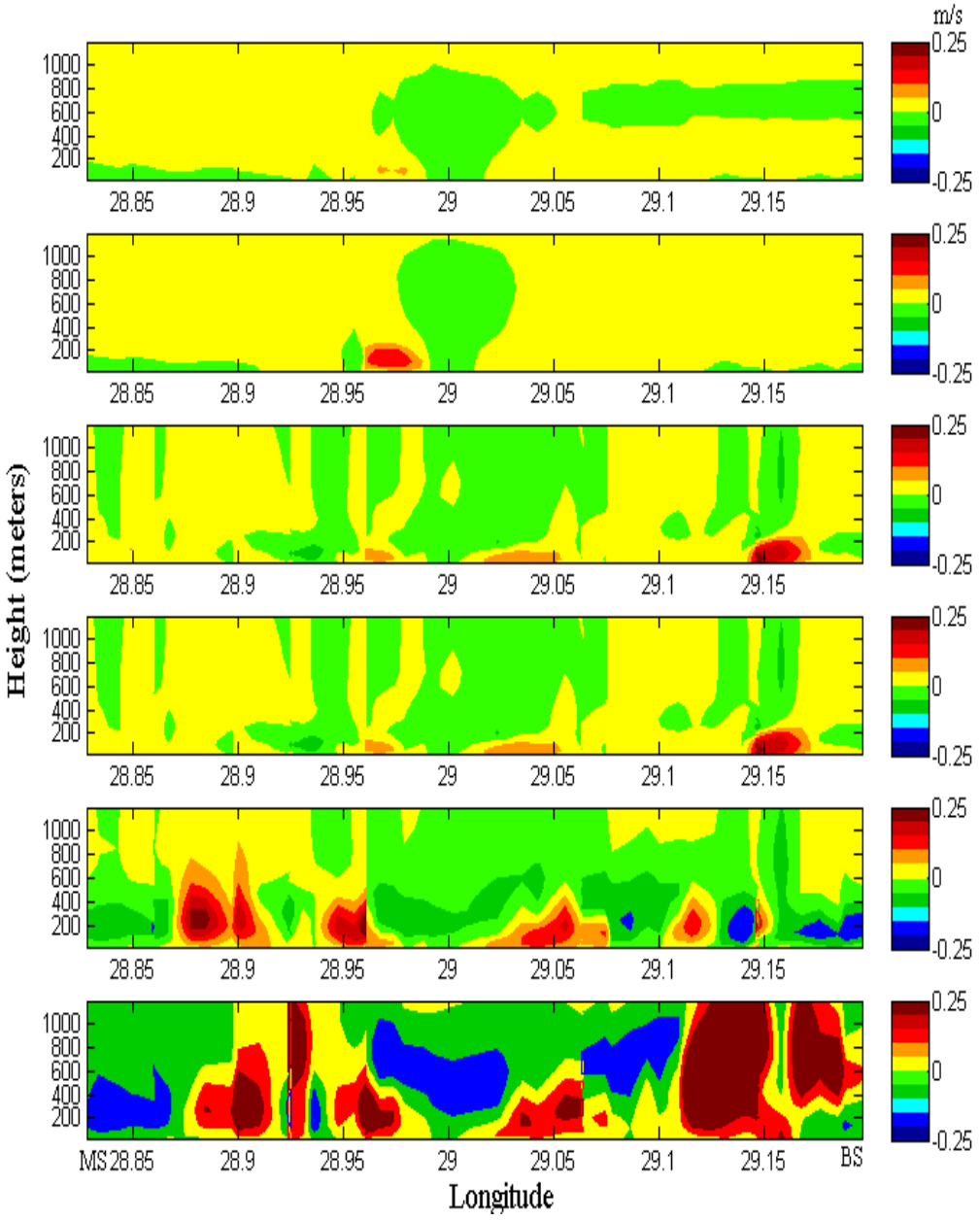

Figure 5.40 : Vertical velocity (m/s) changes in height at 0600 UTC a) flat, b) flat-strait, c) real topo strait, d) real topo-island e) ne-current and f) sw-current.

The contribution of the urbanization to the flow is clearly seen in Figures 5.39e and 5.39f. The sea breeze is more intense on the both sides of the strait since the urban

region increases the temperature gradient on the sw-current case. Convergence over the urban region keeps the sea breeze close to shoreline on the sw-current case since the southwesterly flow positively contributes to the temperature gradient. However, on the ne-current case, northeasterly wind causes weak temperature gradient that produces the weaker sea breeze on the south of the domain. This weak sea breeze moves more inland than the southwesterly wind

Existence of the convergent region over the domain because of the surface diversity is also seen on those simulations. Rising air corresponding with the convergence reaches up to 1000 m and also the convergence is dominant on both sides of the Bosphorus (shown in Figure 5.40e and 5.40f). This convergence zone is overwhelmed in time and when the sea breeze overcomes the convergence it moves into the inland. Other idealized cases show weak convergences area only near the strait since there is no urban region over the domain on those case. The ne-current simulation indicates a re-current circulation over the western urban region at 200 m whereas southwesterly flow distorts the re-current circulation (see Figures 5.39e and 5.39f). Under the southerly initial wind condition, the sea breeze extents with height up to 200 m where the re-current circulation is observed on the northerly initial wind.

5.3 Real Case Simulations

One of the objectives of this study is to understand the physical mechanisms of local flows over Istanbul. Due to the complexity of the domain, it is difficult to explain the behaviour of the local flow. In the first part of the study a mesoscale model is performed for idealized cases. After gaining some insights from those hypothetical simulations, real-case simulations are performed for winter and summer. Two dates are determined based on criteria that are necessary for the existence of a sea-land breeze and urban heat island circulations. These criteria are well-known from the previous studies, which are high pressure system with calm and cloud free conditions (Oke, 1987).

From synoptic flow charts and satellite images which are provided by the State Meteorological Service of Turkey, 08 July 2007 and 09 December 2006 are specified as a representative of the criteria for summer and winter, respectively (shown in Figure 5.41 and Figure 5.42). The main concern is to investigate the mesoscale flows such as, land-sea breeze and urban heat island on both winter and summer conditions

in the light of sensitivity simulations and further determine the model performance for the domain. Synoptic charts show that the cold high pressure system sidling from the north is centered over the Eastern Anatolia extending through the west of Turkey on 09 December 2006 and synoptic chart shows calm condition. However, high clouds are seen over the domain from Figure 5.43a. Although clear weather is a recommended condition for the analysis of mesoscale flow, it is difficult to find the cloud free sky in wintertime. Therefore, 09 December 2006 is used to simulate the wintertime mesoscale circulation. The high pressure is settled on Atlantic Ocean throughout the Europe including the Marmara Region of Turkey on 08 July 2007 (shown in Figure 5.42) and clear sky dominates on this day as expected (see Figure 5.43b).

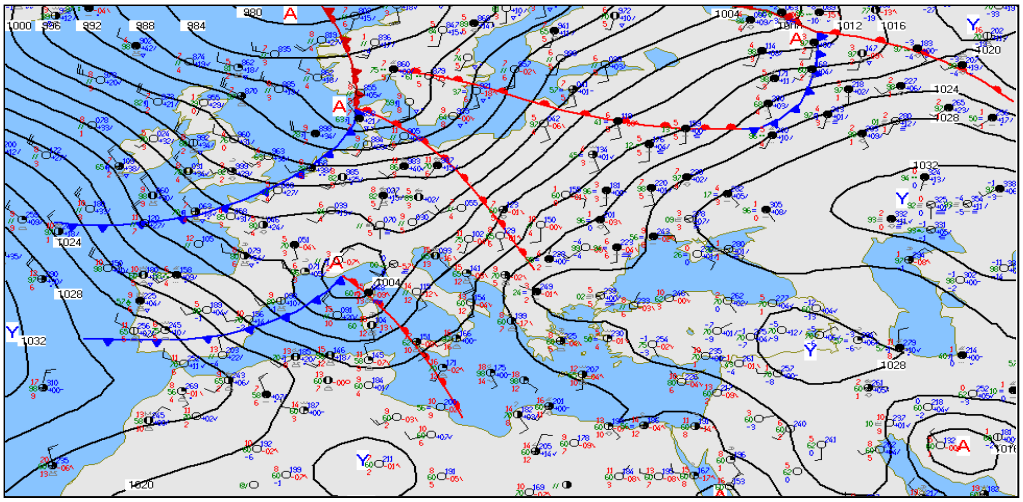

Figure 5.41 : Synoptic chart at the surface at 0000GMT on 09th December 2006.

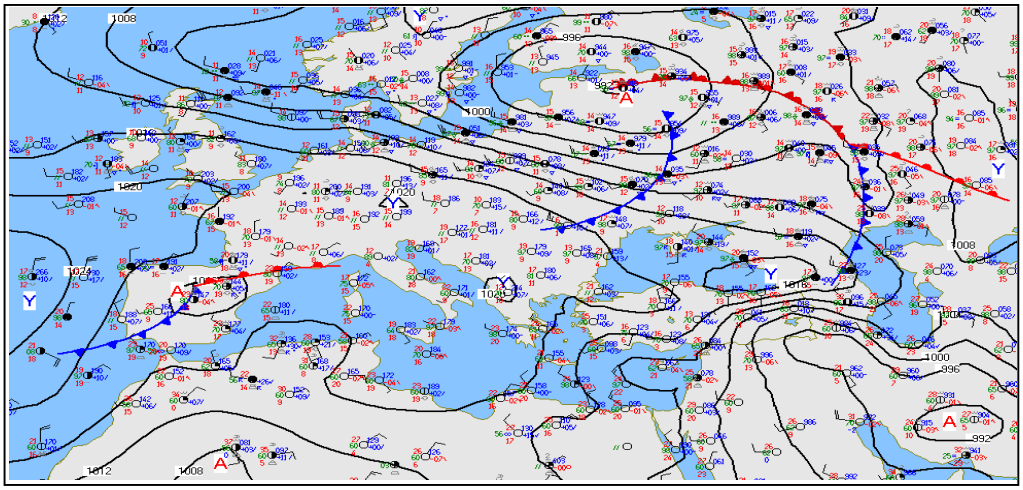

Figure 5.42 : Synoptic chart at the surface at 0000GMT on 08th July 2007.

a)

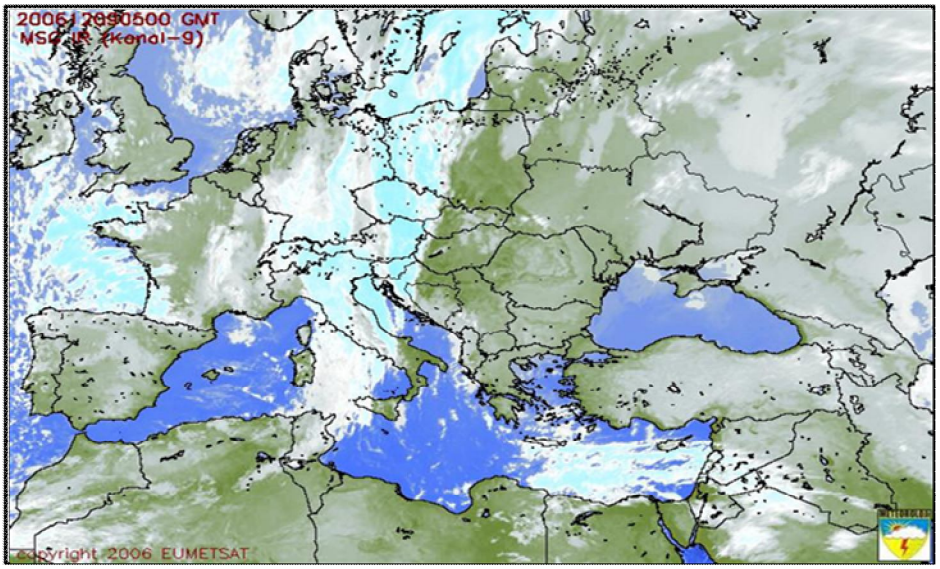

b)

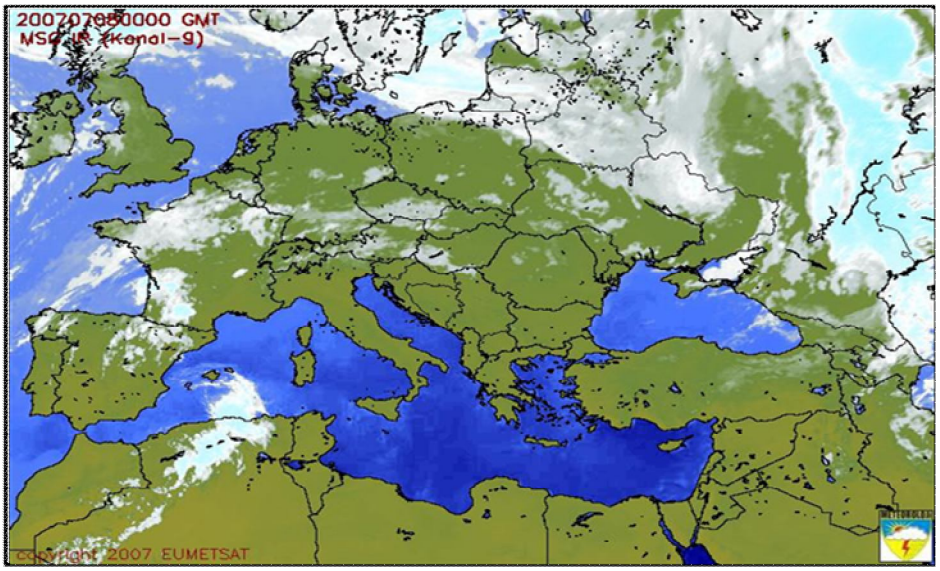

Figure 5.43 : Satellite images for real case simulations a) on 09th December 2006, and b) on 08th July 2007.

Analysis on 09 December 2006

Initial and boundary conditions to initialize the OMEGA are provided by NCEP 3 hourly AVN dataset with 1.0x1.0 degrees horizontal resolution. The Sea Surface Temperature (SST) is provided every six hours by FNMOC (Fleet Numerical Meteorology and Oceanography Center), which is approximately 12 km resolution at the equator and 9 km at the mid-latitudes. The OMEGA is set up using three nested domains where the horizontal resolution changes from 60 to 0.56 km with 35 vertical

levels up to 20,988 m as used in the sensitivity simulations. After generating the mesh, land-use data including 99 land-use types (given in Table A1.1) used by the OMEGA is modified based on the report prepared by the Municipality of Istanbul as used in the sensitivity simulations (Figure 5.44). As it is mentioned previously, simulations are performed for two days and model outputs are produced every hour. Geopotential height at 500 hPa on 08 December 2006 is utilized to compare the observation and OMEGA outputs in order to obtain the information to show that how accurately the model simulates the conditions (shown in Figure 5.45 and Figure 5.46).

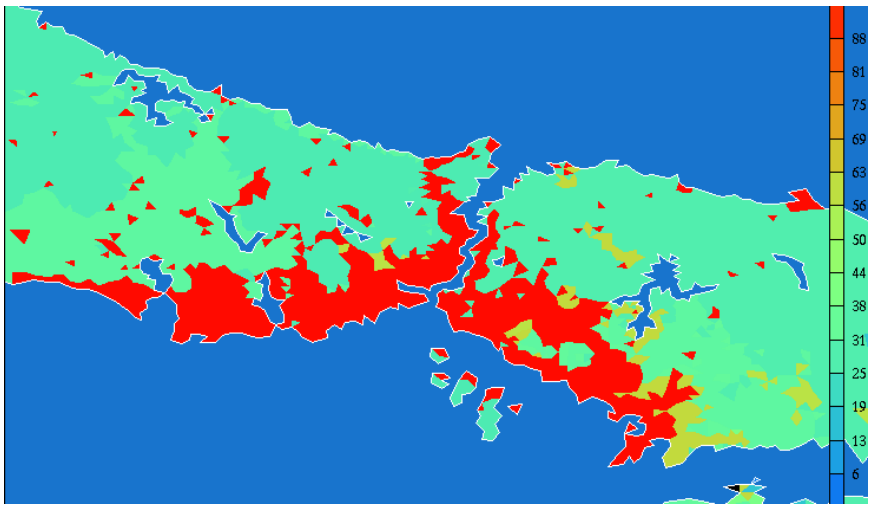

Figure 5.44 : Land-use type over study domain (red color is urban areas, green is forest and town and short crop, yellow represent forest, field and woody savanna).

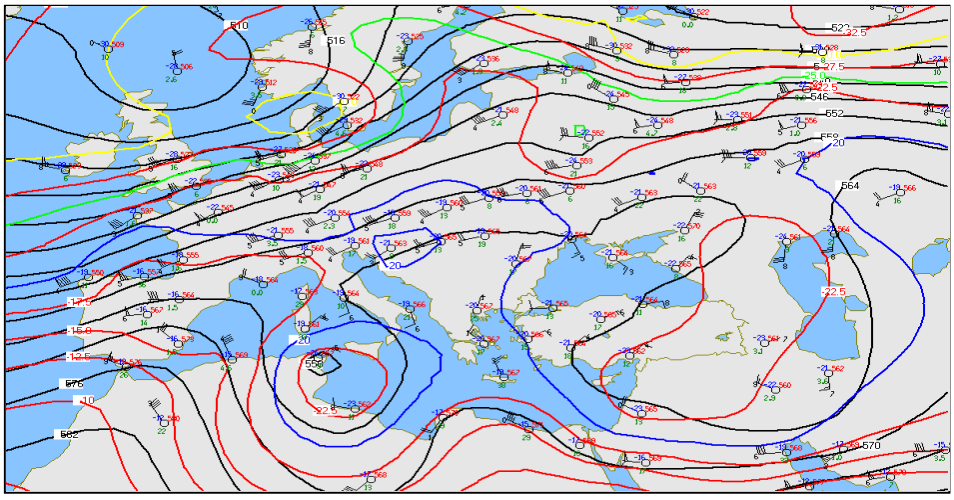

Figure 5.45 : 500 hPa Geopotential Height on 08 December 2006 (black line is 500 hPa contour).

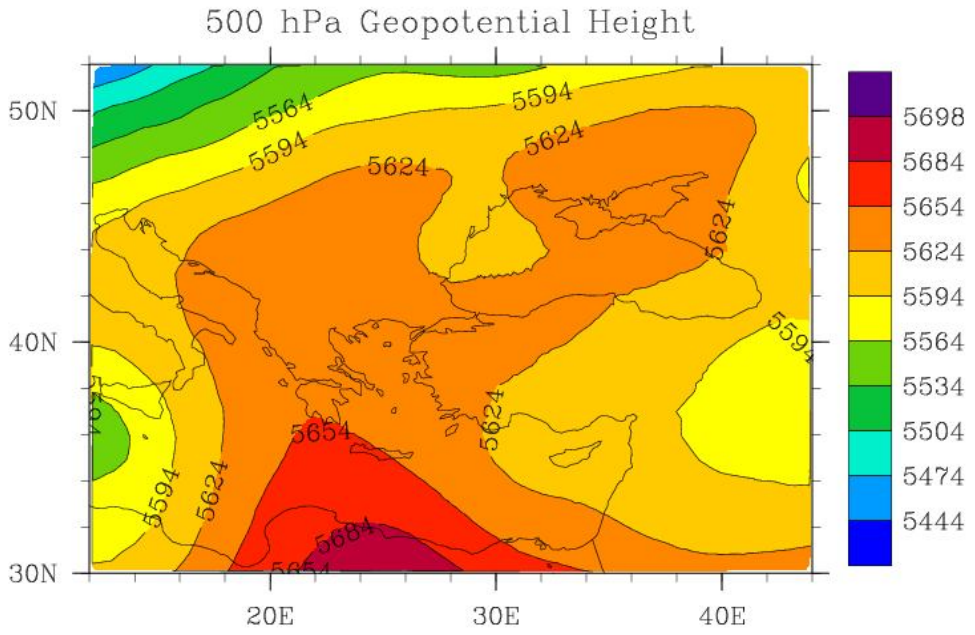

Figure 5.46 : OMEGA 500 hPa Geopotential Height on 8th December 2006.

The model underestimates the geopotential height (approximately 15hPa) and the 500hPa patterns correspond quite well (shown in Figure 5.45 and Figure 5.46). The high pressure center from the eastern Mediterranean reaches the western and central Black Sea passing through the center of Turkey at 500 hPa geopotential height for observation and also OMEGA results give the high pressure pattern over Turkey, especially close to the Mediterranean coast and the warm ridge sidling from the east to Turkey.

Table 5. 5 : Upper air error statistics for 08 December 2006-10 December 2006.

Level (mb)	TEMPERATURE (°C)			WIND SPEED (knots)			WIND DIRECTION (Degree)		
	mE	mAE	RMSE	mE	mAE	RMSE	mE	mAE	RMSE
850	0.89	1.15	1.56	-3.54	4.36	5.71	-13.28	45.59	72.88
500	0.27	0.99	1.36	-4.56	5.06	6.43	-11.97	34.73	55.22
350	0.46	1.10	1.46	-6.17	6.56	8.65	-14.05	39.15	58.09
100	0.45	1.15	1.49	-6.23	7.19	9.47	-14.30	37.40	54.47

The model upper air observations are compared against the actual observation via calculating error statistics. The statistics are produced for mean error (mE), mean absolute error (mAE), and root-mean-square error (RMSE) for temperature, wind speed, and wind direction. Table 5.5 shows these error statistics at various pressure levels that are computed 2-day simulation duration (0000 08 December 2006-0000 10 December 2006). Since only one sounding observation station, Goztepe, is

available for the comparison, the OMEGA cell locates closest to this observation site is used for the comparison. The statistical results indicate that the OMEGA model predicts the meteorological conditions reasonably well. For example, upper air temperature statistics show less than 1^{o}C temperature bias, less than mAE 1.5^{o}C, and less than 1.5^{o}C RMSE.

The study is focused on Istanbul and its outskirt, which is the third nested domain in the model, and large scale flow is initially from southwest over the domain (shown in Figure 5.46). Time evolution of the local flow over the domain shows the land-sea breeze cycle on the winter simulation. The land breeze continues by the late in the morning and then after the sea breeze (SB) starts. It is first seen on the southern part of the domain at 0900 UTC (1100 LST) and an hour later fully developed sea breezes are observed on both part of the domain. However, inland penetration of the northern sea breeze is faster than the southern sea breeze.

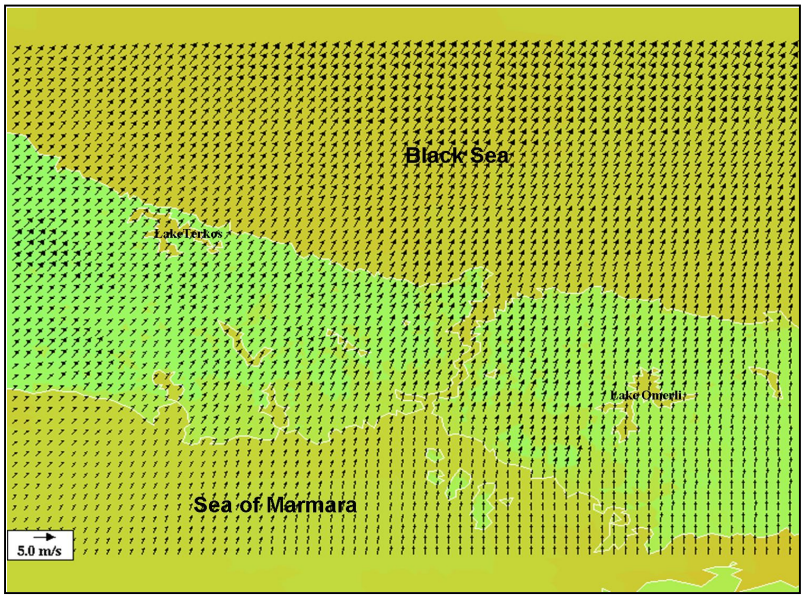

Figure 5.47 : Initial flow of the model on 8th December 2006 at 0000 UTC.

Cross-section similar to the sensitivity simulations (see Figure 5.38a) is analyzed when the sea breeze is fully developed at 1000 UTC (1200 LST). The sea breeze circulation with its positive and negative values of U component of the wind is observed close to the surface both sides of the strait (Figure 5.48a). Circulation between non-urban and urban regions restrict the penetration of the sea breeze by contributing to the temperature gradient between land and water. Hence, convergence occurs over the urbanized area akin to the sensitivity cases. Also, weak

re-current circulation is observed over the western part convergence area. Re-current circulation locates between 300 m and 500 m. Positive vertical velocity values correspond with the convergence due to the difference between the urban and non-urban surface properties (shown in Figure 5.48b).

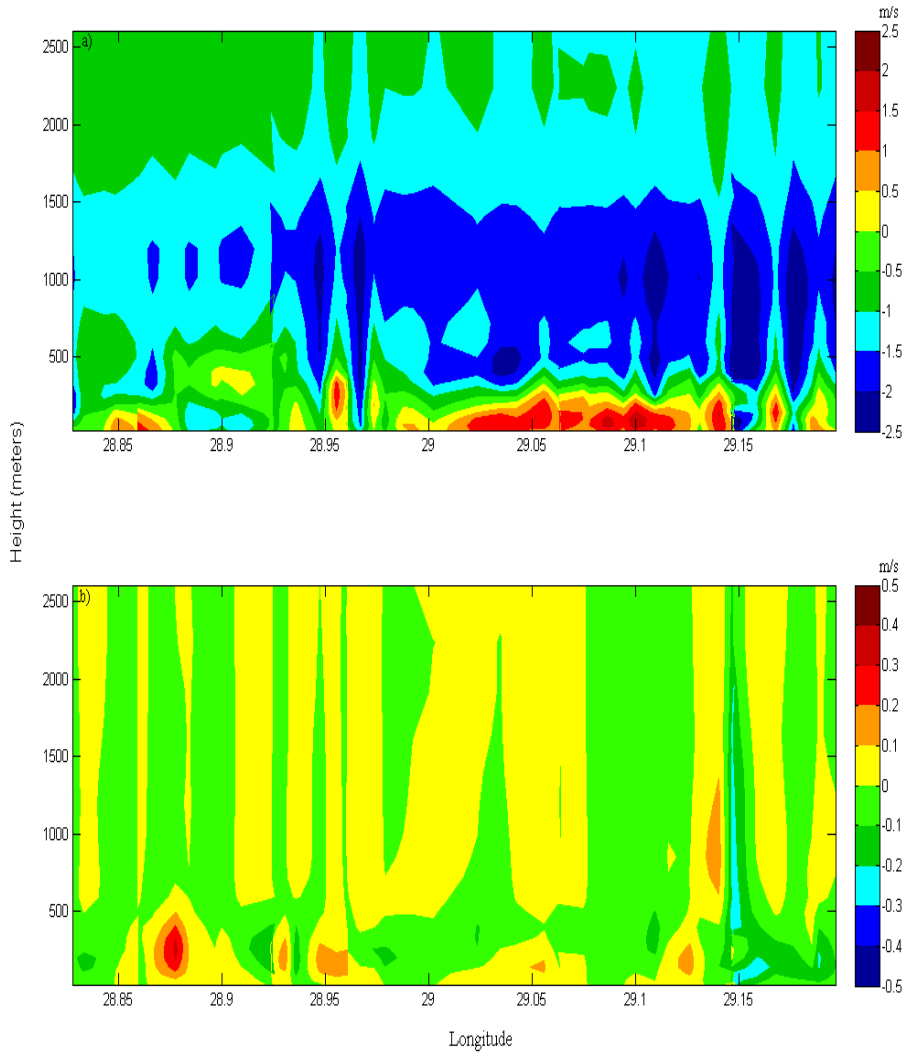

Figure 5.48 : a) U component of the wind and b) vertical velocity on 9th December 2006 at 1000 UTC at 30 m.

In addition to the sea-land breeze, lakes in the domain have contribution on the local scale circulations. Diversity of small water bodies in Istanbul makes local scale circulation more complex interacting with the Black Sea at north and the Sea of Marmara at the south. Lake-breeze circulations at two lakes Omerli and Terkos also show similar characteristics to the sea breeze. The lake-breeze begins at 0900 UTC (1100 LST) at Omerli and Terkos. Since two water bodies surround Istanbul, it is expected to merge SBs over the domain. According to Xian and Pielke (1991), SB

cells meet before 1200 LST over small landmasses and intensity of the SB is weak. It was concluded from their studies that the SB cells from both coasts merged at the center of the domain between 1400 and 1700 LST for the landmass with 100-150 km width. In this study, two SB flows converge at 1300 UTC (1500 LST) close to the southern part of the domain where the urbanization is dense (shown in Figure 5.49). The densely urbanized region in the south hinders the inland sea breeze progress. Thus, the convergence zone is located over the urban region, which is also deduced from the sensitivity simulations that urban-rural border acts as a buffer zone for the sea breeze progress. Fast progress of the northern sea breeze surmounts the southern sea breeze. Hence, land breeze begins on the south earlier than it begins in the north (at 1600 UTC) while it starts at 1700 UTC (1900 LST) on the north of the domain.

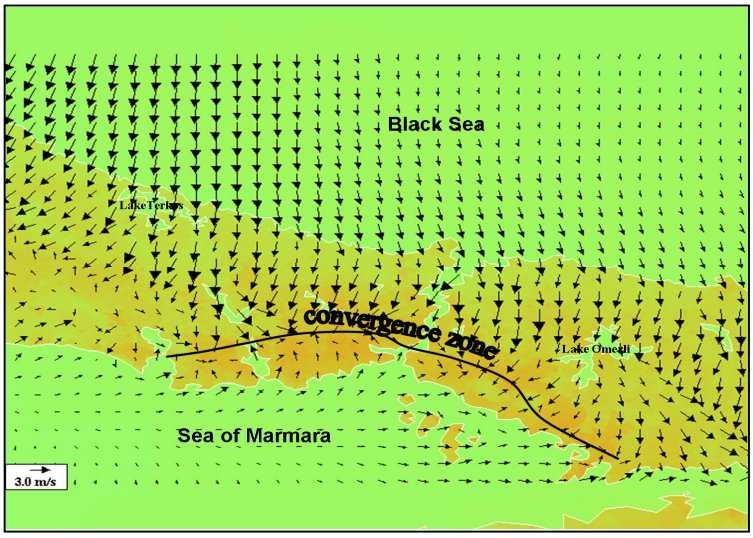

Figure 5.49 : Sea Breeze convergence on 9th December 2006 at 1300 UTC (1500 LST).

An hour later, both coasts are affected by the fully developed land breezes. As similar to the sensitivity simulations, two conspicuous channeled flows occur over the domain. One is the northerly channeled flow over the Bosphorus, which starts to blow with onset of the sea breeze and lasts until onset of the land breeze. The other is located between islands and the eastern part of the domain. The strong northerly channeled flow blows along the strait and finally fans out end of the strait. Discrepancy of the roughness length engenders a channeled flow since conducted sensitivity simulations show that although topography has contribution on the

channeled flow over the Bosphorus, the main reason is the roughness length difference between land and water.

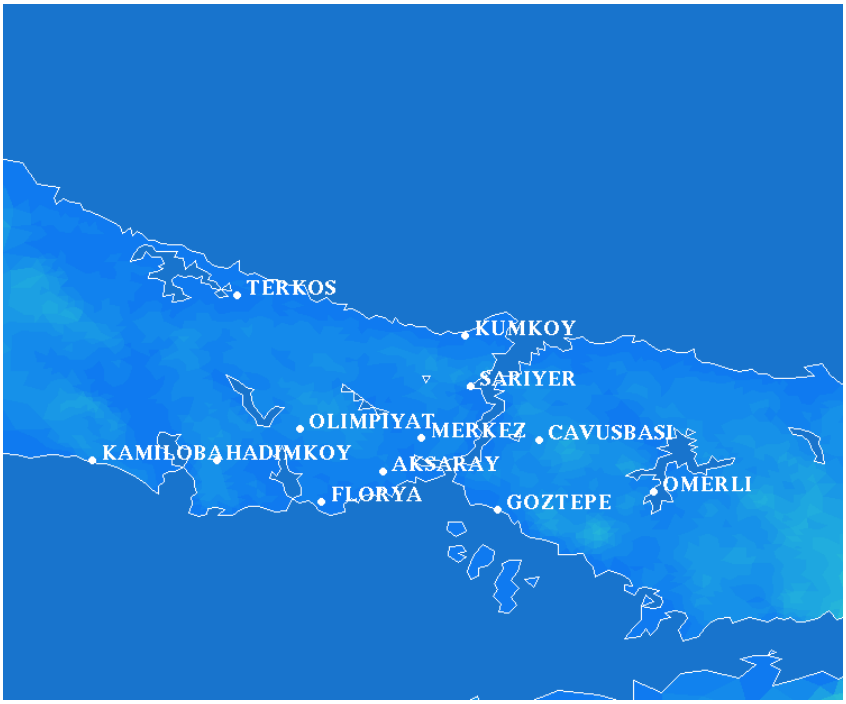

Figure 5.50 : Locations of AWOS stations.

Deficiency of the data network is the main problem for modeling studies when evaluating the results. Data from Automated Weather Observation System (AWOS) has been gathered in Istanbul since 2004. Thus, these data network, shown in Figure 5.50, are the only data that can be used for hourly comparison at the surface. The time zone difference is taken into account when evaluating the data. Meteogram and hodograph plots are carried out using UTC+0200 time correction on model results.

Meteogram is used to compare the time variation of model results and observations for temperature, wind speed, and direction. Changes on these parameters are the indicator of the existence of a sea breeze. The onset of the sea breeze is marked by a fall in temperature, an increase in humidity, a rise in wind speed, and a rapid change in wind direction (Atkinson, 1981). Comparisons at the observation stations are conducted by taking close cell points based on the station latitude and longitude information. Diurnal temperature distribution of the model can be accepted as representative of observation although model simulation results of most stations overestimate approximately 1-2^{o}C (*c.f.* Figure 5.51). The model temperature at Merkez, Cavusbası, Terkoz, Hadımkoy, and Kumkoy stations show more decrease at

nighttime (~5^{o}C). The maxima of the daytime temperature distribution at these stations are shifted 1-2 hours on the simulations since results of the model show the late starting time of the morning heating. As it is obvious that it is not a point-to-point comparison, therefore, when evaluating the results the resolution difference between the model data points and the available measured data locations should be taken into account. Moreover, model mesh in OMEGA does not have the regular size grid cells. Some of the cells have high resolutions while some of them are relatively coarse.

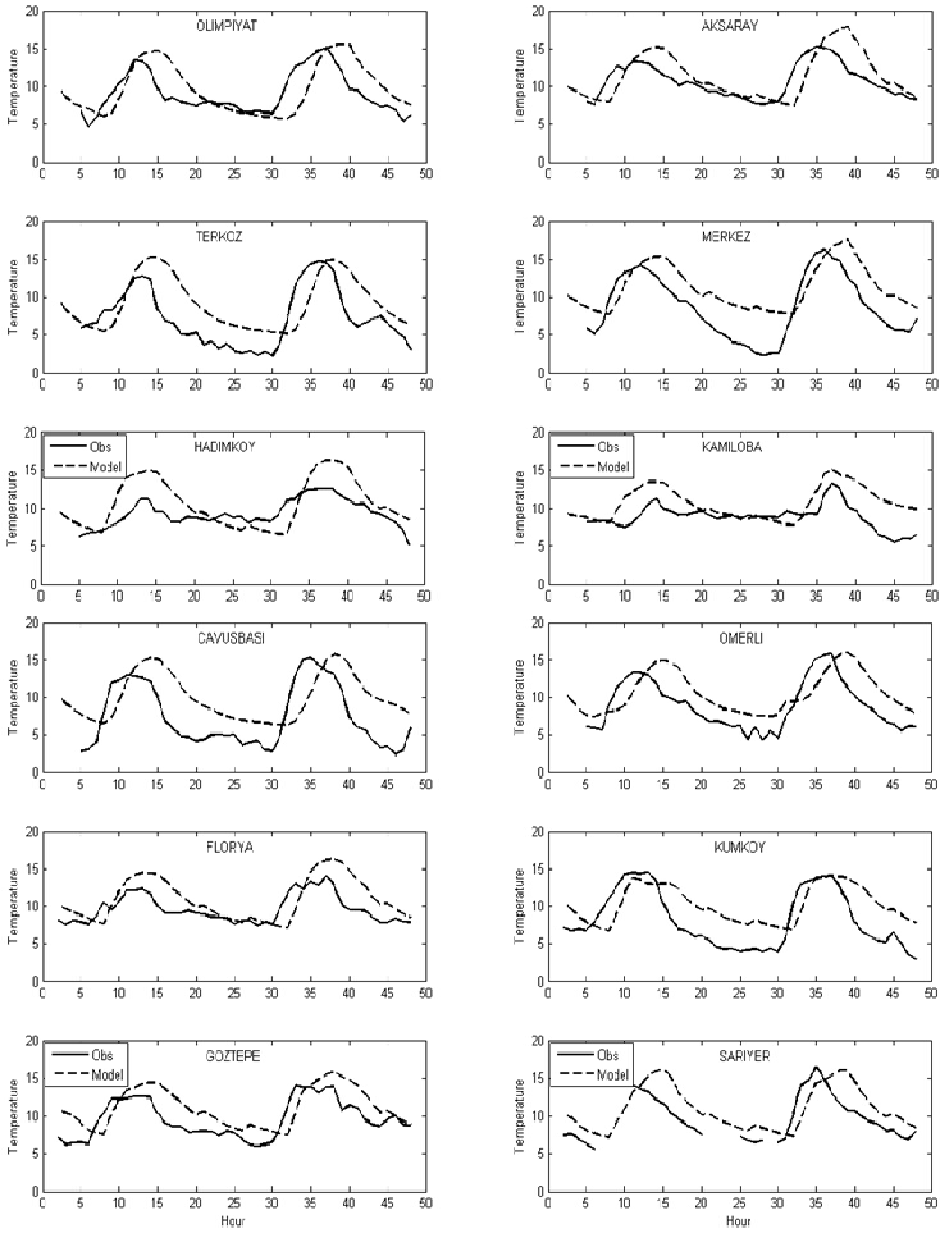

Figure 5.51 : Meteograms of temperature on 08-10 December 2006, solid line is observation and dash line is model results.

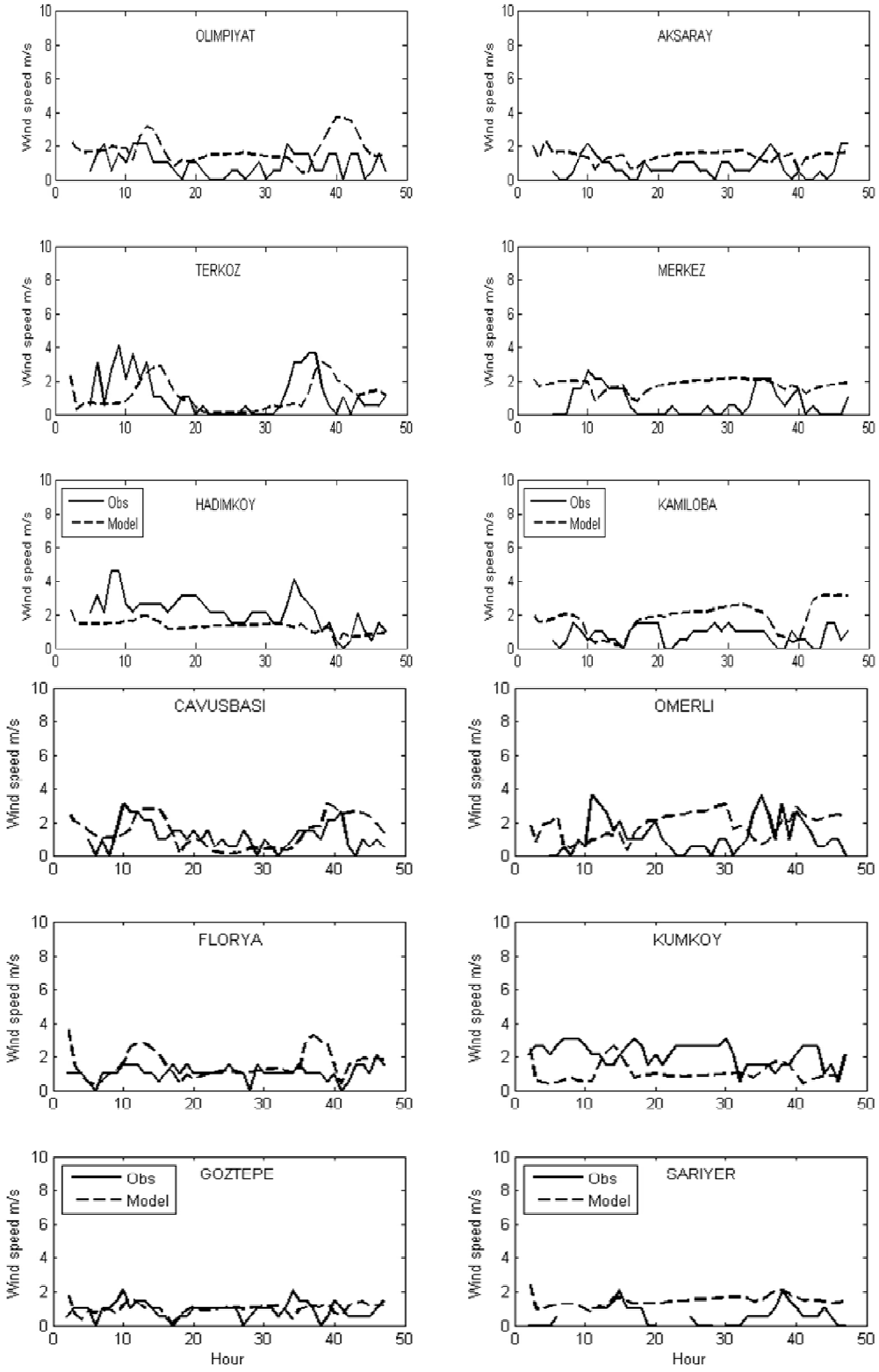

Figure 5.52 : Meteograms of wind speed on 08-10 December 2006, solid line is observation and dash line is model results.

Wind speed comparison is also revealed in Figure 5.52. Wind speed and direction are obtained from the first layer of the model which is at 30 m. Since the data from the observations are at 10 m, wind speed is extrapolated from 30 m to the 10 m for the model wind speed to compare model and observation using following equation proposed by Hanna and Britter (2002).

$$u_2(10m) = u_1(30m)\ ln\ (10\ m / z_o) / ln\ (30m / z_o) \quad \textbf{(5.1)}$$

where u_2 is wind speed at 10 m and u_1 is wind speed at 30 m and z_o is the roughness length. z_o values used in the formula is obtained from Table A1.1. Wind speed taken from simulations corresponds to the observations. While order of magnitude of the wind speed is consistent with observations, model generally underestimates the wind speed especially in Kumkoy, Hadimkoy and Terkoz stations. Nevertheless, there is no possible way to extrapolate the wind direction data from 30 m to 10 m comparison for wind direction is conducted using 30 m model wind direction data. Thus, data distribution of the wind direction varies (shown in Figure B.1). Some of the stations on model results show 300 degree difference with observation. In addition, some observation stations have no complete data on simulation days. Especially, coastal stations have data gap which might not been measured by the instruments due to the wind variability.

Hodograph shows the direction of the wind traced by the end point of the wind vectors in time, introduced by Haurwitz (1947). Harwitz (1947) explained the diurnal rotation of the sea breeze by means of the Coriolis force. Common insight is “the rotation of the hodograph is clockwise (anticyclonic) in Northern Hemisphere”. However, theoretical and observational investigations revealed that there is not a certain rule of which the sea breeze is closed ellipse with clockwise rotation (CR) (Harwitz, 1947; Kusuda & Alpert, 1983; Alpert et al., 1984; Simpson, 1996). Balance between the pressure-gradient, advection and friction terms are explained as the cause of the direction of the sea breeze rotation (Kusuda & Alpert, 1983; Alpert et al., 1984). Alpert et al. (1984) mentioned that low friction toward the north in Northern Hemisphere might cause a decrease in the frequency of anticlockwise rotation (ACR). They also emphasized that topographic forcing gives rise to ACR. Topographical constraint has been pointed out as a responsible cause of ACR and rather complex, non-elliptic shape of the hodograph by Staley, 1957; Steyn & Kallos, 1992; Furberg et al., 2002; Prtenjak, 2003; Sicardi et al., 2005.

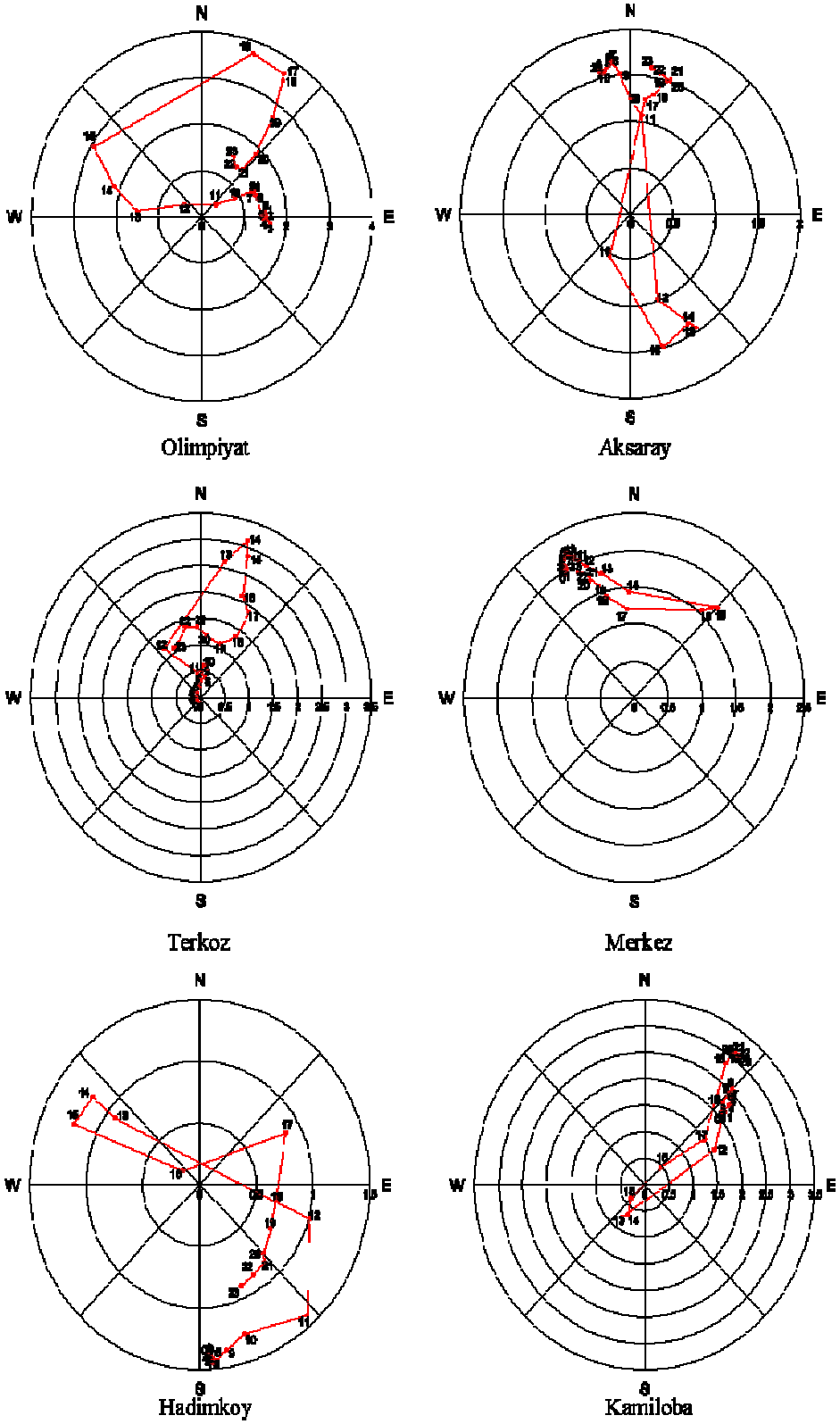

Figure 5.53 : Model hodographs of AWOS stations on 09 December 2006.

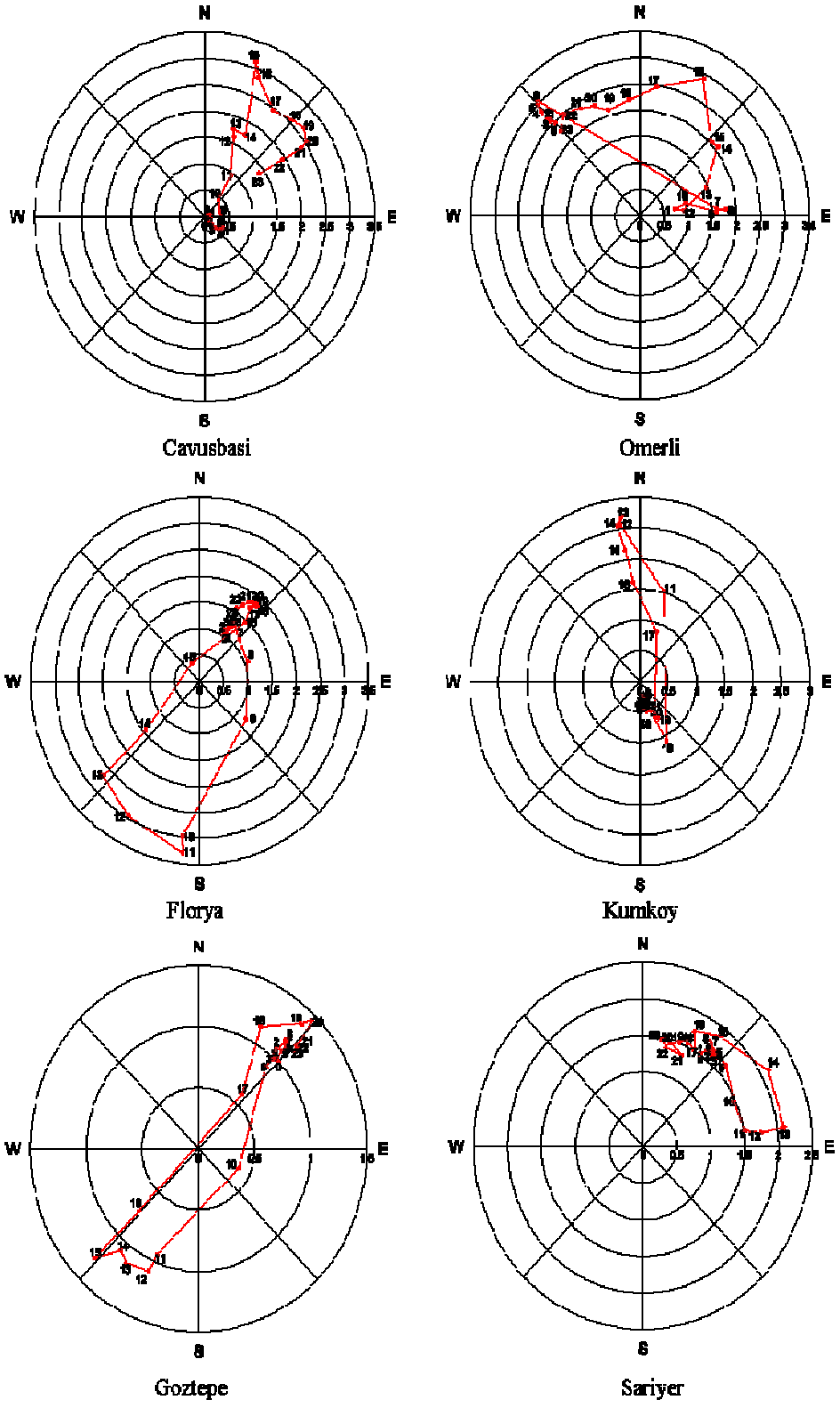

Figure 5. 53 (contd.): Model hodographs of AWOS stations on 09 December 2006.

Since hodograph can be used as a good representative of the sea-land breeze, hodograph plots are prepared from the OMEGA model cells close where the observation stations are located. Hodographs are shown in Figure 5.53 for the wintertime (09 December 2006). Most of the stations show the clockwise rotation corresponding to the common thought that hodograph is clockwise in Northern Hemisphere. However there are stations that show the opposing wind rotations (anticlockwise). The striking point is that hodograph rotation close to entrance (i.e. Kumkoy and Sariyer stations) and exit (i.e. Florya and Goztepe stations) of the Bosphorus show the different rotations and shapes. Namely, while the hodographs at Florya and Goztepe stations show clockwise rotation, Kumkoy and Sariyer stations display anticlockwise rotation on 09 December 2006. On the other hand, shape of the hodograph is either bisectional or non-elliptical at the stations, but not ellipse as explained by Haurwitz (1947).

From the theoretical studies, the balance between the pressure gradient, the Coriolis force and the friction have been explained as a reason for elliptical shape of the hodograph. Nevertheless, non-elliptic hodograph is associated with the topographic features. Studied area in this study, Istanbul and its surroundings, have no rough topography. Valleys, plains and heights are grouped as geomorphologic units. Altitude of the region rises up to 350 m in the east and 200-350 m in the west of Istanbul. Although peneplains on both sides of the Bosphorus have no distinct shape, light wavy structure characterizes the geomorphology of Istanbul. It can be deduced from the previously performed hypothetical simulations in this study that even smooth terrain gives rise to difference on the local flow. In addition, shape of the shoreline is pointed out as another reason for the anticlockwise rotation of the diurnal wind whether shoreline is concave or convex (McPearson, 1970), which might be the cause of the different rotation at the entrance and the exit of the Bosphorus.

Analysis on 08 July 2007

One of the well-known features of the sea breeze is that it frequently develops during the late spring and summer. July 8th is determined as the eligible day for studying the sea breeze since it provides calm and clear sky with high pressure system. This condition carries on a few days.

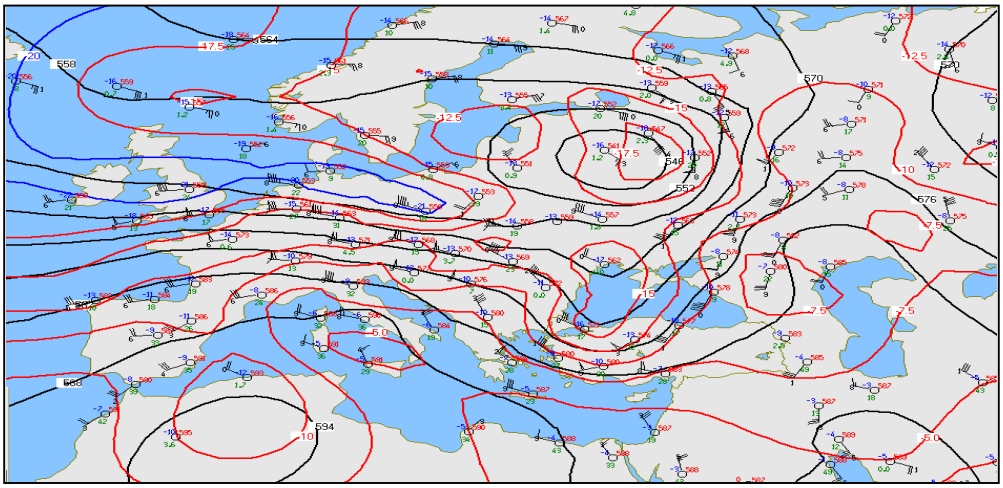

Figure 5.54 : 500 hPa Geopotential Height on 07 July 2007 at 0000 GMT (black line is 500 hPa contour).

Corresponding with synoptic chart at the surface, 500hPa synoptic chart shows low pressure system over Russia, which is sidling towards Turkey (Figure 5.54). Simulation begins at 0000 UTC on 7th of July and ends on 9th of July. The model outputs and observations show the similar location of the trough on the 500 hPa synoptic charts however it is deep in the model results (shown in Figure 5.54 and Figure 5.55). On the other hand, while location of the ridge sidling from Africa is well simulated, it is less strength in the model.

The model upper air results are compared against the actual observation as it is similar to the wintertime comparison. Table 5.6 indicates the error statistics at various pressure levels for 2-day forecast duration (0000 07 July 2007-0000 9 July 2007). Goztepe station is used for the comparison location as previously explained. The statistical results show that the OMEGA model predicts the meteorological conditions reasonably well. For example, upper air temperature statistics show less than 1^{o}C temperature bias, less than mAE 1.5^{o}C, and less than 2^{o}C RMSE.

Table 5. 6 : Upper air error statistics for 07 July 2007-09 July 2007.

Level (mb)	TEMPERATURE (^{o}C)			WIND SPEED (knots)			WIND DIRECTION (Degree)		
	mE	mAE	RMSE	mE	mAE	RMSE	mE	mAE	RMSE
850	1.33	1.67	2.04	-2.41	5.07	6.91	28.07	42.11	70.74
500	0.19	1.31	1.62	-1.90	5.23	6.76	8.33	25.46	43.35
350	0.10	1.25	1.54	-2.50	6.01	7.75	6.61	23.01	39.61
100	0.60	1.51	1.99	-3.31	6.90	8.73	2.10	18.34	32.13

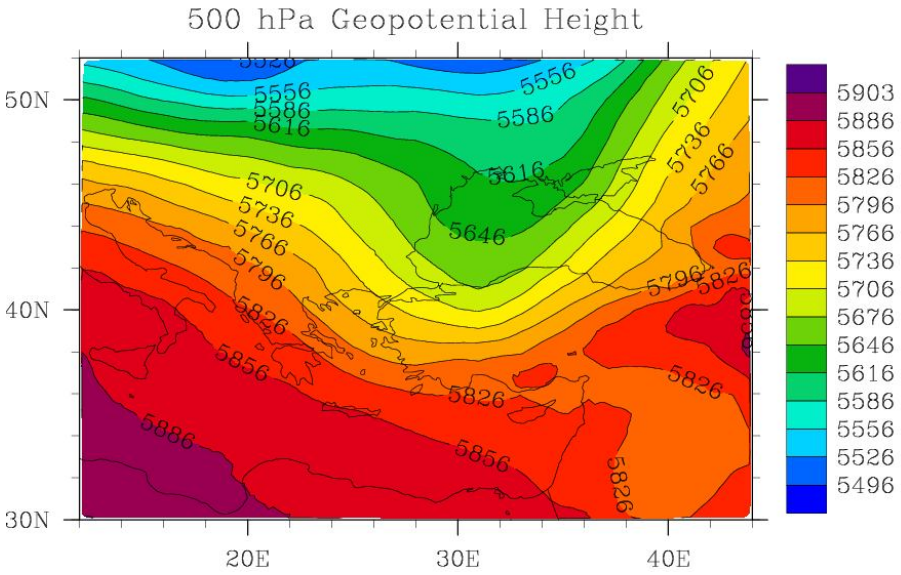

Figure 5.55 : OMEGA 500 hPa Geopotential Height on 7th July 2007.

As a consequence, the model has a quite well performance to represent the pattern of the initial conditions. Initial flow is from the northwest as seen in Figure 5.56. Corresponding to the theory, land breeze occurs early in the morning and continues until at 0400 UTC (0700 LST) and sea breeze begins early in the summer when two real case simulations are compared. It starts on the southeast part of Istanbul at 0600 UTC and an hour later similar feature is seen on the southwest and northeast. That is, the full developed sea breeze structure is seen on both coasts at 0700 UTC (1000 LST). Cross-section from the location similar to the Figure 5.38a is used to determine the urban region contribution to the flow over the southern part of the domain.

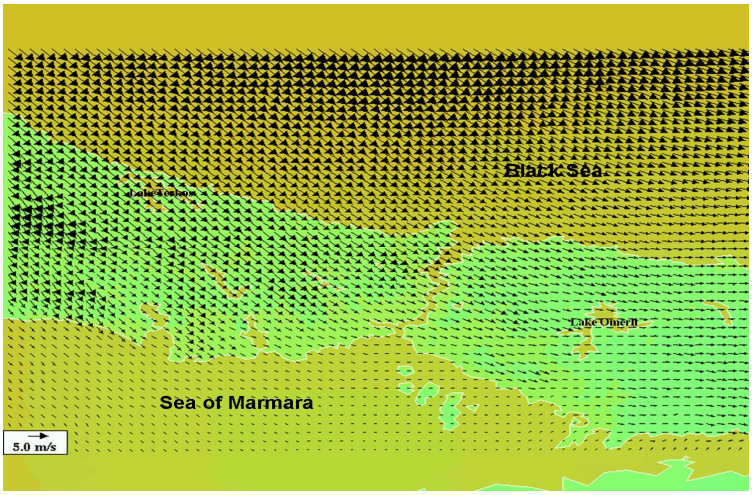

Figure 5.56 : Initial flow of the model on 7th July 2007 at 0000 UTC.

It is observed that strong sea breeze progresses to the inland on the eastern part of the domain (Figure 5.57a). Strong sea breeze locates close to shoreline and it does not penetrate farther inland on the eastern part. However, a weak convergence occurs between the urban and non-urban regions. U component of the wind shows that the sea breeze extents up to 600 m. Above 600 m opposite wind direction is observed up to 1000 m. Two strong positive vertical velocity values, which is the indicator of the rising air motion, are seen on between urban and non-urban boundary. The location where the strong sea breeze invasion occurs is shown in Figure 5.57b.

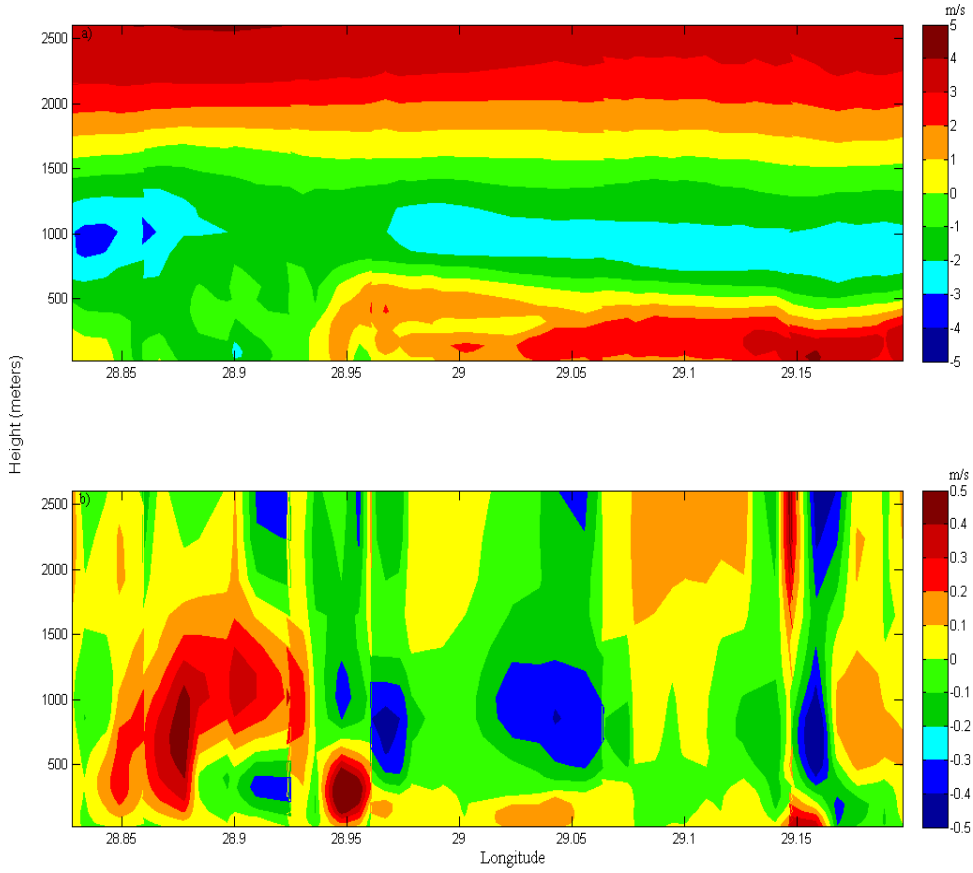

Figure 5.57 : a) U component of the wind and b) vertical velocity on 8th July 2007 at 0700 UTC at 30m.

Beside of the sea breeze circulation, lake-breeze circulation is also observed over the domain. Lake-breeze begins at 0700 UTC (1000 LST) over Lake Omerli and strong sea breeze flows from the north dissipates the lake breeze at 0900 UTC (1200 LST). On the other hand, another large water body, Lake Terkos, has no clear lake breeze type of circulation. Interaction with the Black Sea can be the reason for not seeing a sea breeze circulation over the Lake Terkos since strong sea breeze push the flow

toward the south before the onset of a lake-breeze. If the land is a peninsula or an island, sea breeze flows on both sides propagate to the inland and face at some point over the domain, which results in a convergence zone. Relation of the landmass width, geostrophic wind, and atmospheric stability with sea breeze merge is studied by Xian and Pielke (1991). They inferred that landmass width is important at equator for the intensity and spatial scale of the sea breezes whereas the Coriolis force plays a key role at midlatitude. Moreover, they implied that non-zero synoptic flow causes a weak SB due to the weak SB on the windward coast than zero synoptic flow conditions. Existence time of the sea breeze merge in summer simulation is at 0800 UTC (1100 LST) (see Figure 5.58).

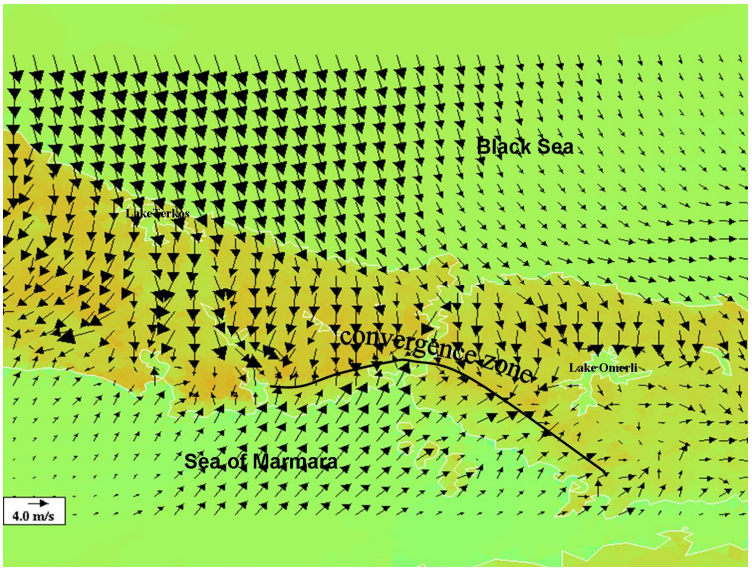

Figure 5.58 : Sea breeze convergence zone on 8th July 2007 at 1000 UTC.

During the sea breeze circulation, the channeled flow is stronger than the winter simulation and strongly channeled flow blows along the straits as seen in the winter simulation with a difference of the advection from wall sides of the strait towards the inland. Occurrence of the channeled flow due to the presence of the island is also seen in summer simulation. The main difference of channeling due to the island is that the time of its occurrence. While channeling occurs during the sea breeze in winter, it is seen during the land breeze circulation early in the morning in summer. Land breeze circulation is seen again at 1900 UTC (2200 LST) in summer but channeling is not observed at this time.

In addition to the spatial distribution of the land-sea breeze circulation, station based surface comparison is conducted for temperature, wind speed, and wind direction so as to evaluate the point-to-point performance of the model for summertime simulation. Diurnal cycle of the temperature is well simulated. Model overestimates the temperature 1-2 ^{o}C at the stations however the estimation amount is 3-5^{o}C at night for Terkoz, and Cavusbasi stations. However, almost all stations have good agreement with observations in general (Figure 5.59).

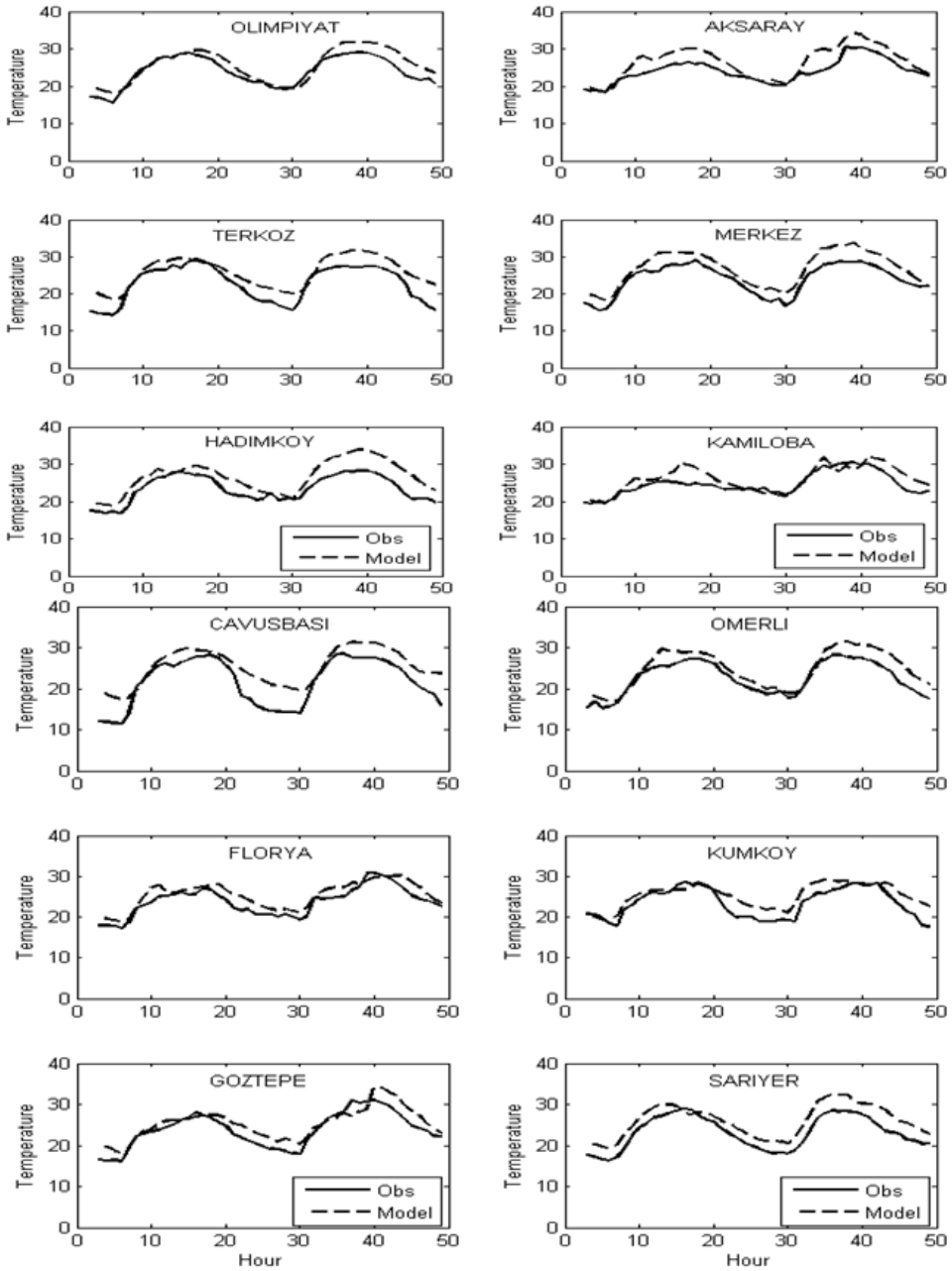

Figure 5.59 : Meteograms of temperature on 07-09 July 2007, solid line is observation and dash line is model results.

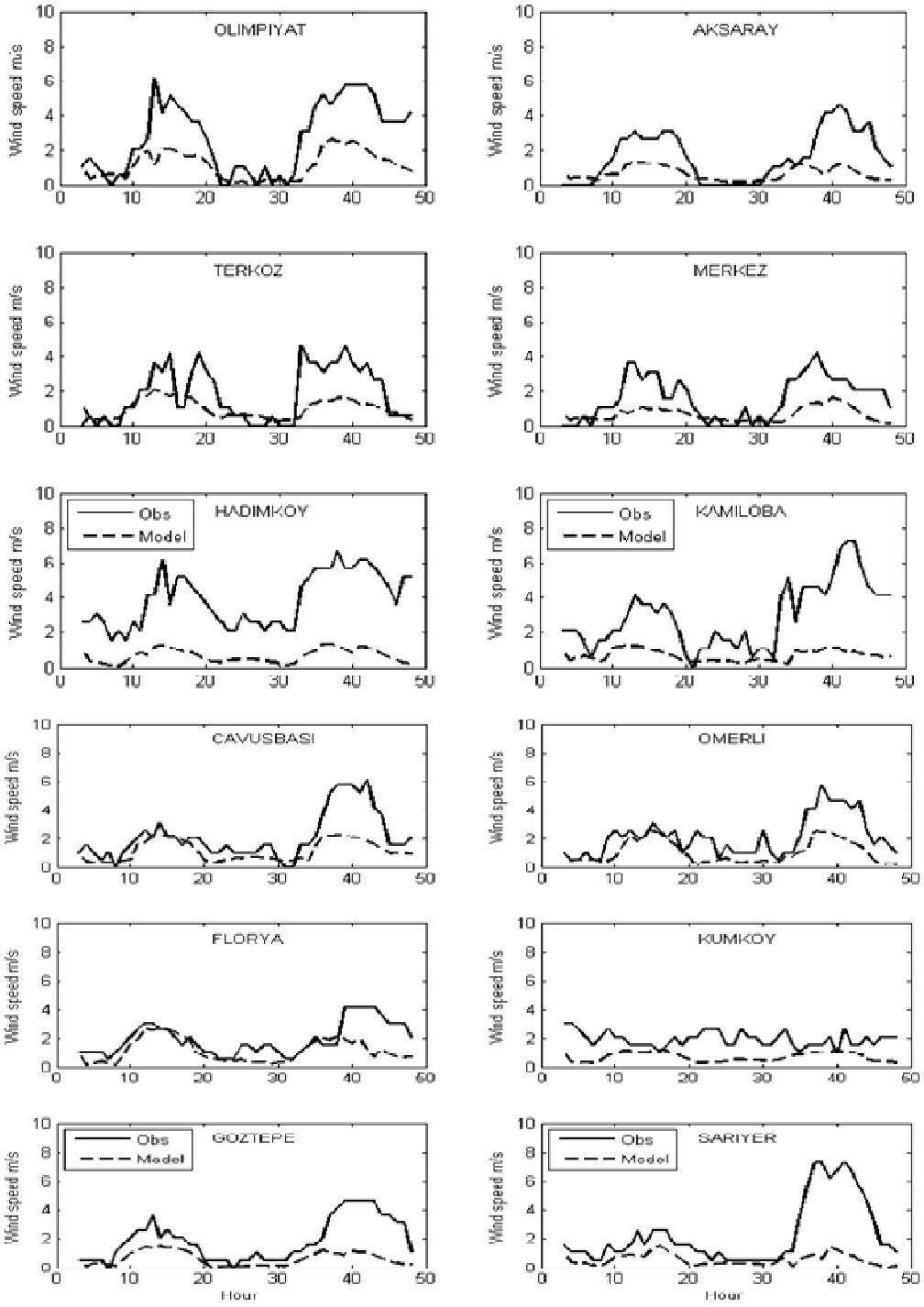

Figure 5.60 : Meteograms of wind speed on 07-09 July 2007, solid line is observation and dash line is model results.

Model underestimates the wind speed at some stations, especially; the amount of underestimation at inland stations is more than the coastal stations such as Hadimkoy and Kamiloba. The resolution difference between the model cell locations and the height difference between the model and observation stations might be responsible

for the difference in wind speed. However, Goztepe and Sariyer stations have a quite big difference on the second simulation day. The increase in the wind speed and variation on the wind direction is good indicators of the sea breezes. The wind speed rise is seen early in the morning on both model and observation. Also, difference of the onset time of the sea breeze between the north and south can be seen from Figure 5.60. Sea breeze blows at 0700 LST at Kumkoy station at north while it starts at 0900-1000 LST at Goztepe and Florya stations at south.

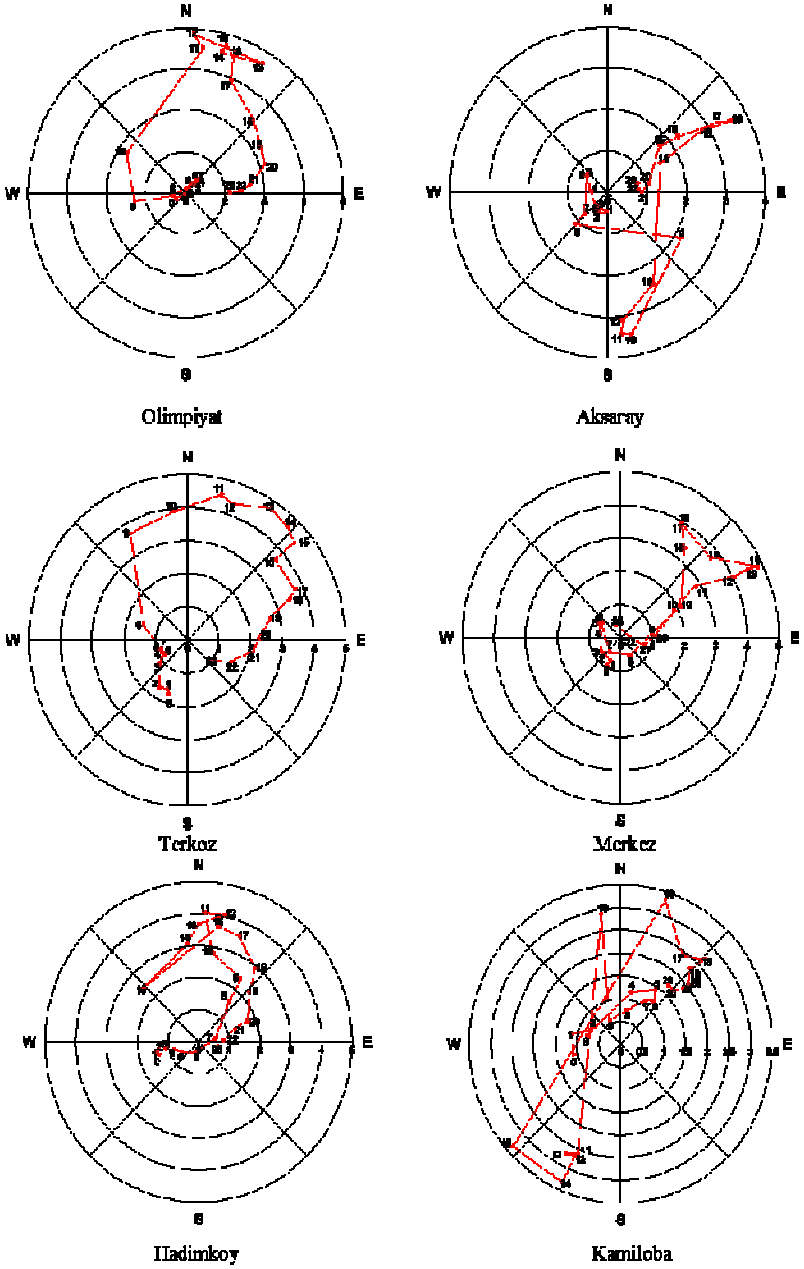

Figure 5.61 : Model hodographs of AWOS stations on 08 July 2007.

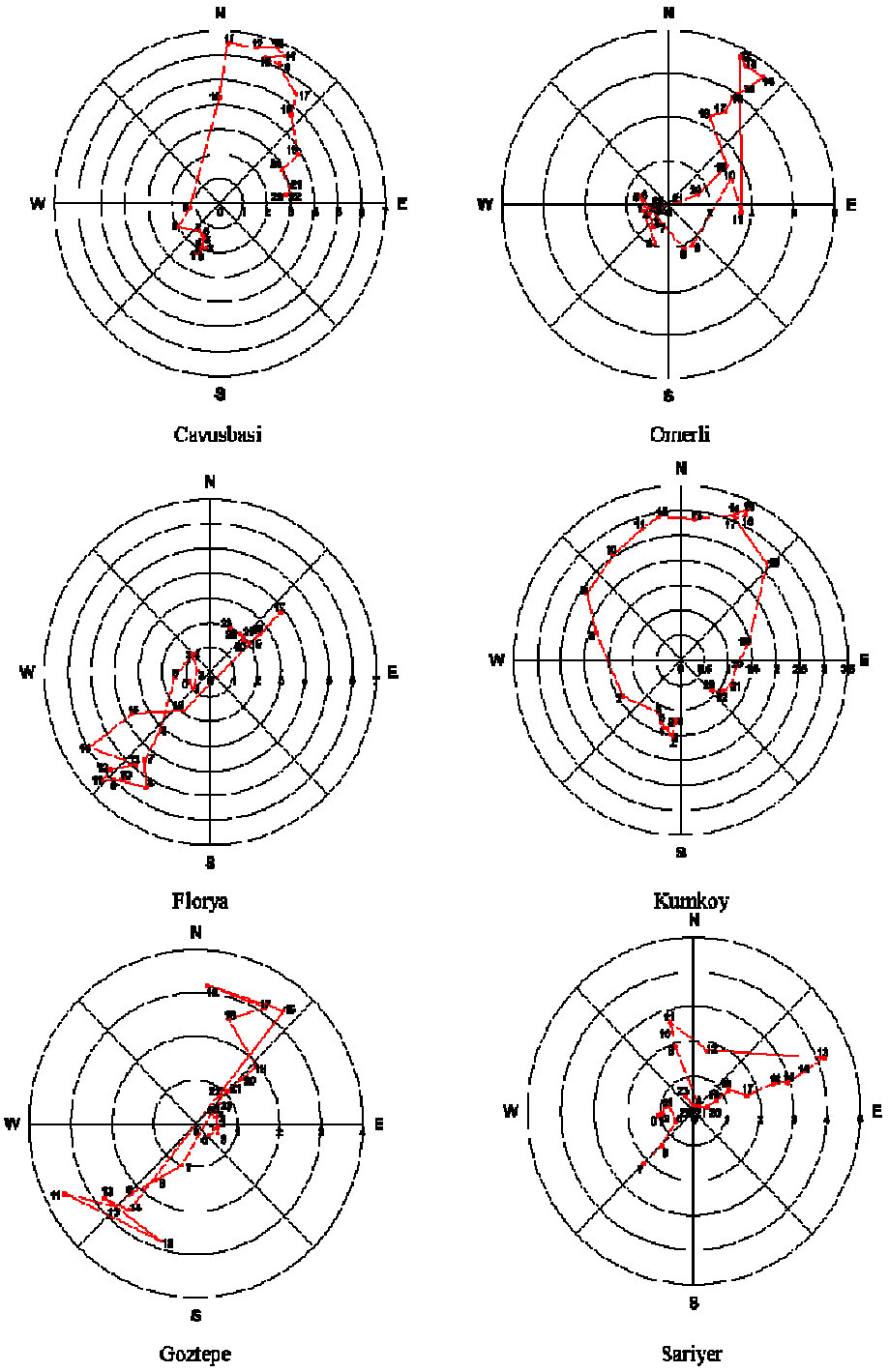

Figure 5. 61 (contd.) : Model hodographs of AWOS stations on 08 July 2007.

The wind direction shows the rapid changes during the day, which can be more than 300 degree. This difference between the model and observation is because the first layer of the model data is at 30 m. Figure B.1 shows the comparison between observations at 10 m and model at 30 m. In addition to this shortcoming, coastal

stations (Kumkoy, Sariyer, Florya and Goztepe) have no observation values on most of the day, which makes the comparison difficult to determine the onset time of the sea breeze. On the other hand, even though it is not possible to deduce the general direction changes from one or two measurement point, available measurements show the similar sea breeze onset time.

Hodographs for summer simulation shows the similar rotation directions with winter simulation at some stations while the shape of the hodograph is generally different. The most noticeable feature is circular shape of the hodographs at Kumkoy, Terkoz and Olimpiyat stations (Figure 5.61). Another noteworthy difference is the rotation of the hodographs especially, at the coastal stations (Kumkoy, Sariyer, Florya and Goztepe). Rotation is clockwise at Kumkoy and Sariyer stations in summer simulation while it is anti-clockwise in winter. Stations at the exit of the Bosphorus (Goztepe and Florya) show complex rotation directions in summer; however, they are clockwise in winter. Besides, inland stations Merkez and Aksaray have anti-clockwise rotation in summer while it is clockwise in winter. Common wind direction at the exit of the Bosphorus is bidirectional (i.e., northeast–southwest) on both winter and summer simulations, which shows that the flow is channeled. Since it is considered that Istanbul has a smooth territory, it can be concluded that the main reason for the different rotation of the hodographs is because of the atmospheric conditions. Onset of a land-sea breeze circulation is sensitive to the large-scale flow over a region. Moreover, shape of the shoreline also plays a key role for coastal stations.

6. RISK ASSESSMENT STUDY for The STRAITS of ISTANBUL and CANAKKALE

Hazardous atmospheric releases are dominated by atmospheric flows of a spectrum of scales (i.e., microscale, mesoscale and global scale). These flows possess various time and space scales, for example thermal and mechanical forcing causes diurnal cycle circulations such as urban heat island, land-sea breeze, and mountain-valley circulations. Local flow over Istanbul is intended to be understood by conducting idealized and real case numerical studies in the previous part of the study. After gain some insight from these results, it is focused on the pollution distribution over Istanbul. The results indicate that strong northerly flow occurs over the Bosphorus, which is significant since the Marmara region and the Bosphorus and the Dardanelles is the important water way in terms of maritime trade, and they are densely populated areas. Therefore, since the many tanker accidents occur in this waterway, a risk assessment study is conducted in the light of the idealized and real case studies.

During the past three decades, many mesoscale meteorological models have been developed (for example; ETA, MM5, RAMS, WRF and OMEGA) to forecast significant atmospheric phenomena. Afterwards, scientists have been interested in probabilistic calculations. In addition to these studies, some efforts have been spent to add micro-scale effects on the mesoscale models (Chen et al., 2001, Bacon et al., 2001). Urban scale air pollution and air quality modeling approaches are of recent concern such as, toxic releases and hazardous materials that affect human health. In this sense, many transport and dispersion researches were conducted by Warner et al., 2001; Walter and Miller, 2000; Westphal et al., 1999; Boybeyi et al., 1995.

Not only nuclear or biologic explosions causes vital danger during wars but also seeming solely innocent events can result in hazard that maritime material transportation is hidden danger for human. Turkey has an important role for some countries having coastal region near the Black Sea such as Russia, Bulgaria, Ukraine, Georgia and Romania. For transportation and commercial purposes, the Sea of Marmara, 224 km length, and straits, Strait of Istanbul is 31 km and Strait of Dardanelles is 70 km length, have been used as a waterway (Undersecretariat for

Maritime Affairs). These straits are very narrow channels in which navigation is very difficult for tankers, so there have been many accidents that it is very risky for settlements. Approximately 50,000 tankers, which have variety kind of burdens such as, oil, dry burden etc. pass using this waterway in a year and every year this number has been rapidly increased. Figure 6.1a and 6.1b show amount of tankers passed the Straits from 1996-2007. Table 6.1 and Table 6.2 give the amount of annual accidents and amount of annual carriage materials with tankers.

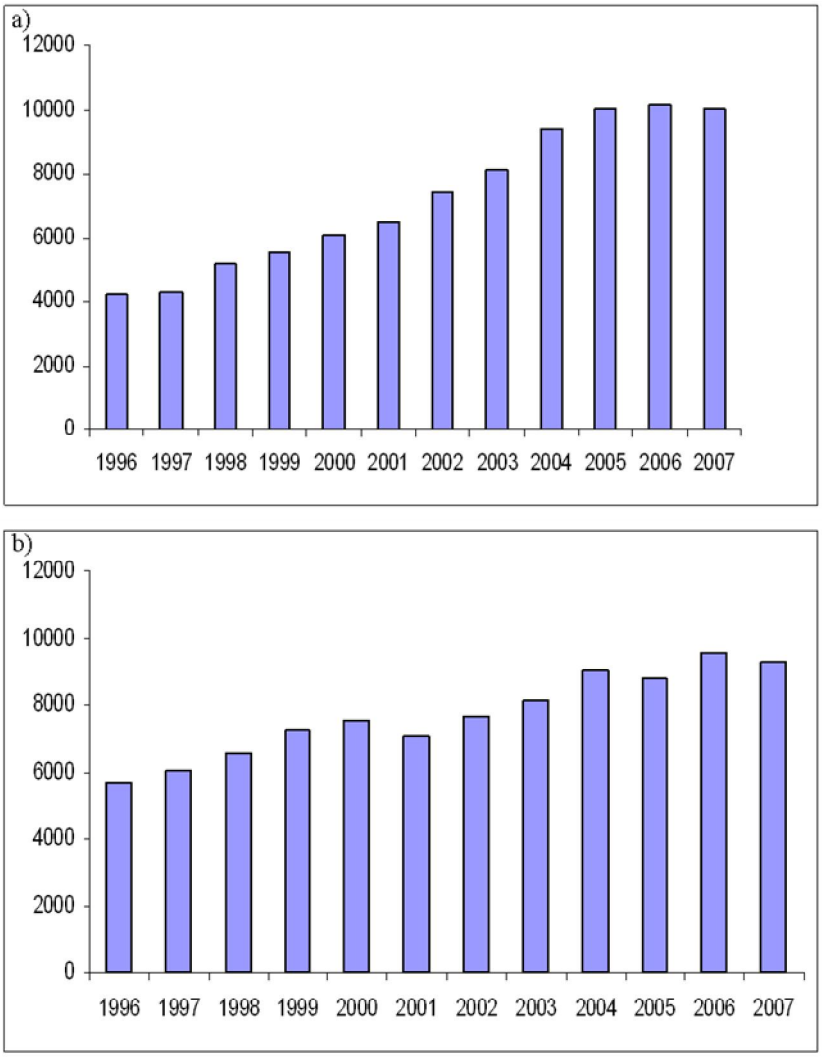

Figure 6. 1 : Number of annual tanker passes with dangerous materials over a) the Bosphorus and b) the Dardanelles Straits.

Mainly, crossing these narrow channels topography, weather conditions and human slips cause accidents in this region. There is a strong need to understand transport patterns of hazardous atmospheric releases originating from an accident in the straits

of Istanbul and Canakkale and the corresponding potential impacts on the region. Since densely populated areas (e.g., the cities of Istanbul and Canakkale) are located on both sides of the channels with approximately 20% of the city population, tanker accidents post great danger to the region's population. Therefore, hazardous material releases from the past and potential future accidents may affect both water and air, and consequently may affect the human health.

Table 6. 1: Amount of yearly incidents (adapted from Undersecretariat for Maritime Affairs)

Year of the incident	Amount of the incident
1999	126
2000	117
2001	131
2002	93
2003	115
2004	151
2005	147
2006	116
2007	117

Table 6. 2 : Amount of Yearly Dangerous Material (adapted from Undersecretariat for Maritime Affairs)

Year	Istanbul (Ton)	Canakkale (Ton)
1996	60.118.953	79.810.052
1997	63.017.194	80.485.711
1998	68.573.523	81.974.831
1999	81.515.453	95.932.049
2000	91.045.040	102.570.327
2001	100.768.977	109.625.682
2002	122.953.338	130.866.598
2003	134.603.741	145.154.920
2004	143.448.164	139.203.656
2005	143.567.196	148.951.376
2006	143.452.401	152.725.701
2007	143.939.433	149.320.062

Even though spread area and concentration of hazardous materials play a significant role in atmospheric transport and dispersion (AT&D) studies, meteorological parameters (such as, wind speed, and direction and atmospheric turbulence and stability) play even greater role in AT&D studies. This may be particularly important when the flow and transport patterns are studied in the Marmara region. For example, over the area of Istanbul, both local scale and mesoscale flows may play an important role in AT&D processes due to the presence of complex topography, urbanization. Therefore, diffusion characteristics may be more important than the transport characteristics.

6.1 Experimental Design

Most of the world population lives in coastal areas. For example, Turkey is one of the countries, a peninsula of about 820,000 km² area, located strategically important geography bounding Europe and Asia continents, surrounded by Black Sea, Marmara Sea and Mediterranean Sea. The most populated region is the Marmara region with 67,000 km^2 area that has two straits, Istanbul (Bosphorus) and Canakkale (Dardanelles) Straits (shown in Figure 6.2).

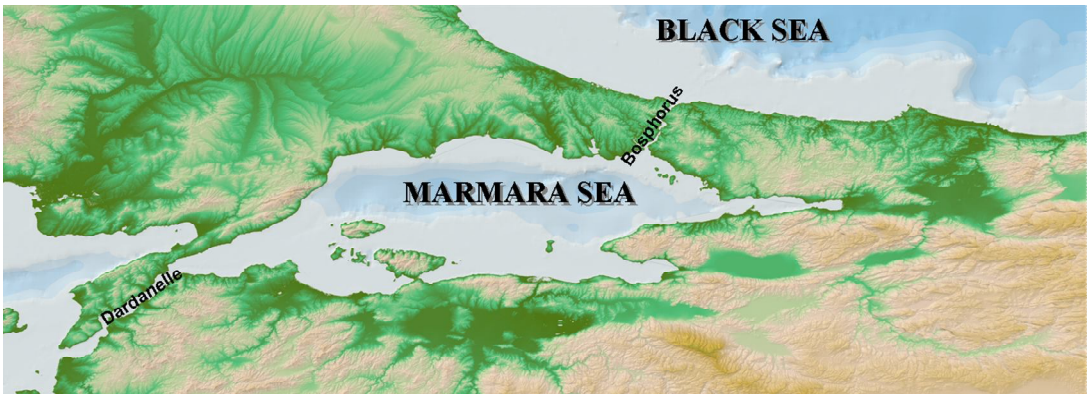

Figure 6. 2 : Map of study area (visualized from 90m resolution SRTM data).

Mesoscale numerical model OMEGA is performed to determine the risky area after any tanker accident over this significant waterway. The model has a Lagrangian particle AT&D model that can be used either in an embedded mode within OMEGA or an off-line mode using pre-calculated OMEGA meteorological fields as input (Boybeyi et al., 2001). The Lagrangian particle AT&D model is composed of a dispersion algorithm that advects tracers using the OMEGA-resolved mean wind field, while simultaneously solving a diffusion model that simulates the effect of unresolved sub-grid scale turbulence (Yamada and Bunker 1988; Uliasz 1990).

The particle model provides a comprehensive injection and dispersion capability for particles or discrete mass elements. The user can choose to initialize multiple release locations for the particles. The user can also choose the altitude of release, the injection time interval, the start and stop time of the injection, and the number of particles to be released.

The unstructured grid of the model provides flexibility to facilitate the gridding of arbitrary surfaces and volumes in three dimensions (e.g., to terrain features). In particular, unstructured grid cells in the horizontal dimension can increase local

resolution statically to better capture the important physical features of atmospheric flow. This grid feature provides smooth transition from high resolution where needed to low resolution elsewhere. In addition to the static grid adaptation, the model can adapt its grid dynamically to the evolving flow features and motions. Dynamic grid adaptation increases the spatial resolution only where needed, automatically during run time, thus optimizing the use of the computational resources. The variable resolution and adaptive nature of the OMEGA grid can, for example, adapt to urban plumes, thus resolving the large-scale dynamics as well as the local scale circulations associated with fine scale representation of urban outflow.

6.2 Methodology

The methodology used in this study is based on Probability Distribution (PD) contours for the exceedance of different thresholds for surface dosage field. OMEGA is performed for a full one-year time period (i.e., year 2004). A day is specified for each week to perform 24 hours simulations due to the computational cost of the model. Thus, 106 model runs are conducted for both day and night to represent one-year atmospheric conditions so as to provide inputs to the ADM model. Model outputs are saved every hour for the AT&D model simulations. Since the computational cost is not efficient to utilize the same grid resolution, the model grid statically adapted to the geographical region with a changing grid resolution in 1-2 km to provide finer grid resolution. This feature allows more realistic simulations of local scale circulations, and hence provides a framework to account for their impact on the climatological hazardous material release transport patterns.

Hazard release simulations are performed using the AT&D model. Since different sets of AT&D model runs will be performed, it is more economical to run the AT&D model in off-line mode using pre-calculated hourly OMEGA outputs as input to the AT&D model. From hypothetical release, concentration and surface dosage fields are calculated for different time durations (e.g., 3, 6 and 12 hours). The simulated plumes from these runs are used in examining the impact of plumes on regional scale air pollution.

The PD calculation is conducted by simply tagging concentration calculation cells with either “1” or “0”, depending on whether the value is above or below the specified threshold. These binary numbers are summed over all runs to calculate the

exceedance numbers. Dividing the exceedance numbers by the total number of model simulations provides the PD numbers and PD contours gives the predicted probability of exceedance. This approach allows us to study the impact of plumes and/or puffs originating from any hypothetical accidental release. Atlas of PD contours for different threshold values of concentration and dosage fields can also be created using this methodology.

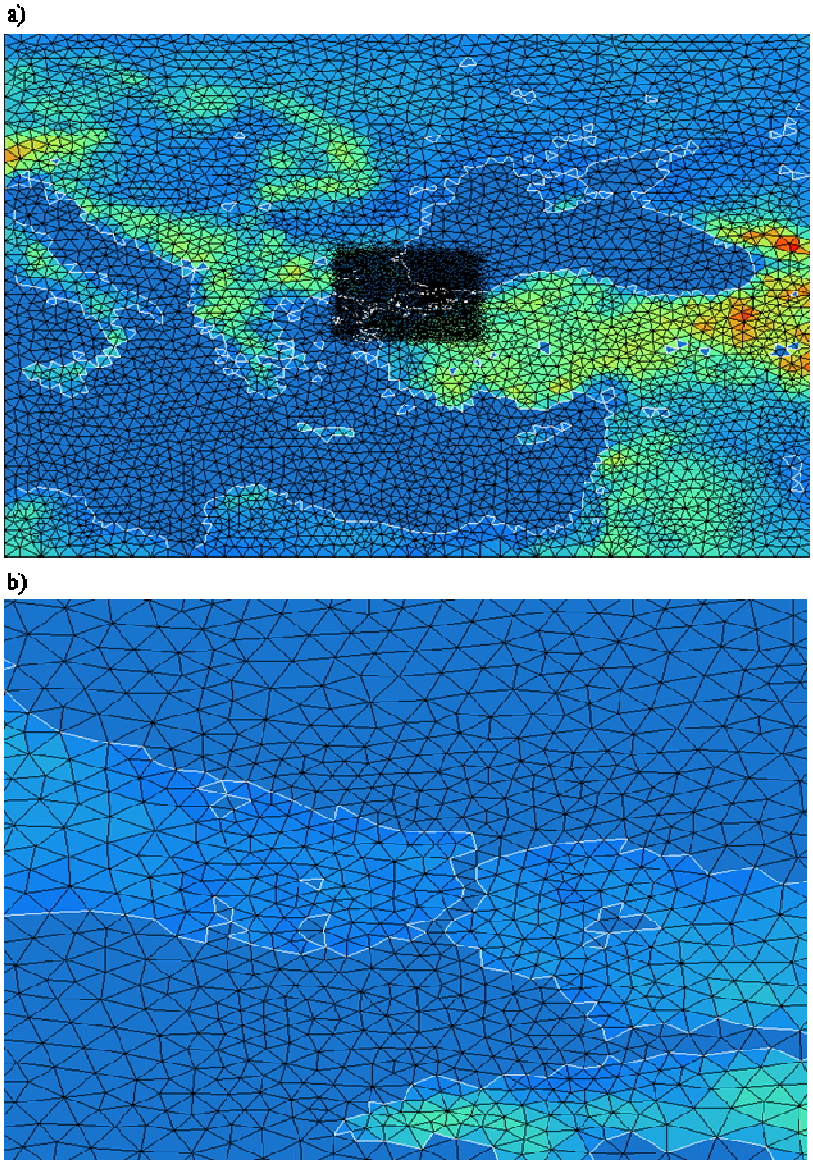

Figure 6. 3 : Mesh structure of the OMEGA simulation domain for risk assessment.

Triply nested grid domain (shown in Figure 6.3) with the course domain locates between the 52.00 ^{o}N-12.05 ^{o}E and 30.00 ^{o}N-44.00 ^{o}E is used in this part of the

study. The grid structure does not change during the simulation and 17802 cells are generated for the mesh. Horizontal grid resolution is for courser grids 60 km and 2 km for the finer grid. 35 vertical layers are used ranging from 30 m to 20,988 m in our model design. Model initial and boundary conditions are prepared from Medium-Range Forecast Model (MRF) gridded data sets from NCEP. OMEGA is used to simulate weekly 2004 to handle meteorological fields, especially wind and turbulence fields to force the ADM.

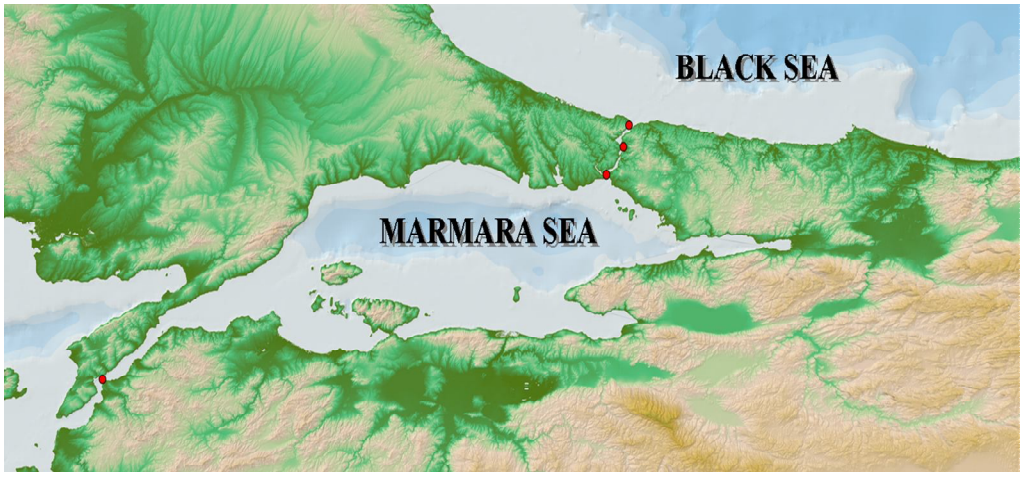

Figure 6. 4 : Release point locations for ADM.

Release point for the ADM is specified based on the reports that show where tanker accidents occur frequently over the domain. According to the reports of the tanker accidents, three locations are determined for the Bosphorus: at the entrance of the channel, in the middle of the channel and at the outflow of the channel and one location is determined for the Dardanalles, the narrowest point, Kilitbahir (Figure 6.4).

6.3 Analysis of Results

Although OMEGA has embedded ADM, each model is performed separately to obtain contribution of the each point on the settlement areas. For the ADM setup, model resolution is defined 500 m. Although many accidents have occurred in this region, there is no measurement or study about release material and amount of release. Therefore, some assumptions are made hypothetically for source strength and threshold values. It is supposed that hypothetically 500 kg pollutants are emitted to the atmosphere after a tanker accident. The risk assessment study concentrates on

the surface dosage which is the time integrated concentration. Release time interval continues instantaneously during the whole simulation time. The ADM simulations are conducted for both day and night time. In this study, particle distribution obtained depending on meteorological conditions provided from mesoscale atmospheric model simulations. Lagrangian particle model, basis of wind parameter, provided from OMEGA model on this research. Wind pattern of the model shows that the dominant wind directions over the domain are from NE and SW for the simulation period. In general sense, NE and SW directions are known as dominant wind directions respectively in wintertime and summertime over the Marmara region. Depending on the wind distribution, the ADM simulations show the NE-SW particle distribution (Figure 6.5). Figures 6.5a and 6.5b include both day and nighttime releases for year 2004.

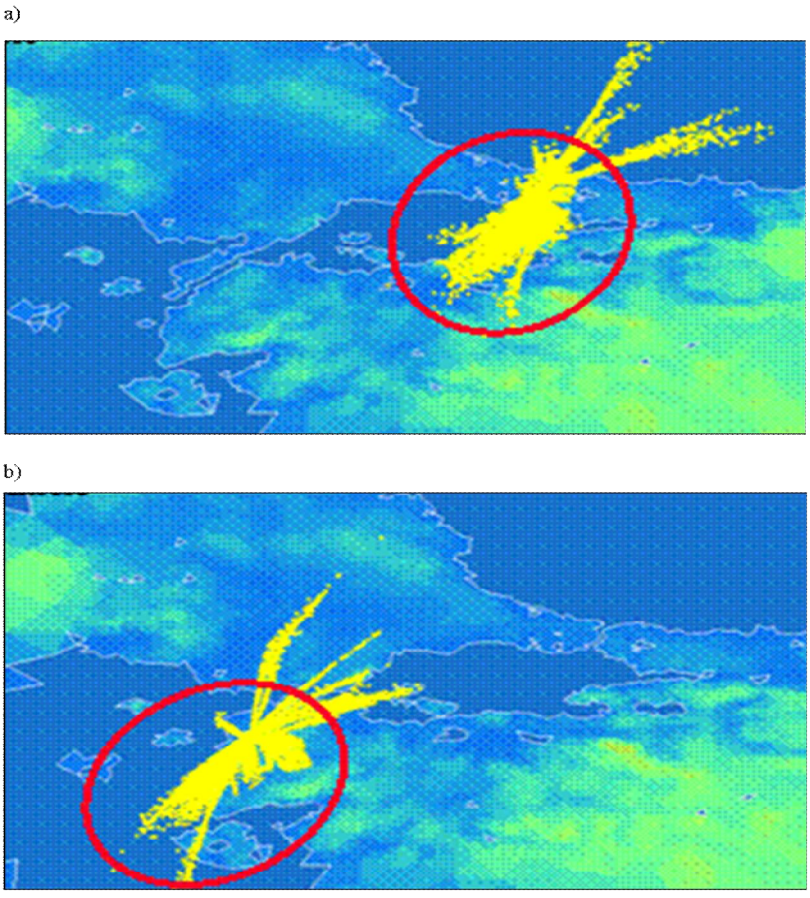

Figure 6. 5 : ADM particle distribution over a) Istanbul and b) Canakkale.

In order to calculate probability of exceedance (POE), surface dosage values from the ADM are calculated based on threshold values; 95%, 80%, 50% and 20%, as

explained in the previous paragraphs. Only second release point results are used for visualization in Istanbul since all release points have the similar distribution for concentration and dosage. Results reveal that the most dangerous regions are located on both sides of the straits which are also the most populated areas. POE indicates the 80% and 50% of plume amount move towards the south of Canakkale and Istanbul. It is encountered less dangerous pollution situations departing from release points.

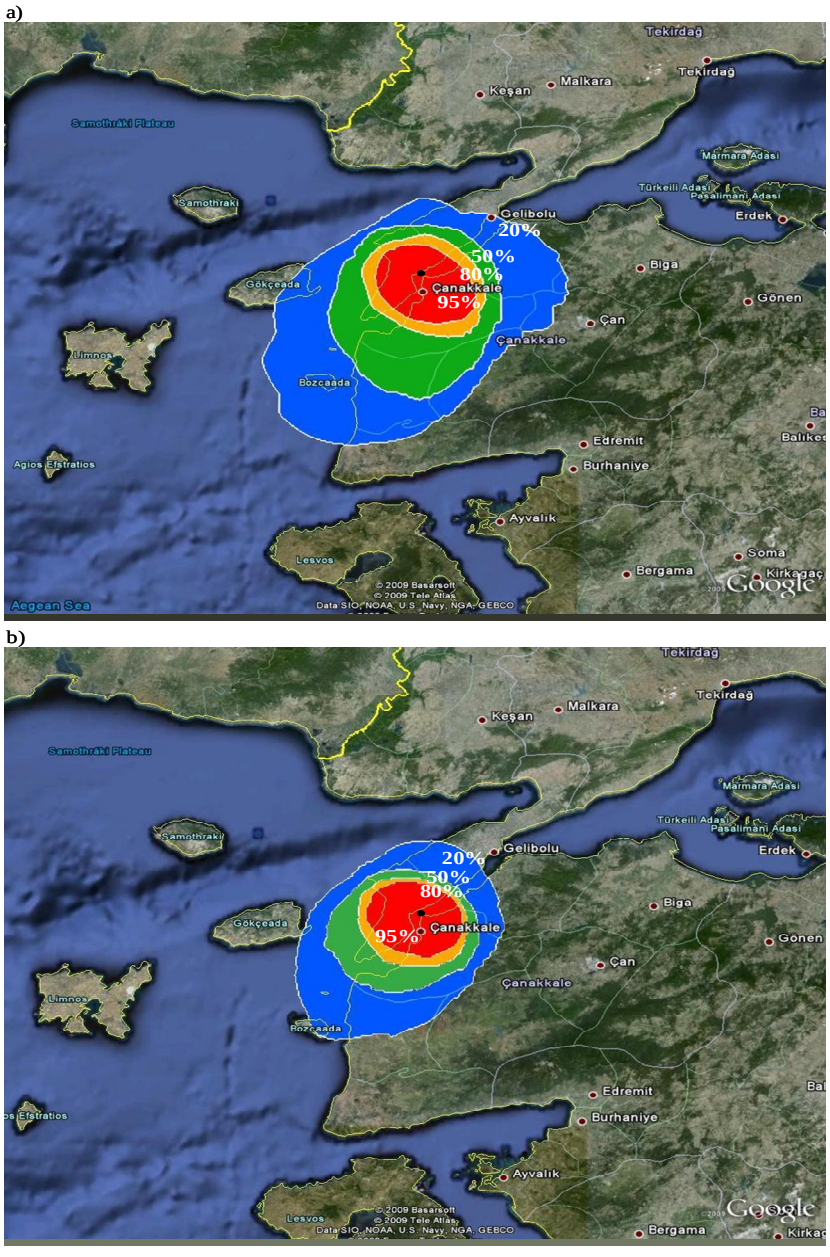

Figure 6. 6 : POE of surface dosage (%) over Canakkale after 3 hour , a) daytime and b) nighttime (black dot is release point).

a)

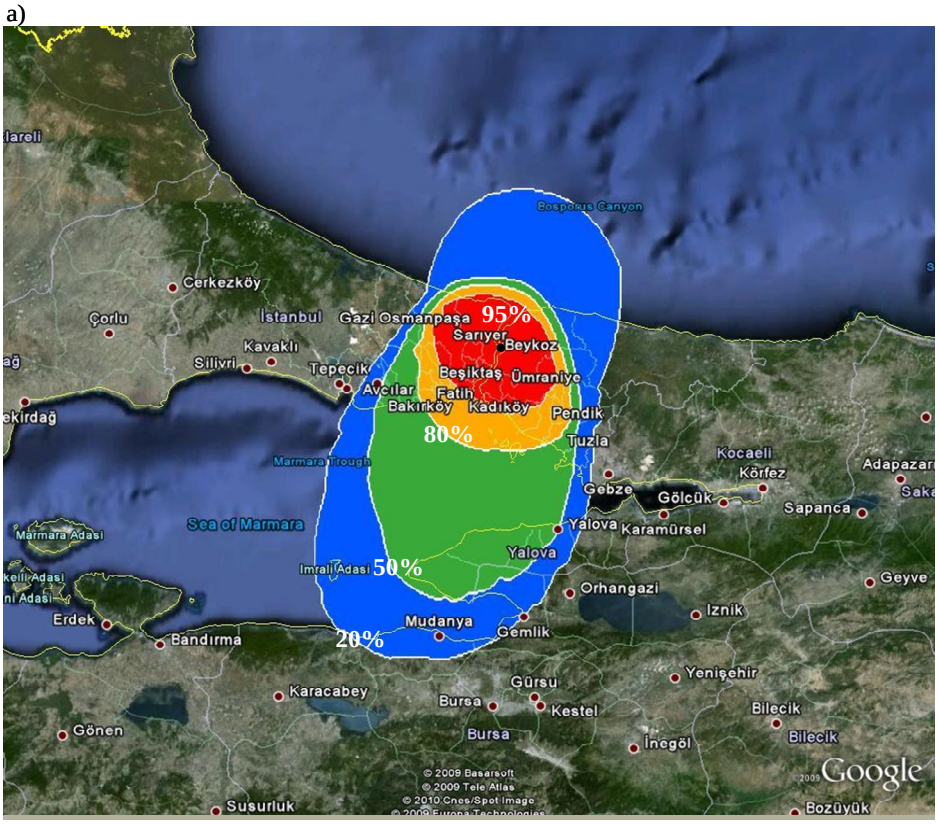

b)

Figure 6. 7 : POE of surface dosage (%) over Istanbul after 3 hour , a) daytime and b) nighttime (black dot is release point).

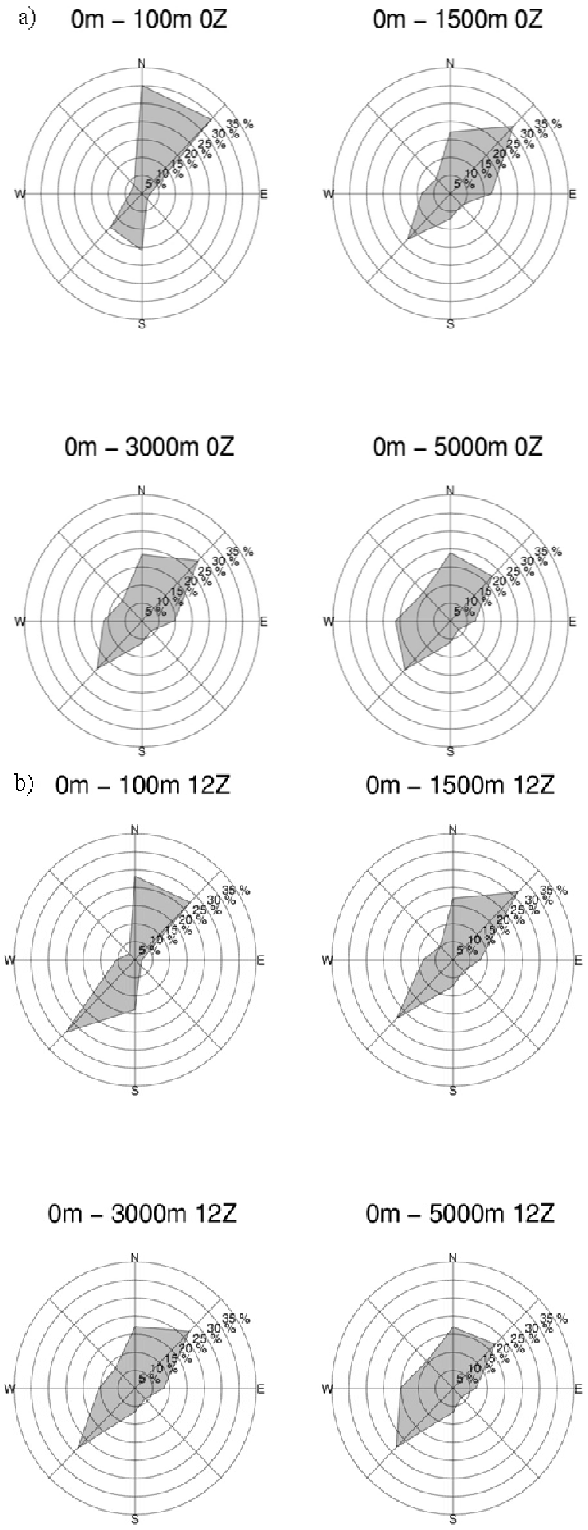

Figure 6. 8 : Istanbul upper-air station wind rose plots for year 2004, a) nighttime and b) daytime.

In this study, model is performed both night and daytime and as seen from Figure 6.6a-b and Figure 6.7a-b. Since three release points show the similar 3 hourly POE

distribution, only second release point, in the middle of the Bosphorus, is given in Figure 6.7. General behaviour shows that the plume spreads more on days while the impact area is very confined (Figures 6.6a-b and Figure 6.7a-b). 95% of the pollutants spread over the domain at night while it attenuates its effects during the day over the Bosphorus. Day and night POE patterns are similar for the Dardanelles. After a tanker accident, pollutants mostly affect the area close to release points.

Validation of the model results is a problem for region since very sparse observation stations are available in this region. Vertical structure of the wind pattern is significant indicator to understand the particle behaviour in the atmosphere, which only Istanbul has a upper-air observation station for validation and hence, comparison in between model and observation can be conducted for only Istanbul. Vertical wind pattern obtained using wind rose at different heights, which showed that NE-SW is also dominant at vertical levels (Figure 6.8a, and 6.8b).

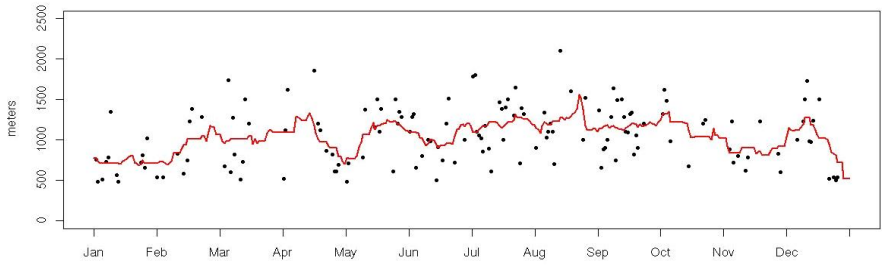

Figure 6. 9 : PBL height plots from observation (dots) and model (solid line).

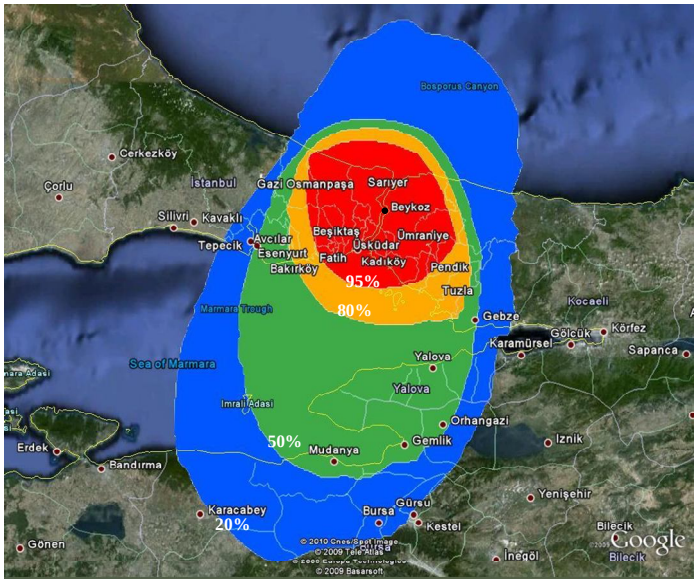

Figure 6. 10 : POE distribution in Istanbul with 50 ton source strength after 3 hour (black dot is release point).

a)

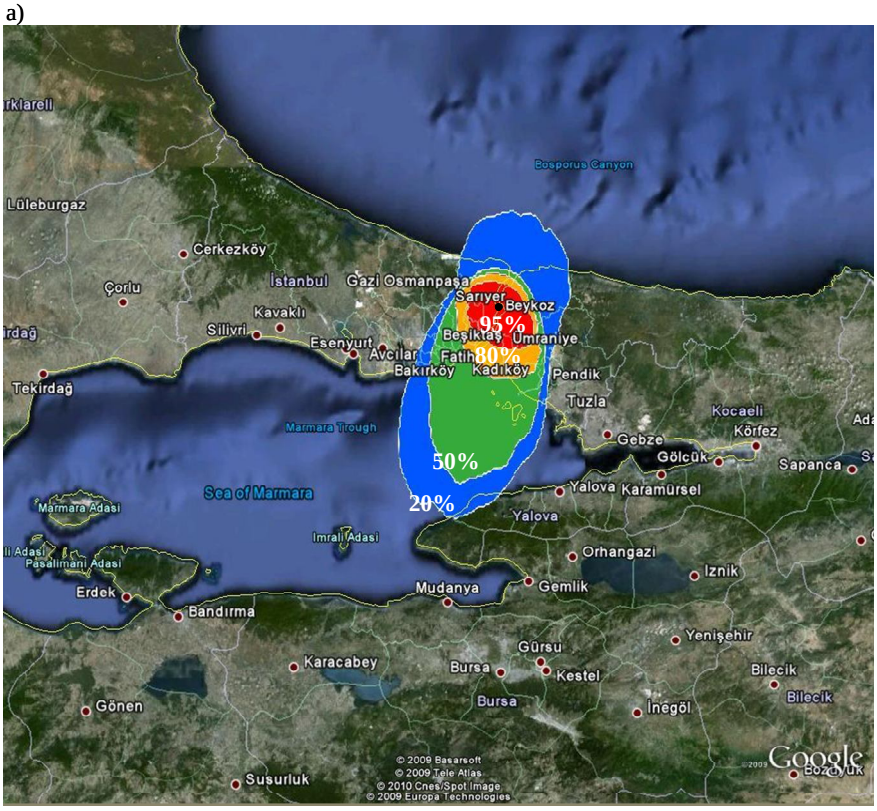

b)

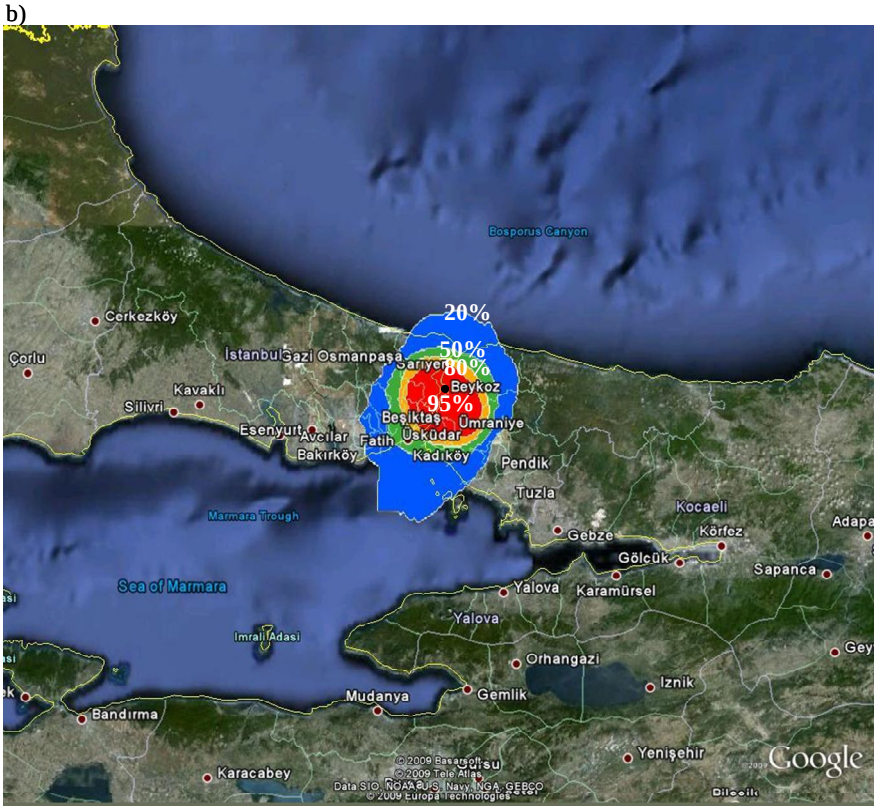

Figure 6. 11 : POE distribution for 10 times increase in threshold values in Istanbul after 3 hour, a) day and b) night (black dot is release point).

Particle or plume transportation in the atmosphere is directly related to atmospheric planetary boundary layer (PBL) which plays a significant role on determining the vertical and horizontal distribution of the plume or particle. PBL can be supposed as a lid, which constrains pollutants and affects pollutant travel structure depending on its height and it also traps particle and causes accumulation of pollutant, which influences amount of air pollution in a region. Figure 6.9 shows that observation and the model PBL heights are in good agreement and the PBL height changing range is in 750-1500 m. Simulations show the predominant northeast-southwest release direction for both straits during the simulation period.

On this research, continuous particle releases are performed in every 20 seconds first and then some sensitivity tests are conducted to understand how plume behaviour reacts against these changes. Sensitivity tests include changes in source strength, release time of pollutants and different threshold values for both concentrations and dosages. When the source strength or time release is increased dosage dispersion area enlarges. For instance, sensitivity run with 50 ton particle release in 24 hours reveals that particles disperses more than the particle release case with 500 kg although the dispersion direction is similar (see in Figure 6.10). If threshold value of concentration and dosage increased ten times, dispersion area of particles decreases as shown in Figure 6.11 and Figure 6.12.

a)

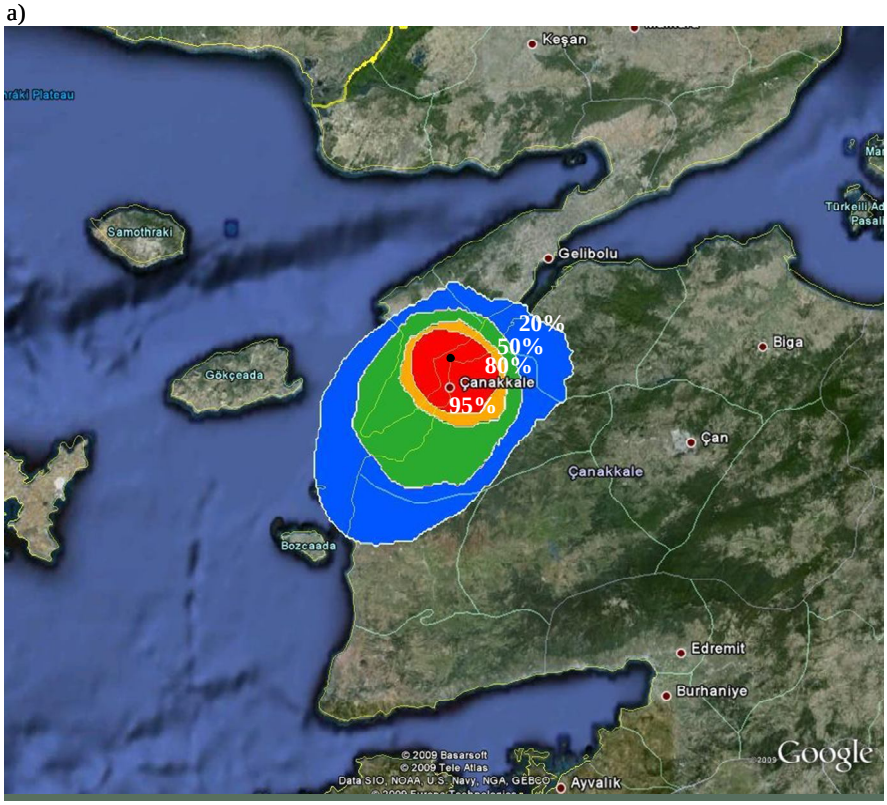

b)

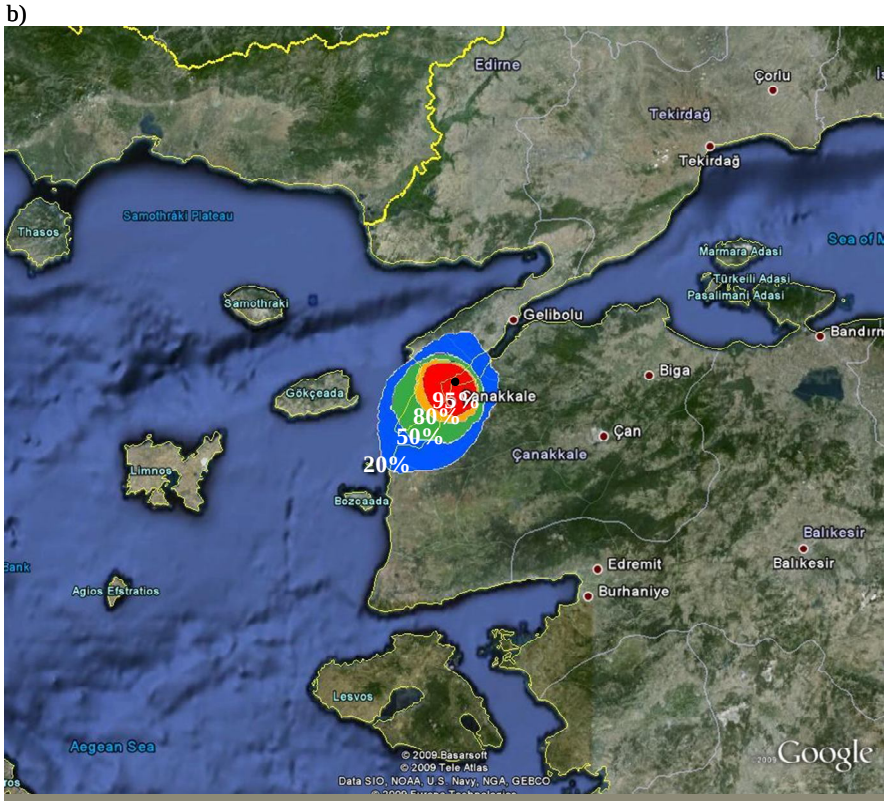

Figure 6. 12 : POE distribution for 10 times increase in threshold values in Canankkale after 3 hour, a) day and b) night (black dot is release point).

7. CONCLUSION and RECOMMENDATIONS for FUTURE WORK

7.1 Conclusion

The first part of the study focuses on statistical and numerical investigation of urbanization in Istanbul. Thermal structures of the urbanized stations (Goztepe and Florya) are examined by using suburban and rural stations on a monthly basis before and after 1980. Non-parametric Mann-Kendall test is applied to the minimum temperature dataset. Sequential Mann-Kendall trend analysis is also used to determine the abrupt change in the trends. Statistically significant positive trends are observed in Goztepe, Florya and Kandilli stations for the period between 1951 and 2004. Spring and summer seasons are found to be have statistically significant positive trends for all stations except Kumkoy stations using seasonal Mann-Kendall test. Analysis of annual minimum temperature differences between urban, suburban and rural stations shows significant positive trends for all pairs when the reference station is taken Kumkoy. However, when the Bahcekoy is used as a reference rural station all pairs except Kirecburnu-Bahcekoy indicate the significantly positive trend. The sequential Mann-Kendall analysis depicts that the starting point of the trend change is after 1980 if the selected reference station is Bahcekoy, however, when Kumkoy is the reference trend starts in 1970. Statistical analysis shows that the urban heat island of Istanbul is developed in summer season.

The atmospheric mesoscale model is also conducted to investigate the urbanization effect on overlying atmosphere. Based on the findings from statistical analysis, the mesoscale model, MM5, is performed for July. Simulation results indicate two surface heat island cells located on the European and Asian sides of Istanbul. The maximum temperature difference for 6 a.m. is around $1^{o}C$ between 1951 and 2004. The two cells merge and spread southward at higher atmospheric levels. The simulations reveal that the urban heating effects penetrate 600-800 m in the atmosphere and a cooling layer is observed aloft. Model results also show the warmer, drier and calm conditions for Istanbul dute to the urbanization.

Statistical and model results give insight about urbanization and its behaviour in the atmosphere. However, Istanbul has considerable complexity because of the narrow strait, its hilly topography, the coastlines and the lakes besides urbanization. It is clear that it is not possible to resolve the important features of Istanbul such as the Bosphorus, some small water bodies and the coastline shape using the MM5 model with 3 km spatial resolution. Therefore, another mesoscale atmospheric model, OMEGA, which better captures the coastal and mountain areas, is performed in the second part of the study.

One of the major goals of this part of the study is to understand the local flow contribution to the particle dispersion since the flow in a region is affected by wide range of scales and also their interactions with each other. Therefore, the topography and terrain induced mesoscale circulations and their contribution to the local circulation is the other concern for the study area. Istanbul and its outskirts are chosen as a study region for this part of the study because of twofold: first and important one is the dense data network availability relative to the other coastal cities. Second, Istanbul is the most crowded city in Turkey thus, the quality of the life is affected by means of the local circulation, for instance many people can suffer from air pollution as a result of the changed circulation characteristics either because of the geographic features or growing build-up area. Therefore, understanding contribution of the mesoscale circulations to the local flow in Istanbul makes this study noteworthy.

Geographic location of the city is complex since the city is surrounded by two seas from the north and the south, the Black Sea and the Marmara Sea, respectively. Moreover, the Bosphorus splits the city into two parts. Orientation of the city and its mixed size lakes make convenient to study sea-land breeze and lake breeze circulations. Besides, increasing population in Istanbul (according to the recent population report, approx. 10 million people live in the city) makes necessity to investigate the urban heat circulation and its interaction with other mesoscale circulations and possible effects of those on the lives of people. The well-known properties of the urban heat island are increasing heat capacity of the city due to the changing albedo and increasing roughness length due to the increasing building height which affect the flow characteristics over a city. All these properties result in sultry weather conditions with increasing temperature and decreasing wind speed.

Additionally, the more population brings the more air pollution with growing urbanization. As known the sea breeze circulation provides better conditions for human life in contrast to the inconvenient conditions due to the urbanization. Moreover, interaction of the sea-land breeze and the urban heat circulations is inevitable for the urbanized coastal cities. Thus, flow cycle of the sea-land breeze circulation may cause the heavy pollution due to the reversible characteristics of the flow depending on the diurnal cycle. All those reasons indicate the necessity of investigation of the flow features in Istanbul. Therefore, local scale circulation in Istanbul is investigated by using a mesoscale model with new mesh generation technique.

In order to investigate the mesoscale circulations, two different types of simulations are performed. These simulations are named as idealized and real case simulations during the course of the research. Idealized simulations are conducted to analyze contribution of each property of the geography and atmospheric flow condition, individually. In other words, within these simulations each change is applied to the model one-by-one. By doing so, the only modification is applied to the model. For instance, in order to investigate only the effect of the Bosphorus on the region while the other properties are kept constant, the Bosphorus is added to the domain. Another property such as topography effect is studied by utilizing the model topography and the flat topography. In addition to these geographic modifications, changes of the initial flow conditions are studied by keeping current land-use/land cover properties as a model land-use map while changing geostrophic wind direction. Hence, all the possible combinations for the domain are conducted adding each of them to the model. A series of numerical experiments are performed to examine the role of the surface induced mesoscale circulations and initial flow features on the local scale circulation.

The analyses focus on investigating the flow characteristics over the strait and the land. The results of the numerical experiments suggest that the presence of a channel or strait affects the flow and delays the onset of the sea breeze over the strait. However, the sea breeze moves fast through the strait from both edges due to the increase in land-water temperature gradient. Moreover, the life span of the sea breeze is short on the flat-strait case. On the contrary to the flat surface simulation with strait, the flat surface simulation without strait shows the re-current circulation on the

upper model layers. Since the studied domain is surrounded by two water bodies, it is common to observe the convergence zone somewhere at the domain due to the merge of two sea breezes. Flat-strait run demonstrates the first convergence over the strait at 0800 UTC. However, fully developed convergence zone occurs at 0900 UTC over the domain for the flat case. In addition to those flat surface simulations, another test run is performed with strait using topography which is generated by the OMEGA model. As it has been implied by many scientists, topography may influence the circulation in a region. If the rough topography is under consideration, differences in the circulation can be obviously attributed to the orography due to the upslope-downslope or upvalley-downvalley circulations. Although it cannot be expected that a city with smooth topography such as Istanbul would have a significant effect on the circulation, still topography in Istanbul gives rise to changes on the flow characteristics. The sea breeze circulation starts at 0700 UTC for the flat-strait case while it is at 0600 UTC on the topography case with strait. Topography attenuates the inland penetration and the intensity of the southerly sea breeze over the strait. Actual land-use types and all the geographic features are implemented into the model by using the similar background flow in order to infer the effect of the more realistic conditions. The land-use data presents the urbanized region on the south of Istanbul. Therefore, the presence of the urban area provides enough temperature gradient between land and water that causes the early onset of the sea breeze on the south of the domain. Furthermore, the northerly flow over the strait is fast on this case while the southerly sea breeze is weak. Meanwhile, information of the prevailing wind directions over the domain, which is obtained from observations depict that the northeasterly and southwesterly directions are dominant over the domain. It is essential, therefore, to conduct a numerical simulation with southwesterly wind direction as a second significant wind direction. Therefore, another test case is performed for actual land-use type under the southwesterly wind condition. This study indicates that onset time of the sea breeze starts early. In addition, the northerly sea breeze is strong in all cases over the strait starting at late in the morning. Convergence occurs due to the merge of two sea breezes in all simulations and the existence time of the convergence is at 0800 UTC for all cases except for the uniform flat surface without strait. The more striking feature over the strait is the persistent strong northerly flow which starts early at noon over the domain. The presence of the

strait channelled the flow through the strait. Moreover, topography positively contributes to the channelling.

The general flow characteristics over the land are similar to the flow over the strait. The onset of the sea breeze is observed in the morning and later northerly and southerly sea breeze meet. Then after, northerly flow overwhelmed the southerly sea breeze. Hence, persistent northerly flow blows over the domain. However, the northerly flow turns to the southerly at late afternoon. Additionally, convergence due to the sea breeze merge indicates the general behaviour that it occurs at 0800 UTC over the domain for all the cases except for the uniform flat case. Although main properties are quite similar, there are also discrepancies between the flow over the strait and land, hidden in details. First of all, progress of southerly sea breeze is farther inland towards the land which produces strong winds keeping the temperature gradient high. Another difference is observed on the channelled flow. Even though the flow over the land is northerly starting at early noon, it is not strong as much as over the strait, which is the indicator of the channelling. Simulations with current land-use data which present the effect of urbanization on the local flow show the difference depending on the location. Southerly flow is dominant in the morning over the land since the urbanization keeps the land warm even early in the morning.

Furthermore, even the east and west parts of the domain behave in a different manner. The continuous southerly wind at north in the morning, which represents the land breeze blows, start from far inland on the eastern part of the domain when the actual land-use data is utilized in the model. It is believed that downslope-downvalley flows affect the flow over the region since the topography is relatively smooth on the western part of the domain. Also, it should be noted that the land-use types are differerent on the east and west of the domain. However, the west part of the domain allows the stronger northerly wind than the eastern part due to the topography difference. In addition to the terrain difference and land-use difference, the islands on the southeastern part also contribute to the local flow due to the channelling effect between the mainland and small islands.

All the sensitivity simulations exhibit that urbanization changes the flow characteristics. If the background flow direction is considered, characteristics of the sea breeze circulation are affected by the urban-induced circulation. Both northeasterly and southwesterly winds contribute to the onset of the sea breeze in the

southern part of the domain. Moreover, urbanization affects the characteristics of the sea breeze such as, existence time and duration of the sea breeze circulation. The sea breeze duration is 8 hours on the east of the domain under the northeasterly flow while it is 3 hours for the southwesterly condition. However, it is 8 hours at west of the domain both for northeasterly and southwesterly wind directions. In addition, the northerly background wind attenuates the southerly sea breeze while the southerly flow enhances the southerly sea breeze flow by means of the urbanization. Hence, it is deduced that interaction between large scale flow and urbanization change the local flow characteristics. Onshore large scale flow allows the land breeze to occur on the north part while there is no effective land breeze occurs on the south part of the domain. Offshore large-scale flow on the south, where the urbanization is dominant, prevents the onset of a land breeze circulation since urbanization keeps the surface warmer as observed in the morning. Hence, temperature gradient does not allow onset of the land breeze over the urban region. However, a strong land breeze circulation can be observed on the north under offshore flow condition.

Inland penetration of the sea breeze is affected by the presence of the urban areas on the south of the domain. A convergence exists over the urban region due to the urban heat circulation and southerly sea breeze meeting. The flow is from the non-urban to the urban region contributes to existence of this convergence before existence of the convergence due to the merging of the two sea breezes. Thus, the urban area traps the sea breeze and prevents it to progress into farther inland. Therefore, the sea breeze only affects the very narrow area on the south of the domain in the early morning while the sea breeze on the north penetrates more inland under the southerly flow condition. The sea breeze penetrates more inland on the south however, it occurs very close to the northern shoreline on the north under northerly flow condition. It is concluded that onshore initial flow conditions provide onset of the sea breeze close to the shoreline since contribution of the urbanization increases the temperature gradient while offshore flow provides extended inland penetration of the sea breeze due to the decrease in temperature gradient. Opposing circulation or re-current circulation over the sea breeze, observed from the sensitivity simulations, is another significant feature in terms of the pollution transportation and distribution over the region.

By keeping findings from sensitivity simulations in mind, research is extended to real case simulations; two simulations are performed which are representative of the specified summertime and wintertime circulation characteristics of the local circulation. These two cases determine the basis of existence criteria of sea-land breeze and urban heat island circulations. The OMEGA model simulates the large-scale patterns quite well for both cases while it underestimates the magnitude. Land breeze is observed until late in the morning and onset time of the sea breeze is 0900 UTC (1100 LST) for specified wintertime simulation. As it is found from the sensitivity simulations, the sea breeze first starts on the south of the domain due to the urbanization effect. However, although sea breeze delays on the north part, it moves fast. Urbanized region prevent to inland progress of the sea breeze as it is also found on hypothetic simulations. Convergence zone where two sea breezes encounter is observed at 1300 UTC (1500 LST) on wintertime simulation whereas the time for convergence occurrence changes between 0800-0900 UTC (1000-1100 LST) in the sensitivity simulations. Lake breezes can be observed at 0900 UTC on two big lakes (Lake Omerli and Lake Terkos). The land breeze starts first on the south due to the warm urban region. Two channelled flow over the region is observed; one is located over the Bosphorus that is also found on the sensitivity simulations and the second one is located in between the mainland and islands. Roughness length difference is the forcing mechanism for the channelling flow.

The results for summertime simulation show that the sea breeze begins at first on the south as found on the wintertime simulation. Yet, onset time of the sea breeze is at 0500 UTC (0800 LST). Fully developed sea breezes over the domain and also a lake breeze on Lake Omerli are observed at 0700 UTC (1000 LST). However, no lake breeze circulation is observed on Lake Terkos since the strong sea breeze prevents the occurrence of a lake breeze. The merging time of the sea breeze is at 1000 UTC (1300 UTC) on the specified summertime simulation. Moreover, the flow over the Bosphorus is strong in the summer simulation.

A series of comparisons is analyzed between results of simulations and meteorological observations for temperature, wind direction and wind speed. Comparisons show that the OMEGA model simulates daily temperature change but, it overestimates the temperature. The OMEGA model underestimates the wind speed but the order of the magnitude matches with the observations. Results of wind

direction from the simulations at the observation stations do not show any systematic behaviour. However, at some observation stations a sudden change on the wind direction, which is one of the indicators of the sea breeze circulation, is observed.

Hodographs at the surface are plotted for both simulations to understand the flow rotation. The wind shows clockwise and anticlockwise rotations over the domain with bisectional and non-elliptic shape of the hodograph. Since hodographs on both winter and summer simulations depict different flow rotation, it is concluded that large scale flow has dominant effect on the flow rotation. Beside, the shape of the shoreline also influences the rotation of the flow. The different shapes of the hodographs might result from orography and shape of the shoreline even though study domain has no steep terrain.

Another goal of this study is to determine the air pollutant pattern after any tanker accident over the Marmara Region through the narrow Dardanelles and Bosphorus straits. Increased number of shipping throughout the strategically important waterway has heightened fears of a major accident which could have serious environmental consequences and endanger the health of the residents. The main purpose of this study is to prepare a map of the mainly risky areas in the case of an accident. This map is obtained by calculating the probability of exceedance of concentration and dosage values at the surface from the Atmospheric Dispersion Model (ADM).

The OMEGA model, which is a fully non-hydrostatic, three-dimensional prognostic model based on an adaptive, unstructured triangular prism grid, has been used extensively in this research. Embedded ADM in OMEGA provides to work on transport and diffusion of air pollutants using either Lagrangian or Eularian dispersion techniques. Since the movement of the pollutant is governed by atmospheric motion, it is essential to provide information about atmospheric motions. This information can be obtained either from meteorological observations or atmospheric models. As the meteorological observations are not enough to represent the general state of atmosphere due to the coarse temporal and spatial resolution, meteorological models are mostly used to obtain the wind information and the turbulence field.

Although OMEGA has capability to run the ADM as on-line and off-line modes, off-line simulations are performed to analyze the behaviour of each specified release

point where a tanker accident mostly occurs throughout the Straits. ADM requires information of the amount of the released material and its duration in addition to the location information of the release points. Since there is no source strength or released material information or measurement available, some assumptions are applied to the ADM. Particle distribution from the release points is obtained by using forward trajectory method based on Lagrangian technique. Amount of surface concentration and dosage over the study domain is calculated so as to contour the POE for the Straits to map the risky areas. The POE calculation bases on the count of the number of maximum concentration and maximum dosage. Contour maps are prepared based on 95%, 80%, 50%, and 20% probability values.

Results demonstrate that if any accident occurs the path of the pollutants is dominantly towards the south-southwest direction. Wind rose from the observation reveals the bidirectional (NE-SW) wind direction on both day and night. In addition, a similar behaviour of the flow is observed with altitude. The main direction of the flow over both straits shows similarities. The most risky area is close to the release points. However, concentration or dosage looses its intensity when moving away from the release points. As there is no information for source strength, sensitivity runs are conducted to analyze the effect of an increase in the amount of source. For this purpose, the ADM is forced setting the source strength to 50 ton for a chosen release point. Sensitivity runs show the enlarged concentration and dosage contour pattern with increasing released material after a tanker accident while shape of the pattern is same. It is also found that POE is also sensitive to the threshold values.

The study is conducted for only year 2004 due to the computational cost of the model. Observational upper-air data analysis shows that these results can be expanded to explain the general behaviour of pollutant distribution since five-year observation datasets give flow characteristics similar to year 2004. The PBL height, which is important so as to determine the particle trap height, also shows monthly changes between 750 m-1500 m during the simulation period. The originality of this study is that it can provide a view to decision makers to make regulation in terms of public health. Although this study has no information for emergency response because of the computational cost and input data requirements to the model, it gives the general view of particle distribution when any incident occurs.

7.2 Recommendations for Future Work

Strategic significance of the Straits and dense population on the coastal cities make the investigations noteworthy. The fundamental mechanism providing dispersion of air pollution is the atmospheric motion so understanding the flow characteristics is important. Due to the lack of available data for the comparison, only the Bosphorus is taken into consideration in the course of the study. This work is motivated by sensitivity simulations in order to exemplify the different factors effects on the local circulations. Even though the horizontal resolution used in the course of the research is fine, the model topography needs modification by the user. Especially, the narrow strait needs modification. It is necessary, therefore, to use high resolution topography data and also high resolution land-use data in the model. Sea-land breeze and urbanization are the main foci in this study. Although it has been concluded from many studies in the literature that steep topography has striking effect on a circulation, sensitivity simulations in the course of the study show that hilly topography contributes to the local circulation as well. As a matter of fact that more detailed investigations should be conducted using either 2-D or 3-D numerical simulations for Istanbul. Moreover, simulations should be supported with observations.

Although the numerical technique is used by the OMEGA model gives better land/water boundary separation, the computational cost causes the limited simulation facilities using the model. Thus, it is not possible to perform long time simulation using the OMEGA model. Since the numerical technique is more complex, parameterization schemes in the model are as simple as possible. Improvement of the parameterizations in the model corresponding with its numerical technique is the essential need to represent the atmospheric motion accurately. Modelling study should be supported by implementing available surface and upper-air data network and its long-term continuity.

There is a considerable amount of work for hazard material dispersion in the world. The first part of the study needs more observation data to verify the simulations and also have better performance from the ADM. Since the data is very sparse, there is always uncertainty while evaluating the results. If the data network is dense,

observations can be assimilated to the OMEGA model to obtain better simulation results for the flow that carries pollutants to long distance. Few observation stations should be mounted to the critical points along the Straits. Long time simulations are also necessary to map the frequency of hazardous material release. The general characteristic of the flow should be determined from simulations since it gives the spatial flow distribution. Meanwhile, extreme flow conditions may cause danger and should be investigated. Turkey's power to regulate commercial shipping through the Straits is limited by the 1936 Treaty of Montreux that delineates the Straits as an international waterway. Although subsequent international agreements have given Turkey the right to regulate the right of passage through the Straits, Turkey has not been stringently enforcing the shipping laws. These types of studies provide scientific evidences to the decision makers.

In addition to the air pollution, water pollution is another significant issue that should be studied. As the number of ships passing through the Straits grows, the risk of an incident increases. Furthermore, the traffic will likely to increase as the six countries surrounding the Black Sea develop economically. With tonnage on the rise as well, the threat of collision is not the only danger: on December 29, 1999, the Volgoneft-248, a 25-year old Russian tanker, ran aground and split into two in close proximity to the southwest shores of Istanbul. More than 800 tons of the 4,300 tons of fuel oil on board spilled into the Marmara Sea, covering the coast of Marmara with fuel-oil and affecting about 5 square miles of the sea. By keeping these dangers in mind, a coupled atmosphere-ocean model should be performed to evaluate the dispersion of the pollutant both in the atmosphere and the water. Also, an operational system should be developed for immediate response since performing a numerical model takes long time to obtain necessary information.

By depicting the public health in danger due to the heavy shipping traffic, decision makers take advantages from scientific research which facilitates asserting public rights. Investigations also provide decision makers to prepare emergency plans and mitigation strategies for possible tanker accidents since variety kind of dangerous materials (i.e., LPG, oil, petrol etc.) has been carried using this waterway.

REFERENCES

Abbs D.J., 1986. Sea Breeze Interactions along a Concave Coastline in Southern Australia: Observations and Numerical Modelling Study, *Mon. Wea.Rev.*, **114**, 831-848.

Abe S. and Yoshida T., 1982. The Effect of the Width of a Peninsula to the Sea Breeze, *J. Meteorol.Soc. Japan*, **60**(5), 1074-1084.

Alpert P., Kusuda M., and Abe N., 1984. Anticlockwise Rotation, Eccentricity and Tilt Angle of the Wind Hodograph. Part II: an Observational Study, *J. of Atmos. Sci.*, **41**, 3568-3583.

Alpert P., **Osetinsky I., Ziv B., and Shafir H.,** 2004. Semi-Objective Classification for Daily Synoptic Systems: Application to the Eastern Mediterranean Climate Change, *Int. J. Climatol.*, **24**, 1001-1011.

Andre J. C., De Moor G., Lacarrere P., Therry G., and du Vachat R., 1978. Modeling the 24-hour evolution of the mean and turbulent structures of the planetary boundary layer, *J. Atmos. Sci.*, **35**, 1861-1883.

Anderson G.E.,1971. Mesoscale Influences on Wind Field, *J. Appl. Meteorol.*, **10**, 377-386.

Anthes R. A., 1977a. A cumulus parameterization scheme utilizing a one-dimensional cloud model, *Mon. Wea. Rev.*, **105**, 270-286.

Anthes R. A., 1977b. Hurricane model experiments with a new cumulus parameterization scheme. *Mon. Wea. Rev.*, **105**, 287-300.

Arnfield A.J., 2003. Two Decades of Urban Climate Research: A Review of Turbulence, Exchanges of Energy and Water and the Urban Heat Island, *Int. J. Climatol.*, **23**, 1-26.

Arritt R.W., 1989. Numerical Modelling of the Offshore Extent of Sea Breezes, Q.J.R. Meteorol. Soc., **115**, 547-570.

Arritt R.W., 1993. Effects of the Large-Scale Flow on Characteristic Features of the Sea Breeze, J. of Appl. Meteorology, **32**, 116-125.

Arya, S. P., 1999. *Air Pollution Meteorology and Dispersion*, Oxford University Press, pp. 157.

Arya S. P. S., 1988. *Introduction to Micrometeorology*. Academic Press, New York.

Atkinson B.W., 1971. The Effect of an Urban Area on the Precipitation from a Moving Thunderstorm, *J. Appl. Meteor.*, **10**, 47-55.

Atkinson B.W., 1981. *Meso-scale Atmospheric Circulations*, Academic Press, London, pp. 495.

Atkinson B.W., 2003. Numerical Modelling of Urban Heat Island Intensity, *Boundary-Layer Meteorology*, **109**, 285-310

Atwater M. A., and Brown Jr. P.S., 1974. Numerical; calculation of the latitudinal variation of solar radiation for an atmosphere of varying opacity. *J. Appl. Meteor*., **13**, 289-297.

Bacon, D. P., and Sarma R. A., 1991. Agglomeration of dust in convective clouds initialized by nuclear bursts, *Atmos. Environ.*, **25A**, 2627–2642.

Bacon, D. P., Ahmad N. N., Boybeyi Z., Dunn T.J., Hall M. S., Lee P. C. S., Sarma R. A., Turner M. D., Waight K. T., Young S. H., and Zack J. W., 2000. A Dynamically Adapting Weather and Dispersion Model: The Operational Multiscale Environment model with Grid Adaptivity (OMEGA), *Mon. Wea. Rev.*, **128**, 2044-2076.

Bacon, D. P., 2003. Operational Multiscale Environment model with Grid Adaptivity (OMEGA) System Design, Copyright 2001, Science Applications International Corporation, pp. 1–124.

Baik J.-J., Kim Y.-H., and Chun H.-Y., 2001. Dry and Moist Convection Forced by an Urban Heat Island, *J. Appl. Meteor.*, **40**, 1462-1475.

Bechtold P., Pinty J.-P., and Mascart P., 1991. A numerical Investigation of the Influence of large-Scale Winds on Sea Breeze and Inland Breeze type Circulations, *J. Appl. Meteor.*, **30**, 1268–1279.

Beljaars, A. C. M., and Holtslag A. A. M., 1991. Flux parameterization over land surfaces for atmospheric models, *J. Appl. Meteor*., **30**, 327–341.

Bergström H., and Juuso N., 2006. A Study of Valley Winds Using theMIUU Meso-scale Model, *Wind Energy*, **9**, 109-129.

Berry, E. X., and R. L. Reinhardt, 1974a. An analysis of cloud drop growth by collection: Part I.Double distributions. *J. Atmos. Sci.*, **31**, 1814-1824.

Berry, E. X., 1974b. An analysis of cloud drop growth by collection: Part II. Single initial distributions. *J. Atmos. Sci*., **31**, 1825-1831.

Best M.J., 2006. Progress towards better weather forecasts for city dwellers: from short range to climate change, *Theor. Appl.Climatol.*, **84**, 47-55.

Bornstein R.D., 1968. Observation of the Urban Heat Island Effect in New York City, *J. Appl. Meteor.*, **7**, 575-582.

Bornstein R.D. and Johnson D.S., 1977. Urban-Rural Wind Velocity Differences, *Atmos. Environ.*, **11**, 597-604.

Bornstein R.D. and Lin Q., 2000. Urban Heat Islands and Summertime Convective Thunderstorms in Atlanta: Three Case Studies, *Atmos. Environ.*, **34**, 507-516.

Boybeyi, Z., Raman S., and Zannetti P., 1995. Numerical investigation of possible role of local meteorology in Bhopal gas accident, *Atmos. Environ*., **29**, 479–496.

Boybeyi, Z. and Bacon D., 1996. *The accurate representation of meteorology in mesoscale dispersion models, in Environmental Modeling – Vol. 3 (Computer Methods and Software for Simulating Environmental Pollution and its Adverse Effects)*, P. Zannetti, Ed., Computational Mechanics Publications, Southampton.

Boybeyi, Z. and Raman S., 1996. *Mesoscale Atmospheric Transport and Diffusion Processes, Dynamics of Atmospheric Flows: Part I Atmospheric Transport and Diffusion Processes*, Edited by M. P. Sing and S. Raman, Computational Mechanics Publications.

Boybeyi, Z., N. N. Ahmad, D. P. Bacon, T. J. Dunn, M. S. Hall, P. C. S. Lee, R. A. Sarma, and T. R. Wait, 2001. Evaluation of the Operational Multiscale Environment Model with Grid Adaptivity against the European Tracer Experiment. *J. Appl.* Met. **40**, 1541-1558.

Briggs, G.A., 1969. Plume Rise. **TID-25075**. U.S. Atomic Energy Commission, *Available from the National Technical Information Service*, U.S. Department of commerce, Springfield, VA 22151, pp. 85.

Briggs, G.A., 1979. Analytic modeling of drainage flows. *Draft Document, Atmospheric Turbulence and Diffusion Laboratory, NOAA.* Available from EPA, Environmental Sciences Research Lab., Research Triangle Park, NC 27722.

Brown, M.J., and M.D. Williams, 1998. An urban canopy parameterization for mesoscale meteorological models, Preprints, *Second Urban Environment Conference*, AMS, Albuquerque, NM.

Brown M.J., 2000. Urban parameterizations for mesoscale meteorological models. *Mesoscale Atmospheric Dispersion*, Ed. Z. Boybeyi, Chapter 5, pp. 193–255. Southampton, UK, WIT Press.

Burian S.J. and Shepherd M., 2005. Effect of Urbanization on the Diurnal Rainfall Pattern in Houston, Hydrological Processes, **19**, 1089-1103.

Celikoyan M.T., 2004. Monitoring and analysis of landuse changes in historical periods for the city of Istanbul by means of aerial photography and satellite imagery. Istanbul Technical University, *Ph.D. Thesis*: Istanbul

Chang, J. T., and Wetzel P. J., 1990. Effects of spatial variations of soil moisture and vegetation on the evolution of a prestorm environment: A numerical case study. *Mon. Wea. Rev.*, **119**, 1368–1390.

Changnon S.A., Huff F.A., and Semonin R.G., 1971. METROMEX: An Investigation of Inadvertent Weather Modification, *Bulletin American meteorological Society*, **52** (10)**,** 958-968.

Changnon S.A., 1978. Urban Effects on Severe Local Storm as St. Louis, *J. Appl. Meteor.*, **17**, 578-586.

Changnon S.A., and Huff F.A., 1986. The Urban-related Nocturnal Rainfall Anomaly at St. Louis, *J. Climate and Applied Meteorology*, **25**, 1985-1995.

Charnock H., 1955. Wind stress on a water surface, *Quart. Jl. R. Met. Soc.*, **81**, 639-640.

Chen, F., and J. Dudhia, 2001. Coupling an advanced land-surface/hydrology model with the Penn State/NCAR MM5 modeling system. Part I: Model implementation and sensitivity. *Monthly Weather Review*, **129**, 569-585.

Childs P.P. and Raman S., 2005. Observation and Numerical Simulation of Urban Heat Island and Sea Breeze Circulations over New York City, *Pure and Applied Geophysics*, **162**, 1955-1980.

Chow F.K., Weigel A. P., Street R. L., Rotach M. W. and Xue M., 2006. High-Resolution Large-Eddy Simulations of Flow in a Steep Alpine Valley. Part I: Methodology, Verification, and Sensitivity Experiments, *J. Appl. Meteorology and Climatology*, **45**, 63-86.

Clapp, R. B., and Hornberger G. M., 1978. Empirical Equations for Some Soil Hydraulic Properties, *Water Resour. Res.*, **14**, 601–604.

ClappierA., Martilli A, Grossi P., Thunis P., Calpini B., Graziani G., Van Den Bergh H., 2000. Effect of Sea Breeze on Air Pollution in the Greater Athens Area. Part I: Numerical Simulations and Field Observations, *J. Appl. Meteor.*, **39**, 546-562.

Coceal O. and Belcher S.E., 2005. Mean Winds through an Inhomogeneous Urban Canopy, *Boundary-Layer Meteorology*, **115**, 47-68.

Colacino M., and Rovelli A., 1983. The yearly averaged air temperature in Rome from 1782 to 1975, *Tellus*, **35A**, 389-397.

Colle B.A and Mass C.F., 2000. High_Resolution Observations and Numerical Simulations of Easterly Gap Flow through the Strait of Juan de Fuca on 9-10 December 1995, *Mon. Wea. Rev.*, **128**, 2398-2422.

Crutzen P.J., 2004. New Directions: The Growing Urban Heat and Pollution "Island" Effect -Impact on Chemistry and Climate, *Atmos. Environ.*, **38**, 3539-3540.

Daley R., 1991. *Atmospheric Data Analysis*, Cambridge University Press, pp. 457.

Danard M., 1977. A Simple Model for Mesoscale Effects of Topography on Surface Winds, *Mon. Wea. Rev.*, **105**, 572-581.

Dandou A., Tombrou M., Akylas E., Soulakellis N., Bossioli E., 2005. Development and Evaluation of an Urban Parameterization Scheme in the Penn State/NCAR Mesoscale Model (MM5), *Journal of Geophysical Research-Atmosphere*, **110**(D10), Art.No.D10102.

Deardoff J. W., 1974. Three-dimensional study of the height and mean structure of a heated planetary boundary layer, *Boundary Layer Meteorology*., **7**, 81-106.

Deardoff J. W., 1978. Efficient prediction of ground surface temperature and moisture with inclusion of a layer of vegetation, *J. Geophys. Research*, **83**(C4), 1889-1903.

Deardoff J. W., 1980. Stratocumulus-capped mixed layer derived from a three-dimensional model, *Boundary-Layer Meteorology*., **18**, 495-527.

Dickinson R.E., Henderson-Sellers A., Kennedy P. J., and Wilson M. F., 1986. Biosphere Atmosphere Transfer Scheme (BATS) for the NCAR Community Climate Model. *NCAR Tech. Note* **NCAR/TN-275+STR**, pp. 69.

DiMego, G. J., 1988. The National Meteorological Center regional analysis system, *Mon. Wea. Rev.*, **116**, 977–1000.

Dixon P.G. and Mote T., 2003. Patterns and Causes of Atlanta's Urban Heat-Initiated Precipitation, *J. Appl. Meteor*., **42**, 1273-1284.

Doran J.C. and Zhong S., 2000. Thermally Driven Gap Winds into the Mexico City Basin, *J. Appl. Meteor*., **39**, 1330-1340.

Eckman R.M., 1998. Observations and Numerical Simulations of Winds within a Broad Forested Valley, *J. Appl. Meteor*., **37**, 206-219.

Egger J., Bajrachaya S., Egger U., Heinrich R., Reuder J., Shayka P., Wendt H, and Wirth V., 2000. Diurnal Winds in the Himalayan Kali Gandaki Valley. Part I: Observations, *Mon. Wea. Rev*., **128**, 1106-1122.

Erinc S., 1996. *Klimatoloji ve Metodları*, Istanbul Universitesi Deniz Bilimleri ve Cografya Enstitusu, Istanbul.

Estoque M.A., 1962. The Sea Breeze as a Function of the Prevailing Synoptic Situation, *J. Atmos. Sci.*, **19**, 244-250.

Fast J. D., Zhong S., and Whiteman C.D., 1996. Boundary Layer Evolution within a Canyonland Basin. Part II: Numerical Simulations of Nocturnal Flows and Heat Budgets, *J. Appl. Meteor.*, **35**, 2162-2178.

Fast J. D., Torcolini J.C., and Redman R., 2005. Pseudovertical Temperature Profiles and the Urban Heat Island Measured by a Temperature Datalogger Network in Phoenix, Arizona, *J. Appl. Meteor.*, **44**, 3-13.

Federico S., Dalu G.A., Bellecci C., Colacino M., 2000. Mesoscale energetics and flows induced by sea-land and mountain-valley contrast, *Ann. Geophysicae*, **18**, 235-246.

Finkele K., 1998. Inland and Offshore Propagation Speeds of a Sea Breeze from Simulations and Measurements, *Boundary-Layer Meteorology*, **87**, 307-329.

Fisher E.L., 1960. An Observational Study of the Sea Breeze, *Journal of Meteorology*, **17**, 645-660.

Fisher E.L., 1961. A Theoretical Study of the Sea Breeze, *Journal of Meteorology*, **18**, 216-233.

Fletcher, N. H., 1962. *The Physics of Rainclouds.* Cambridge University Press, pp. 386.

Frizzola J.A. and Fisher E.L., 1963. A Series of Sea Breeze Observations in the New York City Area, *J. Appl. Meteorol.*, **2**, 722-739.

Frysinger J.R, Lindner B.L., and Brueske S.L., 2003. A statistical Sea-Breeze Prediction Algorithm for Charleston, South Carolina, *Weather and Forecasting*, **18**, 614-625.

Furberg M., Steyn D.G. and Baldi M., 2002. The Climatology of Sea Breezes on Sardinia, *Int. J. Climatol.*, **22**, 917-932.

Gallo K.P., Mcnab A.L., Karl T.R., Brown J.F., Hood J.J., and Tarpley J.D., 1993. The use of NOAA AVHRR data for assessment of the Urban Heat Island effect, *J. Appl. Meteorol*., **32**, 899-908.

Garratt J.R. and Physick W.L., 1985. The Inland Boundary Layer at Low Latitudes: II-Sea Breeze Influence, *Boundary-Layer Meteorology*, **33**, 209-231.

Gedzelman S.D., Austin S., Cermak R., Stefano N. Partridge S., Quesenberry S. and Robinson D.A., 2003. Mesoscale Aspects of the Urban Heat Island around New York City, *Theor. Appl. Climatol.*, **75**, 29-42.

Gilliam R.C., Raman S. and Niyogi D.D.S., 2004. Observation and Numerical Study on the Influence of Large-Scale Flow Direction and Coastline Shape on Sea Breeze Evolution, *Boundary-Layer Meteorology*, **111**, 275-300.

Givati A., and Rosenfeld D., 2004. Quantifying Precipitation Suppression Due to Air Pollution, *J. Appl. Meteor.*, **43**, 1038-1056.

Goosens C., and Berger A., 1986. Annual and Seasonal Climatic Variations over the Northern Hemisphere and Europe during the Last Century. *Annals Geophysica,* **4**, 385 – 399.

Gross G. and Wippermann F., 1987. Channeling and Countercurrent in the Upper Rhine Valley: Numerical Simulations, *J. Climate and Appl. Meteor.*, **26** (10), 1293-1304.

Hanna S.T. and Britter R.E., 2002. Wind Flow and Vapor Cloud Dispersion at Industrial and Urban Sites, *American Institute of Chemical Engineers*, New York.

Haurwitz B., 1947. Comments on the Sea Breeze Circulation, *Journal of Meteorology*, **4**, 1-8.

Hess, S.L., 1959. *Introduction to Theoretical Meteorology*, Holt, Rinehart, and Winston, New York, pp. 362.

Huff F.A., and Changnon J.R., 1972. Climatological Assessment of Urban Effects on Rainfall in the St. Louis Region, *J. Appl. Meteor.*, **17**, No: 5, 565-577.

Huff F.A., and Changnon J.R., 1973. Precipitation Modification by Major Urban Areas, *Bulletin American Meteorological Society*, **54** (12), pp. 1220-1232.

Huff F.A., and Vogel J.L., 1978. Urban, Topographic and Diurnal Effects on Precipitation at St. Louis, *J.Appl. Meteor.*, **11**, 823-842.

Jackson P.L. and Steyn D.G., 1994. Gap Winds in a Fjord. Part I: Observations and Numerical Simulation, *Mon. Wea. Rev.*, **122**, 2645-2665.

Jacobs C. A., Pandolfo J. B., and Atwater M. A., 1974. A description of a general three dimensional numerical simulation model of a coupled air-water and/or air-land boundary layer. *IFYGL final report*, **CEM Report No. 5131-509a**.

Jauregui E., and Romales E., 1996. Urban Effects on Convective Precipitation in Mexico City, *Atmos. Environ.*, **30**, 3383-3389.

Jin M., Dickinson R.E. and Zhang D., 2005. The Footprint of Urban Areas on Global Climate as Characterized by MODIS, *Journal of Climate*, **18**, 1551-1565.

Kain J.S. and J.M. Fritsch, 1990. A one-dimensional entraining/detraining plume model and its application in convective parameterization. *J. Atmos. Sci*., **47**, 2784-2802.

Kalande B.D., and Oke T.R., 1980. Suburban energy balance estimates for Vancouver, B. C., using the Bowen ratio energy balance approach. *J. Appl. Met*., **19**, 791-802.

Kanda M., 2007. Progress in Urban Meteorology: A Review, *J. Meteorol. Soc. Japan*, **85B**, 363-383.

Kallos G., Kassomenos P., and Pielke R.A., 1993. Synoptic and Mesoscale Weather Conditions during Air Pollution Episodes in Athens,Greece, *Boundary-layer Meteorology*, **62**, 162-184.

Karaca M, Tayanç M., and Toros H., 1995a. The Effects of Urbanization on Climate of Istanbul and Ankara: A First Study. *Atmos. Environ.. Part B: Urban Atmosphere*, **29**(23), 3411-3421.

Karaca M., Anteplioglu U., and Karsan H., 1995b. Detection of Urban Heat Island in Istanbul, Turkey. *Il Nuovo Cimento*, **18**, 49-55.

Karaca M., Deniz A., and Tayanç M., 2000. Cyclone Track Variability and its Relation with Regional Climate of Turkey, *Int. J. Climatol,* **20**, 1225-1236.

Kasten F., and Czeplak G., 1980. Solar and terrestrial radiation dependent on the amount and type of cloud, *Solar Energy*, **24**, 177-189.

Kaufmann P. and Weber R.O., 1998. Directional Correlation Coefficient for Channeled Flow and Application to Wind Data over Complex Terrain, *Journal of Atmospheric and Oceanic Technology*, **15**, 89-97.

Khemani L.T. and Murty BH.V.R., 1973. Rainfall variations in an urban industrial region, *J. Appl. Meteorol*., **12**, 187-194.

Kim Y.H., and Baik J.J., 2005. Daily maximum urban heat island intensity in large cities of Korea. *Theoretical and Applied Climatology*, **79**(3-4), 151-164.

Kim Y.H., and Baik J.J., 2005. Spatial and Temporal Structure of the Urban Heat Island in Seoul. *Journal of Applied Meteorology*, **44**(5), 591-605.

Kinouchi T., and Yoshitani J., 2001. Simulation of the Urban Heat Island in Tokyo with future possible increases of anthropogenic heat, vegetation cover and water surface. *Proceedings of The 2001 International Symposium on Environmental Hydraulics.*

Kondo H. and Gambo K., 1979. The Effect of the Mixing Layer on the Sea Breeze Circulation and the Diffusion of Pollutants Associated with Land-Sea Breezes, *J. Meteor. Soc. Japan*, **57**, 560-574.

Kondo H., 1990. A Numerical Experiment on the Interaction between Sea Breeze and Valley Wind to Generate the so-called "Extended Sea Breeze", *J. Meteor. Soc. Japan*, **68**, 435-445.

Kondratyev J., 1969. *Radiation in the Atmosphere.* Academic Press, New York, pp. 912.

Kossmann M. and Sturman A., 2003. Pressure-Driven Channeling Effects in Bent Valleys, *J. Appl. Meteor.*, **42**, 151-158.

Kuhn P. M., 1963. Radiometeorsonde observations of infrared flux emissivity of water vapor, *J.Appl. Meteor*., **2**, 368-378.

Kuo H. L., 1965. On formation and intensification of tropical cyclones through latent heat release by cumulus convection, *J. Atmos. Sci*., **22**, 40-63.

Kuo, H. L., 1974. Further studies of the parameterization of the influence of cumulus on large scale flow, *J. Atmos. Sci*., **31**, 1232–1240.

Kuo Y. H., and Anthes, R. A., 1984: Semiprognostic tests of Kuo-type cumulus parameterization schemes in an extratropical convective system, *Mon Wea. Rev.*, **112**, 1498-1509.

Kusaka H., Kimura F., Hirakuchi H. and Mizutori M., 2000. The Effects of Land-Use Alteration on the Sea Breeze and Daytime Heat Island in the Tokyo Metropolitan Area, *J. Meteor. Soc. Japan*, **78**, 405-420.

Kusaka H., and Kimura F., 2004. Coupling a single-layer urban canopy model with a simple atmospheric model: Impact on Urban Heat Island simulation for an idealized case, *J. Meteorol. Soc. Japan*, **82**(1), 67-80.

Kusuda M. and Alpert P., 1983. Anti-Clockwise Rotation of the Wind Hodograph. Part I: Theoretical Study, *J. of Atmos. Sci*., **40**, 487-499.

Kuwugata T.and Kimura F., 1997. Daytime Boundary Layer Evolution in a Deep Valley. Part II: Numerical Simulation of the Cross-Valley Circulation, *J. Appl. Meteor*., **36**, 883-895.

Lackmann G.M. and Overland J.E., 1989. Atmospheric Structure and Momentum Balance during a Gap-Wind Event in Shelikof Strait, Alaska, *Mon. Wea. Rev.*, **117**, 1817-1833.

Lamptey B.L., Barron E.J. and Pollard D., 2005. Impacts of Agriculture and Urbanization on The Climate of The Northeastern United States, *Global and Planetary Change*, **49**(3-4), 203-221.

Landsberg H., 1981. *Urban Climate*. Academic Press, New York.

Legates, D. R., and C. J. Willmott, 1992. Monthly Average Surface Air Temperature and Precipitation. Digital raster data on a 30 minute geographic (lat/long) 360x720 grid. In: Global Ecosystems Database Version 1.0: Disc A. Boulder, CO: NOAA National Geophysical Data Center. 48 independent and 4 derived single-attribute spatial layers on CD-ROM, 47.2 MB.

Lemonsu A. and Masson V., 2002. Simulation of a Summer Urban Breeze over Paris, *Boundary-Layer Meteorology*, **104**, 463-490.

Lemonsu A., Bastin S., Masson V., and Drobinski P., 2006. Vertical Structure of the Urban Boundary Layer over Marseille under Sea Breeze Conditions, *Boundary-Layer Meteorology*, **118**, 477-501.

Li J-G., and Atkinson B.W., 1999. Transition Regimes in Valley Airflows, *Boundary-Layer Meteorology*, **91**, 385-411.

Lin, Y.-L., Farley R. D., and Orville H. D., 1983. Bulk parameterization of the snow field in a cloud model, *J. Climate Appl.Meteor*., **22**, 1065–1092.

Lin, Y.-L., 2007. *Mesoscale Dynamics*, Cambridge University Press, UK.

List, R. J., 1971. Smithsonian Meteorological Tables. Smithsonian Institution Press, Washington, D. C.

Liu, J., Chen, J., Black, T., and Novak, M., 1996. E-e modeling of turbulent airflow downwind of a model forest edge. *Bound.-Layer Meteor*., **77**, 21-44.

Liu M., Westphal D.L., Holt T.R., and Xu Q., 2000. Numerical Simulation of a Low-Level Jet over Complex Terrain in Southern Iran, *Mon. Wea. Rev.*, **128**, 1309-1327.

Loose T., and Bornstein R. D., 1977. Observation of Mesoscale Effects on Frontal Movement Through and Urban Area, *Mon. Wea. Rev*., **105** (5), 563-571.

Lowry W.P., 1998. Urban effects on precipitation amount, *Progress in Physical Geography*, **22**(4), 477-520.

Lu R., and Turco R.P., 1994. Air Pollutant Transport in a Coastal Environment. Part I: Two-Dimensional Simulations of Sea-Breeze and Mountain Effects, *J. Atmos. Sci.*, **51**, 2285-2308.

Lu R., and Turco R.P., 1995. Air Pollutant Transport in a Coastal Environment-II. Three Dimensional Simulations Over Los Angeles Basin, *Atmos. Environ*., **29**, 1499-1518.

Lyons W.A., 1972. The Climatology and Prediction of the Chicago Lake Breeze, *J. Appl. Meteorol*., **11**, 1259-1270.

Mahrer, Y., and Pielke R. A., 1977. The effects of topography on the sea and land breezes in a two-dimensional numerical model, *Mon. Wea*. *Rev*., **105**, 1151–1162.

Mahrt L., and Pan H., 1984. A Two-Layer Model of Soil Hydrology, *Boundary-Layer Meteorology*, **29**, 1-20.

Martilli A., 2002. Numerical Study of Urban Impact on Boundary Layer Structure: Sensitivity to Wind Speed, Urban Morphology, and Rural Soil Moisture, *J. Appl. Meteor*., **41**, 1247-1266.

Martilli A., 2003. A Two-Dimensional Numerical Study of the Impact of a City on Atmospheric Circulation and Pollutant Dispersion in a Coastal Environment, *Boundary-Layer Meteorology*, **108**, 91-119.

Martilli A., Roulet Y.-A., Junier M., Kirchner F. Rotach M., and Clappier A., 2003. On the Impact of Urban Surface Exchange Parameterizations on Air Quality Simulations: The Athens Case, *Atmos. Environ*., **37**, 4217-4231.

Marshall, J. S., and Palmer, W. M., 1948. The distribution of raindrops with size, *Journal of Meteorology*, **5**, 165-166.

Maruyama, T., 1999. Surface and inlet boundary conditions for the simulation of turbulent boundary layer over complex rough surfaces. *J. Wind. Eng. Ind. Aerodyn.*, **81**, 311-322.

Masson V., 2006. Urban surface modeling and the meso-scale impact of cities, *Theor. Appl. Climatol*, **84**, 35-45.

Matzinger N., Andretta M., Van Gorsel E., Vogt R., Ohmura A. and Rotach M.W., 2003. Surface Radiation Budget in an Alpine Valley, *Q. J. R. Meteorol. Soc.*, **129**, 877-895.

McCumber M. C., and Pielke R. A., 1981. Simulation of the Effects of Surface Fluxes of Heat and Moisture in a Mesoscale Numerical Model 1. Soil Layer, *J. Geophysical Research*, **86**, 9929-9938.

McCorcle, M. D., 1988. Simulation of soil moisture effects on the Great Plains low-level jet, *Mon. Wea. Rev.*, **116**, 1705-1720.

McDonald J. E., 1960. Direct absorption of solar radiation by atmospheric water vapor, *Journal of Meteorology*., **17**, 319-328.

McKee T.B., and O'Neal R.D., 1989. The Role of Valley Geometry and Energy Budget in the Formation of Nocturnal Valley Winds, *J. Appl. Meteor*., **28**, 445-456.

McNider R.T., and Pielke R.A., 1984. Numerical Simulation of Slope and Mountain Flows, *J. Climate and Applied Meteorology*, **23**, 1441-1453.

McPherson R.D., 1970. A Numerical Study of the Effect of a Coastal Irregularity on the Sea Breeze, *J. Appl. Meteor*., **9**, 767-777.

Melas D., Ziomas I.C. and Zerefos C.S., 1995. Boundary Layer Dynamics in an Urban Coastal Environment under Sea Breeze Conditions, *Atmos. Environ.*, **29** (24), 3605-3617.

Mellor G. L., and Yamada T., 1974. A hierarchy of turbulence closure models for planetary boundary layers, *J. Atmos. Sci*., **31**, 1791-1806.

Mellor G. L. and Yamada T., 1982. Development of a turbulence closure model for geophysical fluid problems, *Rev. Geophys. Space Phys*., **20**, 851-875.

Molinari, J., and Dudek M., 1986. Implicit versus explicit convective heating in numerical weather prediction models. *Mon. Wea. Rev*., **114**, 1822–1831.

Montávez J.P., Rodríguez A., and Jiménez J.I., 2000. A study of the Urban Heat Island of Granada. *Int. J. Climatol.,* **20**, 899-911.

Moran, M. D., 1992: Numerical modeling of mesoscale atmospheric dispersion. *Ph.D. Dissertation*, Colorado State University, Fort Collins, CO, pp.758.

Morris C.J.G., Simmonds I., and Plummer N., 2001. Quantification of the Influences of Wind and Cloud on the Nocturnal Urban Heat Island of the Large City, *J. Appl. Meteorology*, **40**, 169-182.

Moorthy K.K., Pillai P.S. and Babu S.S., 2003. Influence of changes in the prevailing synoptic conditions on the response of aerosol characteristics to land and sea breeze circulations at a coastal station, *Boundary Layer Meteorology,* **108**, 145-161.

Neumann J., 1951. Land Breezes and Nocturnal Thunderstorms, *Journal of Meteorology*, **8**, 60-67.

Neumann J., 1977. On the Rotation Rate of the Direction of Sea and Land Breezes, *J. Atmos. Sci*, **34**, 1913-1917.

Neumann J., 1984. The Coriolis Force in Relation to the Sea and Land Breezes- A Historical Note, *Bulletin American Meteorological Society*, **65**, 24-26.

Nicholls M.E., Pielke R.A., and Cotton W.R., 1991. A Two-Dimensional Numerical Investigation of the Interaction between Sea Breezes and Deep Convection over the Florida Peninsula, *Mon. Wea. Rew.*, **119**, 298-323.

NitisT., Kitsiou D., Klaic Z.B., Prtenjak M.T. and Moussiopoulos N., 2005. The effects of basic flow and topography on the development of the sea breeze over a complex coastal environment, *Q. J. R. Meteorol. Soc.*, **131**, 305-327.

Noilhan, J., and Planton S., 1989. A simple parameterization of land surface processes for meteorological models. *Mon. Wea. Rev.*, **117**, 536–549.

Ohashi Y., and Kida H., 2002. Local Circulations Developed in the Vicinity of Both Coastal and Inland Urban Areas. Part II: Effects of Urban and Mountain Areas on Moisture Transport, *J. Appl. Meteor.*, **43**, 119-133.

Ohashi Y., and Kida H., 2004. Local Circulations Developed in the Vicinity of Both Coastal and Inland Urban Areas: A Numerical Study with a Mesoscale Atmospheric Model, *J. Appl. Meteor.*, **41**, 30-45.

Oke T.R., 1982. The energetic basis of the Urban Heat-Island, *Quarterly Journal of The Royal Meteorological Society,* **108** (455), 1-24.

Oke T.R, 1987: *Boundary Layer Climates*, Second Edition, Cambridge University Press, pp. 423.

Olson, J. S., 1992. World Ecosystems (WE1.4). Digital Raster Data on a 10-minute Geographic 1080x2160 grid. In: Global Ecosystems Database Version 1.0: Disc A. Boulder, CO: NOAA National Geophysical Data Center.

Ookouchi Y., Uryu M. and Sawada R., 1978. A Numerical Study on the Effects of a Mountain on the Land and Sea Breezes, *J. Meteor. Soc. Japan*, **56**(5), 368-385.

Pearson R.A., 1973. Properties of the Sea Breeze Front as Shown by a Numerical Model, *J. Atmos. Sci.*, **30**, 1050-1060.

Philandras C.M., Metaxas D.A. and Nastos P.T., 1999. Climate variability and urbanization in Athens, *Theoretical and Applied Climatology,* **63**, 65-72.

Physick W.L., and Abbs D.J., 1991. Flow and Plume Dispersion in a Coastal Valley, *J. Appl. Meteor*., **31**, 64-73.

Pielke R.A., 1974. A Three-Dimensional Numerical Model of the Sea Breezes over South Florida, *Mon. Wea. Rev.*, **102**, 115-139.

Pielke R.A., 1984. *Mesoscale Meteorological Modeling*, Academic Press, California USA, pp. 474.

Population Reference Bureau, 2005. 2005 World Population Data Sheet. http://www.prb.org/pdf05/05WorldDataSheet_Eng.pdf

Prtenjak M.T., 2003. Main Characteristics of Sea/Land Breezeas along the Eastern Coast of the Northern Adriatic, *Geofizika*, **20**, 75-92.

Proctor, F. H., 1987. The Terminal Area Simulation System / Volume I: Theoretical Formulation, *NASA Contractor Report* **4046**.

Pruppacher, H. R., and Klett J. D., 1978. Microphysics of Clouds and Precipitation. *D. Reidel*, pp. 714.

Ramanathan et al., 2001. Aerosol, Climate and the Hydrological Cycle, *Science*, **294**, 2119-2124.

Ramankutty N., and Foley J., 1999. Estimating Historical Changes in Global Land Cover: Croplands from 1700 to 1992, *Global Biogeochemical Cycles*, **13**, 997-1028.

Rampanelli G., Zardi D., and Rottuno R., 2004. Mechanism of Up-Valley Winds, *J. Atmos. Sci.*, **61**, 3097-3111.

Reed T.R., 1931. Gap Winds of the Strait of Juan De Fuca, *Mon. Wea. Rev*., **59**, 373-376.

Richiardone R. and Brusasca G., 1989. Numerical experiments on urban heat island intensity, *Q. J. R. Meteorol. Soc.*, **115**, 983-995.

Rosenfeld D., 2000. Suppression of Rain and Snow by Urban and Industrial Air Pollution, *Science*, **287**, 1793-1796.

Rotach M.W., 1999. On the influence of the urban roughness sublayer on turbulence and dispersion, *Atmos. Environ*., **33**, 4001-4008.

Rotunno R., 1983. On the Linear Theory of the Land and Sea Breeze, *J. Atmos. Sci.*, **40**, 1999-2009.

Rozoff C.M., Cotton W.R., and Adegoke J.O., 2003. Simulation of St. Louis, Missouri, Land Use Impacts on Thunderstorms, *J. Appl. Meteor*., **42**, 716-738.

Sarrat C., Lemonsu A., Masson V., and Guedalia D., 2006. Impact of Urban Heat Island on Regional Atmosperic Pollution, *Atmos. Environ*., **40**, 1743-1758.

Sasamori, T., 1972. A linear harmonic analysis of atmospheric motion with radiative dissipation, *J. Meteor. Soc. Japan*, **50**, 505–518.

Savijarvi H. and Liya J., 2001. Local Winds in a Valley City, *Boundary-Layer Meteorology*, **100**, 301-319.

Schmidt, F.H., 1947. An Elementary Theory of the Land and Sea Breeze Circulation, *J. of Meteor.*, **4**, 9-20.

Schweitzer, P.N., 1993. Modern Average Global Sea-Surface Temperature. CD-ROM, U.S. Geological Survey Digital Data Series DDS-10.

Seaman N.L., Ludwing F.L., Donall E.G., Warner T.T., and Bhumralkar C.M., 1989. Numerical Studies of Urban Planetary Boundary-Layer Structure under Realistic Synoptic Conditions, *J. Appl. Meteor.*, **28**, 760-781.

Sellers, W. D., 1965. *Physical Climatology*, University of Chicago Press, Chicago, pp. 272.

Sen O.L., Wang Y.,and Wang B., 2004a. Impact of Indochina deforestration on the East-Asian Moonsoon, *Journal of Climate*, **17**, 1366-1380.

Sen O.L., Wang Y.,and Wang B., 2004b. Impact of re-greening the desertification lands in northern China: implication from a regional climate model experiment, *Journal of the Meteorological Society of Japan*, **82**(6), 1679-1693.

Sensoy S., Demican M., Ulupinar Y. and Balta I., 2008. Türkiye İklimi, Meteoroloji Genel Mudurlugu, in Turkish.

Sha W., Kawamura T., and Ueda H., 1991. A numerical Study on Sea/Land Breezes as a Gravity Current: Kelvin Helmholtz Billows and Inland Penetration of the Sea-Breeze Front, *Journal of the Atmospheric Sciences*, **48**(14), 1649-1665.

Shepherd J.M., and Burian S.J., 2003. Detection of Urban-Induced Rainfall Anomalies in a Major Coastal City, *Earth Interactions*, **7**, 1-17.

Shreffler J. H., 1979a. Urban-Rural Differences in Tower-Measured Winds, St. Louis, *J. Appl. Meteor.*, **18**, 829-835.

Shreffler J. H., 1979b. Heat Island Convergence in St. Louis during Calm Periods, *J. Appl. Meteor.*, **18**, 1512-1520.

Sicardi V., Galmarini S., Riccio A., and Steyn D., 2005. Simulation of Land-sea Breeze Circulation on Sardinia Island using MM5 Mesoscale Model, *1st Conference on Harbours and Air Quality*, Genova 15th-17th June 2005.

Simpson J.E., 1994. *Sea Breeze and Local Wind*, Cambridge University Press, UK.

Simpson J.E., 1996. Diurnal Changes in Sea Breeze Direction, *J. of Appl. Meteor.*, **35**, 1166-1169.

Smith R.B., 1982. Synoptic Observations and Theory of Orographically Disturbed Wind and Pressure, *J. Atmos. Sci.*, **39**, 60-70.

Smolarkiewicz, P. K., 1984. A fully multidimensional positive definite advection transport algorithm with small implicit diffusion, *J. Comput. Phys.*, **54**, 325–362.

Someshwar D., Mohanty U. C., and Sharma O. P., 1988. Study of Kuo-type cumulus parameterizations during different epochs of the Asian summer monsoon, *Mon. Wea. Rev.*, **116**, 715-729.

Sorbjan, Z. and Uliasz, M., 1982. Some numerical urban boundary-layer studies. *Bound.-Layer Meteor.*, **22**, 481-502.

Srinivas C.V, Venkatesan R., Somayaji K.M., and Sing A.B., 2006. A Numerical Study of Sea Breeze Circulation Observed at a Tropical site Kalpakkam on the East Coast of India,Under different Synoptic Flow Situations, *J. Earth Syst. Sci*., **115**(5), 557-574.

Staley D.O., 1957. The Low-Level Sea Breeze of Northwest Washington, *J. of Meteorology*, **14**, 458-470.

Stephan K., Kraus H., Ewenz C.M. and Hacker J.M., 1999. Sea Breeze Front Variations in Space and Time, *Meteorology and Atmospheric Physics*, **70**, 81-95.

Steyn D.G. and Kallos G., 1992. A Study of the Dynamics of Hodograph Rotation in the Sea Breezes of Attica, Greece, *Bound.–Layer Meteor.*, 58, 215-228.

Streutker D.R., 2003. Satellite-Measured Growth of The Urban Heat Island of Houston, Texas, *Remote Sensing of Environment* , **85**(3), 282-289.

Stull R.B., 1988. *An Introduction to Boundary Layer Meteorology*, Kluwer Academic Publisher, Netherlands.

Svensson G., 1998. Model Simulations of the Air Quality in Athens, Greece, during the MEDCAPHOT-TRACE Campaign, *Atmos. Environ*, 32, 2239-2268.

Taha H., 1997. Urban climates and heat islands: albedo, evapotranspiration, and anthropogenic heat, *Energy and Buildings*, **25**, 99-103.

Tayanç M., Karaca M., and Yenigün O., 1997. Annual and Seasonal Air Temperature Trends Patterns of Climate Change and Urbanization Effects in Relation with Air Pollutants in Turkey, *Journal of Geophysical Research* , **102** (D2), 1909-1919.

Tereshchenko I.E., and Filonov A.E., 2001. Air temperature fluctuations in Guadalajara, Mexico, from 1926 to 1994 in relation to urban growth, *Int. J. Climatol*, **21**, 483-494.

Thielen J. and Gadian A., 1997. Influence of Topography and Urban Heat Island Effects on the Outbreak of Convective Storms under Unstable Meteorological Conditions: A Numerical Study, *Meteorol. Appl*., **4**, 139-149.

Thielen J., Wobrock W., Gadian A. Mestayer P.G. and Creutin J.D., 2000. The Possible Influence of Urban Surfaces on Rainfall Development: A Sensitivity Study in 2D in the Meso-γ-Scale, *Atmospheric Research*, 54, 15-39.

Thompson W.T., Holt T. and Pullen J., 2007. Investigation of a sea breeze front in an urban environment, *Q. J. R. Meteorol. Soc.*, **133**, 579-594.

Thorsson S., and Eliasson I., 2003. An intra-urban thermal breeze in Göteborg, Sweden, *Theor. Appl. Climatol.*, **75**, 93-104.

Tiedtke, M., 1986. The parameterization of moist processes. Part 2: Parameterization of cumulus convection. *ECMWF Lecture Note* No. 3.3, pp. 53.

Turkes M., 1990. Türkiye'de Kurak Bölgeler ve Önemli Kurak Yıllar, *Doktora Tezi*, Istanbul Universitesi Deniz Bilimleri ve Coğrafya Enstitüsü, Istanbul.

Turkish State Meteorological Service, 2008. Araştırma ve Bilgi İşlem Daire Başkanlığı İstasayon Verileri.

Ueda H., Mitsumoto S., and Kurita H., 1988. Flow Mechanism for the Long-Range Transport of Air Pollutants by the Sea Breeze Causing Nighttime High Oxidant, *J. Appl. Meteor.*, **27**, 182-187.

Uliasz, M., 1990. Development of the mesoscale dispersion modeling system using personal computers. Part I: Models and computer implementation, *Meteor. Z.*, **40**, 110–120.

Unger J., Sümeghy Z., and Zoboki J., 2001. Temperature Cross-Section Features in an Urban Area, *Atmospheric Research*, **58**, 117-127.

Urano, A., Ichinose, T. and Hanaki, K., 1999. Thermal environment simulation for three dimensional replacement of urban activity. *J. Wind. Eng. Ind. Aerodyn*., **81**, 197-210.

Url-1 <*http://www.srh.weather.gov/srh/jetstream/ocean/seabreezes.htm.*>, accessed at 02.03.2006.

Url-2 <*http://EETD.LBL.gov/HeatIsland*>, accessed at 15.04.2007.

Url-3 <*http://www.denizcilik.gov.tr/tr/istatistik*>, accessed at 05.09.2008.

Url-4 <*hptt://www.mmm.ucar.edu/mm5/documents*>, MM5 tutorial, accessed at 02.05.2009.

Van Den Heever S.C., and Cotton W.R., 2007. Urban Aerosol Impacts on Downwind Convective Storms, *J. Appl. Meteor. and Climatol.*, **46**, 828-850.

Van Ulden A.P. and. Holtslag A.A.M., 1985. Estimation of Atmospheric Boundary Layer Parameters for Diffusion Applications, *J. Appl. Meteor.*, **24**, 1196-1207.

Voogt J.A., and Oke T.R., 2003. Thermal Remote Sensing of Urban Climates. *Remote Sensing of Environment*, **86**(3), 370-384.

Vukovich F.M. and Dunn J.W., 1978. A Theoretical Study of the St. Louis Heat Island: Some Parameter Variations, *J. Appl. Meteor.*, **17**, 1585-1594.

Vukovich F.M., King W.J., Dunn J.W., and Worth J.J.B., 1979. Observations and Simulations of the Diurnal Variation of the Urban Heat Island Circulation and Associated Variations of the Ozone Distribution: A Case Study, *J. Appl. Meteor.*, **18**, 836-854.

Walsh J.E., 1974. Sea Breeze Theory and Applications, *J. Atmos. Sci*., **31**, 2012-2026.

Walter F.D., and E. Miller, 2000. Uncertainty, ensembles and air quality dispersion modeling: applications and challenges. *Atmospheric Environment*, **34**, 4667-4673.

Wang G., and Jenkins G.S., 2002: Deserts and desertification. *Encyclopedia of Atmospheric Sciences*, J.R .Holton, J.A. Curry, and J.A. Plye, Eds., Academic Press., pp. 633-640.

Warner T.T., R.-S. Sheu, J.F. Bowers, R.I. Skyes, G.C. Dodd and D.S. Henn, 2002. Ensemble simulations with coupled atmospheric dynamic and dispersion models: Illustrating uncertainties in dosage simulations. *J. of Appl. Meteor*., **41**, 488-504.

Weber R.O. and Kaufmann P., 1998. Relationship of Synoptic Winds and Complex Terrain Flows during the MISTRAL Field Experiment, *J. Appl. Meteor*., **37**, 1486-1496.

Weigel A. P., and Rotach M. W., 2004. Flow Structure and Turbulence Characteristics of the Daytime Atmosphere in a Steep and Narrow Alpine Valley, *Q.J.R. Meteorological Society*, **130**, 2605-2627.

Weigel A.P., Chow F.K., Rotach M.W., Street R.L. and Xue M., 2006. High-Resolution Large-Eddy Simulations of Flow in a Steep Alpine Valley. Part II: Flow Structure and Heat Budgets, *J. Appl. Meteorology and Climatology*, **45**, 87-107.

Westphal D.L., T. R. Holt, S. W. Chang, N. L. Baker, T. F. Hogan, L. R. Brody, R. A. Godfrey, J. S. Goerss, J. A. Cummings, D. J. Laws, C. W. Hines, 1999. Meteorological Reanalyses for the Study of Gulf War Illnesses: Khamisiyah Case Study. *Weather and Forecasting*, **14**, 215-241.

Wexler, A., 1976. Vapor pressure formulation for water in the range 0° to 100°C-- A Revision, *J. Res. Natl. Bur. Stand.*, **80a**, 775.

Whiteman C.D., 1982. Breakup of Temperature Inversions in Deep Mountain Valleys: Part I. Observations, *J. Appl. Meteor*., **21**, 270-289.

Whiteman C.D., and McKee T.B., 1982. Breakup of Temperature Inversions in Deep Mountain Valleys: Part II. Thermodynamic Model, *J. Appl. Meteor*., **21**, 290-302.

Whiteman C.D. and Doran J.C., 1993. The Relationship between Overlying Synoptic-Scale Flows and Winds within a Valley, *J. Appl. Meteor*., **32**, 1669-1682.

Whiteman C.D., McKee T.B., and Doran J.C., 1996. Boundary Layer Evolution within a Canyonland Basin. Part I: Mass, Heat, and Moisture Budgets from Observation, *J. Appl. Meteor.*, **35**, 2145-2161.

Whiteman C.D., 2000. *Mountain Meteorology: Fundamentals and Applications*, Oxford University Press, pp. 343.

Whiteman C.D., Pospichal B., Eisenbach S., Weihs P., Clements C., Steinacker R., Mursch-Radlgruber E. and Dorninger M., 2004a. Inversion Breakup in Small Rocky Mountain and Alpine Basins, *J. Appl. Meteor.*, **43**, 1069-1082.

Whiteman C.D., Haiden T., Pospichal B., Eisenbach S., and Steinacker R., 2004b. Minimum Temperature Diurnal Temperature Ranges, and Temperature Inversions in Limestone Sinkholes of Different Sizes and Shapes, *J. Appl. Meteor.*, **43**, 1224-1236.

Whiteman C.D., Eisenbach S., Pospichal B., and Steinacker R., 2004c. Comparison of Vertical Soundings and Sidewall Air Temperature Measurements in a Small Alpine Basin, *J. Appl. Meteor.*, **43**, 1635-1647.

Wilson, N. and Shaw, R., 1977. A higher order closure model for canopy flow. *J. Appl. Meteor.*, **16**, 1197-1205.

Wisner, C. H., Orville H. D., and Meyers C., 1972. A numerical model of a hail-bearing cloud. *J. Atmos. Sci.*, **29**, 160-1181.

Xian, Z. and R.A. Pielke, 1991. The effects of width of land masses on the development of sea breezes. *J. Appl. Meteor.*, **30**, 1280-1304.

Yagüe C., Zurita E., and Martinez A., 1991. Statistical analysis of the Urban Heat Island, *Atmos. Environ*., **25 B**, 327-332.

Yamada, T., 1982. A numerical study of turbulent airflow in and above a forest canopy. *J. Met . Soc. Japan*, **60**, 439-454.

Yamada T. and Bunker S., 1988. Development of a nested grid, second moment turbulence closure model and application to the 1982 ASCOT Brush Creek data simulation. *J. Appl. Meteorol.* **27**, 562–578.

Yan H. and Anthes R.A., 1987. The Effect of Latitude on the Sea Breeze, *Mon.Wea. Rev.*, **115**, 936-956.

Yoshikado H., 1981. Statistical Analyses of the Sea Breeze Pattern in relation to general weather conditions, *J. of Meteorological Society of Japan*, **59**, 98-108.

Yoshikado H. and Kondo H., 1989. Inland Penetration of the Sea Breeze over the Suburban Area of Tokyo, *Bound.-Layer Meteorology*, **48**, 389-407.

Yoshikado H., 1992. Numerical Study of the Daytime Urban Effect and Its Interaction with the Sea Breeze, *J. Appl. Meteor.*, **31**, 1146-1164.

Yoshikado H., 1994. Interaction of the Sea Breeze with Urban Heat Islands of Different Sizes and Locations, *J. of Meteorological Society of Japan*, **72**, 139-142.

Yoshikado H. and Tsuchida M., 1996. High Levels of Winter Air Pollution under the Influence of the Urban Heat Island along the Shore of Tokyo Bay, *J. Appl. Meteor.*, **35**, 1804-1813.

Zängl G, Egger J., and Wirth V., 2001. Diurnal Winds in the Himalayan Kali Gandaki Valley. Part II: Modeling, *Mon. Wea. Rev*., **129**, 1062-1080.

Zhong S. and Takle E.S., 1993. The Effects of Large-Scale Winds on the Sea-Land Breeze Circulations in an Area of Complex Coastal Heating, *J. Appl. Meteor.*, **32**, 1181-1195.

Zhou L.M., Dickinson R.E., Tian Y.H., Fang J.Y., Li Q.X., Kaufmann R.K., Tucker C.J., Myneni R.B., 2004. Evidence for a Significant Urbanization Effect on Climate in China. *Proceedings of The National Academy of Sciences of The United States Of America*, **101** (26), 9540-9544.

Zhu M. and Atkinson B.W., 2004. Observed and Modeled Climatology of the Land-Sea Breeze Circulation over the Persian Gulf, *Int. J. Climatol*., **24**, 883-905.

APPENDICES

APPENDIX A

A1.1 Fundemental Equation of MM5

The equations for the nonhydrostatic model's basic variables excluding moisture in terms of terrain following coordinates (x, y, σ) will be given in the following lines.

Pressure

$$\frac{\partial p'}{\partial t} - \rho_0 g w + \gamma p \nabla \cdot V = -V \cdot \nabla p' + \frac{\gamma P}{T}\left(\frac{\dot{Q}}{C_p} + \frac{T_0}{\theta_0} D\theta\right) \quad \textbf{(A1.1)}$$

Momentum (x-components)

$$\frac{\partial u}{\partial t} + \frac{m}{\rho}\left(\frac{\partial p'}{\partial x} - \frac{\sigma}{p^*}\frac{\partial p^*}{\partial x}\frac{\partial p'}{\partial \sigma}\right) = -V \cdot \nabla u + v\left(f + u\frac{\partial m}{\partial y} + v\frac{\partial m}{\partial x}\right) - ew\cos\alpha - \frac{uw}{r_{earth}} + D_u \quad \textbf{(A1.2)}$$

Momentum (y-components)

$$\frac{\partial v}{\partial t} + \frac{m}{\rho}\left(\frac{\partial p'}{\partial y} - \frac{\sigma}{p^*}\frac{\partial p^*}{\partial y}\frac{\partial p'}{\partial \sigma}\right) = -V \cdot \nabla v + u\left(f + u\frac{\partial m}{\partial y} + v\frac{\partial m}{\partial x}\right) + ew\sin\alpha - \frac{vw}{r_{earth}} + D_v \quad \textbf{(A1.3)}$$

eu and ew representing the neglected components of the Coriolis force, where $u\frac{\partial m}{\partial y}$, $v\frac{\partial m}{\partial x}$, and r_{earth}, represent curvature effects, and m is map scale factor.

Momentum (z-components)

$$\frac{\partial w}{\partial t} - \frac{\rho_0}{\rho}\frac{g}{p^*}\frac{\partial p'}{\partial \sigma}\frac{g p'}{\gamma p} = -V \cdot \nabla w + g\frac{p_0}{p}\frac{T'}{T_0} - \frac{g R_d}{C_p}\frac{p'}{p} + e(u\cos\alpha - v\sin\alpha) + \frac{u^2 + v^2}{r_{earth}} + D_w \quad \textbf{(A1.4)}$$

eu and ew representing the neglected components of the Coriolis force, where $e = 2\Omega\cos\lambda$, $\alpha = \phi - \phi_c$, λ is latitude, ϕ is longitude, and ϕ_c is central longitude.

Thermodynamics

$$\frac{\partial T}{\partial t} = -V \cdot \nabla T + \frac{1}{\rho C_p}\left(\frac{\partial p'}{\partial t} + V.\nabla p' - \rho_0 g w\right) + \frac{Q}{C_p} + \frac{T_0}{\theta_0} D_\theta \quad \textbf{(A1.5)}$$

Advection Terms

$$V \cdot \nabla A = mu\frac{\partial A}{\partial x} + mv\frac{\partial A}{\partial y} + \dot{\sigma}\frac{\partial A}{\partial \sigma} \quad \textbf{(A1.6)}$$

where

$$\dot{\sigma} = -\frac{\rho_0 g}{p^*}w - \frac{m\sigma}{p^*}\frac{\partial p^*}{\partial x}u - \frac{m\sigma}{p^*}\frac{\partial p^*}{\partial y}v \quad \textbf{(A1.7)}$$

Divergence Term

$$\nabla \cdot V = m^2\frac{\partial}{\partial x}\left(\frac{u}{m}\right) - \frac{m\sigma}{p^*}\frac{\partial p^*}{\partial x}\frac{\partial u}{\partial \sigma} + m^2\frac{\partial}{\partial y}\left(\frac{v}{m}\right) - \frac{m\sigma}{p^*}\frac{\partial p^*}{\partial y}\frac{\partial v}{\partial \sigma} - \frac{\rho_0}{p^*}g\frac{\partial w}{\partial \sigma} \quad \textbf{(A1.8)}$$

Prognostic equations exist for water vapor and microphysical variables. Physics parameterizations in MM5 such as for cumulus parameterization, PBL scheme, explicit moisture scheme, radiation scheme, surface scheme have many options in MM5. Therefore details of the physical options can be found in MM5 tutorial.

A1.2 Lateral Boundary Conditions

Terrestarial and real-time atmospheric data are horizontally interpolated from a latitude-longitude grid to a mesoscale rectangular domain by the TERRAIN and REGRID programs for different projections (Mercator, Lambert Conformal or Polar Stereographic). Model provides to use surface observation and rawinsonde data to implement more mesoscale detail by LİTTLE_R/RAWINS moduls using a successive-scan Cressman or multiquadric technique. Vertical interpolation from pressure levels to the σ-levels of the MM5 model is provided by the program INTERPF. Program INTERPB can be used to interpolate data from σ-levels to pressure levels and NESTDOWN module interpolates model data to a finer grid.

Numerical models require lateral boundary conditions to start a simulations. Horizontal wind, temperature, pressure and moisture fields are specified for four boundaries. The boundary values come from either analyses at the future times, or a previous coarser-mesh simulation (1-way nest), or from another model's forecast (in real-time forecasts). For real-time forecasts the lateral boundaries depend on a global-model forecast (MM5 tutorial, 2009).

The model uses these discrete-time analyses by linearly interpolating them in time to the model time. The analyses completely specify the behaviour of the outer row and column of the model grid. In the next four rows and columns in from the boundary, the model is nudged towards the analyses, and there is also a smoothing term. The

strength of this nudging decreases linearly away from the boundaries. The model uses a boundary file with information for the five points nearest each of the four boundaries at each boundary time to apply this conditions. The interior values from these analyses are not required unless data assimilation by grid-nudging is being performed, so disk-space is saved by having the boundary file just contain the rim values for each field (MM5 tutorial, 2009).

Two-way nest boundaries are similar but are updated every coarse-mesh timestep and have no relaxation zone. The specified zone is two grid-points wide instead of one.

MM5 uses topography and landuses, gridded atmospheric sea-level pressure, wind, temperature, relative humidty and geopotential height data at 1000, 850, 700, 500, 400, 300, 250, 200,150 and 100 mb pressure levels. Datasets for initial and boundary can be obtained either NCEP or ECMWF (MM5 tutorial, 2009).

APPENDIX A2

A2.1 Fundamental Equation Sets of OMEGA

OMEGA uses a fully elastic non-hydrostatic equation set, including applicable assumptions. The five mixing ratios for water substances were briefly classified into three groups: water vapor, Q_v; precipitating water substances, Q_p (rain, snow or hail); and non-precipitating water substances, Q_n(ice crystal, water vapor or water droplets). The equations are calculated in their conservative form consistent with the fully elastic mass-conservation equation. This form is better suited for upwind advection schemes that were used in OMEGA, which have significantly less numerical diffusion.

The atmospheric pressure and density were decomposed into a time-variant hydrostatic base state and a perturbation upon that state such that;

$$p(x,y,z,t) = p_0(x,y,z) + p'(x,y,z,t), \text{ and} \quad \textbf{(A2.1)}$$

$$\rho(x,y,z,t) = \rho_0(x,y,z) + \rho'(x,y,z,t) \quad \textbf{(A2.2)}$$

$$\frac{\partial p_0}{\partial z}(x,y,z) = -g\rho_0(x,y,z) \quad \textbf{(A2.3)}$$

Bacon (2003) states that the conservative advection terms appear on the left side of each equation. The source terms on the right side of the momentum equation include buoyancy and gravitational effects, $-(\rho-\rho_0)g\hat{r}$ (where $\hat{r}$ is the radial unit vector), and the Coriolis force $(-2\rho\Omega\times V)$. Variable F represents the subgrid-scale turbulence contributions. For the remaining equations, T is the temperature, L_j and S_j denote latent heat and rate of phase conversion of either vaporization, fusion or sublimation; and W_p represents the terminal velocity of each of the precipitating water substances. S_j depends on the microphysics that governs the rate of phase transitions and W_a depends on the assumed size distribution and mass of the hydrometeors. M_n, and

M_p are the non-precipitating and precipitating microphysics source terms and subscript "a" refers to transport of aerosol or gas (Bacon et al., 2000).

Following equations use in the model for the conservation of mass, momentum and energy.

Conservation of mass:

$$\frac{\partial \rho}{\partial t} + \nabla \cdot (\rho V) = F_p \qquad \textbf{(A2.4)}$$

$$\frac{\partial \rho Q_n}{\partial t} + \nabla \cdot (\rho \rho_n V) = \rho M_n + F_{Q_n} \qquad \textbf{(A2.5)}$$

$$\frac{\partial \rho Q_p}{\partial t} + \nabla \cdot (\rho Q_p V) = \rho M_p + \frac{\partial}{\partial z}\left(Q_p W_p \rho\right) + F_{Q_p} \qquad \textbf{(A2.6)}$$

$$\textit{and } \frac{\partial \rho Q_a}{\partial t} + \nabla \cdot (\rho Q_a V) = \rho M_a + \frac{\partial}{\partial z}\left(Q_a W_a \rho\right) + F_{Q_a} \qquad \textbf{(A2.7)}$$

The subscript a refers to aerosols or gases, and ρ represents the dry air density calculated from the total density as

$$\rho = \rho / (1 + Q_{vapor}) \qquad \textbf{(A2.8)}$$

Conservation of momentum:

$$\frac{\partial \rho V}{\partial t} + \nabla \cdot (\rho V V) = -\nabla p' - \left(\rho - \rho_0\right) g \hat{r} - 2\rho \Omega \times V + F_M \qquad \textbf{(A2.9)}$$

The density used in equation 3.10 is the total density.

Conservation of energy:

$$\frac{\partial E}{\partial t} + \nabla \cdot (EV) = \frac{E}{C_p T} \sum_j (L_j S_j) + S_R + F_h \qquad \textbf{(A2.10)}$$

The initial energy density E is calculated from the total pressure as

$$E = p^{1-\kappa} \left(\frac{p_{ref}^{\kappa}}{R_d} \right) \qquad \textbf{(A2.11)}$$

and throughout the simulation pressure is diagnosed from energy density using relationship. Potential temperature, θ, and temperature, T, are related by Poisson's equation,

$$T = \theta\left(\frac{p}{p_{ref}}\right)^{\kappa} \qquad \textbf{(A2.12)}$$

where $p_{ref} = 1000mb$, $\kappa = R_d / C_p = 0.286$, R_d is the gas constant for dry air at constant, and C_p is the specific heat of dry air at constant pressure. S_R represents the contribution of radiation flux to heating the atmosphere (Bacon et al., 2000).

Navier-Stokes equations on an unstructured grid in horizontal and a structured grid in vertical are basis of the OMEGA model hydrostatic elements. While calculating the momentum, the Coriolis parameter, the pressure gradient and buoyancy terms in the momentum are calculate explicitly along with the advection terms. An implicit vertical filter and an explicit horizontal filter are applied to the vertical momentum calculation.

A2.2 Model Physics

The OMEGA model includes radiation transport which is important in determining the solar heating of the earth surface and the atmosphere. Cloud microphysics and convective parameterization are important to indicate distribution of the vertical moisture, energy and the formation of precipitation. Atmospheric turbulence is important in the rate of the surface moisture and energy enters the atmosphere (Bacon, 2003).

A2.2.1 Turbulence and the planetary boundary layer

Parameterization of turbulence in OMEGA has horizontal and vertical parts. The horizontal diffusion is a function of the deformation of momentum, and multilevel planetary boundary layer (PBL) model is used for the vertical diffusion. There are two approaches to implement the PBL into a mesoscale model. One approach is to parameterize the entire PBL as one layer. The reason why the single layer PBL is complex is that it lies in the variety and interdependence of atmospheric processes acting on different scale. The second approach is to use multiple levels in the PBL so as to resolve the boundary layer structure efficiently and explicitly. The atmospheric PBL in OMEGA is treated as three layers: the viscous sublayer, the surface layer and the transition layer (Bacon, 2003).

A2.2.1.1 Viscous sublayer

The viscous sublayer is defined as the level where the molecular motion becomes important near the ground. Temperature and specific humidity are related to their ground values in the viscous sublayer (Deardorf, 1974).

$$\bar{\theta}_{z0} = \theta_G + 0.0962(\theta / k)\left(u\ z_0 / \nu\right)^{0.45} \quad \textbf{(A2.13)}$$

$$and\ \ \bar{q}_{z0} = q_G + 0.0962(q / k)\left(q\ z_0 / \nu\right)^{0.45} \quad \textbf{(A2.14)}$$

By analogy for other gaseous and atmospheric materials (χ)

$$\bar{\chi}_{z0} = \chi_G + 0.0962(\chi / k)\left(q\ z_0 / \nu\right)^{0.45} \quad \textbf{(A2.15)}$$

ν is the kinematic viscosity of air, k, von Karman's constant, u_*, the friction velocity, z_0, the surface roughness length, θ_*, the subgrid scale temperature flux, and q_*, the subgrid scale moisture flux. The variation of pressure is ignored and $\bar{u} = \bar{v} = \bar{w} = 0$ is assumed in the viscous layer.

A2.2.1.2 Surface layer

There is no exact definition of surface layer which may be more than one model layer and it is immediately above the viscous sublayer. The surface layer is above the viscous sublayer where small-scale turbulence dominates the transfer of energy, moisture, and momentum. The vertical fluxes variation is roughly less than 10% in vertical. The depth of this layer usually varies from 10 m to 100 m. Beljiaars and Holstslag (1991) formulae are mostly used in mesoscale models in which

$$u_* = kV_1 / \left[\ln\left(z_1 / z_0\right) - \psi_M\left(z_1 / L\right) + \psi_M\left(z_0 / L\right)\right] \quad \textbf{(A2.16)}$$

$$\theta_* = k\left(\theta_1 - \theta_s\right) / \left[\ln\left(z_1 / z_0\right) - \psi_H\left(z_1 / L\right) + \psi_H\left(z_0 / L\right)\right], \quad \textbf{(A2.17)}$$

$$q_* = k\left(q_1 - q_s\right) / \left[\ln\left(z_1 / z_0\right) - \psi_H\left(z_1 / L\right) + \psi_H\left(z_0 / L\right)\right], \text{ and} \quad \textbf{(A2.18)}$$

$$\chi_* = k\left(\chi_1 - \chi_s\right) / \left[\ln\left(z_1 / z_0\right) - \psi_H\left(z_1 / L\right) + \psi_H\left(z_0 / L\right)\right] \quad \textbf{(A2.19)}$$

$V_1, \theta_1, q_1, and\ \chi_1$ are wind speed, potential temperature, specific humidity, and other gas concentrations at the first model level in the atmosphere, respectively. $\theta_s, q_s, and\ \chi_s$ are the corresponding surface values, u_* is the friction velocity, θ_* is the temperature scale, q_* is the humidity scale, χ_* is the other gaseous scale, k is the von Karman constant (k =0.4), z_1 is the height of the first model level, and L is the

Monin-Obukhov length, ψ_M and ψ_H are dimensionless stability functions of height. These integral functions for unstable surface layer are given by

$$\psi_M = 2\ln\left[(1+x)/2\right] + \ln\left[(1+x^2)/2\right] - 2\tan^{-1}(x) + \pi/2 \quad \textbf{(A2.20)}$$

$$\psi_H = 2\ln\left[(1+x^2)/2\right] \quad \textbf{(A2.21)}$$

where $x = (1-16z/L)^{1/4}$

In stable surface layer the following formulae are used

$$-\psi_M = a\frac{z}{L} + b\left(\frac{z}{L} - \frac{c}{d}\right)\exp\left(-d\frac{z}{L}\right) + \frac{bc}{d} \quad \textbf{(A2.22)}$$

$$-\psi_H = \left(1 + \frac{2}{3}\frac{az}{L}\right)^{3/2} + b\left(\frac{z}{L} - \frac{c}{d}\right)\exp\left(-d\frac{z}{L}\right) + \frac{bc}{d} - 1 \quad \textbf{(A2.23)}$$

where $a = 1$, $b = 0.667$, $c = 5$, $d = 0.35$, and z/L is a non-dimensional stability parameter. The Monin-Obukov stability length, L is defined as

$$L = \frac{\overline{\theta} u_*^2}{kg\theta_*} \quad \textbf{(A2.24)}$$

where $\overline{\theta}$ is the average air temperature near the surface, and *g* is the gravity.

A2.2.1.3 Transition layer

The turbulent region from the surface up to the top of the PBL is called transition layer. Depending on the turbulent strength generated at the ground surface, the PBL depth varies. The PBL height can be considered to be the depth of turbulent activity. Forced convection loses its effects with height rapidly than thermal convection in this layer. Thus, this layer is generally well-mixed and is characterized by free convection involving large eddies associated with thermals and heat plumes. Turbulence can be parameterized in terms of the mean flow, which leads to the closure problem. The 2.5 level turbulence kinetic energy (TKE) closure technique is used in OMEGA. TKE closure takes an account the physics of the atmosphere in the formulation of the eddy diffusivity, K. The level 2.5 closure technique developed by Mellor-Yamada (1974) is used for the vertical turbulent exchange above the surface layer. The level 2.5 turbulence closure is based on the following prognostic equation for the turbulent kinetic energy, *e*:

$$\frac{\partial(\rho e)}{\partial t} = -\nabla \cdot (\rho e V) + \nabla_r \cdot (K_e \nabla_r \rho e) + \left[-\overline{u'w'}\frac{\partial u}{\partial z} - \overline{v'w'}\frac{\partial v}{\partial z} + \frac{g}{\theta}\overline{w'\theta'} \right] - \varepsilon \quad \textbf{(A2.25)}$$

The first two terms on the right hand side represent advection and turbulent transport of TKE (∇_r represents the radial gradient), the third term in the bracket represent both shear and buoyancy production of TKE, and the forth term dissipation of turbulent energy. Several terms on the right hand side must be parameterized in this scheme. The eddy fluxes are parameterized using Deardorf (1980) formulas,

$$\left(\overline{u'w'}, \overline{v'w'}\right) = -K_m \left(\frac{\partial u}{\partial z}, \frac{\partial v}{\partial z} \right) \quad \textbf{(A2.26)}$$

$$\left(\overline{w'\theta'}\right) = -K_h \left(\frac{\partial \theta_v}{\partial z} \right), \text{ and} \quad \textbf{(A2.27)}$$

$$\left(\overline{w'q'}\right) = -K_q \left(\frac{\partial q}{\partial z} \right) \quad \textbf{(A2.28)}$$

Energy dissipation ε is parameterized using Kolmogorov's hypothesis,

$$\varepsilon = c_\varepsilon e^{3/2} / \ell \quad \textbf{(A2.29)}$$

where c_e is a constant equal to 0.17. In the 2.5 level turbulence closure scheme, the prognostic equations of all second-order moments are reduced to algebraic equations. It allows the expression of eddy diffusivities after considerable algebraic reduction in the following simple form:

$$K_m = \ell (2e)^{1/2} S_M \quad \textbf{(A2.30)}$$

$$K_h = \ell (2e)^{1/2} S_H \quad \textbf{(A2.31)}$$

$$\text{and } K_e = \ell (2e)^{1/2} S_e \quad \textbf{(A2.32)}$$

where non-dimensional eddy diffusivities S_M and S_H are obtained from

$$S_M (6A_1A_2G_M) + S_H (1 - 3A_2B_2G_H - 12A_1A_2G_H) = A_2 \text{ and} \quad \textbf{(A2.33)}$$

$$S_M (1 + 6A_1^2 G_M - 9A_1A_2G_H) - S_H (12A_1^2 G_H + 9A_1A_2G_H) = A_1(1 - 3C_1) \quad \textbf{(A2.34)}$$

$$G_M = \frac{\ell^2}{2e}\left[\left(\frac{\partial u}{\partial z}\right)^2 + \left(\frac{\partial v}{\partial z}\right)^2 \right] \quad \textbf{(A2.35)}$$

$$\text{and } G_H = -\frac{\ell^2}{2e}\frac{g}{\theta}\frac{\partial \theta_v}{\partial z} \quad \textbf{(A2.36)}$$

After Mellor and Yamada (1982), empirical constants are assigned (A_1, A_2, B_1, B_2, C_1, S_e) = (0.92, 0.74, 16.6, 10.1, 0.08, 0.20). In order to reduce the singularities of the 2.5 level closure scheme, assumption for $G_M \le 0.033$ and $G_M \le 0.825 - 25G_H$ is conducted. The turbulent length scale ℓ is unknown and needs to be parameterized in terms of the known variables. After Mellor and Yamada (1982)

$$\ell = \frac{k(z + z_0)}{1 + k(z + z_0)/\ell_\infty} \qquad \textbf{(A2.37)}$$

where ℓ_∞ is the primary length scale defined as

$$\ell_\infty = \alpha \frac{\int_0^H \sqrt{e\, z\, dz}}{\int_0^H \sqrt{e\, dz}} \qquad \textbf{(A2.38)}$$

α is a constant coefficient of the order of 0.1. The stable mixing length is modified with an upper limit using following equation which is proposed by Andre et al. (1978) to change the mixing length from natural to the slightly stable condition.

$$\ell \le 0.75 \left[\frac{2e}{\frac{g}{\theta}\frac{\partial \theta_v}{\partial z}} \right]^{1/2} \qquad \textbf{(A2.39)}$$

A2.3 Air-Surface Interactions

Temperature and humidity at the roughness level are used as boundary conditions in OMEGA. These variables must be calculated prognostically taking the interaction of the atmosphere and the land surface into account. Using numerical models it has been demonstrated that local circulations as strong as sea breezes can be generated by the land surface characteristics contrasts such as, vegetation type, soil texture and moisture (McCorcle, 1988; Chang and Wetzel, 1990). The land surface scheme in OMEGA is proposed by Noilhan and Planton (1989). Only one energy balance is used for whole soil-vegetation system. A single surface skin temperature, T_s, and surface air humidity q_s are computed for the canopy and the ground. The calculation of two distinct temperatures for the soil surface and the vegetation requires an

evaluation of radiative and turbulent transfers between the soil, the plant, and the air inside the canopy, which increases the complexity of the scheme (Bacon, 2003).

Table A2. 1 : Soil parameters for the USDA textural classes (Bacon, 2003).

Category	Type of soil	η_σ	$\eta_{\omega\dot{\iota}.\tau}$	$\eta_{\phi\chi}$	Ψ_σ	$K_{\eta\sigma}$	β	$\rho_i\chi_\iota$	A_0	$X_{\gamma\sigma\alpha\tau}$
1	Sand	0.395	0.068	0.135	-0.121	$1.76x10^{-4}$	4.05	$1.463x10^6$	0.26	3.222
2	Loam sand	0.410	0.075	0.150	-0.090	$1.563x10^{-4}$	4.38	$1.404x10^6$	0.27	3.057
3	Sandy loam	0.435	0.114	0.195	-0.218	$3.41x10^{-3}$	4.90	$1.320x10^6$	0.28	3.560
4	Silt loam	0.485	0.179	0.255	-0.786	$7.2x10^{-6}$	5.30	$1.271x10^6$	0.29	4.418
5	Loam	0.451	0.155	0.240	-0.478	$7.0x10^{-6}$	5.39	$1.212x10^6$	0.30	4.111
6	Sandy clay loam	0.420	0.175	0.255	-0.299	$6.3x10^{-6}$	7.12	$1.175x10^6$	0.28	3.670
7	Silty clay loam	0.477	0.218	0.322	-0.356	$1.7x10^{-6}$	7.75	$1.317x10^6$	0.26	3.593
8	Clay loam	0.476	0.250	0.325	-0.630	$2.5x10^{-6}$	8.52	$1.225x10^6$	0.24	3.995
9	Sandy loam	0.426	0.219	0.310	-0.153	$2.2x10^{-6}$	10.4	$1.175x10^6$	0.22	3.058
10	Silty loam	0.492	0.283	0.370	-0.490	$1.0x10^{-6}$	10.4	$1.115x10^6$	0.21	3.729
11	Clay	0.482	0.286	0.367	-0.405	$1.3x10^{-6}$	11.4	$1.089x10^6$	0.20	3.600
12	Silt	0.485	0.179	0.535	-0.786	$8.0x10^{-6}$	5.30	$0.836x10^6$	0.14	3.970

The land surface scheme allows two soil layers and a single vegetation canopy. The evolution of four variables is computed by the scheme: the surface temperature of the soil-vegetation medium T_s, the soil water contents in the upper and lower soil layers η_1 and η_2, and the amount of liquid water retained on the foliage W_d. Primary and secondary parameters are used to describe the main physical processes in a soil-vegetation system. Primary parameters are specified by spatial distribution, and secondary parameters can be associated with the values of the primary parameters. Type of soil texture and type of land are the primary parameters that the land-use in the modeling is classified into several categories characterized by those two numerical indices. The secondary parameters which describe a variety of physical characteristics of soil are listed in Table A2.1 (Bacon, 2003).

A2.3.1 Surface temperature

Ground temperature T_s is the indicator of surface variation. OMEGA calculates ground temperature using force-restore rate equation of Deardorff (1978).

$$\frac{\partial T_s}{\partial t} = C_T G_0 + \Omega\left(T_{ds} - T_s\right) \qquad \textbf{(A2.40)}$$

where Ω is angular velocity of the earth $\left(\Omega = 7.27229\times10^{-5}\,s^{-1}\right)$, and G_0 is the heat storage rate in the soil-vegetation medium, which is sum of all the atmospheric fluxes at the surface

$$G_0 = R_0 + H_{anthrop} - \left(H_0 + L_c E_0\right) \qquad \textbf{(A2.41)}$$

where R_0 is the net radiation at the surface, $H_{anthrop}$ is the anthropogenic heat flux, H_0 and $L_c E_0$ are the sensible and latent heat fluxes from the atmosphere. Monin-Obukov similarity theory is used to parameterize the surface turbulent fluxes. The turbulent subgrid scale friction velocity, u_*, temperature scale, θ_*, and humidity scale, q_* are used to calculate the sensible heat flux to the atmosphere, H_0 and the latent heat flux from evaporation or dew formation, $L_c E_0$.

$$H_0 = \rho C_p\, u_*\, \theta_* \qquad \textbf{(A2.42)}$$

and $L_c E_0 = \rho L_c\, u_*\, q_*$ **(A2.43)**

If urban and industrial areas are considered, $H_{anthrop}$ may be used to complete the forcing terms in the force-restore equation. Diurnal forcing of T_s by the heat storage rate in the soil-vegetation medium, G_0, is given from the first term on the right hand side of equation 3.41, and second term tends to restore T_s to the mean soil temperature T_{ds}.

The combination of capacities of vegetation C_{veg}, and soil C_g are weighted by vegetation cover (veg) and bare soil cover (1-veg) gives the thermal capacity C_T (Noilhan and Planton, 1989).

$$\frac{1}{C_T} = \frac{veg}{C_{veg}} + \frac{1-veg}{C_g} \qquad \textbf{(A2.44)}$$

The value of C_{veg} $\left(10^{-3} K^{-1} m^2 J^{-1}\right)$ is related to the weak heat storage and transfer ability of vegetation. The thermal capacity of soil

$$C_g = \frac{\sqrt{2\Omega}}{I_s} \qquad \textbf{(A2.45)}$$

is given by its thermal inertia

$$I_s = \sqrt{\rho_s c_s \lambda_s} = \frac{\rho_s c_s d_s}{\sqrt{\tau_1}} \quad \textbf{(A2.46)}$$

where ρ_s is the density of soil, c_s is the specific heat of soil, and λ_s is thermal soil conductivity coefficient. T_{ds} represents the constant mean deep soil temperature at the diurnal temperature cycle penetrative soil depth

$$d_s = \sqrt{\frac{\tau_1 \lambda_s}{\rho_s c_s}} \quad \textbf{(A2.47)}$$

where τ_1 is the period of 1 day.

The soil properties in Equation A2.45 are represented by the soil texture and the soil moisture. This dependence is deduced from the analytical expression given by Noilhan and Planton (1989)

$$C_g = C_{g_{sat}} \left(\frac{\eta_s}{\eta} \right)^{b/2\log 10} \quad \textbf{(A2.48)}$$

where $C_{g_{sat}}$, η_s, and b are estimated for each soil texture from Table A2.1.

A2.3.2 Surface flux of radiation

Two empirical functions provide to obtain the net shortwave solar radiation at the surface. The first function is a Rayleigh transmission function which involves the effects of molecular scattering and absorption by permanent gaseous such as oxygen, ozone, and carbon dioxide (Atwater and Brown, 1974)

$$G = 0.485 + 0.515\left[1.041 - 0.16\left(\frac{0.000949p + 0.051}{\cos Z}\right)^{1/2}\right] \quad \textbf{(A2.49)}$$

where p is pressure in mb. A second function used in the model calculates the absorptivity of water vapor (McDonald, 1960).

$$a_w = 0.077\left[\frac{r(z)}{\cos Z}\right]^{0.3} \quad \textbf{(A2.50)}$$

where r is the optical path length of water vapor above the layer z given by

$$r(z) = \int_z^{top} \rho\, q\, dz \quad \textbf{(A2.51)}$$

The net shortwave solar radiation at the surface is

$$R_S = \begin{cases} (1-A_g)(a_1 \cos Z + a_2)(G - a_w)(1 - b_1 N_E^{b_2}) \cos Z > -a_2/a_1 \\ 0 \qquad\qquad\qquad\qquad\qquad\qquad \cos Z \le -a_2/a_1 \end{cases} \qquad \textbf{(A2.52)}$$

where A_g is the albedo, the empirical coefficients are $a_1 = 990 Wm^{-2}$, $a_2 = -30 Wm^{-2}$, and Z is the zenith angle.

$$\cos Z = \cos\psi \cos\delta \cos H + \sin\psi \sin\delta \qquad \textbf{(A2.53)}$$

ψ is the latitude, δ the solar declination, which is a function of Julian day, and H the solar hour angle

$$H = \frac{\pi(t-12)}{12} \qquad \textbf{(A2.54)}$$

where t is local time in hours. The cloud effects on the incoming radiation are parameterized applying the effective cloud cover N_E proposed by Kasten and Czeplak (1980).

$$N_E = (N_T + N_L)/2 \qquad \textbf{(A2.55)}$$

N_T is the total cloud cover, and N_L is the low clouds cover. Empirical coefficients are $b_1 = 0.75$, and $b_2 = 3.4$.

The net longwave radiation has two components; one is incoming radiation from the atmosphere (atmospheric radiation), and second is ongoing radiation from the surface (terrestrial radiation)

$$R_L = R_{L\downarrow} - R_{L\uparrow} \qquad \textbf{(A2.56)}$$

The incoming longwave radiation is;

$$R_{L\downarrow} = c_1 T_a^6 + c_2 N_E \qquad \textbf{(A2.57)}$$

$c_1 = 5.31 \times 10^{-13} Wm^{-2} K^{-6}$, $c_2 = 60 Wm^{-2}$, and the reference air temperature T_a at $z = 50m$ is recommended by Van Ulden and Holtslag (1985). The outgoing longwave radiation from the surface arises from Stefan-Boltzman law

$$R_{L\uparrow} = \varepsilon_g T_s^4 \qquad \textbf{(A2.58)}$$

ε_g is the emissivity for the ground surface specified in terms of land-use categories, σ is the Stefan-Boltzman's constant $(5.67\times10^{-8} Wm^{-2}K^{-4})$. The net radiation flux at ground level is defined as

$$R_0 = R_S + R_L \qquad \textbf{(A2.59)}$$

The surface energy budget is updated every time-step in order to enable an updated ground temperature. The ground temperature is related to the potential temperature in the lowest model cell by the following equation:

$$\theta_{sfc} = T_g\left(\frac{P_{ref}}{P}\right)^{\kappa} \qquad \textbf{(A2.60)}$$

P_{ref} is the reference pressure, 1000 *mb*.

A2.3.3 Soil hydrology

The energy balance of the surface is affected by the soil wetness by changing the surface albedo, by affecting the soil heat flux through the thermal diffusivity, and by determining the partitioning of the heat fluxes into latent and sensible heat flux. The 2-layer soil model developed by Mahrt and Pan (1984) is used to represent the soil moisture in the model. Following prognostic equation is used to describe the transport of water in the soil in the model.

$$\frac{\partial\eta}{\partial t} = \frac{1}{\rho_w}\frac{\partial W_s}{\partial z} + A(z) \qquad \textbf{(A2.61)}$$

η is the volumetric soil moisture content, ρ_w is the density of liquid water, W_s is the moisture flux within the soil. Extraction of the soil water by roots due to the transpiration E_{tr} from vegetation canopy is given by the term $A(z)$. The soil moisture flux is expressed as

$$W_s = K_\eta \rho_w \frac{\partial(\Psi + z)}{\partial z} \qquad \textbf{(A2.62)}$$

or in alternate form as $W_s = D_\eta \rho_w \frac{\partial\eta}{\partial z} + K_\eta \rho_w$ **(A2.63)**

K_η is the hydraulic conductivity, the potential energy needed to extract water against capillary and adhesive forces in the soil is represented by the moisture potential, Ψ, and the diffusivity, D_η, is defined as

$$D_\eta = K_\eta \frac{\partial \Psi}{\partial \eta} \tag{A2.64}$$

The parameters K_η, D_η, and Ψ are related to η through a set of simple relationships presented by Clapp and Hornberger (1978) and applied by McCumber and Pielke (1981)

$$K_\eta = K_{\eta s}\left(\frac{\eta}{\eta_s}\right)^{2b+3} \tag{A2.65}$$

$$D_\eta = -\frac{bK_{\eta s}\Psi_s}{\eta}\left(\frac{\eta}{\eta_s}\right)^{b+3} \tag{A2.66}$$

$$\Psi = \Psi_s\left(\frac{\eta_s}{\eta}\right)^{b} \tag{A2.67}$$

Percentage of clay, silt and sand (Table A2.1) determines the USDA soil texture classes which is used to specify the exponent b, saturated hydraulic conductivity $K_{\eta s}$, saturated moisture potential Ψ_s, and soil moisture at field capacity (soil porosity) η_s. Following Mahrt and Pan (1984) equation (4.50) is integrated over two slabs of the soil, from $z = 0$ to $z = -0.05\ m$, and from $z = -0.05\ m$ to $z = -1.0\ m$. This gives two prognostic equations for the mean volumetric water content in the upper thin layer, η_1, and in the lower layer, η_2.

$$\frac{\partial \eta_1}{\partial t} z_1 = -\left(D_\eta \frac{\partial \eta}{\partial z}\right)_i - K_{\eta i} + \frac{P_g - E_g}{\rho_w} - f_{root}\, E_{tr} \tag{A2.68}$$

$$\frac{\partial \eta_2}{\partial t}(z_2 - z_1) = -\left(D_\eta \frac{\partial \eta}{\partial z}\right)_i + K_{\eta i} - K_{\eta 2} - (1 - f_{root})\, E_{tr} \tag{A2.69}$$

By assuming that the upper soil layer contains fraction f_{root} of root mass the root extraction term $A(z)$ is integrated while the remaining fraction of roots $1 - f_{root}$ is within the lower soil layer. Continuity at the soil surface requires that the flux W_s of water in the soil at $z = 0$ equals of the sum of the flux P_g of liquid water reaching the ground surface and the evaporation E_g from the soil surface

$$-D_{\eta 1}\frac{\partial \eta}{\partial z} - K_{\eta i} = \frac{P_g - E_g}{\rho_w} \tag{A2.70}$$

The gradient of soil water content at the interfacial level, $-z_1$, is evaluated as a finite

difference assuming that the mean value of η for each layer is represented for the midlevel of the layer

$$\left(D_\eta \frac{\partial \eta}{\partial z}\right)_i = 2\mathrm{D}_{\eta i} \frac{\eta_1 - \eta_2}{z_2} \quad \textbf{(A2.71)}$$

In order to maintain continuity, this term is taken equal (except sign) for both soil layers. The largest value of η_1, and η_2 is used to evaluate the diffusivity $D_{\eta i}$ and the hydraulic conductivity $K_{\eta i}$. The gradient term in Equation 3.72 is calculated between the surface and the midlevel of the upper layer using the surface values of soil water content η_1, and η_2. It allows for calculation of the near-surface soil water content η_1 from Equation A2.68 diagnostically. Depending on the amount of water content, thermal properties of soil and its albedo vary. The soil heat capacity, $\rho_s c_s$, is calculated as

$$\rho_s c_s = (1-\eta_s)\,\rho_i c_i + \eta \rho_w c_w \quad \textbf{(A2.72)}$$

where dry volumetric soil heat capacity, $\rho_i c_i$, is tabulated for each soil class in Table 1, and $\rho_w c_w$ are corresponding values for liquid water. The thermal conductivity of soil is given by McCumber and Pielke (1981)

$$\lambda_s = \max\left(419 \exp\left(-P_f - 2.71\right), 0.172\right) \quad \textbf{(A2.73)}$$

where $P_f = \log(-\Psi/100)$. The value of the soil albedo is obtained by using the effect of soil wetness

$$A_g = A_\eta + A_z \quad \textbf{(A2.74)}$$

$$A_\eta = A_0(1-\Delta),\ \Delta = \min(\beta_g, 0.5), \quad \textbf{(A2.75)}$$

and the effect of solar zenith angle

$$A_z = 0.01\left(\exp\left(0.003286 Z^{1.5}\right) - 1\right) \quad \textbf{(A2.76)}$$

Basic soil albedo, A_0, is listed in Table A2.1. The Halstedt parameter β_g is defines by

$$\beta_g = \begin{cases} 0.5\left[1 - \cos\left(\pi \eta_0 / \eta_{fc}\right)\right] & \eta_0 \le \eta_{fc} \\ 1 & \textit{otherwise} \end{cases} \quad \textbf{(A2.77)}$$

This expression allows evaporation from the surface at the potential rate when the

soil moisture η_0 exceeds the field capacity η_{fc} which corresponds to the hydraulic conductivity of 0.1 mm/day (Table 3.1).

A2.3.4 Water intercepted by canopy

The amount of the liquid water, W_d , intercepted by the foliage due to dew formation or rainfall is governed by the prognostic equation (Deardorff, 1978)

$$\frac{\partial W_d}{\partial t} = vegP - E_r + R_r \qquad \textbf{(A2.78)}$$

where P is the precipitation rate at the top of the vegetation, E_r is the direct evaporation from the fraction δ of the foliage covered with a film of water when positive and the dew flux when negative. R_r is the runoff of the interception reservoir which occurs when W_d exceeds a maximum value $W_{d\max}$ depending on the density of the canopy (Dickinson et al., 1986)

$$W_{d\max} = h_w vegLAI \qquad \textbf{(A2.79)}$$

where h_w is the maximum storage of water, assumed to be equal 0.0002 m. The wet fraction of the canopy δ is calculated following Deardorff (1978)

$$\delta = \begin{cases} \left(W_d / W_{d\max}\right)^{2/3} & for\ E_r > 0 \\ 1 & for\ E_r < 0 \end{cases} \qquad \textbf{(A2.80)}$$

The flux of liquid water reaching the ground surface

$$P_g = (1 - veg)P + R_r \qquad \textbf{(A2.81)}$$

includes the non-intercepted rainfall and the runoff from the canopy.

A2.3.5 Water areas

Representation of water bodies in OMEGA model is in simple form. Due to the large heat capacity of water and strong surface mixing, initial surface temperature of the water bodies, T_{sea} , is implemented based on climatological data after then it is assumed to be constant during the simulation period. The air above the water surface is assumed fully saturated by water vapor

$$q_0 = q_{sat}(T_{sea}) \qquad \textbf{(A2.82)}$$

The spatial variation of surface roughness length, z_0 , is specified based on land-use

categories over land while Charnock's relationship (Charnock, 1955) is used to determine the roughness length over water surfaces

$$z_0 = a_1 \frac{u^2}{g} \qquad \textbf{(A2.83)}$$

Although the coefficient a_1 in the equation has been found to be somewhat variable, 0.018 is included in the model (Arya, 1988). Based on the observations 0.0015 cm is implemented on the z_0 .

A2.4 Microphysics

The OMEGA microphysics uses the category of *bulk water microphysics* in which the production rates are functions of the total mass density of each water species (Lin et al., 1983). The water species are represented as cloud droplets, vapor, ice crystals, rain and snow in OMEGA, however co-existence of liquid and solid phases of water is not allowed which means that neither supercooled liquid nor melting solids can exist in the model domain. Condensation (or evaporation) of cloud water, autoconversion of cloud water to rain, condensation on (or evaporation of) raindrops, accretion of cloud water by raindrops, fallout of rain, and generation of ice crystal growth, autoconversion of ice crystals to snow, deposition on (or sublimation of) snow, accretion of ice crystals by snow, and fallout of snow are the microphysical processes in OMEGA.

A2.4.1 Computational treatment

The local Courant number which is a function of the velocity (advective or acoustic) in the cell and the dimension of the cell defines the time step used for integration in OMEGA. The time step can range from sub-second to tens of seconds depending on the flow characteristics. Therefore the microphysical time step is expected to be roughly five to ten seconds. In OMEGA the water substances are categorized into five species: vapor, cloud droplets, ice crystals, rain, and snow. In the following equations *Q* will represent the mixing ratio of a hydrometeor class and suffixes *V*, *C*, *I*, *R*, and *S* will refer to water vapor, cloud droplets, ice crystals, rain and snow, respectively. The cloud droplets and ice crystals are assumed to be monodispersed and nonprecipitating. Size distributions of raindrops and snow crystals are described using Marshall and Palmer (1948) type relationships. These are given as:

$$N(d_R) = N_{0R}\exp\left(-\frac{d_R}{\Lambda_R}\right) \quad \textbf{(A2.84)}$$

$$N(d_S) = N_{0S}\exp\left(-\frac{d_S}{\Lambda_S}\right) \quad \textbf{(A2.85)}$$

$N(d)$ is number concentration at diameter d, and d_R and d_S are the particle diameters for rain and snow, respectively. N_{0R}, and N_{0S} are y-intercepts of the distribution of rain and snow, which represents the limiting number concentration as diameter tends to zero. Λ_R ,and Λ_S represent the slope of the respective inverse-exponential distribution (Bacon, 2003).

A2.4.2 Evaluate local temperature from potential temperature

Bacon (2003) states that the prognostic thermodynamic variable is $\rho\theta$, where ρ is the density and θ is the potential temperature ($\rho\theta$ in effect is the energy density). The microphysical processes are driven by temperature instead of potential temperature in the microphysical processes. Therefore, the temperature is calculated from the potential temperature. The temperature and the potential temperature are related via the Poisson equation,

$$T = \theta\left(-\frac{P}{P_{ref}}\right)^{\kappa} \;;\; \theta = T\left(-\frac{P}{P_{ref}}\right)^{-\kappa} \quad \textbf{(A2.86)}$$

$$P_{ref} = 1\times10^{5}\,Pa \text{ and } \kappa = \frac{R_d}{c_p} = 0.286 \quad \textbf{(A2.87)}$$

R_d is the gas constant of day air, and c_p the specific heat of day air at constant pressure.

A2.4.3 Evaluation of microphysical parameters

The microphysical processes which contain any type of phase change need the respective latent heats. The saturation vapor pressures have to be considered because the phase change processes depend upon the local saturation condition. Other processes need the specific heats of water, ice, vapor, and air, and parameters such as the diffusivity of vapor are required to compute the rate of sublimation or condensation of the precipitating hydrometeors. Since the all equations compute

based on temperature, once the temperature is determined, it is possible to evaluate microphysical processes (Bacon, 2003).

A2.4.3.1 Latent heat

Latent heats of vaporization and fusion are assumed to changes only with temperature, T by Pruppacher and Klett (1978).

$$L_v(T) = 2.50078\times10^{6}\left(\frac{T_0}{T}\right)^{y} \text{ J/Kg} \qquad \textbf{(A2.88)}$$

where $y = 0.167 + 3.67\times10^{-4}\ T$, and $T_0 = 273.16\ K$

$$L_f(T) = \begin{cases} \left.\begin{matrix} 3.3369\times10^{5} + 2030.6\left(T - T_0\right) \\ -10.467\left(T - T_0\right)^2 \end{matrix}\right\} & \text{J/Kg} \quad \text{if } T \le T_0 \\ 3.3369\times10^{5} \quad \text{J/Kg} & \text{if } T > T_0 \end{cases} \qquad \textbf{(A2.89)}$$

The latent heat of sublimation is given as;

$$L_s(T) = L_v(T) + L_f(T) \qquad \textbf{(A2.90)}$$

Since the latent heat of sublimation varies very slightly with temperature, it can be assumed to be a constant at $2.83237\text{x}10^{-7}$ J/Kg. Hence, latent heats calculate by using the following scheme. The latent heat of vaporization is computed using equation A2.88 above melting temperatures and the latent heat of fusion is calculated as

$$L_f = L_s - L_v \qquad \textbf{(A2.91)}$$

The latent heat of fusion is calculated as a function of temperature using equation A2.89 if temperature is less than melting and the latent heat of vaporization is computed as;

$$L_v = L_s - L_f \qquad \textbf{(A2.92)}$$

A2.4.3.2 Specific heat and other parameters

The specific heat of water and ice are given by Pruppacher and Klett (1978) (in units of J/Kg-K) as

$$C_w(T) = \begin{cases} 5400.0 & \text{if } T < 223.16 \\ 4217.8 + 0.3471(T - T_0)^2 & \text{if } 223.16 < T \le T_0 \\ \left.\begin{array}{l} 4178.0 + 0.01298(T - 308.16)^2 \\ \quad + 1.591\times10^{-5}(T - 308.16)^4 \end{array}\right\} & \text{if } T < T_0 \end{cases} \quad \textbf{(A2.93)}$$

$$\text{and } C_I(T) = \begin{cases} 2106.1 + 7.327(T - T_0) & \text{if } T \le T_0 \\ 2106.1 & \text{if } T > T_0 \end{cases} \quad \textbf{(A2.94)}$$

The dynamic viscosity of air is given by List (1971) as

$$\begin{aligned} \mu_D(T) &= 1.8325\times10^{-5}\,\frac{416.6}{T + 120.0}\left(\frac{T}{296.16}\right)^{1.5} \\ &= 1.49629\times10^{-6}\left(\frac{T^{1.5}}{T + 120.0}\right) \end{aligned} \quad \textbf{(A2.95)}$$

The molecular viscosity, v_m is

$$v_m(P,T) = \mu_D \rho \quad \textbf{(A2.96)}$$

The thermal conductivity of air is (Wisner et al., 1972)

$$\begin{aligned} k_T(T) &= 1414.0\times10^{-5}\,\mu_D(T) \\ &= 2.11575\times10^{-3}\left(\frac{T^{1.5}}{T + 120.0}\right) \end{aligned} \quad \textbf{(A2.97)}$$

The diffusivity of water vapor in air is (Pruppacher and Klett, 1978)

$$\begin{aligned} D_v(P,T) &= 2.11\times10^{-5}\left(\frac{101325.0}{P}\right)\left(\frac{T}{T_0}\right)^{1.94} \\ &= 4.0119\times10^{-5}\,\frac{T^{1.94}}{P} \end{aligned} \quad \textbf{(A2.98)}$$

The Schmidt number is defined as the ratio of the molecular viscosity to the diffusivity of water vapor in air or

$$N_{Sc}(P,T) = \frac{v_m(P,T)}{D_v(P,T)} = 3.72963\times10^{-2} R_d\,\frac{T^{0.56}}{T + 120.0} \quad \textbf{(A2.99)}$$

A2.4.3.3 Local supersaturation evaluation

Condensation/evaporation and deposition/sublimation depend on the amount of water vapor that exists in excess of the saturation limit at that point in space. Hence

the local saturation vapor pressures (over water and ice surfaces) are calculated. The saturation vapor pressures are only the functions of temperature. Variation of the saturation vapor pressure with temperature is given by the Clausius-Clapeyron equation (Hess, 1959).

The method, used by Proctor (1987) in which the saturation vapor pressures (over water and ice surfaces) are computed using the following polynomial fits to experimental data (Wexler, 1976, 1977) is adopted:

$$e_{sw}(T) = \exp(-2991.2729T^{-2} - 6017.0128T^{-1} + 17.87643854 - 0.028354721T + 0.17838301\times10^{-4}T^{2} - 0.84150417\times10^{-9}T^{3} + 0.44412543\times10^{-12}T^{4} + 2.858487\ln T) \quad \textbf{(A2.100)}$$

$$e_{si}(T) = \exp(-5865.3696T^{-1} - 22.241033 + 0.013749042T - 0.34031775\times10^{-4}T^{2} + 0.26967687\times10^{-7}T^{3} + 0.6918651\ln T\ln T) \quad \textbf{(A2.101)}$$

The saturation mixing ratios of water vapor over a water surface is Q_{vs} and over an ice surface it is Q_{si}, which can be calculated from e_{sw} and e_{si}, respectively as;

$$Q_{vs} = \frac{e_{sw}(Q_v + \varepsilon)}{P} \quad \textbf{(A2.102)}$$

$$Q_{si} = \frac{e_{si}(Q_v + \varepsilon)}{P} \quad \textbf{(A2.103)}$$

where $\varepsilon = R / R_d = 0.622$.

A2.4.3.4 Calculation of the ice nuclei concentration

Ice nuclei (IN) are aerosols that a small fraction of the atmosphere serves as ice nuclei. Water vapor can deposit on ice nuclei to form ice crystals. Only some of ice nuclei are active at any given temperature. Fletcher (1962) showed that number of concentration of active ice nuclei are a function of local temperature.

$$n_{IN} = \begin{cases} 10^{9} & \text{if } T < 230.95 \\ \beta_{IN} \exp 0.6\{(T_M - T)\} & \text{if } 230.95 \le T \le T_M \\ 0 & \text{if } T_M < T \end{cases} \quad \textbf{(A2.104)}$$

$\beta_{IN} = 0.01\, m^{-3}$. Observations depict the IN concentrations can vary by factor of 10 at a location and temperature (Pruppacher and Klett, 1978).

A2.4.3.5 Calculate Λ's and fall velocities for rain, and snow

Rain, and snow are defined by the inverse exponential distributions as

$$N_{0R} = 2.25\times10^{7}\left(\frac{Q_R}{\rho}\right)^{0.375}$$
$$N_{0S} = 5.5\times10^{6}\exp\left[-0.088\left(T - T_M\right)\right] \quad \textbf{(A2.105)}$$

The slopes of the inverse exponential distributions can be calculated as

$$\Lambda_R = \left(\frac{\rho Q_R}{\pi N_{0R}\delta_W}\right)^{0.25} \text{ and } \Lambda_S = \left(\frac{\rho Q_R}{\pi N_{0S}\delta_S}\right)^{0.25} \quad \textbf{(A2.106)}$$

where δ_W and δ_S are the densities of water, and snow respectively given as. $\delta_W = 1000$ Kg/m^3 and $\delta_S = 100$ Kg/m^3.

Terminal fall velocities of precipitating hydrometeors are calculated from a single particle fall velocity averaged over the respective distribution in a mass-weighted manner. The mass-weighted fall velocities for rain and snow are calculated as follows:

$$W_R = \left(-0.267 + 2.06\times10^{4}\Lambda_R - 2.045\times10^{7}\Lambda^{2R} + 9.06\times10^{9}\Lambda^{3R}\right)\left(\frac{1.2}{\rho}\right)^{0.4} \quad \textbf{(A2.107)}$$

$$W_S = \begin{cases} 1.1\left(\frac{1.2}{\rho}\right)^{0.5} & \text{if } T < T_M \\ 2.5\left(\frac{1.2}{\rho}\right)^{0.5} & \text{if } T \geq T_M \end{cases} \quad \textbf{(A2.108)}$$

A2.4.3.6 Production rates of non-precipitating hydrometeors

It is possible to evaluate the production/loss of the hydrometeors since local thermodynamic state and key microphysical parameters are computed. Since their smaller size increases the surface area to volume ratio, the non-precipitating hydrometeors respond quickly to changes in their surroundings. Q will denote the mixing ratios, ΔQ the change in Q, and P the rate of change of mixing ratios with time. The subscripts of ΔQ and P will indicate the microphysical process involved. The non-precipitating hydrometeors consist of the cloud droplets and the ice crystals.

Because of the computational efficiency, calculations are performed in a model cell if one of the participant species is significantly non-zero in that cell (Bacon, 2003).

Freezing of Cloud Droplets

Ice nuclei initiate the water freeze. Large water drops generally contain enough impurities that they freeze at or near 0°C (T_M). If small droplets do not involve any ice nuclei, they can exist in liquid phase at temperatures far below 0°C. Even small droplets will spontaneously freeze at about –40°C. In OMEGA, no supercooled liquid is allowed to exist. Therefore, if $T \leq T_M$, all cloud droplets are frozen to produce ice crystals as shown in the following relation:

$$\left.\begin{aligned} Q_I &= Q_I + Q_C \\ \Delta Q_{CFZN} &= Q_C \\ Q_C &= 0 \end{aligned}\right\} \quad \text{if } T \leq T_M \qquad \textbf{(A2.109)}$$

Melting of Ice Crystals

If $T > T_M$ all ice crystals in that cell are melted to form cloud droplets by the following:

$$\left.\begin{aligned} Q_C &= Q_C + Q_I \\ \Delta Q_{IMLT} &= Q_I \\ Q_I &= 0 \end{aligned}\right\} \quad \text{if } T > T_M \qquad \textbf{(A2.110)}$$

If $T > T_M$ Compute Condensation/Evaporation

Depending on the water vapor excess, the amount of cloud water vapor condensed into liquid which is present at a grid point. Since the excess vapor is assumed to condense into cloud droplets or undergo deposition to form ice crystals instantaneously, supersaturated conditions cannot exist in the model domain.

The excess water vapor will start to condense when supersaturation exists. Latent heat of vaporization is released since condensation proceeds and increases the temperature and the saturation vapor pressure of air. Thus the initial water vapor excess ΔQ_V is used not only for condensation, but also for the increase in vapor capacity of the air. ΔQ_1 , and ΔQ_2 denote the amount of water vapor condensed, and the amount of extra vapor the air can hold due to the increase in temperature such that the total ΔQ is given by

$$\Delta Q = \Delta Q_1 + \Delta Q_2 \qquad \textbf{(A2.111)}$$

The increase in temperature ΔT due to the release in latent heat when ΔQ_1 vapor is condensed is

$$\Delta T = \frac{L_v \Delta Q_1}{c_p} \qquad \textbf{(A2.112)}$$

This increase in temperature increases the saturation vapor pressure as given by the Clausius-Clapeyron equation,

$$\frac{de_s}{e_s} = \frac{L_v}{R_v}\frac{dT}{T^2} \qquad \textbf{(A2.113)}$$

It was assumed that in each grid cell the pressure does not change during the microphysical adjustments in an isobaric process;

$$\frac{dQ_{vs}}{Q_{vs}} = \frac{de_s}{e_s} \qquad \textbf{(A2.114)}$$

$$\Delta Q_2 = Q_{sv}\frac{L_v \Delta T}{R_v T^2} = \frac{L_v^2 Q_{sv} \Delta Q_1}{c_p R_v T^2} \qquad \textbf{(A2.115)}$$

Define a fraction r such that $\Delta Q_1 = r\,\Delta Q$. Then,

$$r = \frac{\Delta Q_1}{\Delta Q} = \frac{\Delta Q_1}{\Delta Q_1 + \Delta Q_2} = \Delta Q_1 \left\{ \Delta Q_1 + \frac{L_v^2 Q_{sv} \Delta Q_1}{c_p R_v T^2} \right\}^{-1} = \left\{ 1 + \frac{L_v^2 Q_{sv}}{c_p R_v T^2} \right\}^{-1} \qquad \textbf{(A2.116)}$$

Thus the amount of water vapor to be condensed or the maximum amount of cloud water that can be evaporated can be written as;

$$\Delta Q_{CCND} = r\Delta\Delta = \frac{Q_v - Q_{sv}}{1 + \frac{L_v^2 Q_{sv}}{c_p R_v T^2}} \qquad \textbf{(A2.117)}$$

Initiation of Ice Crystals

The production rate of ice crystals via the deposition nucleation depends on the ice nuclei number concentration, which depends on the local temperature. Cloud ice is initiated when temperatures less than –16°C. The rate of cloud ice is near zero at the higher temperatures. 12.9μm and 10^{-12} kg are assumed the maximum diameter and maximum mass, respectively for the initiated crystals. The amount of ice initiated by this process is controlled by the maximum ice crystal mass and the IN concentration

and by the available supersaturation with respect to an ice surface. The maximum ice mixing ratio is obtained by growing all crystals to 12.9μm is

$$\Delta Q_{I1} = \frac{10^{-12} n_{IN}}{\rho} \quad \textbf{(A2.118)}$$

Depositional growth driven by the supersaturation can be used to derive The maximum ice mixing ratio in a manner analogous to the condensation adjustment (Equation A2.120) by replacing L_v by L_s, and Q_{vs} by Q_{si}. Thus,

$$\Delta Q_{I2} = \frac{Q_v - Q_{si}}{1 + \frac{L_s^2 Q_{si}}{c_p R_v T^2}} \quad \textbf{(A2.119)}$$

$$\Delta Q_{ICWV1} = \min\left(\Delta Q_{I1}, \Delta Q_{I2}\right) \quad \textbf{(A2.120)}$$

If $T \leq T_M$ Compute Deposition/Sublimation

After ice crystal initiation, if excess vapor over ice saturation still exists, existing ice crystals grow by deposition. The depositional growth rate of ice crystals is given by

$$\frac{\partial Q_I}{\partial t} = 65.2\sqrt{\frac{Q_I \rho}{n_{IN}}} \frac{Q_v - Q_{si}}{Q_{si} A^* + B^*} \quad \textbf{(A2.121)}$$

where $A^* = \frac{L_v}{k_T T}\left(\frac{L_s}{R_v T} - 1\right)$ **(A2.122)**

and $B^* = \frac{1}{\rho D_v}$ **(A2.123)**

where D_v is the diffusivity of water vapor given by Equation A2.108. This rate has to be limited by the maximum cloud ice. This is given by ΔQ_{I2};

$$P_{IDEP} = \min\left(\frac{\partial Q_I}{\partial T}, \frac{\Delta Q_{I2}}{\Delta T}\right) \quad \textbf{(A2.124)}$$

If (Q_v–Q_{si}) is negative then sublimation occurs.

A2.4.3.7 Adjust mixing ratios of non-precipitating hydrometeors

The mixing ratios of cloud droplets, ice crystals and water vapor are adjusted before compute the production/loss of precipitating hydrometeors.

$$
\begin{aligned}
Q_C &= Q_C + \Delta Q_{CCND} \\
Q_I &= Q_I + P_{IDEP}\Delta t + \Delta Q_{ICWV1} \\
Q_v &= Q_v - \Delta Q_{CCND} - P_{IDEP}\Delta t - \Delta Q_{ICWV1}
\end{aligned}
\qquad \textbf{(A2.125)}
$$

The temperature adjustment is determined from

$$
P_{IDEP} = \left(\Delta Q_{CFZN} - \Delta Q_{IMLT}\right)L_f + \Delta Q_{CCND}L_v + \left(\Delta Q_{ICWV1} + P_{IDEP}\Delta t\right)L_s \qquad \textbf{(A2.126)}
$$

A2.4.3.8 Production rates of precipitating hydrometeors

Evaluation of the production/loss of the larger precipitating hydrometeors will be given in the following.

Production of Rain by Melting of Snow

In OMEGA, all snow melts instantaneously to rain above 0°C (T_M);

$$
\left.
\begin{aligned}
Q_R &= Q_R + Q_S \\
\Delta Q_{SMLT} &= Q_S \\
Q_S &= 0
\end{aligned}
\right\} \quad \text{if } T > T_M \qquad \textbf{(A2.127)}
$$

Production of Snow by the Freezing of Raindrops

The production of rain produced by melting of snow assumes that all rain freezes to snow below 0°C instantaneously;

$$
\left.
\begin{aligned}
Q_S &= Q_S + Q_R \\
\Delta Q_{RFZN} &= Q_R \\
Q_R &= 0
\end{aligned}
\right\} \quad \text{if } T \le T_M \qquad \textbf{(A2.128)}
$$

Autoconversion of Cloud Droplets to Form Rain

It has been assumed the cloud droplets to be monodisperse, however in reality they exist in all sizes. Larger droplets or rain drops is formed by the interparticle collisions and coalesce. This process forms rain is termed autoconversion. The rate of production of rain from cloud droplets via autoconversion is given by (Berry and Reinhardt, 1974a and 1974b)

$$
P_{RACV} = 7.26\times10^{-3}\left[10^{20}\left(\frac{\sigma}{0.38}\right)r_c^4 - 0.4\right]\rho Q_C^2\left[\left(\frac{\sigma}{0.38}\right)^{1/3} r_C 10^6 - 7.5\right] \qquad \textbf{(A2.129)}
$$

where $r_c = \left(\dfrac{3\rho\rho_C}{4\pi\pi_C\delta_W}\right)^{1/3}$ is the mean cloud droplet radius, σ is the dispersion

coefficient of the cloud droplet distribution, and N_C is the cloud condensation nuclei (CCN) concentration.

Collection of Cloud Droplets by Raindrop

Since the raindrops have a much higher fall speed than the cloud droplets raindrops collect cloud droplets. The size of cloud droplets is the indicator for the collection efficiency. While large droplets will have high collection efficiency, very small droplets have a collection efficiency of zero. The production rate due to this collection mechanism is;

$$P_{RAC} = \frac{15\pi}{38} \Lambda_R^3 N_{0R} W_R Q_C E_{RCD} \qquad \textbf{(A2.130)}$$

where E_{RCD} is computed from a polynomial fit to experimental data (Proctor, 1987) given by

$$E_{RCD} = \begin{cases} 0 & \text{if } r_c < 1.2\mu\text{m} \\ \left.\begin{array}{l} -0.275544 + 0.26249\times10^{6} r_c \\ -1.8896\times10^{10} r_c^2 + 4.4626\times10^{14} r_c^3 \end{array}\right\} & \text{if } 1.2\mu\text{m} \le r_c < 20\mu\text{m} \\ 1 & \text{if } 20\mu\text{m} \le r_c \end{cases} \qquad \textbf{(A2.131)}$$

Condensation Evaporation of Raindrops

Since the saturation vapor pressure over a curved surface with smaller radius of curvature is higher than over a surface with larger radius of curvature the smaller cloud droplets are allowed to evaporate first. If the environment is supersaturated vapor can condense onto the raindrops. The following expression takes into account the ventilation effect of the falling raindrop

$$P_{RCND} = \frac{2\pi(Q_v - Q_{sv}) N_{0R} \Lambda_R^2 \left(1 + 0.3194027 N_{Sc}^{1/3} \sqrt{\frac{\Lambda_R W_R}{\nu_m}}\right)}{Q_{sv} \frac{L_v \rho}{k_v T}\left(\frac{L_v}{R_v T} - 1\right) + \frac{1}{D_v}} \qquad \textbf{(A2.132)}$$

Autoconversion of Ice Crystals to Snow

If the cloud ice mixing ratio exceeds a threshold Q_{IMAX} cloud ice conversion to snow (via stochastic collection, or autoconversion) occurs. A fraction of extra cloud ice is converted to snow according to the formula

$$P_{SRCV} = (Q_I - Q_{IMAX})E_{SCI} \times \frac{1}{\Delta t} \quad \textbf{(A2.133)}$$

where E_{SCI} in the collection efficiency of snow for ice crystals given by

$$E_{SCI} = \exp(0.03(T - T_m)) \quad \textbf{(A2.134)}$$

Q_{IMAX} is set to $1x10^{-3}$ kg/kg in the OMEGA.

Collection of Ice Crystals by Snow

As raindrops collect cloud droplets by virtue of their difference in slip velocity, snowflakes collect ice crystals. The production rate of snow due to this collection of ice crystals is given by

$$P_{SACI} = 0.5\pi. \ {}_{0S}W_S \Lambda_S^3 Q_I E_{SCI} \quad \textbf{(A2.135)}$$

Deposition/Sublimation of Snow

The deposition onto snow is calculated similar to condensation on raindrops. The following equation also takes into account the ventilation factor of falling snow:

$$P_{SDEP} = \frac{2\pi(Q_v - Q_{si})N_{0S}\Lambda_S^2\left(0.86 + 0.21N_{Sc}^{1/3}\sqrt{\frac{\pi\Lambda_S W_S}{v_m}}\right)}{Q_{si}\frac{L_v\rho}{k_T T}\left(\frac{L_s}{R_v T} - 1\right) + \frac{1}{D_v}} \quad \textbf{(A2.136)}$$

A2.4.3.9 Adjust mixing ratios of hydrometeors

The mixing ratios of the hydrometeors and water vapor are adjusted by

$$\begin{aligned} Q_R &= Q_R + (P_{RACV} + P_{RCND} + P_{RAC})\Delta t \\ Q_S &= Q_S + (P_{SACV} + P_{SDEP} + P_{SACI})\Delta t \\ Q_C &= Q_C - (P_{RACV} + P_{RAC})\Delta t \\ Q_I &= Q_I - (P_{SACV} + P_{SACI})\Delta t \\ Q_v &= Q_v - (P_{RCND} + P_{SDEP})\Delta t \end{aligned} \quad \textbf{(A2.137)}$$

A2.4.3.10 Adjust temperature to include latent heat release

By taking the latent heat released or absorbed during condensation/evaporation, deposition/sublimation, and freezing/melting involving the precipitating hydrometeors into account, the final step is the temperature adopt for the cell. The

change in sensible heat balances the total latent heat released in the following equation:

$$c_p \Delta T = \left(\Delta Q_{RFZN} - \Delta Q_{SMLT}\right) L_f + P_{RCND} \Delta t L_v + P_{SDEP} \Delta t L_s \qquad \textbf{(A2.138)}$$

This equation defines the temperature difference because of the latent heat release. After the temperature is updated, new potential temperature values are calculated using the Poisson's equation.

A2.4.3.11 Computation of precipitation fluxes

The fluxes are straight up and down at the top and bottom faces of each cell due to precipitation. The mixing ratio changes to rain and snow is computed using following formulation.

$$\frac{\partial Q_R}{\partial t} = \frac{1}{\rho} \frac{\partial \left(\rho Q_R\right)}{\partial z'} W_R \quad \text{and} \quad \frac{\partial Q_S}{\partial t} = \frac{1}{\rho} \frac{\partial \left(\rho Q_S\right)}{\partial z'} W_S \qquad \textbf{(A2.139)}$$

where z' denotes the local vertical direction.

A2.4.3.12 Convective parameterization

The purpose of the OMEGA mode is to solve large convective areas explicitly; however there will be regions that are not resolved sufficiently. The contribution of subgrid-scale deep cumulus convection on cumulus parameterization was circumvented by Kuo (1965, 1974) and modified by Anthes (1977) to incorporate the effect of subgrid scale deep cumulus convection on the local environment with cumulus parameterization. In OMEGA, the convective parameterization applies to convectively unstable regions to deep penetrative convection and in those regions the total horizontal moisture convergence exceeds a critical value. In OMEGA, there is smooth transition from regions where no convective parameterization is applied to where it is applied. This is achieved by a factor in the cumulus adjustment scheme changing between 0 and 1 depending on cell area, while explicit cloud microphysics is active over the whole domain.

The total rate of moisture accession, M_t, per unit horizontal area is given by the convergence of moisture in the column of atmosphere above the unit area plus the surface evaporation, thus

$$M_t = -\int_0^{z_t} \rho \nabla_H \cdot V q dz + \delta_c \rho_0 C_D V_0 q_s - q_a \qquad \textbf{(A2.140)}$$

where z_t is the model top, q the cell averaged mixing ratio, q_s the saturation value corresponding to sea-surface temperature, q_a the air value just over the sea, C_D the drag coefficient, ρ the density, ρ_0 air density in the surface layer, V_0 wind speed at the surface layer, and δ_c is an indicator such that

$$\delta_c = \begin{cases} 0, & \text{over land} \\ 1, & \text{over water} \end{cases} \qquad \textbf{(A2.141)}$$

Hence, evaporation within the surface layer is considered only over the sea when

$w_0 > 1$ cm s^{-1}, and $\dfrac{\partial \theta_e}{\partial z} < 0$,

where w_0 is the vertical velocity in the surface layer, and θ_e is the equivalent potential temperature. It is assumed that there in no direct evaporation effects on the generation of deep cumulus convection over land. The drag coefficient is determined using the surface layer similarity relationships as follows:

$$C_D = \frac{\beta k^2}{\left[\ln\left(\frac{z}{z_0}\right) - \Psi_M\left(\frac{z}{L}\right)\right]\left[\ln\left(\frac{z}{z_0}\right) - \Psi_H\left(\frac{z}{L}\right)\right]} \qquad \textbf{(A2.142)}$$

where β is a constant and set to 1.35, k the von Karman's constant, Ψ_M and Ψ_H the integral functions, z_0 the surface roughness height. The moisture M_t is used to make cloud columns (T_c, q_c) from environmental air (T, q). Part of the moisture (M_1) will condense and precipitate, raising the temperature from T to T_c and the remainder (M_2) will increase the mixing ratio of the cloud column from q to q_c,

$$M_1 = \frac{c_p}{L_c} \int_{z_{cb}}^{z_{ct}} \rho \, T_c - T \, dz \qquad \textbf{(A2.143)}$$

$$M_2 = \int_{z_{cb}}^{z_{ct}} \rho \, q_c - q \, dz \qquad \textbf{(A2.144)}$$

where c_p is the specific heat at constant pressure, L_c latent heat of condensation, z_{cb} and z_{ct} the bottom and top of the cloud, respectively. Hence the total amount of water vapor is calculated by the sum of the two integrals

$$M_c = M_1 + M_2 = \int_{z_{cb}}^{z_{ct}} \rho \frac{c_p}{L_c} T_c - T + q_c - q \, dz \qquad \textbf{(A2.145)}$$

The rate of cloud production per unit time, C (or fractional area), is calculated proportional to the convergence of water vapor and evaporation for the column divided by the amount of water vapor which is necessary to produce the model cloud as follows:

$$C = \frac{M_t}{M_c} \qquad \textbf{(A2.146)}$$

$C\Delta t$ gives the total production of cloud during time Δt. Kuo introduced a division of the convergence moisture. There are two fractions; bM_t of the total which increases the humidity of the air, and another fraction is $(1\text{-}b)M_t$, which is condensed and precipitates as rain or is carried away with the latent heat warming the air. It is important to evaluate the parameter b properly. Anthes (1977a) proposed that b depends on the mean relative humidity in the air column that when the atmosphere is dry moistening strong and the moistening is weak when the atmosphere wet.

$$b = \begin{cases} \left[\dfrac{\left(1 - \overline{RH}\right)}{\left(1 - RH_c\right)} \right]^n & \text{if } \overline{\mathrm{RH}} \geq \mathrm{RH_c} \\ 1 & \text{if } \overline{\mathrm{RH}} < \mathrm{RH_c} \end{cases} \qquad \textbf{(A2.147)}$$

where $\overline{\mathrm{RH}}$ is the mean environmental relative humidity in the air column, RH_c is the critical relative humidity, and n a positive exponent. Hence, when RH is less than RH_c, only environmental moistening is available. Value of n=1 and RH_c =0.5 were chose by Anthes (1977b) for the axisymmetric hurricane model. However, a number of studies have indicated that the b value computed with n=1 and RH_c =0.5 is too large and consequently convective heating, drying, and rainfall rates are underestimated. In a study on semi-prognostic tests of Kuo-type schemes in an extratropical convective system, Kuo and Anthes (1984) found that the simulated rainfall rate agrees with observations when n is between 2 and 3, and RH_c is between 0.25 and 0.50. Someshwar Das *et al*. (1988) found that the best results are obtained for values of n between 3 and 5, and RH_c between 0 and 0.25 when conducting the Asian summer monsoon period. In the ECMWF numerical forecasting model, n=3 and RH_c=0 are used (Tiedtke 1986). As a compromise between these values, in the OMEGA model n and RH_c are specified as 3 and 0.5, respectively.

Assuming the large-scale forecast is made for a time step Δt giving a temperature T_e without the effects of cumulus convection. Then, applying the parameterization scheme gives a temperature $T(t+\Delta t)$ such that

$$T(t+\Delta t) = T_e + (1-b)C\Delta\Delta(T_c - T_e) \qquad \textbf{(A2.148)}$$

and the corresponding equation for mixing ratio $q(t+\Delta t)$ after the parameterization is applied is

$$q(t+\Delta t) = q_e + (1-b)C\Delta\Delta(q_c - q_e) \qquad \textbf{(A2.149)}$$

The precipitation from the subgrid cloud scale is used in warming the air from T_e to T. Therefore, the rate of precipitation per unit time per unit volume in the column is calculated by

$$pr_{cl} = \int_{t}^{t+\Delta t}\int_{z_{cb}}^{z_{ct}} \frac{1-b\ C\ c_p T_c - T_e}{L_c}\, dz\ dt \qquad \textbf{(A2.150)}$$

When the vertically integrated moisture convergence rate exceeds a critical value of 10^{-5}kgm^{-2}s^{-1} (Anthes 1977b) cumulus convective processes are activated, on evaluating the subgrid scale cloud effects. There is a need to determine the cloud base z_{cb} and cloud top z_{ct}. Lifting condensation level (LCL) of each air parcel is utilized to determine the cloud base. The temperature T_c and mixing ratio q_c inside the cloud are assumed as those on a moist adiabatic passing through the lifting condensation level. The cloud top is identified as the height where cloud temperature T_c becomes less than the environment temperature T_e.

A2.5 Radiation

Separate parameterizations are developed for short and long wavelengths and the radiative source-sink term in the conservation of energy equation (A2.10) can be written as:

$$S_R = \left(\frac{\partial T}{\partial t}\right)_{LW} + \left(\frac{\partial T}{\partial t}\right)_{SW} \qquad \textbf{(A2.151)}$$

The terms on the right hand side represent temperature change resulting from longwave and shortwave radiative divergence flux in the vertical direction. Since variation of the radiative energy divergence is much larger in the vertical direction on

the mesoscale, its horizontal direction is neglected. The method of parameterizing vertical flux takes into account the absorption of shortwave radiation by water vapor and the longwave energy emitted by water vapor and carbon dioxide using the computationally efficient technique of Sasamori (1972) which is essentially similar to Mahrer and Pielke (1977). Separate parameterizations for long and short wavelengths are convenient to use in the model due to the separation of wavelength in the atmospheric radiation spectra.

A2.5.1 Shortwave radiative flux

The diurnal variation of the solar flux is computed from the following equation on a horizontal surface at the top of the atmosphere.

$$S = S_0 \cos Z \qquad \textbf{(A2.152)}$$

$$\cos Z = \cos\Psi\cos\delta\cos H + \sin\Psi\sin\delta \qquad \textbf{(A2.153)}$$

where S_0 is the solar constant, Z the zenith angle, ψ the latitude, δ the solar declination, a function of Julian day, and H the solar hour angle. It is assumed that shortwave absorption in the atmosphere is only due to water vapor and the heating of the atmosphere by this radiation is then given by

$$\left(\frac{\partial T}{\partial t}\right)_s = \begin{cases} 0.231\dfrac{S_0 \cos Z}{\rho C_p}\left[\dfrac{r(z)}{\cos Z}\right]^{-0.7}\dfrac{dr}{dz} & \cos Z > 0 \\ 0 & \cos Z \le 0 \end{cases} \qquad \textbf{(A2.154)}$$

where *r(z)* is the optical path length of water vapor above the layer *z* and is given by

$$r(z) = \int_z^{top} \rho\, q dz. \qquad \textbf{(A2.155)}$$

A2.5.2 Longwave radiative flux

The normal optical thickness, integrated over all wavelengths is represented by the broadband emissivity, ε, used for the parameterization of longwave radiative flux in atmospheric models. Water content of the air affects the emissivity in clear and cloudy air. Water vapor and carbon dioxide (CO2) are the longwave radiation emitters. The path length for water vapor (Δr_j) is in units of g cm^{-2} and computed for each vertical layer as

$$\Delta r_j = \rho_j \; q_j \left(z_{j+1} - z_j \right) = -\frac{\left(P_{j+1} - P_j \right)}{g} q_j \qquad \textbf{(A2.156)}$$

and the path length for carbon dioxide (Δc_j) expressed in units of millibars is

$$\Delta c_j = -0.4148239 \left(P_{j+1} - P_j \right) \qquad \textbf{(A2.157)}$$

In order to calculate the total path length, they are summed up from the first level to the ith level to give as follows

$$r_{i+1} = \sum_{j=1}^{i} \Delta r_j \text{ and } c_{i+1} = \sum_{j=1}^{i} \Delta c_j \qquad \textbf{(A2.158)}$$

where $r_1 = c_1 = 0$ at the surface. The emissivity for water vapor was derived from data in Kuhn (1963) and is given in Jacobs *et al.*, (1974) by

$$\varepsilon_r (i,j) = \begin{cases} 0.113 \log_{10} (1 + 12.63 \bar{r}) & \log_{10} \leq -4 \\ 0.104 \log_{10} \bar{r} + 0.440 & -4 < \log_{10} \bar{r} \leq -3 \\ 0.121 \log_{10} \bar{r} + 0.491 & -3 < \log_{10} \bar{r} \leq -1.5 \\ 0.146 \log_{10} \bar{r} + 0.527 & -1.5 < \log_{10} \bar{r} \leq -1.0 \\ 0.161 \log_{10} \bar{r} + 0.542 & -1.0 < \log_{10} \bar{r} \leq 0 \\ 0.136 \log_{10} \bar{r} + 0.542 & \log_{10} \bar{r} > 0 \end{cases} \qquad \textbf{(A2.159)}$$

where $\bar{r} = |r_i - r_j|$ is the optical path length between the ith and jth level. The emissivity function for carbon dioxide is given by Kondratyev (1969) by

$$\varepsilon_{CO_2} (i,j) = 0.185 \left[1 - \exp \left(-0.3919 |c_i - c_j|^{0.4} \right) \right] \qquad \textbf{(A2.160)}$$

Total emissivity for each depth between level i and level j is then given by

$$\varepsilon (i,j) = \varepsilon_r (i,j) + \varepsilon_{CO_2} (i,j) \qquad \textbf{(A2.161)}$$

The downward and upward radiative fluxes at a level N can be computed using the above emissivity functions as

$$R \downarrow (N) = \sum_{j=N}^{top-1} \frac{\sigma}{2} \left(T_{j+1}^4 + T_j^4 \right) \left[\varepsilon (N, j+1) - \varepsilon (N, j) \right] + \sigma T_{top}^4 \left[1 - \varepsilon (N, top) \right] \qquad \textbf{(A2.162)}$$

$$R \uparrow (N) = \sum_{j=1}^{n-1} \frac{\sigma}{2} \left(T_{j+1}^4 + T_j^4 \right) \left[\varepsilon (N, j) - \varepsilon (N, j+1) \right] + \sigma T_G^4 \left[1 - \varepsilon (N, 1) \right] \qquad \textbf{(A2.163)}$$

where T_G and T_{top} are the temperatures at the ground level and model top, respectively and σ is the Stefan-Boltzman constant. Thus the radiative cooling at each level *N* except the ground level is calculated by using the following formulation

$$\left(\frac{\partial T}{\partial t}\right)_{LW} = \frac{1}{\rho C_p}\frac{\left[R\uparrow(N+1) - R\uparrow(N) + R\downarrow(N) - R\downarrow(N+1)\right]}{z(N+1) - z(N)} \quad \textbf{(A2.164)}$$

where *LW* denotes the longwave radiation and z is the height. Radiative transfer is computationally expensive without simplification. In OMEGA, it is needed to be simple parameterizations since complexity of the mesh is computationally much expensive. Sasamori's technique (1972) simplifies the computing procedure assuming an isothermal atmosphere for radiative transfer. The temperature change resulting from longwave radiative flux divergence is calculated at each level *N* as

$$\left(\frac{\partial}{\partial t}\right)_{LW} = \frac{1}{\rho C_p}\frac{\left(\sigma T_N^4 - \sigma T_G^4\right)\left[\varepsilon(N+1,1) - \varepsilon(N,1)\right] + \left(\sigma T_{top}^4 - \sigma T_N^4\right)\left[\varepsilon(N+1,top) - \varepsilon(N,top)\right]}{z(N+1) - z(N)} \quad \textbf{(A2.165)}$$

A2.6 Model Initial and Boundary Conditions

The OMEGA data preprocessor converts a diverse mixture of real-time atmospheric and surface data as an input into an OMEGA simulation. Two datasets produces from this process; one is the initial values of all the model's dependent variables and the surface based model parameters, second dataset consists of the time-dependent behaviour of all the model's dependent variables along the lateral boundaries of the simulation domain. The OMEGA analysis and initialization procedure have seven steps: 1) ingestion of the available data prepared by the PREPDAT module and the preliminary INIT file created by the GENINIT module, 2) objective analysis of sea surface temperature data, 3) processing and quality control of surface and upper air data, 4) objective analysis of surface and upper air data, 5) adjustments to ensure that the analyzed data meet desired constraints, 6) generation of objective analysis performance statistics, and 7) output of the initialization data to a modified INIT file.

The OMEGA data preprocessor uses the multivariate algorithm by DiMego (1988), which adapts in a natural way to the unstructured grid. The analysis proceeds horizontally layer by layer, cell by cell. The analysis is performed at the top center of each OMEGA grid cell as well as at the bottom of the lowest layer of cells. Corrections to the first-guess field for height and wind are computed using the multivariate algorithm and for relative humidity are computed using the simpler univariate algorithm. Corrections are computed for an entire layer and smoothed with a four-point smoother before being added to the first-guess. The smoother uses the value at a given cell to 50% of the original value adding 1/6 the value at each of the

three adjacent cells. OMEGA defines grid locations by absolute altitude hence, the height corrections are converted to pressure corrections. The variables are vertically interpolated to cell centroids. Temperature is analyzed only at the surface and is derived hydrostatically from the pressure at the top and bottom of the cell, at cell centroids. If a level is less than 10 mb from the last analyzed level, the analysis at this level is skipped. The corrections to the first guess are then interpolated from the corrections at the nearest analyzed layers above and below. This reduces the problem of noisy temperature fields due to small differences in the height correction at closely spaced analysis layers. As it is proposed by DiMego (1988) the surface temperature data are used to hydrostatically adjust the surface height increment in the lowest levels. The surface height increment is used directly at the ground. The surface height increment is hydrostatically corrected by assuming that the surface temperature perturbation is valid over in the first few model levels above the ground (up to about 40 mb above the surface). The corrected height increment is considered to be valid at the model level. Only the nearest height increment to a given level is included in the analysis matrix at any given grid point. This has the effect of influencing the thickness field near the ground so that the hydrostatically derived temperature field closely resembles a direct surface temperature analysis (Bacon, 2003).

Boundary conditions for computational domain is provided from large scale forecast models such as the Nested Grid Model, the Eta Model, or the Medium Range Forecast model run at National Center for Environmental Prediction (NCEP), or the Navy Operational Global Atmospheric Prediction System (NOGAPS) run at the Navy Fleet Numerical Meteorology and Oceanography Center. Boundary conditions at user-specified time intervals are calculated based on one of these forecasts and linear interpolation is used to determine boundary values at intermediate times. The lateral boundaries are open. Interior values of outflow boundaries interior value are used in the calculation of the fluxes across the boundary faces instead of forcast data. A radiative boundary condition with a uniform phase speed is used on outflow boundaries to allow the propagation of acoustic disturbances across the boundaries. A “nudging” scheme is applied at the each time step to the new values of all variables, which nudges values in cells immediately inside the boundary to the forecast values in the ghost cells across the boundary. The velocity normal to each

boundary face and the fluxes across the face are calculated using the forecast data at inflow boundaries. Initial values of density and potential temperature are calculated in a hydrostatic balance and remain fixed throughout the simulation at the top of the computational domain. A homogenous Neumann boundary condition is applied to the horizontal components of momentum when the vertical momentum is assumed to be zero. Hence, the upper boundary is considered a rigid, free-slip surface. A diffusive "sponge" behaviour is applied to the vertical component of momentum to minimize the reflection off of the upper boundary. The exponential sponge coefficient approaches zero below the top few layers of the grid. Monin-Obukhov similarity theory is applied in the surface boundary conditions formulation of OMEGA. The theory provides to determine the values of the model prognostic values at a diagnostic level between the first and second computational levels. No-slip condition is used at the ground surface in the OMEGA. The hydrostatic equation is used to calculate the surface pressure from the lowest atmospheric layer in the model. The surface density, ρ, is calculated from the known surface pressure and ground surface temperature using the ideal gas law. A zero flux boundary condition is assumed at the ground for all Eularian tracers (Q_t) and for the turbulent kinetic energy (Bacon, 2003).

A2.7 Urban Parameterization

Urban parameterization has been developed so as to represent modification on the parameters (such as, temperature, wind, moisture etc.) by urban areas. Urban parameterization in the OMEGA is fundamentally based on Brown (2000), which modifies drag and turbulence production into the flow equations and the surface energy budget and heat equation to account for urban influences. These parameterizations endeavor to account for the area-average effect of drag, turbulence production, heating, and surface energy budget modification induced by buildings and urban land-use. Since lack of spatial resolution does not allow mesoscale models to simulate the fluid dynamics and thermodynamics in and around urban structures directly, urban canopy parameterizations are used to approximate the drag, heating, radiation attenuation and enhanced turbulent mixing produced by the sub-grid scale urban elements. In this parameterization, different methods are used above the urban canopy and within the urban canopy. The bulk or area-average parameterization

attempts to implement the urban canopy layer into the mesoscale models. However, the model and the model physics are determined the utility of the urban parameterization.

A2.7.1 Drag force definition

A drag force term can be added to the atmospheric momentum conservation equations to account for obstacle drag. This approach has been successfully used to parameterize the frictional drag due to forest canopies (e.g., Wilson and Shaw, 1977; Yamada,1982; Liu et al., 1996) and has been used in several cases for urban canopies (e.g., Sorbjan and Uliasz, 1982; Brown and Williams, 1998; Urano et al.,1999). Since the drag coefficient approach, modifications can be made to the horizontal components of the momentum equations to account for the area-average effect of the sub-grid urban canopy elements:

$$\frac{DU}{Dt} = -\frac{1}{\rho}\frac{\partial P}{\partial x} + fV - \frac{\partial < uu_j >}{\partial x_j} - f_{urb} C_d a(z) U|U| \qquad \textbf{(A2.166a)}$$

$$\frac{DV}{Dt} = -\frac{1}{\rho}\frac{\partial P}{\partial y} - fU - \frac{\partial < vu_j >}{\partial x_j} - f_{urb} C_d a(z) V|V| \qquad \textbf{(A2.166b)}$$

where f is the Coriolis parameter, the $<u_i u_j>$ are the Reynolds shear stresses, f_{urb} is the fraction of the grid cell covered by urban canopy, $a(z)$ is the canopy area density (surface area of buildings perpendicular to the wind per unit volume of urban canopy), C_d is the drag coefficient, the other variables; ρ is the fluid density, U is the mean velocity in the x- direction and V is the mean wind in the y-direction, and P is the pressure. The drag force will be non-zero within the canopy and "turn-off" at some height above the canopy in response to the canopy area density $a(z)$ term. The drag formulation by Urano et al. (1999) and Sorbjan and Uliasz (1982) is nearly identical to equation 3.167, except that in the latter case they lumped C_d and $a(z)$ together and did not explicitly state that it could vary with height. The major disadvantage of the drag approach is to specify the new terms; f_{urb},, C_d, and $a(z)$ (Brown, 2000).

A2.7.2 Turbulence production/destruction

Enhanced turbulent production is seen in the urban environment due to buildings. Flow separation, recirculation zones, high shear, and production of turbulent eddies

result from the flow blockage, isolated regions of jetting, and adverse pressure gradients associated with the obstacle. Reynolds shear stress term, modified in the urban parameterization is modeled as a first-order gradient diffusion term:

$$< u_i u_j >= -K_m \left(\frac{\partial U_i}{\partial x_j} + \frac{\partial U_j}{\partial x_i} \right) \qquad \textbf{(A2.167)}$$

where K_m is the turbulent eddy diffusivity for momentum.

In mesoscale models using the k-ε or q^2-*l* turbulence closure approach to specify the eddy diffusivity, a turbulent kinetic energy production term can be added to the tke equation to account for urban-induced turbulence, (e.g., Brown and Williams, 1998; Maryuma, 1999; Urano et al., 1999)

$$\frac{Dtke}{Dt} = \delta_{i3} \frac{g}{\Theta} < u_i \theta > - < u_i u_j > \frac{\partial U_i}{\partial x_j} - \frac{\partial < u_j \cdot tke >}{\partial x_j} - \frac{1}{\rho} \frac{\partial < u_i p >}{\partial x_i} - \varepsilon + f_{urb} C_d a(z) \left(|U|^3 + |V|^3 \right) \qquad \textbf{(A2.168)}$$

where $tke = k = q^2/2 = 1/2(<u^2>+<v^2>+<w^2>)$ and ε is the dissipation term. This is the exact form of the tke equation without the closure assumptions used in k-ε or q^2-*l* modeling applied yet. The last term is the tke production term due to sub-grid urban canopy elements, where f_{urb} is the urban fraction of the grid cell, C_d is a drag coefficient, *a(z)* is the canopy area density, and *U* and *V* are the horizontal components of the wind velocity. The absolute value signs on the velocities ensure that the drag term is always a source of turbulent kinetic energy (Brown, 2000).

A2.8 Atmospheric Dispersion Model

Atmospheric dispersion can be seen every atmospheric dynamical process operating on scales larger than molecular dissipation and smaller than the latitudinal variation of the Coriolis force. Mesoscale energy is distributed over a variety of flows, such as mesoscale circulations, mesoscale eddies, and internal gravity waves. Flow dynamics are variable and complex on mesoscale flow which may be hydrostatic or non-hydrostatic. Significant features raging from several meters to several tens of kilometers on with timescales of minutes to many hours may be enclosed by non-hydrostatic motions. Hydrostatic motions including embedded non-hydrostatic motions have motion scales larger than the non-hydrostatic motions. Mesoscale

atmospheric flows own various mesoscale time and space scales. The range of flow scales can affect the transport and diffusion of atmospheric pollutants depending on variations in the mean wind, differential advection due to the vertical and horizontal wind shear, and vertical mixing (*c.f.* Moran, 1992). Time-space flow scale accuracy is important when the mesoscale dispersion processes are studied. Otherwise, significant components of mesoscale transport and diffusion may be neglected (Bacon et al., 2000). Atmospheric Dispersion Model (ADM) has benefit of using the OMEGA model-predicted meteorological fields (such as mean wind component and atmospheric turbulence information) at spatial and temporal resolution of the model since ADM is embedded within the OMEGA. Three dispersion models; an Eularian model, a Lagrangian particale dispersion model, and a probabilistic Lagrangian puff model are implemented in the ADM. These dispersion models advect massless tracers and gases and/or solid and liquid particles using the OMEGA resolved wind field, while simultaneously solving a diffusion model that simulates the effect of unresolved physics including turbulence. Massless tracers and gases are in thermodynamic and dynamic equilibrium with the ambient atmosphere whereas solid and liquid particles are allowed to settle out with a size and density dependent vertical slip velocity due to gravity (Bacon and Sarma, 1991).

A2.8.1 Eularian dispersion model

The OMEGA model assumes that the released gas instantaneously and uniformly fills the OMEGA cell containing the source. The Eularian tracers are assumed to be massless and advected by the mean wind and diffused by its turbulence components (Bacon et al., 2000). The conservation equation for the tracer field is calculated as

$$\frac{\partial Q_t}{\partial t} = -\nabla \cdot (QV) + S_t \qquad \textbf{(A2.169)}$$

where Q_t is the tracer concentration, S_t represents the tracer sources/sinks with subgrid scale turbulent transport fluxes. S_t is defined in the model via their source strength, latitude, longitude and altitude locations. Eularian model is well suited for the reactive nonlinear chemistry and wet deposition which have complex physical processes. Due to its gridpoint calculation independency of the number of sources, Eularian model is also well suited for a large number of geographically fixed sources (Bacon et al., 2000).

A2.8.2 Lagrangian particle dispersion model

The Lagrangian particle dispersion model uses Monte Carlo technique to simulate dispersion of non-buoyant and dynamically passive pollutants released from multiple emission sources with different geometry and release duration (Bacon et al., 2000). Particles fall out with a vertical slip velocity because of the gravity. The terminal velocity, V_t, is used determining the slip velocity. The particle momentum equation used to the terminal velocity calculation.

$$M_p \frac{\partial w}{\partial t} = M_p g \frac{\alpha}{2}\left(0.4 + \frac{24}{R_e}\right) A_p \rho_a w \left\| V_p \right\| \qquad \textbf{(A2.170)}$$

where: $w \equiv$ the component of particle velocity perpendicular to the ground,

$\alpha \equiv$ drag coefficient multiplier for rough spheres,

$g \equiv$ acceleration due to gravity,

$R_e \equiv$ Reynold's number,

$A_p \equiv$ cross-sectional area of the spherical particle, and

$\rho_a \equiv$ ambient air density.

Setting $\frac{\partial w}{\partial t} = 0$ gives

$$V_t = \left(\frac{30\mu}{\rho_a D}\right)\left(-1 + \sqrt{1 + \frac{D^3 g \rho_a \rho_p}{405\mu^2}}\right) \qquad \textbf{(A2.171)}$$

where μ is the dynamic viscosity of air, ρ_a is the ambient air density, ρ_p is the particle density, D is the particle diameter, and g is the acceleration due to the gravity.

The model simulates the dispersion with pseudovelocities at each time step. Effects of two basic dispertion components are simulated by pseudovelocities: 1) transport due to the mean wind, and 2) diffusion due to turbulent velocity fluctuations (Boybeyi et al., 1995). Subsequent positions of each particle (x, y, z) which represents a discrete element of pollutant mass are computed from the following equations:

$$\begin{aligned} x(t+\Delta t) &= x(t) + \left[\bar{u}(t) + u'(t)\right]\Delta t, \\ y(t+\Delta t) &= y(t) + \left[\bar{v}(t) + v'(t)\right]\Delta t, \\ z(t+\Delta t) &= z(t) + \left[\bar{w}(t) + w'(t)\right]\Delta t, \end{aligned} \qquad \textbf{(A2.172-A2.174)}$$

where $\bar{u}, \bar{v},$ and $\bar{w}$ are mean wind components from the OMEGA model, and

u', v', and w' are subgrid-scale turbulent velocity fluctuations. Their statistics are derived from the boundary layer formulation used in OMEGA. The sub-grid scale particle turbulent velocity fluctuations are calculated using a Markov chain scheme;

$$\begin{aligned} u'(t+\Delta t) &= R_{u'}(\Delta t)u'(t) + u''(t+\Delta t), \\ v'(t+\Delta t) &= R_{v'}(\Delta t)v'(t) + v''(t+\Delta t) \\ w'(t+\Delta t) &= R_{w'}(\Delta t)w'(t) + w''(t+\Delta t) \end{aligned} \qquad \textbf{(A2.175-A2.177)}$$

where u'', v'', and w'' are random uncorrelated turbulent velocity components. These random turbulent velocity components distribute in Gaussian with zero mean values, viz., they are characterized by the variances;

$$\begin{aligned} \sigma^2_{r_{u'}} &= \sigma^2_{u'}(1-R^2{}_{u'}), \\ \sigma^2_{r_{v'}} &= \sigma^2_{v'}(1-R^2{}_{v'}), \\ \sigma^2_{r_{w'}} &= \sigma^2_{w'}(1-R^2{}_{w'}), \end{aligned} \qquad \textbf{(A2.178-A2.180)}$$

where $R_{u'}$, $R_{v'}$, and $R_{w'}$ are auto-correlation coefficients for each velocity component and assumed to be exponential;

$$\begin{aligned} R_{u'}(\Delta t) &= \frac{\overline{u'(t)u'(t-\Delta t)}}{\sigma^2_{u'}} = \exp\left(-\frac{\Delta t}{T_L^{u'}}\right) \\ R_{v'}(\Delta t) &= \frac{\overline{v'(t)v'(t-\Delta t)}}{\sigma^2_{v'}} = \exp\left(-\frac{\Delta t}{T_L^{v'}}\right) \\ R_{w'}(\Delta t) &= \frac{\overline{w'(t)w'(t-\Delta t)}}{\sigma^2_{w'}} = \exp\left(-\frac{\Delta t}{T_L^{w'}}\right) \end{aligned} \qquad \textbf{(A2.181-A2.183)}$$

where $T_L^{u'}$, $T_L^{v'}$, and $T_L^{w'}$ are the Lagrangian integral time scales of the sub-grid scale turbulence. Turbulent kinetic energy closure in the OMEGA allows to determine a variety of turbulent statistics which is necessary to run the Lagrangian particle dispersion model are obtained from the level 2.5 Mellor and Yamada scheme (*c.f.* Uliasz, 1990).

A2.8.3 Plume rise

The study of Briggs (1969, 1979) is used as a basis of the plume rise treatment in the model. Using wind and stability values at the point, plume rise equations are applied separately to each puff centroid. This allows to simulate spatial and temporal variations of atmospheric stability. The governing parameter is the buoyancy flux F(m^{-4} s^{-3}), given as;

$$F = \frac{g v_e d_e^2 (T_e - T)}{4T_e} \qquad \textbf{(A2.184)}$$

where g gravitational acceleration, v_e stack gas exit speed, d_e stack exit diameter, T_e stack gas exit temperature, and T ambient temperature. Four different equations (depending on wind speed and stability) are used to determine plume rise. Stability, is also needed to define plume rise given by

$$S = \frac{g}{\theta}\frac{\Delta\theta}{\Delta z} \qquad \textbf{(A2.185)}$$

The equations for plume rise w_p when $S > 4.2\text{x}10^{-2}\text{V}^2/\text{H}^2$ (stable conditions) are

$$\begin{aligned} w_p &= \frac{2.6}{\Delta t}\left(\frac{F}{1000\, S H_s^2 V}\right)^{1/3}\left[(x_t + V\Delta\Delta)^{2/3} - x_t^{2/3}\right] \text{when } V > V_s \\ w_p &= \frac{5.3}{\Delta t}\left(\frac{10\, H_s}{V_s}\right)^{-2/3}\left(\frac{F}{S^{3/2}}\right)^{1/4}\left[(t + V\Delta\Delta)^{2/3} - t^{2/3}\right] \text{when } V \le V_s \end{aligned} \qquad \textbf{(A2.186)}$$

where H_s is stack height, V is horizontal wind speed, and V_s is critical wind speed which are separated 'calm' from 'not calm' conditions for stable conditions as defined by

$$V_s = 0.14 F^{1/4} S^{1/8} \qquad \textbf{(A2.187)}$$

Plume rise is determined using travel time. Maximum plume rise under stable conditions is obtained when

$$t = 10\frac{H_s}{V_s} \qquad \textbf{(A2.188)}$$

when $S > 4.2\text{x}10^{-2}\text{V}^2/\text{H}^2$ (neutral and unstable conditions)

$$\begin{aligned} w_p &= \frac{1.6F^{1/3}}{V\Delta t}\left[(x_t + V\Delta t)^{2/3} - x_t^{2/3}\right] \qquad \text{when } \text{V} > \text{V}_\text{n} \\ w_p &= \frac{1.6F^{1/3}}{V_n\Delta t}\left[(x_t + V\Delta t)^{2/3} - x_t^{2/3}\right] \qquad \text{when } \text{V} \le \text{V}_\text{n} \end{aligned} \qquad \textbf{(A2.189)}$$

where V_n is critical wind speed are separated 'calm' from 'not calm' conditions for neutral or unstable conditions is defined by

$$V_n = \frac{1.6\text{F}^{1/3}}{Z_{\max}}(10H_s)^{2/3} \qquad \textbf{(A2.190)}$$

where Z_{max} is the maximum plume rise wich can be occured during light winds and neutral or unstable conditions.

A2.8.4 Concentration calculation

A new group of Lagrangian puff (*N*) is generated by the probabilistic puff model at a user defined time interval (Δt) in the OMEGA. Local wind speed and turbulence diffusion at the source show the number of puffs released. *N* is chosen distance between two puffs which should be approximately equal to half of the horizontal standard deviation, σ_h. Each puff shows a discrete element of the total material release into the atmosphere. The puffs move via the OMEGA model mean wind field and locations of each puff center are computed by equations (A2.172-A2.174) where turbulence components are omitted. Puff diffusion is estimated based on Taylor's homogenous diffusion theory. It is assumed that the theory is applicable over short time scales (*c.f.* Uliasz, 1990 or Arya, 1999), for example, the time step, Δt, used to transport puffs in OMEGA (Bacon et al., 2000):

$$\begin{aligned} \sigma_x(t+\Delta t) &= \sigma_x(t) + \sigma_u \Delta t && \text{for } t \le 2T_L^u \text{, and} \\ \sigma_x^2(t+\Delta t) &= \sigma_x^2(t) + 2T_L^u \sigma_u^2 \Delta t && \text{for } t > 2T_L^u \end{aligned} \qquad \textbf{(A2.191)}$$

where σ_u is the variance of wind velocity component and T_L^u is the Lagrangian integral timescale. Turbulence characteristics are provided from the turbulence closure scheme in the OMEGA model. σ_y and σ_z are also determined in a similar way (Uliasz, 1990).

The local representation of the turbulence and velocity fields becomes inaccurate when the puffs grow. If the puffs split into the smaller components, the accuracy of the calculation can be maintained. The growth of a puff extends either vertically or horizontally over one cell area of the model is the puff splitting scheme in OMEGA. The puff is divided into two or more puffs which the sum of all puff component's air masses equals the initial puff air mass. Gaussian function is used to distribute the concentration within each puff. σ_x, σ_y and σ_z values of Gaussian function increase with travel time or distance. Information of puff location such as, the material in it, and its geometrical dimensions allows concentration to be determined by summing contribution from each puff. Generalized Gaussian distribution with reflection terms from ground and mixing layer height used to compute local concentration values (Bacon, 2003).

$$C(x,y,z,t) = \frac{Q}{(2\pi)^{2/3}\sigma_x\sigma_y\sigma_z}\exp\left[-\frac{(x-x_c)^2}{2\sigma_x^2}\right]\exp\left[-\frac{(y-y_c)^2}{2\sigma_y^2}\right]\times$$
$$\left\{\exp\left[-\frac{(z-z_c)^2}{2\sigma_z^2}\right]+f_g\exp\left[-\frac{(z+z_c)^2}{2\sigma_z^2}\right]+f_m\exp\left[-\frac{(2z_m-z-z_c)^2}{2\sigma_z^2}\right]\right\} \quad \textbf{(A2.192)}$$

where C is concentration, Q is the mass of puff, x, y, z are position of receptor x_c, y_c, z_c are the position of the puff center point, f_g is the fraction of cloud mass reaching the ground reflected back into cloud mass, f_m is the fraction of cloud mass reaching the mixing layer reflected back into the cloud, z_m is the mixed layer height. The integrated surface dosage can be calculated as

$$\chi(x,y,t) = \int_0^t C\ x,y,0,t'\ dt' \quad \textbf{(A2.193)}$$

Amount of dosage is accumulated on a stationary receptor network.

Table A2. 2: The USGS Global Ecosystem land-use classification and their associated surface properties.

Land Use description	ALB	EMISS	Z0	BSF	ICMN	LAI	RSMIN	TADM	SVF
Urban	0.187	0.850	75.0	0.000	0.000	0.500	40.0	1222.0	0.800
Low Sparse Grassland	0.184	0.900	2.0	0.500	0.100	1.500	40.0	600.0	1.000
Coniferous Forest	0.160	0.900	113.0	0.100	0.200	2.300	150.0	600.0	1.000
Deciduous Conifer Forest	0.160	0.900	113.0	0.100	0.200	2.300	150.0	600.0	1.000
Deciduous Broadleaf Forest	0.160	0.900	90.0	0.100	0.200	2.300	150.0	600.0	1.000
Evergreen Broadleaf Forests	0.160	0.900	240.0	0.100	0.200	2.300	150.0	600.0	1.000
Tall Grasses And Shrubs	0.184	0.900	15.0	0.500	0.100	1.500	40.0	600.0	1.000
Bare Desert	0.200	0.850	0.1	0.100	0.000	0.500	200.0	620.0	1.000
Upland Tundra	0.169	0.900	4.0	1.000	0.000	1.000	200.0	600.0	1.000
Irrigated Grassland	0.184	0.900	3.0	0.500	0.100	1.500	40.0	600.0	1.000
Semi Desert	0.200	0.850	1.0	0.100	0.000	0.500	200.0	620.0	1.000
Glacier Ice	0.500	0.900	0.1	0.000	0.000	0.100	999.0	594.0	1.000
Wooded Wet Swamp	0.179	0.920	66.0	0.100	0.000	1.500	40.0	600.0	1.000
Inland Water	0.016	0.950	0.1	1.000	0.000	0.100	40.0	600.0	1.000
Sea Water	0.016	0.950	0.1	1.000	0.000	0.100	40.0	600.0	1.000
Shrub Evergreen	0.160	0.900	23.0	0.100	0.200	2.300	150.0	600.0	1.000
Shrub Deciduous	0.160	0.900	23.0	0.100	0.200	2.300	150.0	600.0	1.000
Mixed Forest And Field	0.160	0.900	120.0	0.100	0.200	2.300	150.0	600.0	1.000
Evergreen Forest And Fields	0.160	0.900	120.0	0.100	0.200	2.300	150.0	600.0	1.000
Cool Rain Forest	0.160	0.900	113.0	0.100	0.200	2.300	150.0	600.0	1.000
Conifer Boreal Forest	0.160	0.900	75.0	0.100	0.200	2.300	150.0	600.0	1.000
Cool Conifer Forest	0.160	0.900	113.0	0.100	0.200	2.300	150.0	600.0	1.000
Cool Mixed Forest	0.160	0.900	113.0	0.100	0.200	2.300	150.0	600.0	1.000
Mixed Forest	0.160	0.900	113.0	0.100	0.200	2.300	150.0	600.0	1.000
Cool Broadleaf Forest	0.160	0.900	113.0	0.100	0.200	2.300	150.0	600.0	1.000
Deciduous Broadleaf Forest	0.160	0.900	90.0	0.100	0.200	2.300	150.0	600.0	1.000
Conifer Forest	0.160	0.900	113.0	0.200	0.100	2.300	150.0	600.0	1.000
Montane Tropical Forests	0.160	0.900	75.0	0.100	0.200	2.300	150.0	600.0	1.000
Seasonal Tropical Forest	0.160	0.900	113.0	0.100	0.200	2.300	150.0	600.0	1.000
Cool Crops And Towns	0.169	0.900	12.0	1.000	0.000	1.000	40.0	600.0	1.000
Crops And Town	0.169	0.900	12.0	1.000	0.000	1.000	40.0	600.0	1.000
Dry Tropical Woods	0.160	0.900	38.0	0.100	0.200	2.300	150.0	600.0	1.000
Tropical Rainforest	0.160	0.900	240.0	0.100	0.200	2.300	150.0	600.0	1.000
Tropical Degraded Forest	0.160	0.900	180.0	0.100	0.200	2.300	150.0	600.0	1.000
Corn And Beans Cropland	0.169	0.900	6.0	1.000	0.000	1.000	40.0	600.0	1.000
Rice Paddy And Field	0.169	0.900	3.0	1.000	0.000	1.000	40.0	600.0	1.000

Table A2. 2 : (contd.) The USGS Global Ecosystem land-use classification and their associated surface properties.

Land Use description	ALB	EMISS	Z0	BSF	ICMN	LAI	RSMIN	TADM	SVF
Hot Irrigated Cropland	0.169	0.900	6.0	1.000	0.000	1.000	40.0	600.0	1.000
Cool Irrigated Cropland	0.169	0.900	6.0	1.000	0.000	1.000	40.0	600.0	1.000
Cold Irrigated Cropland	0.169	0.900	6.0	1.000	0.000	1.000	40.0	600.0	1.000
Cool Grasses And Shrubs	0.184	0.900	20.0	0.500	0.100	1.500	40.0	600.0	1.000
Hot And Mild Grasses And Shrubs	0.184	0.900	20.0	0.500	0.100	1.500	40.0	600.0	1.000
Cold Grassland	0.184	0.900	5.0	0.500	0.100	1.500	40.0	600.0	1.000
Savanna (Woods)	0.160	0.900	28.0	0.100	0.200	2.300	150.0	600.0	1.000
Mire, Bog, Fen	0.179	0.920	6.0	0.100	0.000	1.500	40.0	600.0	1.000
Marsh Wetland	0.179	0.920	28.0	0.100	0.000	1.500	40.0	600.0	1.000
Mediterranean Scrub	0.184	0.900	10.0	0.500	0.100	1.500	40.0	600.0	1.000
Dry Woody Scrub	0.184	0.900	10.0	0.500	0.100	1.500	40.0	600.0	1.000
Dry Evergreen Woods	0.160	0.900	38.0	0.100	0.200	2.300	150.0	600.0	1.000
Volcanic Rock	0.200	0.850	0.1	0.100	0.000	0.500	200.0	620.0	1.000
Sand Desert	0.200	0.850	0.1	0.100	0.000	0.500	200.0	620.0	1.000
Semi Desert Shrubs	0.184	0.900	3.0	0.500	0.100	1.500	40.0	600.0	1.000
Semi Desert Sage	0.184	0.900	3.0	0.500	0.100	1.500	40.0	600.0	1.000
Barren Tundra	0.169	0.900	1.0	1.000	0.000	1.000	200.0	600.0	1.000
Cool Southern Hemisphere Mixed Forests	0.160	0.900	90.0	0.100	0.200	2.300	150.0	600.0	1.000
Cool Fields And Woods	0.160	0.900	108.0	0.100	0.200	2.300	150.0	600.0	1.000
Forest And Field	0.160	0.900	120.0	0.100	0.200	2.300	150.0	600.0	1.000
Cool Forest And Field	0.160	0.900	120.0	0.100	0.200	2.300	150.0	600.0	1.000
Fields And Woody Savanna	0.160	0.900	45.0	0.100	0.200	2.300	150.0	600.0	1.000
Succulent And Thorn Scrub	0.184	0.900	3.0	0.500	0.100	1.500	40.0	600.0	1.000
Small Leaf Mixed Woods	0.160	0.900	28.0	0.100	0.200	2.300	150.0	600.0	1.000
Deciduous And Mixed Boreal Forest	0.160	0.900	75.0	0.100	0.200	2.300	150.0	600.0	1.000
Narrow Conifers	0.160	0.900	90.0	0.100	0.200	2.300	150.0	600.0	1.000
Wooded Tundra	0.169	0.900	63.0	1.000	0.000	1.000	200.0	600.0	1.000
Heath Scrub	0.184	0.900	6.0	0.500	0.100	1.500	40.0	600.0	1.000
Coastal Wetland - Nw	0.179	0.920	28.0	0.100	0.000	1.500	40.0	600.0	1.000
Coastal Wetland - Ne	0.179	0.920	28.0	0.100	0.000	1.500	40.0	600.0	1.000
Coastal Wetland, Se	0.179	0.920	28.0	0.100	0.000	1.500	40.0	600.0	1.000
Coastal Wetland - Sw	0.179	0.920	28.0	0.100	0.000	1.500	40.0	600.0	1.000
Polar And Alpine Desert	0.169	0.900	1.0	1.000	0.000	1.000	200.0	600.0	1.000
Glacier Rock	0.200	0.850	0.1	0.100	0.000	0.500	200.0	620.0	1.000
Salt Playas	0.169	0.900	0.1	1.000	0.000	1.000	200.0	600.0	1.000

Table A2. 2 : (contd.) The USGS Global Ecosystem land-use classification and their associated surface properties.

Land Use description	ALB	EMISS	Z0	BSF	ICMN	LAI	RSMIN	TADM	SVF
Mangrove	0.160	0.900	90.0	0.100	0.200	2.300	150.0	600.0	1.000
Water And Island Fringe	0.200	0.850	5.0	0.100	0.000	0.500	200.0	620.0	1.000
Land, Water, And Shore	0.200	0.850	5.0	0.100	0.000	0.500	200.0	620.0	1.000
Land And Water, Rivers	0.200	0.850	5.0	0.100	0.000	0.500	200.0	620.0	1.000
Crop And Water Mixtures	0.169	0.900	3.0	1.000	0.000	1.000	40.0	600.0	1.000
Southern Hemisphere Conifers	0.160	0.900	113.0	0.100	0.200	2.300	150.0	600.0	1.000
Southern Hemisphere Mixed Forest	0.160	0.900	90.0	0.100	0.200	2.300	150.0	600.0	1.000
Wet Sclerophylic Forest	0.160	0.900	135.0	0.100	0.200	2.300	150.0	600.0	1.000
Coastline Fringe	0.200	0.850	0.1	0.100	0.000	0.500	200.0	620.0	1.000
Beaches And Dunes	0.200	0.850	0.1	0.100	0.000	0.500	200.0	620.0	1.000
Sparse Dunes And Ridges	0.200	0.850	0.4	0.100	0.000	0.500	200.0	620.0	1.000
Bare Coastal Dunes	0.200	0.850	0.1	0.100	0.000	0.500	200.0	620.0	1.000
Residual Dunes And Beaches	0.200	0.850	0.1	0.100	0.000	0.500	200.0	620.0	1.000
Compound Coastlines	0.200	0.850	5.0	0.100	0.000	0.500	200.0	620.0	1.000
Rocky Cliffs And Slopes	0.200	0.850	5.0	0.100	0.000	0.500	200.0	620.0	1.000
Sandy Grassland And Shrubs	0.184	0.900	1.0	0.500	0.100	1.500	40.0	600.0	1.000
Bamboo	0.160	0.900	15.0	0.100	0.200	2.300	150.0	600.0	1.000
Moist Eucalyptus	0.160	0.900	90.0	0.100	0.200	2.300	150.0	600.0	1.000
Rain Green Tropical Forest	0.160	0.900	150.0	0.100	0.200	2.300	150.0	600.0	1.000
Woody Savanna	0.160	0.900	38.0	0.100	0.200	2.300	150.0	600.0	1.000
Broadleaf Crops	0.169	0.900	6.0	1.000	0.000	1.000	40.0	600.0	1.000
Moist Eucalyptus	0.160	0.900	90.0	0.100	0.200	2.300	150.0	600.0	1.000
Rain Green Tropical Forest	0.160	0.900	150.0	0.100	0.200	2.300	150.0	600.0	1.000
Woody Savanna	0.160	0.900	38.0	0.100	0.200	2.300	150.0	600.0	1.000
Broadleaf Crops	0.169	0.900	6.0	1.000	0.000	1.000	40.0	600.0	1.000
Grass Crops	0.169	0.900	6.0	1.000	0.000	1.000	40.0	600.0	1.000
Crops, Grass, Shrubs	0.169	0.900	11.0	1.000	0.000	1.000	40.0	600.0	1.000
Evergreen Tree Crop	0.160	0.900	100.0	0.100	0.200	2.300	150.0	600.0	1.000
Deciduous Tree Crop	0.160	0.900	100.0	0.100	0.200	2.300	150.0	600.0	1.000
NO DATA	0.000	0.000	0.0	0.000	0.000	0.000	0.0	0.0	0.000
NO DATA	0.000	0.000	0.0	0.000	0.000	0.000	0.0	0.0	0.000
Interrupted areas	0.000	0.000	0.0	0.000	0.000	0.000	0.0	0.0	0.000
Missing Data	0.000	0.000	0.0	0.000	0.000	0.000	0.0	0.0	0.000

APPENDIX B

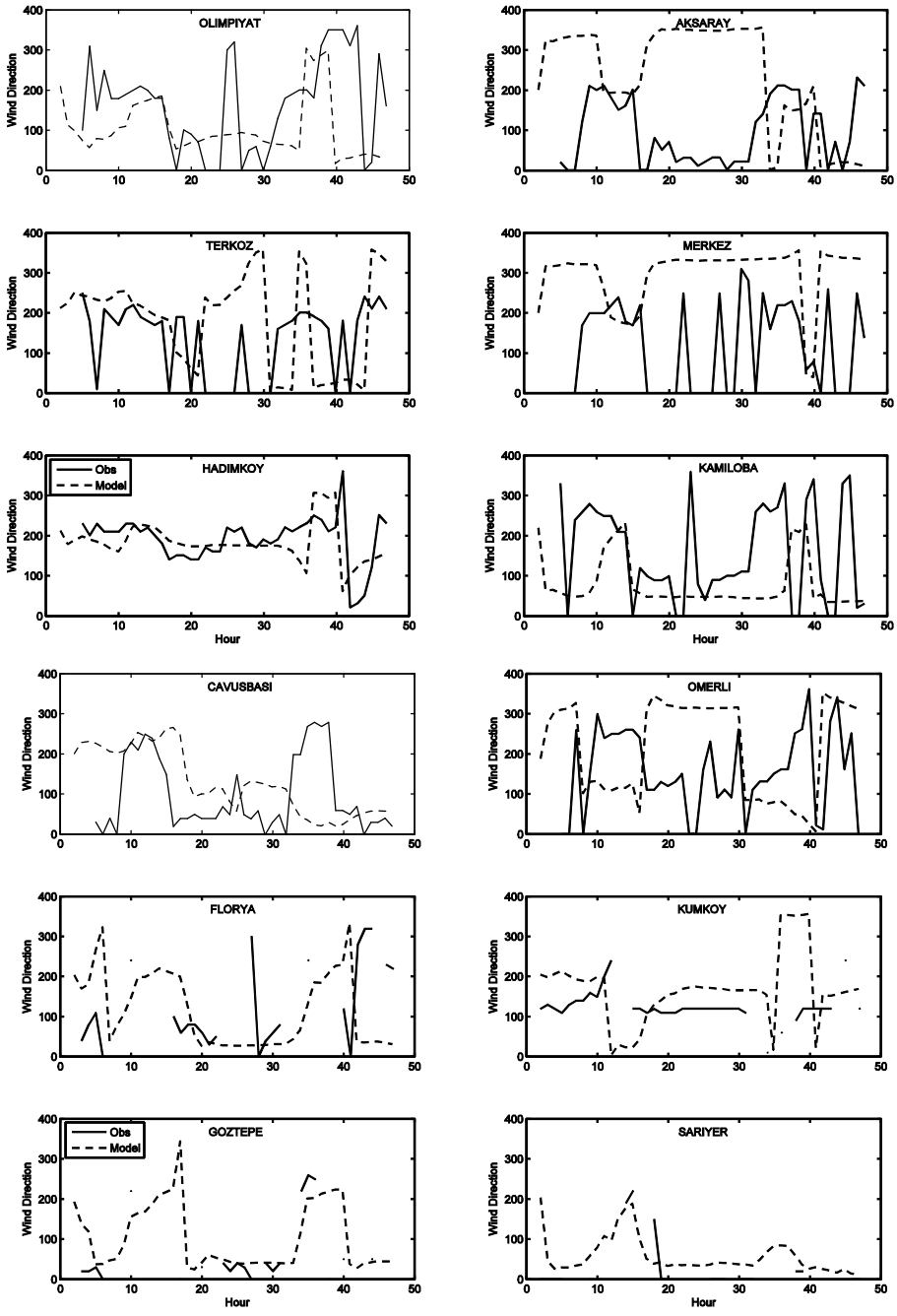

Figure B. 1: Meteograms of wind direction on 08-10 December 2006, solid line is observation and dash line is model results.

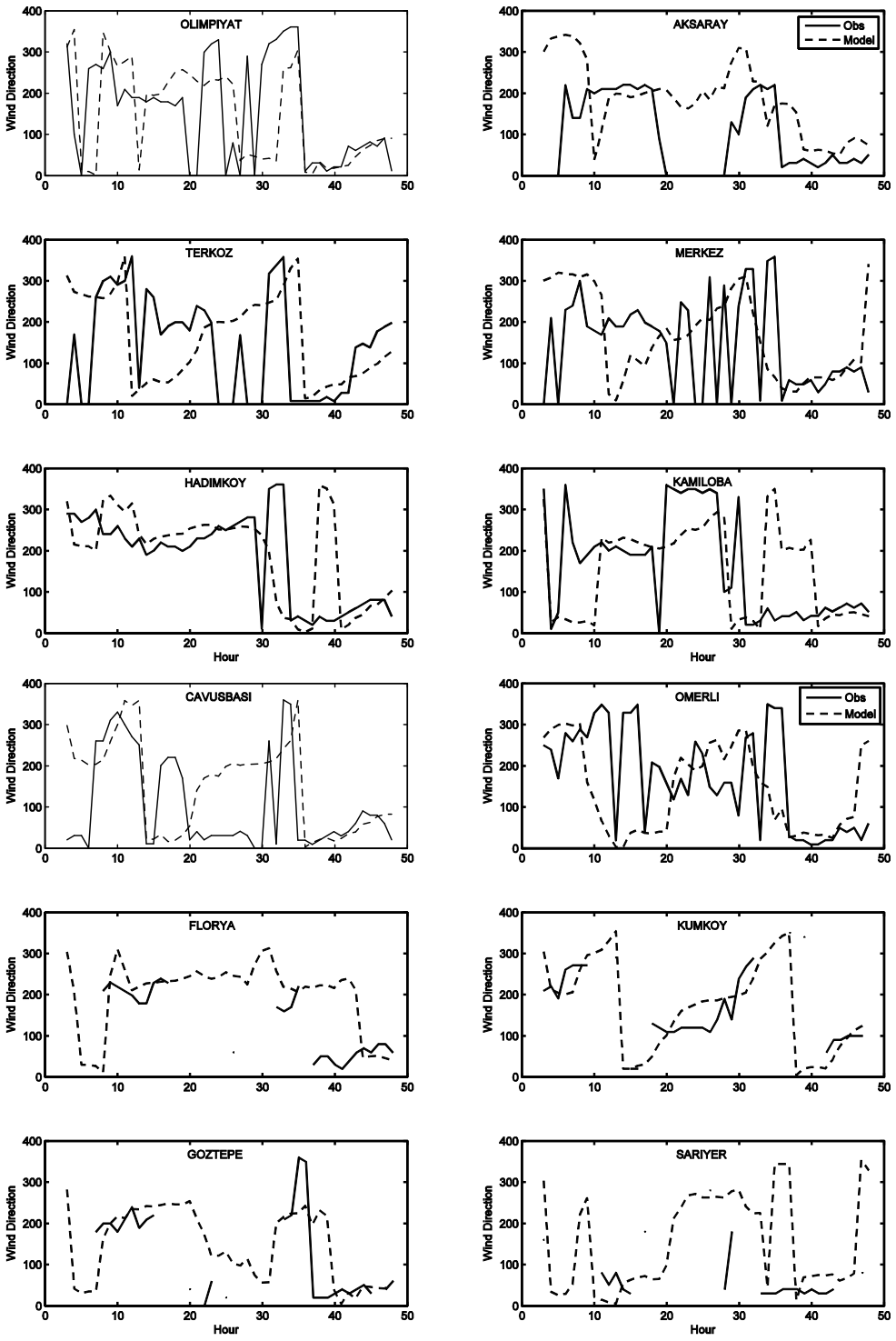

Figure B. 2 : Meteograms of wind direction on 07-09 July 2007, solid line is observation and dash line is model results.

CURRICULUM VITAE

Candidate's full name: Yasemin EZBER

Place and date of birth: Istanbul, 09/04/1977

Permanent Address: Eski Sular C. Cicek S. Ufuk Apt. No:22/3 34450, Sariyer/Istanbul

Universities attended: Istanbul Technical University

B.S. : Meteorological Engineering, 2000.
M.Sc.: Eurasia Institute of Earth Sciences, 2003.

Publications:

- Cervone G., P. Franzese , **Y. Ezber**, and Z. Boybeyi: Risk assessment of atmospheric emissions using machinelearning, Nat. Hazards Earth Syst. Sci. 991-1000, 2008.
- **Ezber Y.**, Şen, Ö.L., Kındap, T., Karaca, M.: Climatic effects of urbanization in Istanbul: A statistical and modeling analysis. International Journal of Climatology, Volume 27, April 2007.

Conferences:

- Cervone G. Franzese P., **Ezber Y.**, and Boybeyi Z.: "Risk Assessment of Atmospheric Hazard Releases using K-means". International Workshop on Spatial and Spatiotemporal Data Mining (SSTDM- 08) In Cooperation with IEEE ICDM 2008. December 15-19 2008.
- G. Cervone, P. Franzese, **Y. Ezber** & Z. Boybeyi: Mesoscale Transport and Dispersion Uncertainty Assessment using Machine Learning. 11th Annual George Mason University Conference on"Atmospheric Transport and Dispersion Modeling", July 10-12, 2007.
- Z. Boybeyi, **Y. Ezber**, G. Cervone & M. Karaca: A Risk Assessment Study for the Strait of Istanbul. 11th Annual George Mason University Conference on"Atmospheric Transport and Dispersion Modeling",July 10-12, 2007.
- Boybeyi, Z., **Ezber, Y.** and Karaca, M.: A Risk Assessment Study for the City of Istanbul. 10th Annual George Mason University Conference on"Atmospheric Transport and Dispersion Modeling",August 1-3, 2006.
- Karaca M., **Ezber Y.**, Şen Ö., Kıdap T.: "Unplanned Urbanization and Climate: Example of Istanbul", Urban Biosphere Reserves:Potantial of Istanbul Workshop, 31 January-1 February 2005, Istanbul.

- Karaca M., **Y. Ezber** and E. Kahya: ”Detecting Climate Change in the Coastal Zone of the Black Sea Region of Turkey”, International Workshop on Black Sea Coastal Air-Sea Interaction Phenomena and Related Impacts and Application, 3-15 May 2004, Constanta, Romania.
- **Ezber Y.**, M.Karaca: “North Atlantic Oscillation: Comparision of two extreme years, “EGU 1st General Assembly 2004, 25-30 April 2004, Nice, France.
- **Ezber Y.**, Y.Sunal, E. Kahya, M. Karaca: ”North Atlantic Oscillation: Comparision of two extreme years”, Sırrı Erinç Symposium 2003,11 -13 September 2003, Istanbul University, Turkey.
- Menteş S.Ş., Y. Tulunay, **Y. Ezber**, Y. Borhan: “The meteorological interpretation of The Refractive Index Variations within the 10m altitude in 1999 Summer and Autumn’’, EGS 2000, 25.th General Assembly, OA19, NICE.